High Pressure Nozzle Guide Vane Cooling System Flow Characteristics



Irene Cresci

St Cross College

University of Oxford

A thesis submitted in partial fulfilment
of the requirements for the degree of
Doctor of Philosophy

Hilary Term 2016

Abstract

The continuous demand from the airlines for reduced jet engine fuel consumption results in increasingly challenging high pressure turbine nozzle guide vane (NGV) working conditions. The capability to reproduce representative boundary conditions in a rig at the combustor-turbine interaction plane is a key feature when testing NGVs in an engine-representative environment. A large scale linear cascade rig to investigate NGV leading edge cooling systems has been designed with particular attention being paid to creating engine representative conditions at the NGV inlet plane. The combustor simulator replicates the main features of a rich-burn design including large dilution jets and extensive endwall film cooling. CFD simulations have been used to develop the design which matches Reynolds number and mainstream-to-dilution jet momentum flux ratio. Detailed measurements of velocity, turbulence and temperature have been acquired at the NGV inlet plane. A thermocouple was manufactured from 12.7 μm diameter wire and carefully calibrated to obtain its time constant in the velocity range of interest. The results are compared to CFD predictions and data in the literature. The time-averaged measurements show that the flow field conditions are dominated by the endwall cooling flows. The time-resolved data show that the measured turbulence length scale reflects the scale of the relevant upstream jets while the spectrum of temperature fluctuations reports a thermal cascade independent of any geometrical features.

Attention was also focused on the flow field downstream of different endwall film cooling holes configurations: three arrangements of a double row of staggered cylindrical holes (lateral pitch-to-diameter ratio of 2 - 3 - 6) and one with intersecting

holes (intersecting angle of 90^o) were experimentally and numerically analyzed. The research quantified the extent by which closer spaced hole configurations provide more effective film coverage. It was found that the turbulent integral length scales are strongly connected to the hole diameter and spacing. It was also found that intersecting holes can potentially reduce the amount of required coolant at a fixed pressure ratio, but offer worst film performance than cylindrical holes. RANS simulations proved successful at predicting the main trends shown by the measurements.

A new concept to increase the pressure margin across the film cooling holes in a specific region of vane LE coolant passage was introduced and developed: an insert was used to cover the area with the highest risk of ingestion, slowing down the flow and increasing the local static pressure. Numerical simulations were initially used to compare different designs and to analyse the impact of the insert on the overall coolant flow distribution. In particular, the effect on the static pressure downstream of the insert was identified as a critical factor that needs to be taken into account during the design process in order to avoid hot gas ingestion in other areas. The experimental campaign proved the ability of this new design to significantly increase the pressure margin in the covered region.

Al nonno Roberto

Acknowledgments

Reaching the end of this thesis,I feel the need to thank a lot of people for their help, presence and support in these last 4 years (and more).

I would firstly like to acknowledge Prof. Peter Ireland for his enduring support and his endless passion for his work: he was a continuous source of inspiration through all my DPhil. I would sincerely thank Prof. M. Bacic (UO), Mr. A. Rawlinson (RR) and Mr. I. Tibbott (RR) for the precious help and continuous feedback. I am extremely grateful to Rolls-Royce for funding my DPhil through the ENTAPS program.

I need to show my deepest gratitude to Gerald Walker for all the incredible patience he showed me in the process of building and assembling the CTI rig. To Dave Mountain and Dave O'Dell, Sam Davies, Leo Verling and Duncan Blake for standing all my last minutes/high priority requests. To Jez Bowles who helped me with the HTA boxes. To Trevor Godfrey for sparing my life when I dropped and broke the fine thermocouple. To Michael Japp for connecting more than 100 pressure tappings for my vanes. To Paul Cox, Hal Surtell and Bill Godfrey for all the work the CTI rig required.

My Oxonian life would have not been the same without my friends: Holt, the best colleague/housemate/friend that Asia has ever given birth to, Inés, my lab frustration sharing friend and my favourite Spanish bride, Josh, thanks for standing the incredibly boring thesis proof-reading, Ioanna, the travel companion, Paola, my Oxonian sister, Alessandra, the one "who talks like me". And everybody else who helped me feeling at home every day.

I need to thank my friends from my "past" lives at VKI, in Florence and Pontassieve: I have never felt you so close as when I was far away. A special mention to the man who first told me to apply for a DPhil in Oxford when I thought "I was not enough": Filippo Coletti, unfortunately life set us apart, but you have been the best mentor/bro ever.

And finally the people I love the most in this big and chaotic world: my incredible family, no words on earth could express how much I have missed you all, and Tancredi, that I have luckily avoid to kill with muesli in Summer 2013.

Nomenclature

Acronyms

ACARE	Advisory Council for Aeronautics Research in Europe
ADS	Aerospace Defence Security (ADS Group)
CFD	Computational Fluid Dynamics
CTI	Combustor-Turbine Interaction
GCI	Grid-Convergence Index
HP	High Pressure
LE	Leading Edge
LES	Large Eddy Simulation
NGV	Nozzle Guide Vanes
PM	Pressure margin
PS	Pressure Side
PSD	Power Density Spectrum
RANS	Reynolds-Averaged Navier-Stokes
RIDN	Rear Inner Discharge Nozzle
RNG	Re-Normalisation Group

RODN	Rear Outer Discharge Nozzle
RQL	Rich-Burn, Quick-Mix, Lean-Burn combustor
RTDF	Radial Temperature Distribution Factor
SA	Spalart-Allmaras turbulence model
SS	Suction Side
TET	Turbine Entry Temperature

Greek Symbols

η	Efficiency
η_{eff}	Film effectiveness
γ	Heat capacity ratio
Λ	Integral length scale
λ	Length scale
μ	Dynamic viscosity
ν	Kinematic viscosity
Φ	Concentration
ρ	Density
τ	Time constant
Θ	Angle

Roman Symbols

A	Section area
A_o/A_i	Diffuser outlet-to-inlet area ratio

C	Vane chord
C_d	Discharge coefficient
C_p	Pressure coefficient
c_p	Specific heat at constant pressure
C_x	Vane axial chord
C_{pr}	Diffuser static pressure recovery coefficient
D	Diameter
E	Voltage
f	Frequency
H	Combustor depth
h	Heat transfer coefficient
J	Coolant-to-mainstream momentum flux ratio
k	Wavenumber
K_d	Diffuser loss coefficient
K_L	Loss coefficient
l	Length
$\dot{m}$	Mass flow rate
Ma	Mach number
Nu	Nusselt number
p	Pressure
pr	Pressure ratio

pr_c	Pressure ratio across the combustor
P	Pitch
Pr	Prandtl number
q	Flow field quantity
$\overline{q}$	Flow field mean quantity
q'	Flow field quantity turbulent fluctuation
R	Radial combustor length
r	Radial coordinate
R_{hw}	Hot-wire resistance
R_{qq}	Autocorrelation of the fluctuating quantity q
Re	Reynolds number
s	Spanwise direction coordinate
T	Temperature
t	Time
Tu	Turbulence intensity
u, v, w	Streamwise, lateral and spanwise velocity components
$\dot{W}$	Net power output
x,y,z	Streamwise, lateral and spanwise directions in Cartesian coordinates

Subscripts

∞	Mainstream conditions
0	Total conditions

40	Mainstream flow conditions at NGV inlet plane
aw	Adiabatic wall conditions
b	Bead conditions
j	Jet conditions
m	Heater mesh conditions
s	Static conditions
SP	Stagnation point conditions
TC	Thermocouple conditions
w	Wire conditions

Contents

Abstract **i**

Acknowledgments **iv**

Nomenclature **vi**

1 Introduction **1**

1.1 Jet engine 2

1.2 Rich Burn Combustor 5

1.3 Turbine cooling state of art 6

1.3.1 Review of cooling methods 8

1.3.2 HP turbine first stage NGVs 9

1.4 Leading edge pressure margin 10

1.5 Aims of the research 14

1.6 Contents of the thesis 14

1.7 Achievements of the research 15

1.8 List of publications 16

2 Literature Review **17**

2.1 Combustor Simulator 17

2.2 Film cooling 19

2.2.1 General considerations 20

2.2.2 Vane endwall cooling 22

2.3 Summary of literature review 24

3 Advanced Leading Edge Cooling Feed System Design 26

3.1 Leading edge insert . . . 26

3.1.1 Motivation . . . 27

3.1.2 Concept . . . 28

3.2 Preliminary design guidelines . . . 31

3.3 Insert geometries studied . . . 33

3.4 CFD simulations . . . 39

3.5 CFD results . . . 40

3.5.1 Stewart plot . . . 52

3.5.2 Average film cooling effectiveness . . . 56

3.6 Methods of improving diffuser performance . . . 57

3.7 Numerical uncertainty . . . 62

3.7.1 The Grid-Convergence Index (GCI) . . . 63

3.7.2 Vane leading edge . . . 64

3.8 Summary . . . 64

4 Experimental Apparatus - CTI Rig 66

4.1 Rig overview . . . 66

4.2 Combustor simulator . . . 67

4.2.1 Engine - rig matching . . . 70

4.2.2 Sensitivity studies . . . 72

4.3 Test section and outlet ducts . . . 74

4.3.1 Vane LE coolant passage discharge coefficient . . . 77

4.4 Suction fan and blower . . . 82

4.5 Coolant pipes . . . 84

4.6 Summary of Chapter 4 . . . 85

5 Instrumentation 86

5.1 Test section without vanes . . . 86

5.1.1 Traverse mechanism . . . 87

5.1.2 Velocity measurements 87
5.1.3 Temperature measurements 95
5.2 Test section with vanes 99
5.2.1 Pressure measurements 99
5.3 Uncertainty analysis of experimental data 101
5.3.1 Orifice meter: Mass flow 101
5.3.2 Four-hole probe: Velocity 102
5.3.3 Hot-wire: Velocity and turbulence 102
5.3.4 Thermocouple: Temperature 103

6 Fine Thermocouple Time Response Study 104
6.1 Experimental time constant estimation 104
6.2 Earlier analytical studies 107
6.3 CFD simulations 109
6.3.1 Uncertainty analysis 111
6.4 Results and comparison 112
6.5 Summary 113

7 CTI Rig: Combustor Simulator 115
7.1 CFD simulations 115
7.1.1 Computational domain 116
7.1.2 Mesh 117
7.1.3 Boundary conditions 118
7.1.4 Numerical uncertainty 119
7.2 Comparison of experiment and CFD 120
7.2.1 Velocity field 121
7.2.2 Temperature field 129
7.3 Summary 138

8 Rear Outer Discharge Nozzle (RODN) 140
8.1 Test section 141

8.2 CFD simulations . . . 141
8.2.1 Passive-scalar tracking method . . . 142
8.3 Results: Cylindrical holes - Pitch effect . . . 144
8.3.1 Velocity field . . . 145
8.3.2 Time spectral analysis . . . 148
8.3.3 Film effectiveness . . . 151
8.4 Results: Intersecting holes - Investigation of the effect of intersecting angle . . . 153
8.4.1 Velocity field: $\Theta = 90^o$ . . . 154
8.4.2 Velocity field: $\Theta = 30^o - 45^o$ . . . 155
8.4.3 Film effectiveness . . . 157
8.5 Summary . . . 159

9 Nozzle Guide Vanes (NGVs) 161
9.1 Tests without LE film cooling injection . . . 161
9.1.1 CFD simulations . . . 162
9.1.2 Experimental measurements . . . 168
9.2 Tests with LE film cooling injection . . . 170
9.2.1 Mainstream . . . 171
9.2.2 LE coolant passage - Static pressure measurements . . . 173
9.2.3 LE coolant passage - Stewart plot . . . 185
9.2.4 LE coolant passage - Pressure losses . . . 190
9.3 Summary . . . 192

10 Conclusions and future research 193
10.1 CTI rig - Combustor simulator . . . 193
10.2 Advanced LE feeding system design . . . 194
10.3 Suggestions for further work . . . 195
10.3.1 CTI rig - Combustor simulator . . . 196
10.3.2 Advanced LE feeding system design . . . 196

Bibliography **204**

Appendices **205**

A Traverse hardware and software **206**

B Vane pressure tapping location **209**

C Combustor simulator: RANS turbulence model **213**

D RODN - More experimental data along y **215**

Chapter 1

Introduction

Turbomachines are devices in which energy is transferred either to or from a continuously flowing fluid by the dynamic action of one or more moving blade rows, resulting in a change in pressure and momentum of the fluid. Gas turbines are relevant because they are the main component in a wide variety of applications (propulsion systems, energy production, industrial process, etc.). Gas turbines, such as the Rolls-Royce Trent 500 engine shown in Figure 1.1, power the majority of current civil aircrafts as they are characterized by a higher power density than internal combustion engines [57].

According to the ADS Group (Aerospace Defence Security), the trade organisation advancing the UK Aerospace, Defence, Security and Space industries, the UK civil aerospace sector currently employs around 230,000 people spread in over 3,000 companies and this industry is the largest in Europe and second largest in the world [17]. ADS forecasts a demand for around 27,000 new aircraft before 2031. The number of people employed and the revenues of such an important business sector justify the interest of Government and industry in investing in the UK long-term global competitiveness in aerospace through applied research such as that reported in this thesis.

Besides the business relevance, another reason that explains manufacturers' interest in investing in gas turbine research is the need to meet the ever more pressing

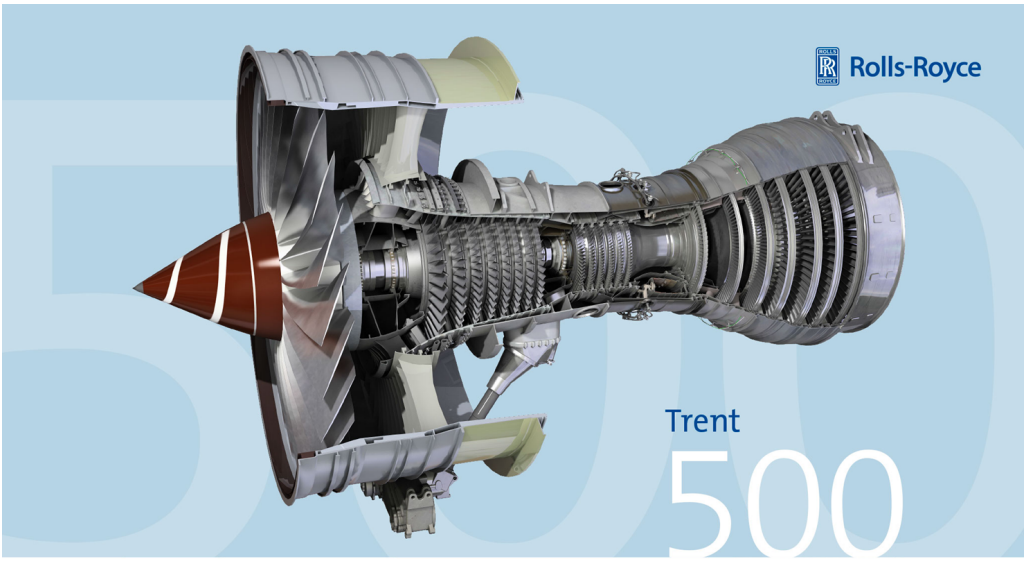


Figure 1.1: **Rolls-Royce Trent 500 turbofan [57]**

limitations for CO_2 and NO_x emissions set by the ACARE (Advisory Council for Aeronautics Research in Europe) targets.

For these motivations development of the gas turbine has drawn the attention from both academics and engine manufacturers.

1.1 Jet engine

The jet engine exploits Newton's third law of motion by forcing fluid rearward from the aircraft to create forward thrust to propel the aircraft. Most modern aircraft engines are turbofan, an arrangement which exploits larger comparative airflows and lower jet velocities than the pure jet engine, thus giving a higher propulsive efficiency [52]. Figure 1.2 reports the sketches of a simple gas turbine, a simple turbojet, where the turbine exhaust is expanded in the propelling nozzle to provide thrust, and a turbofan, a turbojet configuration where the flow is divided into the bypass stream and the core stream by means of a fan driven by the low pressure turbine (indicated as LPT in Figure 1.2) .

Figure 1.3 shows a simple gas turbine cycle (i.e. the Joule or Brayton cycle).

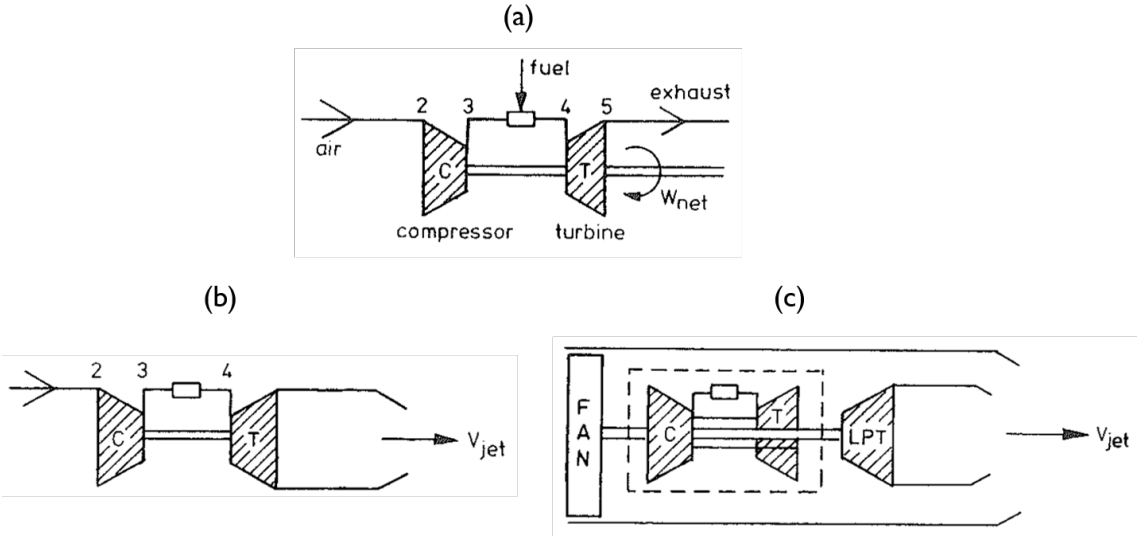


Figure 1.2: **Gas turbine: Simple configuration (a), turbojet (b) and turbofan (c) [15]**

State *1* corresponds to the intake air before it slows down, thereby, increasing in pressure to state *2*, representing the air conditions at the inlet to the compressor. After the compression, the air enters the combustion chamber at state *3* and emerges from the combustor at the state *4*. From state *4* to state *5* the air expands through the turbine and the exhaust nozzle. The expansion across the turbine provides work to power the compressor: in a turbofan engine, the additional work drives the fan which can provide over 85% of the total engine thrust [49] and produces thrust from the exhaust nozzle.

The bypass air flow cycle is shown in Figure 1.4. The slowed down air at the intake, state *2*, is compressed by the fan to state *6*. The air then expands out from the bypass and leaves the nozzle at higher speed, state *7*, thereby producing thrust.

Aircraft engines are naturally complex systems with the air flows through different components (compressor-combustor-turbine) that are arranged in close proximity to minimise installation size and mass. This connection inevitably leads to strong interaction between the components. In particular, the flow discharged by the combustor approaches the turbine at conditions that are very far from uniform

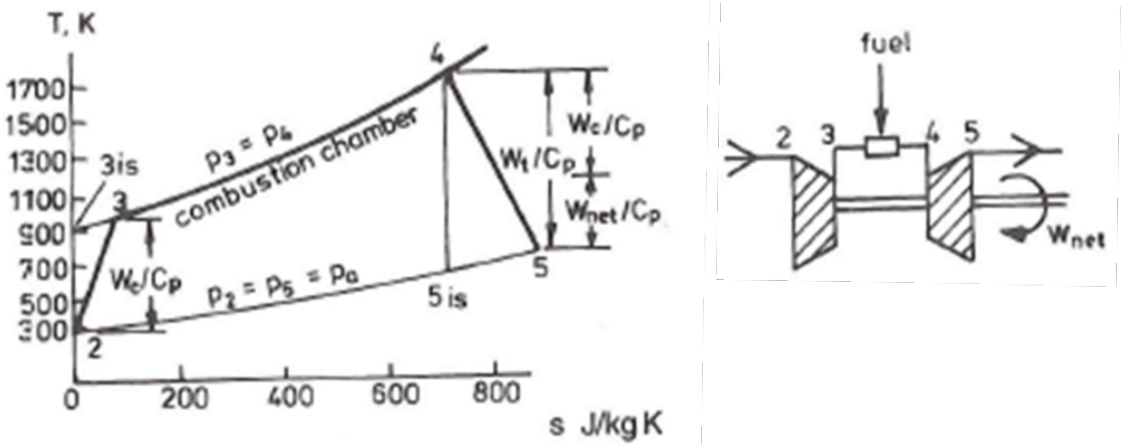


Figure 1.3: **Simple configuration: turbine cycle [15]**

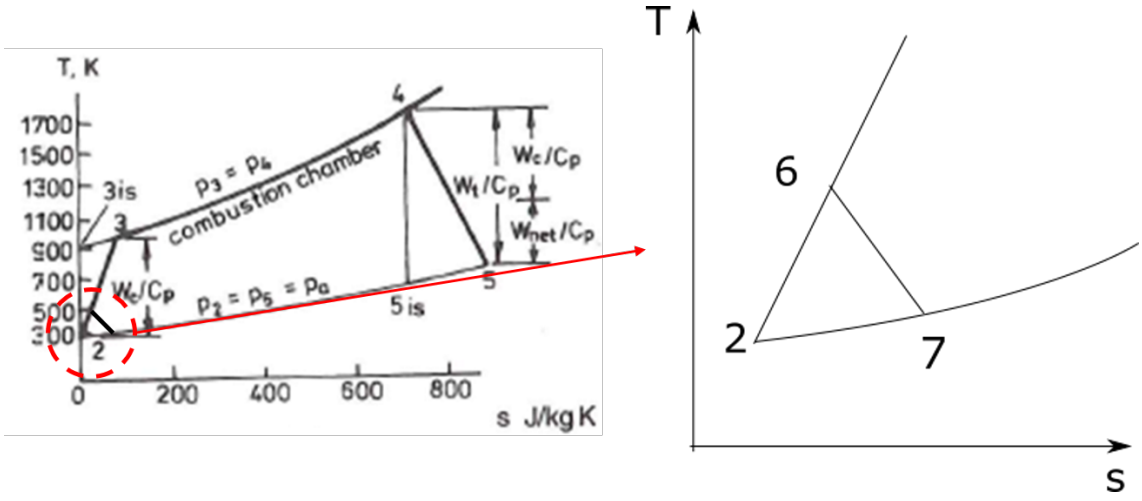


Figure 1.4: **Turbofan configuration: turbine cycle**

with very significant turbulent fluctuations. The interaction between the combustor and turbine was identified as an important research field at the state of the present doctoral research. The key aim of the research was to obtain high-fidelity, high spatial resolution data at a model of the turbine inlet and to reproduce conditions representative of a combustor.

1.2 Rich Burn Combustor

Rich-Burn, Quick-Mix, Lean-Burn (RQL) combustors are normally used in aircraft applications because of reduced cost, weight, fuel burn, noise and improved combustion stability relative to other technologies. A Rolls-Royce RQL combustor, such as the one reported in Figure 1.5, shows a primary rich-burn zone where the combustion products reach high temperatures (the gas peak temperature is usually around 2500 K) which minimizes the production of incomplete combustion products (i.e. soot and carbon monoxide). Dilution air, from the compressor last stage, is introduced downstream of the primary combustion zone to quench the combustion process and to reduce the flow temperature to acceptable levels for the HP Nozzle Guide Vanes (NGVs) and control the NO_x formation [34]. The axial location and area of the quench ports is used to control the stoichiometry and mixing of the coolant with the hot gases. More air is subsequently introduced further downstream through the Rear Inner Discharge Nozzle (RIDN) and the Rear Outer Discharge Nozzle (RODN) to reduce the endwall temperature.

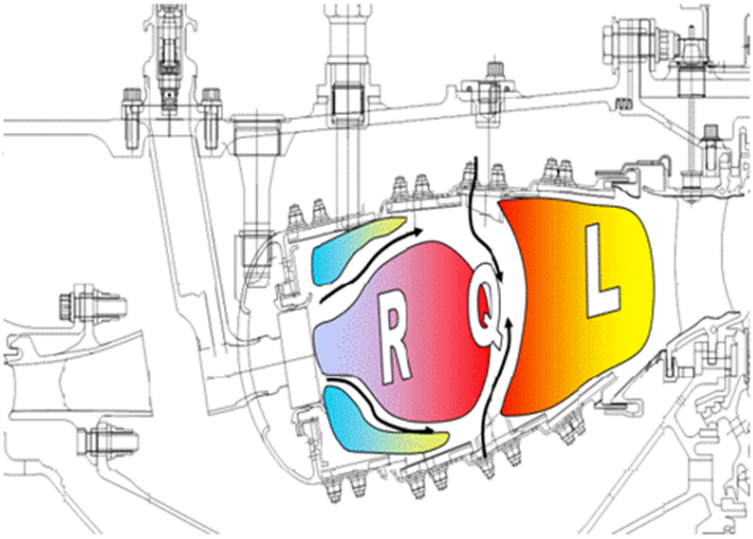


Figure 1.5: **Rolls-Royce RQL combustor [43]**

The interaction between different streams create a very complicated flow field

at the entrance to the HP turbine that needs to be correctly modeled to accurately represent inlet conditions for the HP vane.

1.3 Turbine cooling state of art

The objectives of successful jet engine design are high thermodynamic efficiency, low emissions, acceptable life and costs. Friedrichs [21] recently reported that the development trends that affect the turbine cooling design include the increase in gas Turbine Entry Temperature (TET) and compressor pressure ratio, the decrease of NO_x emissions and the reduction of production and maintenance costs. The rise in TET leads to an increase in engine thrust per unit mass flow rate of air, but also creates important technological challenges for the HP turbine. An increase in pressure ratio allows an increase in cycle efficiency, but at the same time causes an increase of the compressor outlet temperature and the consequent increase of temperature of coolant supplied to the turbine components.

The thrust power per unit mass flow rate of air of a turbofan increases continuously with an increase of TET when the compressor pressure ratio and the engine inlet temperature are held constant [33]. The maximum achievable TET value is limited by technological levels: it is currently around 2000 K while a typical turbine component temperature to achieve acceptable life is around 1200 K [21]. Note that a typical metal melting temperature for a superalloy is around 1600 K. Single crystal nickel-based superalloys allow peak operational temperatures greater than 1300 K but cooling is needed to reach higher temperatures [21].

The use of cooled vanes (like the one shown in Figure 1.6) or blades allows the designer to:

- Increase the specific thrust (by increasing the TET) or
- Decrease the engine weight (by decreasing the component wall thickness) or
- Increase the turbine service life.

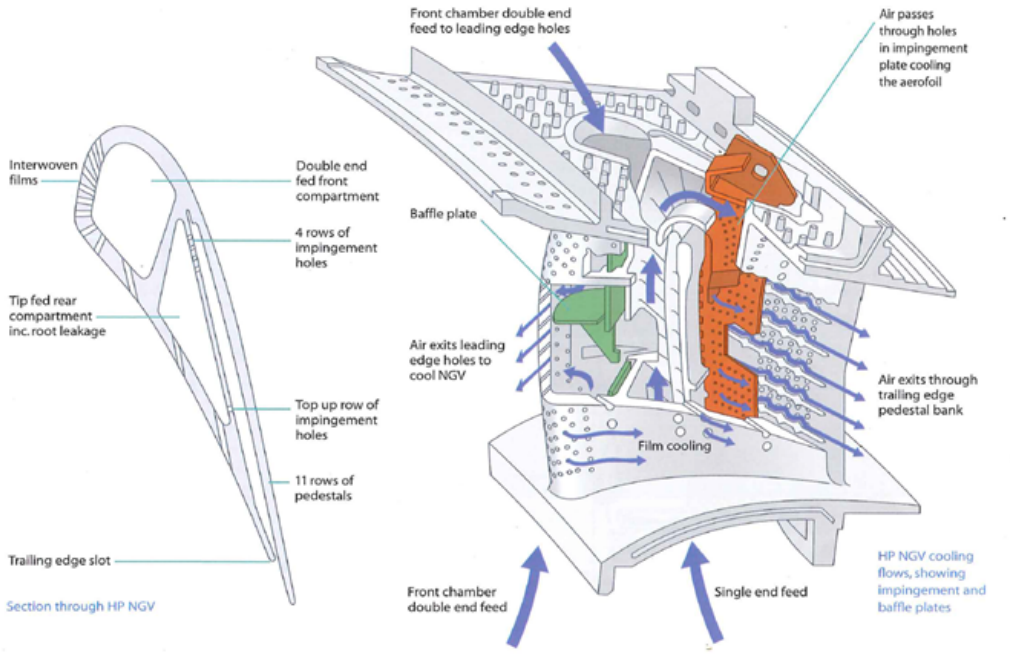


Figure 1.6: **Example of cooled HP NGV [52]**

The disadvantages arising from the use of cooled vanes or blades are:

- Increases in the complexity of the airfoil design and manufacture (with consequent increase in component cost);
- Cycle penalties due to the extraction of air at the end of compressor and reintroduction of the coolant in to the turbine at lower pressure (the vanes in the high pressure turbine typically require 9% of the high pressure compressor entry flow [21]);
- Generation of aerodynamic losses when the coolant is reintroduced in the mainstream through the film cooling holes and the trailing edge slot.

It is evident that the turbine airfoil design requires several compromises, that will be dictated by the specific application demanded conditions. Usually a combination of advanced technologies (special alloys, sophisticated cooling and ceramic coatings) are used. The cooling system must balance the required cooling performance, stress limitations, manufacturing feasibility and costs.

1.3.1 Review of cooling methods

Before describing the author's research in detail, it is helpful to summarise cooling technologies typical of those used in jet engines. According to LeGrives [35], cooling techniques can be classified in two principal groups (Figure 1.7):

- Internal cooling techniques (for external stream temperatures up to 1300-1600 K), such as convection and impingement cooling;
- External cooling techniques (for external stream temperatures greater than 1600 K), for example film cooling.

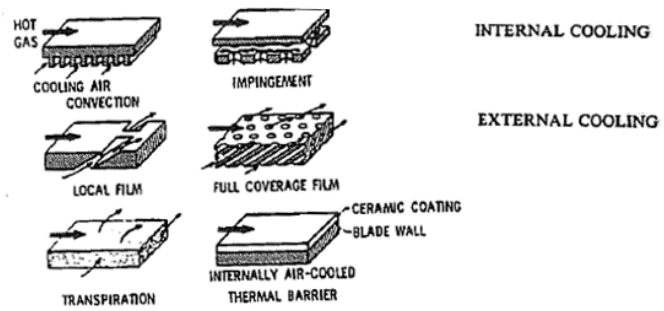


Figure 1.7: **Cooling techniques [33]**

Convection cooling is one of the earliest forms of cooling used in gas turbines: the coolant passes through complex passages, where the heat transfer is often enhanced by the presence of ribs and turbulence generators. Impingement normally requires a sheet metal insert with holes which create cooling jets that impact on the inner surface of the vane: the thin boundary layers and high turbulence cause high temperature gradients in the coolant and consequently high heat transfer coefficients. In film cooling a protective layer of cool air acts as a buffer between the hot main stream gas and the vane external surface: film cooling configurations can consist of a slot, a single row or multiple rows of holes. The combined use of more than one cooling technique differs case by case, depending on the temperature range and many other design constraints.

Part of the author's research focused on film cooling technique on the HP vane LE (Chapters 3 and 9) and on the endwall (Chapter 8). The analytical and computational prediction of film cooling behaviour is complex because of the direct interaction between coolant and mainflow and mixing of the close jets [33]. Bogard and Thole [4] reviewed the main parameters affecting film cooling performance: in particular, they identified momentum flux ratio, mainstream turbulence, hole geometry, configuration and location as variables that govern the film behaviour. The availability of high-resolution experimental data for CFD validation is essential for the development of accurate design tools.

1.3.2 HP turbine first stage NGVs

The NGVs in the HP turbine experience the hottest gas in the engine and are extensively cooled by air bled from the last stage of the compressor where the air pressure is the maximum available. At the maximum cycle temperature the mean hot gas temperature can reach around 2000 K. In order to obtain the required wall temperature reduction on the HP vanes, both internal convective cooling and external film cooling are used (Figure 1.8).

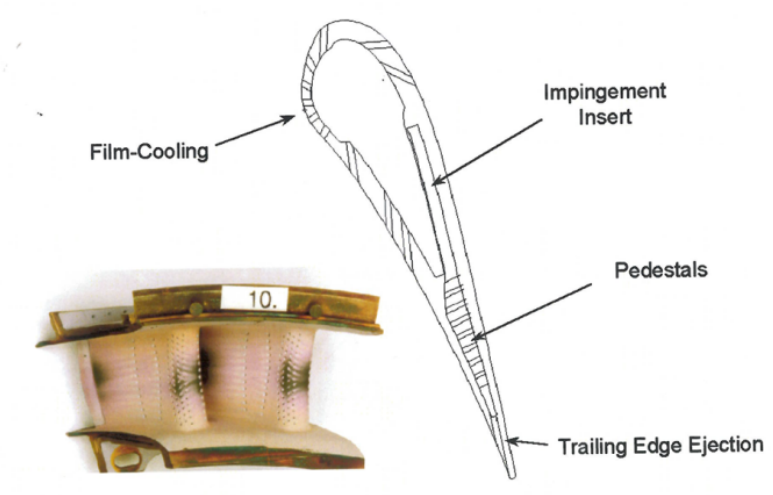


Figure 1.8: **Example of HP turbine first stage NGV [21]**

According to Sargison [58], the main requirements in order to obtain satisfactory

performance are high film effectiveness $\eta_{eff} = \frac{T_{0,\infty} - T_{aw}}{T_{0,\infty} - T_{0,c}}$ (i.e. adiabatic wall temperature T_{aw}, close to the coolant temperature $T_{0,c}$) and low external convective heat transfer coefficient.

Bogard and Thole [4] report that the total cost to replace a single set of high pressure stage vanes is of the order of thousands to tens of thousands of dollars, of which a significant fraction is required to manufacture or repair film-cooling holes in the vane. Generally, airfoils must be replaced or repaired during engine maintenance operations because regions such as the leading or trailing edges have burned away while the main body of the airfoil remains intact [4]. That is one of the main reasons why particular attention is required in the leading edge design which is the main theme of this thesis.

1.4 Leading edge pressure margin

In the HP NGVs the coolant is exhausted from internal cooling passages through several rows of cooling holes on the airfoil external wall with the intent of creating a protective layer between hot main stream gas and the blade surface. The coolant film is typically refreshed with the addition of coolant from downstream rows.

The hot gas reaches the NGVs with a total pressure lower than the compressor discharge conditions due to the pressure losses inside the combustor while the coolant is fed to the vanes at a total pressure closer to the compressor outlet. In order to prevent the hot gas ingestion into the film cooling holes of the stator vane the cooling air must be supplied at conditions that, not only adequately cool the component under the most severe conditions, but also maintain an acceptable pressure margin across each film hole at all engine operating conditions. Conventionally the minimum pressure margin is set to be acceptable at the worst conditions to which the component has to be exposed (corresponding to take-off for aircraft engines). The pressure margin can be evaluated as the ratio between the maximum total pressure difference between coolant and hot gas ($p_{0c} - p_{40}$) and the coolant

supply total pressure p_{0c} and typical values are around 1.03. It can be argued that this thermal design requirement leads to the overuse of valuable coolant at any other operating condition causing the waste of the work used to compress the cooling air and a consequent deterioration in the cycle performance. Another limitation of this design constraint is that, once the minimum pressure ratio across the showerhead holes (Figure 1.8) that are the closest to the stagnation point has been set by the back-flow minimum pressure margin requirements, the pressure ratio across all of the other film cooling rows is predetermined by the supply pressure.

Figure 1.9 reports an example of isentropic Mach number and total to static pressure ratio distributions around the vane leading edge stagnation point ($x/C_x = 0$) and shows how the hot gas pressure rapidly varies in this region. Because the coolant total pressure is approximately uniform along the x axis, this causes a strong increase of pressure difference across the film cooling holes moving away from the stagnation point, especially on the suction side ($x/C_x < 0$), provoking an unnecessary increase of coolant mass flow ejected at these locations.

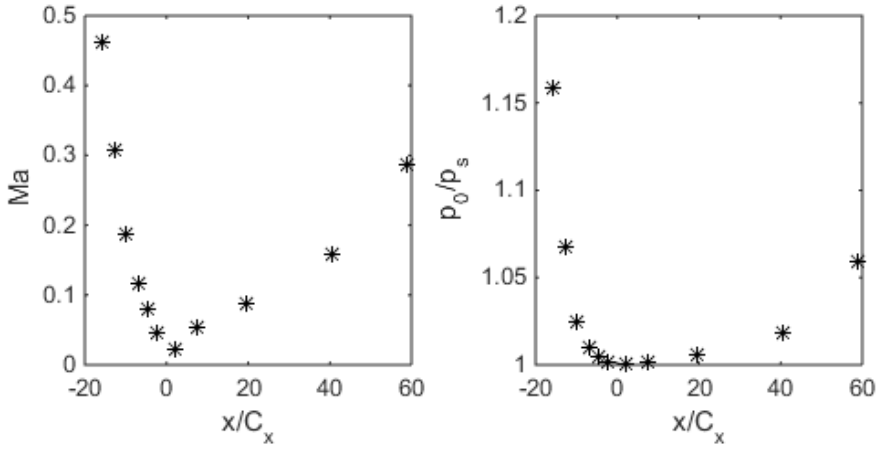


Figure 1.9: **Engine-representative isentropic Mach number (on the left) and total to static pressure ratio (on the right) distributions along a generic HP vane leading edge at the midspan, used as boundary conditions for CFD simulations in Chapter 3**

In a review of the main hot gas path challenges in a gas turbine, Bunker [6]

points out the importance of developing specific cooling designs that can minimize the component thermal stresses avoiding the overuse of coolant at any operating conditions different from the design. The present author's work reported in Chapter 3 addresses this problem.

Gas turbine net power output

The efficiency of a closed-cycle gas turbine can be evaluated from

$$\eta_{cycle} = \dot{W}_{net}/(\dot{m}_{air} \cdot c_p \cdot (T_4 - T_3)) \tag{1.1}$$

where state *3* defines the mainflow conditions at the compressor discharge and *4* at the turbine inlet, according to the nomenclature included in Figure 1.3.

The net power output $\dot{W}_{net}$ depends on the compression ratio $pr = p_3/p_a$ and for the case where the pressure drop inside the combustor is negligible (i.e. $pr = p_3/p_a = p_4/p_a$) it can be calculated (see [15]) as

$$\dot{W}_{net} = \dot{m}_{air} \cdot c_p \cdot T_2 \cdot \left[\eta_{turb} \cdot \frac{T_4}{T_2} \left(1 - \frac{1}{pr^{\frac{\gamma-1}{\gamma}}} \right) - \frac{(pr^{\frac{\gamma-1}{\gamma}} - 1)}{\eta_{comp}} \right] \tag{1.2}$$

To account for the combustor pressure drop, we introduce the pressure ratio across the combustor pr_c, defined as

$$pr_c = \frac{p_4}{p_3} \tag{1.3}$$

for a compression ratio pr the expansion ratio available across the turbine is

$$\frac{p_4}{p_a} = \frac{p_4}{p_3} \cdot \frac{p_3}{p_a} = pr_c \cdot pr \tag{1.4}$$

and the net power output becomes

$$\dot{W}_{net} = \dot{m}_{air} \cdot c_p \cdot T_2 \cdot \left[\eta_{turb} \cdot \frac{T_4}{T_2} \left(1 - \frac{1}{(pr_c \cdot pr)^{\frac{\gamma-1}{\gamma}}} \right) - \frac{(pr^{\frac{\gamma-1}{\gamma}} - 1)}{\eta_{comp}} \right] \tag{1.5}$$

It is evident that an increase of pr_c causes an increase of the available net power output. For the parameters shown in Table 1.1, which are typical of those of a large

civil aircraft engine operating at cruise conditions, Figure 1.10 shows the trend of $\dot{W}_{net}/\dot{m}_{air}$ as a function of pr_c. The combustor is invariably well designed so we are only interested in conditions where $pr_c > 0.9$, shown in Figure 1.11, where the relation between $\dot{W}_{net}\dot{m}_{air}$ and pr_c is almost linear: a pressure drop of 1% across the combustor causes a loss of power output of 0.3%.

Specific heat capacity	c_p [kJ/kg K]	1.244
Heat capacity ratio	γ [-]	1.3
Air temperature at compressor inlet	T_2 [K]	288
Air temperature at turbine inlet	T_4 [K]	2000
Compressor ratio	pr	35
Turbine efficiency	η_{turb} [-]	0.9
Compressor efficiency	η_{comp} [-]	0.9

Table 1.1: **Typical engine design parameters [15]**

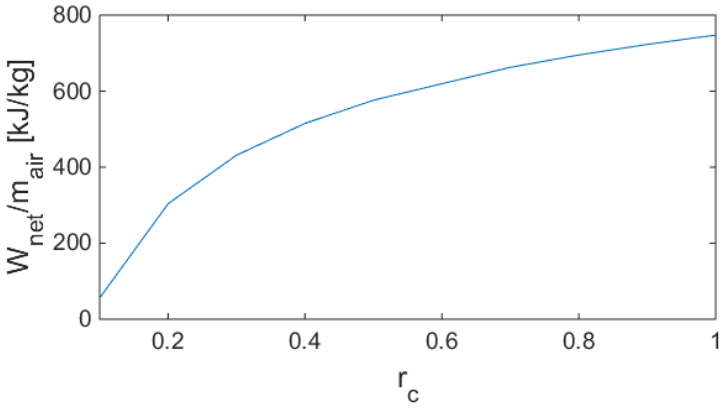


Figure 1.10: **Gas turbine net power output per unit mass flow rate of air**

A reduction of net power results in a penalty in the overall engine performance: therefore it is desirable to minimize the loss across the combustor. If the allowable pressure margin at the HP vane leading edge could be decreased that would allow the engine designer to decrease the pressure drop across the combustor and increase the turbine net power output.

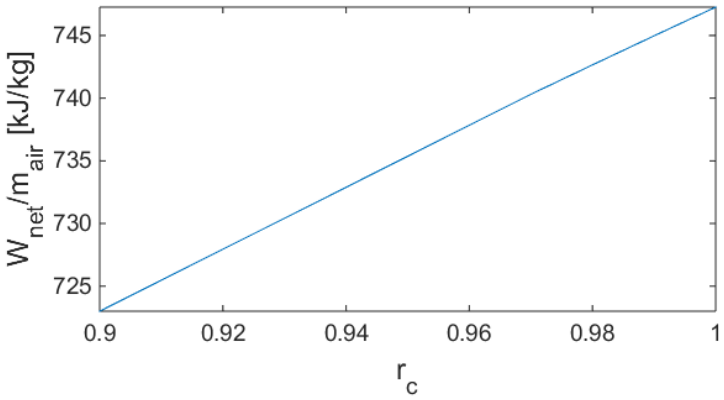


Figure 1.11: **Gas turbine net power output per unit mass flow rate of air** ($0.9 < pr_c < 1$)

1.5 Aims of the research

The scope of this work was to design a low-speed large-scale cascade facility able to simultaneously reproduce the engine-representative distributions of the main flow parameters downstream of a RQL combustor and to allow the author to fully quantify velocity, turbulence intensity and temperature distributions. In this environment it was possible to research a new HP LE cooling design invented by the author to be able to improve the pressure management across the film cooling holes in the stagnation region. The knowledge gained from the LE coolant passage data will be used to explore further design solutions in the future.

1.6 Contents of the thesis

Chapter 2 reports a review of the literature relative to combustor simulator design and testing and a background on vane and endwall film cooling.

Chapter 3 provides a detailed report of the design of a new leading edge feeding system: motivation, basic concept and different possible geometries are discussed. The results of CFD simulations for different cases are presented and compared.

Chapter 4 introduces the experimental facility. The Combustor-Turbine Inter-

action (CTI) rig was manufactured, assembled and commissioned to investigate the flow field downstream of a combustor simulator and the HP LE film cooling pressure margin.

In Chapter 5 the instrumentation used is described and discussed.

Chapter 6 presents the calibration of a 12.7 μm wire chromal/alumel thermocouple. Experimental measurements, CFD and literature predictions are compared and discussed.

Chapter 7 contains the experimental and numerical analysis on the flow field downstream of the facility combustor simulator. Velocity, turbulence and temperature measurements are reported.

Chapter 8 describes the flow field measured downstream of the endwall film cooling holes and compares experimental measurements to CFD predictions.

Chapter 9 details the pressure measurements performed for both the mainstream around the NGVs and inside the Leading Edge (LE) cooling passage to give experimental support to the new design described in Chapter 3.

1.7 Achievements of the research

- This study reports a complete experimental overview of the flowfield downstream of a RQL combustor simulator, including velocity, turbulence intensity and temperature measurements. The measurements reported in this thesis constitute a valuable dataset for the development of numerical prediction tools, such as LES.

- In particular, high-frequency temperature measurements were acquired with a 12.7 μm wire thermocouple purposely built for this application: they showed an unexpected lack of connection between combustor simulator geometric features and the scale of temperature fluctuations.

- In addition, this work numerically and experimentally researched a new LE coolant passage concept patented by the author that can improve the pressure

margin management across the LE film cooling holes.

- The detailed static pressure measurements both inside and outside the LE coolant passage are a unique experimental investigation. The new proposed geometry results confirm that the new geometry performs better than the baseline geometry over all working conditions.

1.8 List of publications

Papers

I. Cresci, P.T. Ireland, M. Bacic, I. Tibbott, and A. Rawlinson. *Realistic velocity and turbulence intensity profiles at the Combustor-Turbine Interaction (CTI) plane in a nozzle guide vane test facility.* In ETC 2015 Proceedings, 2015.

I. Cresci, P.T. Ireland, M. Bacic, I. Tibbott, and A. Rawlinson. *Velocity and turbulence intensity profiles downstream of a long reach endwall double row of film cooling holes in gas turbine combustor representative environment.* In Proceedings of ASME Turbo Expo 2015, GT2015-42307.

I. Cresci, P.T. Ireland, M. Bacic, I. Tibbott, and A. Rawlinson. *Realistic velocity, turbulence intensity and temperature profiles at the Combustor-Turbine Interaction (CTI) plane in a nozzle guide vane test facility.* In IGTC 2015 Proceedings, 2015.

Patents

I. Tibbott, P.T. Ireland, A. Rawlinson and I. Cresci. *HPT NGV Showerhead Cooling Hole Feed Chamber Pressure Recovery Geometry.* US 5593.

I. Cresci, P.T. Ireland, I. Tibbott, and A. Rawlinson. *Cast Impingement System with Inclined Pedestals.* In preparation.

Awards

People's Choice: Student Poster Session at ASME Turbo Expo 2015, I. Cresci, P.T. Ireland, I. Tibbott, and A. Rawlinson. *Temperature fluctuation measurements at the combustor-interaction (CTI) plane in a gas turbine combustor representative environment.*

Chapter 2

Literature Review

This chapter includes a review of the relevant experimental and numerical studies of combustor simulators used for turbine research together with a review of the relevant film cooling literature.

2.1 Combustor Simulator

The importance of achieving realistic boundary conditions in experimental tests and numerical simulations at the Combustor-Turbine Interaction (CTI) plane is reported in several earlier studies discussed below. Previous studies of combustor simulators at the University of Oxford are reported by Povey and Qureshi [54] and Qureshi et al. [55] who reproduced the dimensionless temperature profile at the exit from the combustor: significant heat transfer variations at the surface of vane airfoils and endwalls between a uniform temperature boundary condition and a distorted temperature profile case were found, mainly due to changes in the local gas driving temperature. Combustor exit turbulence also is a key parameter that needs to be matched to engine conditions. Ames [1] asserted that turbulence has a significant effect on NGV stagnation region and pressure surface heat transfer. The reproduction of the actual combustion conditions is very challenging and creates severe limitations on the instrumentation choice. Significantly Moss [46] showed that

combustion has negligible effects on turbulence levels and that dilution jets govern the mainflow features for a combustor from the 1980s.

In order to obtain realistic conditions at the turbine inlet, the jet-to-mainstream momentum flux ratio is a key parameter to be set because it determines the shape of the jet and its trajectory that dictate the combustor exit velocity, turbulence and temperature profiles. Experimental studies have been conducted at Virginia Polytechnic Institute, where Thole et al. [64] compared two different generators: a jet-based turbulence generator, where turbulence levels were adjusted by changing the jet-to-mainstream velocity ratio or the Reynolds number, to a bar-grid turbulence generator. They concluded that the former set-up enables a highly turbulent flow to be generated and, for a certain arrangement, different turbulence intensity levels can be achieved by adjusting the jet-to-mainstream velocity ratio. Barringer et al. [3] designed a combustor simulator to evaluate the development of thermal and velocity fields downstream of a realistic combustor, with a particular focus on the effect of dilution jets. Total pressure, mean and turbulent velocity and temperature measurements are reported. Barringer et al.'s results [3], and the further measurements from Vakil and Thole [69], confirmed once more the dominance of the dilution jets on setting the key parameters and showed a large recirculation region downstream of the jet injection location.

Numerical studies have focused on assessing the ability of different turbulence models to correctly reproduce the experimental data. The apparatus studied by Barringer et al. [3] was modelled and simulated by Stitzel and Thole [61]: RANS simulations with RNG k-ε turbulence model with non-equilibrium wall functions underpredicted turbulence levels compared to the measurements. Holdeman [27] reviewed computational and experimental studies of single, double and opposed rows of dilution jets in a non-reacting combustor. According to his result's the k-ε turbulence model has some limitations in accurately predicting the mixing of opposed jets but it succeeds in predicting the jet penetration.

In recent years more effort has been expended on replicating fully realistic bound-

ary conditions at the CTI plane. Thomas et al. [66] designed a combustor simulator for a low-speed linear cascade facility, able to match Reynolds number and jet-to-mainstream momentum flux ratio to engine conditions, but neither temperature or traverse measurements were taken downstream of the apparatus. Consequently no data were available to inform understanding of the flow physics at this plane of for CFD validation. Cha et al. [8], [9] took detailed flow measurements downstream of a fully featured rich-burn engine combustor at Loughborough University and compared them to RANS and LES simulations. The LES simulation of the entire combustor subsystem reported by the authors was the first of this kind [9], but if this is suitable for academic applications, LES simulations are currently still impractical as a design tool for industrial purposes. This work in particular was very useful to the present author as it provided a dataset which used engine hardware.

From the literature it is clear that CFD shows limitations in predicting the flow field at the CTI section and that high quality experimental data are required to validate the numerical tools. In particular the lack of time-resolved data at engine-representative conditions was noticed.

The goal of the work presented in Chapter 7 was to design a flexible combustor simulator to be installed upstream of a large scale NGV cascade and to use it to obtain high resolution time-averaged and time-resolved velocity and temperature measurements and to compare them to RANS calculations run at the same rig conditions. The data were used to analyze in detail the flow physics at the NGV inlet plane and to produce engine representative conditions at the inlet of a large-scale vane cascade to be used to study leading edge film cooling performance.

2.2 Film cooling

Film cooling technology is used widely throughout the turbine stage to cool different regions. Each area has different geometrical, aerodynamic and heat load constraints and this strongly affects the cooling system design. An example of a

typical cooled vane with endwall film cooling holes is shown in Figure 2.1.

The HP NGV Leading Edge (LE) is subjected to very high temperature gas and very high external heat transfer coefficients near the stagnation point. For this reason, six to eight closely space rows of holes are commonly used to obtain sufficient film coverage and thermal protection. Holes are typically aligned with the mainstream direction, with injection angles arranging from 20^o to 45^o [4].

Film cooling is also needed to keep the component endwall gas temperature at the hub and the casing of the HP NGV at acceptable levels. Challenges in the endwalls regions arise due to the presence of the secondary flows that tend to wash away the film from the endwalls that require high coolant-to-mainstream momentum ratios at the inlet plane: high momentum flux ratios can be used to suppress secondary flows at the endwalls but at increase risk of film lift-off from the surface.

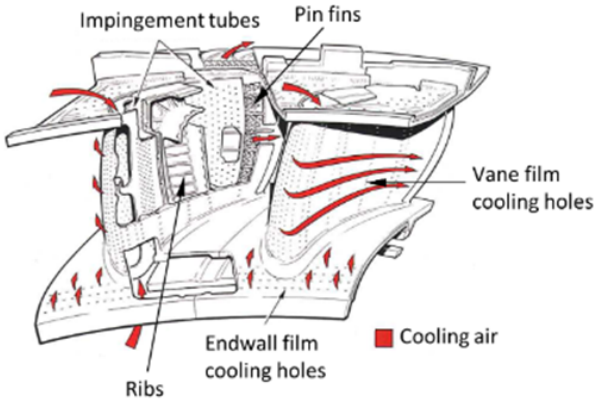


Figure 2.1: **NGV with endwall cooling (image adapted from The Jet Engine [52] by Thomas [65])**

2.2.1 General considerations

The effectiveness of gas turbine airfoil film cooling is dependent on a wide range of flow and geometric variables. The film cooling configuration principally used for cooling turbine airfoils and endwalls normally consists of rows of discrete coolant holes and this arrangement has been one of main focus of numerous papers in litera-

ture. The articles reported in this section were chosen because they refer to studies related to configurations similar to the cases analysed in this thesis. Bogard and Thole [4] identified as some of the main parameters that influence the film performance hole geometry and configuration (such as hole shape, angle, spacing and number of rows), surface curvature and mainstream turbulence. Bogard and Thole [4] reviewed the investigations in the literature of the effect of the previous variables and they noticed the lack of studies with realistic high-turbulence mainstream. The ability to reproduce representative mainstream conditions was considered key to the production of useful experimental results of film cooling systems.

Turbulence levels and velocity profiles downstream of the film injection as a function of different variables have been studied by several authors. Leylek and his coworkers [70], [28] performed a numerical analysis of film cooling flow field for cylindrical and shaped holes up to a maximum blowing ratio, for the cylindrical holes, of 2. They state that turbulence levels downstream of the film injection are set by two main contributions, i.e. the turbulence inside the jet at the hole exit and the difference in velocity across the shear layer between the jet and the mainstream (in particular, this contribution increases with the mismatch between the momentum fluxes). These effects are strongly dependent on the hole configuration and the blowing ratio. Eberly and Thole [16] provided time-resolved measurements of velocity downstream of a single cylindrical film cooling hole with the momentum flux ratio varying between 0.23 and 3.3. The velocity profile showed a peak which moved further from the wall with increasing momentum flux ratio, which was associated with a deeper penetration of the jet into the mainstream. The turbulence intensity generated inside the hole for turbulent mixing increases with the momentum flux, while the contribution due to the shear layer between mainstream and film reaches its lowest peak for momentum flux ratio of unity and then increases with the difference between mainstream and coolant momentum flux, in accordance to Leylek's results [70]. Pietrzyk et al. [51] reported measurements downstream of a single row of 35^o inclined holes with pitch-to-diameter ratio of 3 and blowing ratio of 0.25 -

0.5 - 1. They found that turbulence intensity reaches its peak at the maximum $\frac{du}{dz}$ velocity gradient but then it remains high in the region near the wall, where the shear stress changes significantly from positive to negative. In this configuration, the shear layer is no longer distinguishable at a distance greater than 10 hole diameters downstream.

2.2.2 Vane endwall cooling

The endwall cooling requirements are very specific. The flow upstream of the NGVs is relatively slow compared to the nozzle exit conditions but the coolant is supplied at the same pressure. The higher pressure ratio across the holes at the endwalls upstream of the NGV results in a higher momentum flux ratio that strongly affects the film behaviour.

Leylek and Zerkle [38] state that one of the main governors of film performance is the film trajectory: an attached film results in high film effectiveness, whereas when the film lifts off, the film gets mixed more quickly with the mainstream and the hot gases are entrained close to the wall. The film performance is directly affected by the jet aerodynamics, so a knowledge of the flow field downstream of the injection point is essential to optimize the cooling system design. Ligrani et al. [39] measured film effectiveness data downstream of an effusion system and reported an attendant decrease in film cooling performance as the hole pitch was increased.

Other authors have focused their attention on the effect of the interaction between film and secondary flows at different momentum flux ratios and its effect on film effectiveness. Zhang and Jaiswal [73] measured film cooling effectiveness downstream of a double row of film cooling holes at the vane endwall surface for different coolant-to-mainstream mass flow ratios. The main conclusions from their work are that, at a lower mass flow ratio (i.e. lower momentum flux ratio), the film jets are attached to the wall but the endwall secondary flows dominate the flow field and the flow separates close to the vane leading edge creating an uncovered region, while for mass flow ratios greater than 2 (i.e. high momentum ratio) the occurrence

of jet lift-off decreases the effectiveness just downstream of the injection, but the cooling film tends to dominate the near wall flow field, suppressing the secondary flows and strongly improving the film coverage. Friedrichs [20] describes a method for comparing real engine conditions to experiments on the basis of momentum flux ratio, that was later applied also by Thomas [65]. Thomas' work was used by the present author as a reference case for the geometrical and fluid dynamics scaling of the CTI rig combustor simulator. In his thesis, Thomas [65] studied the effect of the coolant-to-mainstream mass flow ratio across the endwall film cooling holes on the secondary flows varying it between 1 and 6% and he introduced a passive-scalar tracking method to isolate the contribution of individual film cooling holes to cooling effectiveness reaching conclusions in agreement with Zhang and Jaiswal [73].

The reviewed papers show a strong dependence of the flow field downstream of film cooling holes on geometry and mass flow ratio (i.e. momentum flux ratio): the importance of using high mass flow ratio configurations to suppress the mainstream secondary flows was noticed. The lack of high-resolution fluid dynamic measurements for engine configurations with two rows of staggered holes at high blowing ratio was notable.

Maximizing the film effectiveness is important, but a limit to the amount of coolant, under conditions of set pressure difference between coolant and hot gas, is important to avoid excessive aerodynamic and cycle penalties. An interesting system studied by Fletcher [18] with the goal of decreasing the cooling air requirements while enhancing the cooling system convective efficiency in a turbine blade leading edge was the Matrix Cooling Method: this approach consisted of layers of close-packed cooling holes angled to the surface as shown in Figure 2.2. This design proved to be able to offer significant improvements in internal heat transfer coefficients compared to a row of normal jets.

Nowlin [47] developed Fletcher's concept conducting an experimental and computational investigations of the different geometries shown in Figure 2.3: he concluded that the heat transfer increases with the intersection angle Θ while the loss remains

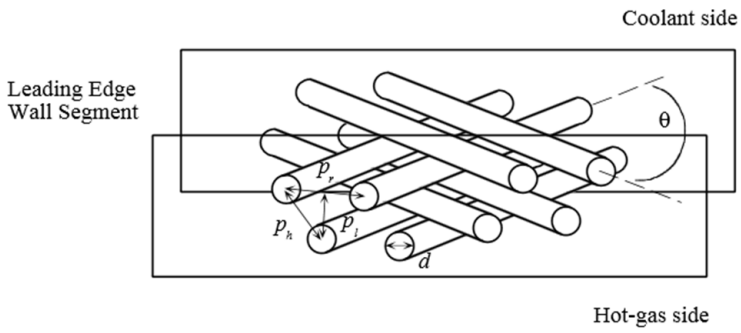


Figure 2.2: **Fletcher's Matrix Cooling Method [18]**

sensibly constant as the angle is increased up to 90^o, beyond which the loss coefficient starts increasing. This geometry has not been tested before at the endwall conditions, but it could be used to decrease the amount of coolant mass flow rate required, should the pressure ratio across the holes be fixed.

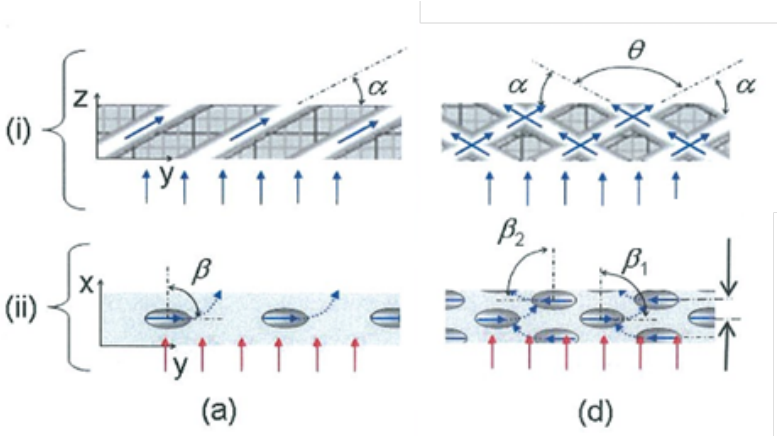


Figure 2.3: **Nowlin's geometries [47]: Straight cylindrical holes (a) and intersecting holes (d)**

2.3 Summary of literature review

The significance of using engine-representative boundary conditions at the CTI plane has been reported by several authors. This is because velocity, turbulence and temperature distributions are dictated by the combustor dilution jet-to-mainstream

momentum flux ratio. The need for high-resolution and time-resolved data at engine-representative conditions emerged, both to increase our physics understanding of the flow field at the CTI plane and to give a complete dataset that can be used to validate numerical tools. This will become increasingly important as LES studies become more common.

The vane leading edge and the endwall results need particular care from the thermal point of view and both regions require intense cooling. The main parameters affecting the film performance are hole geometry (i.e. shape and angle) and configuration (i.e. hole spacing and number of rows) and flow field conditions (i.e. mainstream turbulence level and momentum flux ratio). The film cooling at the vane LE and at the endwalls is subject to very different operating conditions: the coolant-to-mainstream momentum flux ratio at the endwalls is higher than along the vanes and the interaction with secondary flows is relevant.

Nowlin and Fletcher's Matrix Cooling Method was studied with the target to decrease the coolant requirements at set pressure ratio conditions in a vane LE, but this technology had not been applied to the endwall cooling problem.

Chapter 3

Advanced Leading Edge Cooling Feed System Design

In this chapter the design of a new Leading Edge (LE) cooling feed system will be discussed in detail. The target driving the design process was to obtain a vane with improved, relative to conventional systems, flexibility for managing the coolant-to-mainstream pressure margin. This system could be used either to increase the pressure margin (i.e. the confidence that the component will be cooled successfully) or to decrease the pressure drop across the combustor maintaining the same pressure margin (i.e. increase the engine efficiency).

The work reported in this chapter has been patented [67] and obtained a Rolls-Royce Award to Inventors Scheme in 2014.

3.1 Leading edge insert

The application of a new leading edge coolant feed system design was studied using an idealised prismatic leading edge coolant channel, obtained from a two-dimensional extrusion of an engine representative midspan section, as shown in Figure 3.1. The vane was manufactured in two parts to allow the replacement of the leading edge during future experimental campaigns in order to test different coolant

passage geometries.

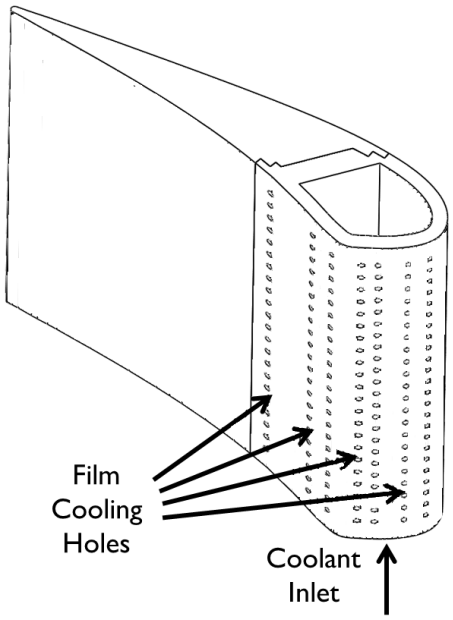


Figure 3.1: **Baseline vane**

3.1.1 Motivation

Film cooling is typically achieved at each vane leading edge through several hole rows: this type of arrangement is called showerhead cooling. Because of manufacturing process variability for gas turbine vanes and blades, Bunker [7] analysed the impact of these uncertainties on the thermal boundary conditions upon the resulting component life. Some manufacturing errors cannot be detected under inspection and, even when this is possible, obtaining sufficiently detailed information on each and every part is time consuming and costly: for this reason a conservative design is required to minimize the number of components that could overheat.

Following the discussion reported in Section 1.4, the ability to maintain an adequate pressure margin across the showerhead is essential because it provides a potential increase to:

- Either the cycle efficiency, by decreasing the minimum safe combustor pressure

drop required at design conditions;

- Or the vane reliability and life, decreasing the number of vanes experiencing hot gas ingestion.

The film cooling holes with the highest ingestion risk are around the stagnation line (i.e. the region where the hot gas experiences the highest static pressure according to Figure 1.9) and near the endwall, where the coolant is introduced (i.e. the region where the coolant velocity is at its maximum and consequently the static pressure is a minimum) as shown in Figure 3.2. Figure 3.2 (a) shows a view of the baseline vane of Figure 3.1 with the stagnation line highlighted in red next to the LE coolant passage flow network. In Figure 3.2 (b) a cross-sectional view of the coolant duct fed from the bottom indicates in blue the region with the highest ingestion risk. An example CFD prediction of the variation of coolant pressure distribution, p_{sc}, with spanwise distance, s/H, inside the LE passage is plotted in Figure 3.2 (c): the decrease in static pressure close to the inlet (s/H = 0) is evident and this can cause flow in the film cooling holes in this region to reverse. The zone with the lowest pressure margin is a critical region that requires particular care during the design process.

The design rule commonly used to avoid hot gas ingestion is that the coolant static pressure p_{sc} inside the LE passage must always be higher than the product of the maximum hot gas static pressure $max(p_{s\infty})$ and a certain pressure margin PM:

$$p_{sc} > max(p_{s\infty}) \cdot PM \tag{3.1}$$

3.1.2 Concept

The mass flow rate inside a channel can be calculated from

$$\dot{m} = \rho A u \tag{3.2}$$

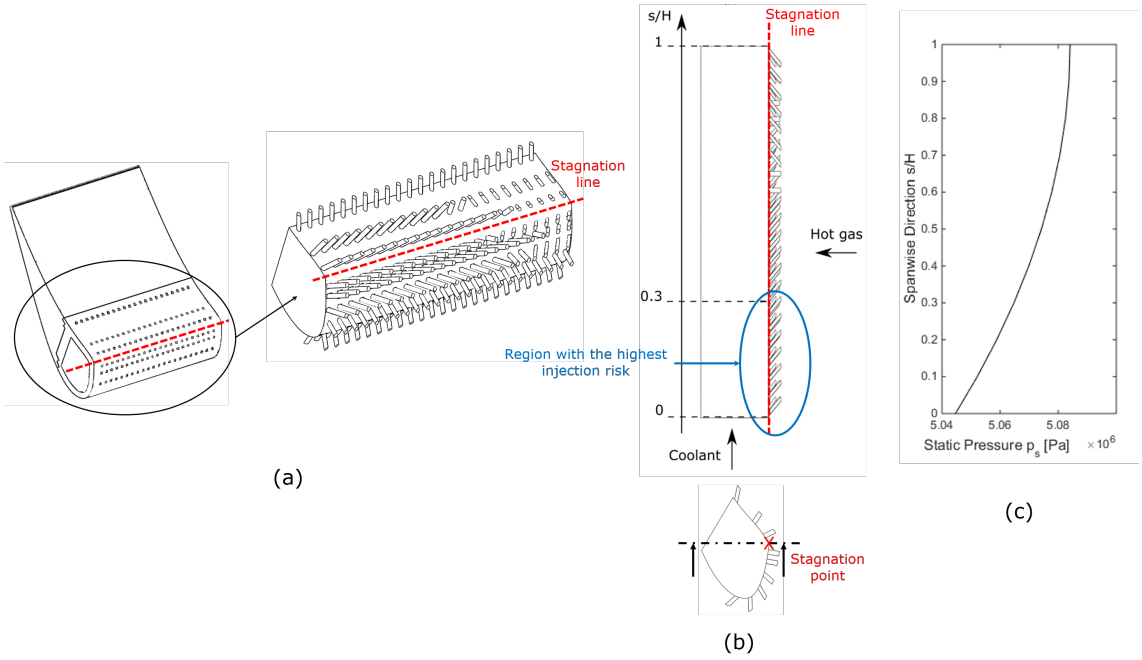


Figure 3.2: **Baseline vane LE coolant passage: (a) Baseline vane and LE coolant duct fluid network; (b) Section view of the LE coolant duct; (c) Static pressure distribution inside the LE coolant duct**

where A is the passage cross-sectional area and u is the mean fluid velocity. For a simple inviscid case, the fluid static pressure and velocity can be combined to define the coolant flow total pressure which does not vary with position

$$p_0 = p_s + 1/2\rho u^2 \tag{3.3}$$

This means that if the total pressure is constant, the static pressure decreases as the velocity increases, i.e. if we require a certain mass flow rate, the duct area has to exceed a certain value (Eq. 3.2) to satisfy Equation 3.1.

The author's research resulted in the invention of a special insert to locally decrease the coolant inlet velocity in the area with the highest ingestion risk and hence increase the static pressure, as shown in the sketch of Figure 3.3. In Figure 3.3 the blue stream (indicated by the blue arrow) feeds the critical region and the green stream flow provides coolant to the rest of the LE. In this case, coolant is only

fed from one end of the vane. Increasing the blue stream inlet area enables the local coolant velocity to be decreased for the same mass flow rate and, following Eq. 3.3, the coolant static pressure, i.e. the local pressure margin (Eq. 3.1) to be increased. An insert can be fitted inside the LE coolant passage to achieve this.

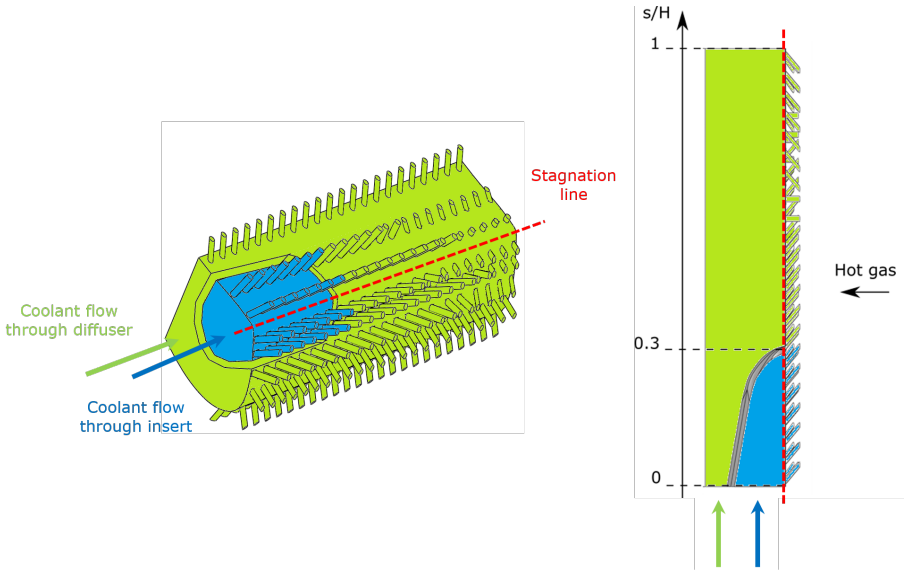


Figure 3.3: **Leading edge insert: Concept**

This approach of locally increasing the static pressure in the critical region enables the designer to:

- Increase the hot gas static pressure (i.e. reduce the pressure drop across the combustor) and, consequently, increase the net output power (Eq. 1.5) and efficiency;
- Or increase the local pressure margin which will decrease the number of vanes that are at risk of overheating.

Another benefit that could be achieved with this concept is the possibility of optimising the mass flow rate (i.e. the blowing ratio) through each hole fed by flow that is introduced by the insert changing the coolant pressure distribution in order to improve the external film performance.

3.2 Preliminary design guidelines

Some preliminary calculations were performed to get a first estimate of the required cross-sectional area distribution inside the insert in the spanwise direction (red section in Figure 3.4).

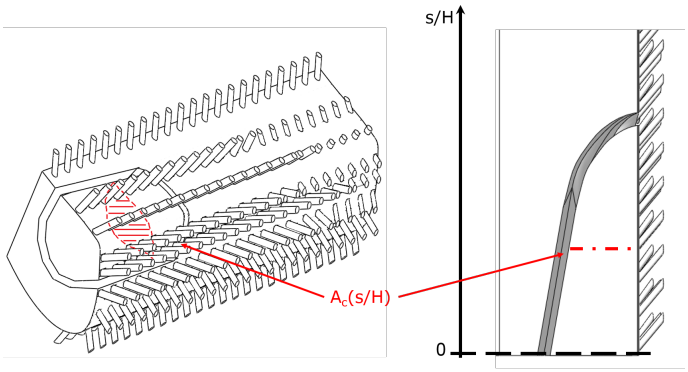


Figure 3.4: **Leading edge insert: Cross-sectional area distribution $\mathbf{A_c(s/H)}$**

1. The minimum allowable area, assuring that the coolant static pressure satisfies Eq. 3.1, can be calculated using the following procedure.

   (a) The coolant mass flow rate decreases along the leading edge passage because of the flow extraction through the film cooling holes. We will approximate the coolant flow variation in the spanwise direction s/H (where H is the combustor height at the NGV inlet plane) as

   $$\dot{m}_c(s/H) \approx (1 - s/H) \cdot \dot{m}_c(0) \tag{3.4}$$

   where $\dot{m}_c(0)$ is the coolant mass flow rate at the LE passage inlet (i.e. s/H=0)

   (b) we will also neglect the effect of friction and apply Bernoulli's equation

   $$p_{0c} = p_{sc} + 1/2\rho u_c^2 \tag{3.5}$$

   (friction is subsequently allowed for in the viscous CFD analysis)

(c) and write

$$u_c(s/H) = \frac{\dot{m}_c(s/H)}{\rho A_c(s/H)} \tag{3.6}$$

Here $u_c(s/H)$ is the coolant mean velocity at the spanwise location s/H.

(d) From Eq. 3.1

$$p_{0c} - 1/2\rho u_c^2 \geq p_{s\infty max} \cdot PM \tag{3.7}$$

$$p_{0c} - 1/2\rho \left[\frac{\dot{m}_c(s/H)}{\rho A_c(s/H)}\right]^2 \geq p_{s\infty max} \cdot PM \tag{3.8}$$

$$p_{0c} - 1/2\rho \left[\frac{(1-s/H)\cdot \dot{m}_c(0)}{\rho A_c(s/H)}\right]^2 \geq p_{s\infty max} \cdot PM \tag{3.9}$$

(e) so the minimum allowable cross-sectional area can be defined as

$$A_{cmin}(s/H) = \frac{(1-s/H)\cdot \dot{m}_c(0)}{\sqrt{2\rho[p_{0c} - p_{s\infty max} \cdot PM]}} \tag{3.10}$$

2. To calculate a first approximation of the variation in required insert cross-sectional area variation in the spanwise direction, the mass flow rate can be calculated from the amount required to supply the films at a particular s/H location from Eq.3.4.

3. Starting from this first approximation further geometry modifications are required in order to take into account some other important design considerations:

   (a) It is essential to optimize the coolant distribution through the film cooling holes to avoid a worsening of the film performance following the insert addition. Both the coolant mass flow rate and its temperature need to considered in the design process. It was noticed by the author that slowing down the coolant flow close to the wall has a significant impact on the fluid temperature. This effect was not analysed any further in the study reported in this thesis, but the author suggests it to be taken into account in future work.

   (b) The flow outside the insert passes through a duct which diffuses in the flow direction as shown in Figure 3.3. It is crucial to keep the total

pressure loss in the diffuser channel outside the insert (the green flow in Figure 3.3) low enough to avoid hot gas ingestion in the holes downstream of the insert. Although the flow slows down in the diffuser, which should increase the static pressure, this benefit can be negated by excessive total pressure loss. If the diffusion is too rapid large separations will be created and, if re-attachment does not take place, the pressure recovery drops dramatically and the outflow from the films becomes very distorted. The area at possible risk of ingestion is highlighted in in Figure 3.5.

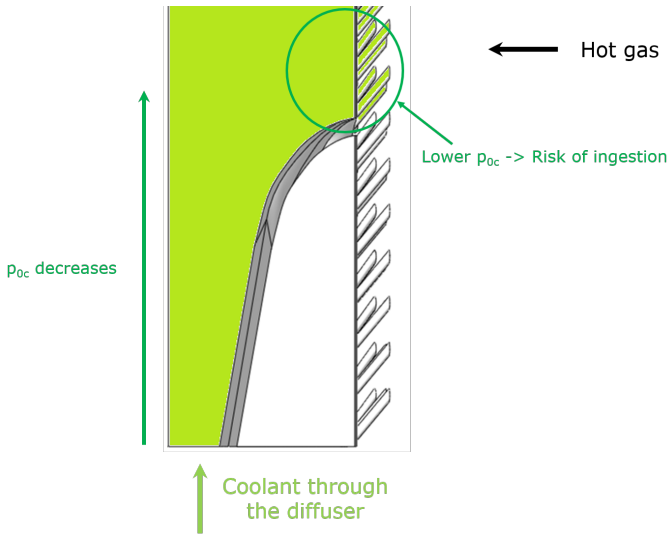


Figure 3.5: **Insert and diffuser (LE coolant passage section view as shown in Figure 3.2)**

3.3 Insert geometries studied

The baseline CAD three-dimensional model used by the author is an extrusion of a section taken from a three dimensional NGV geometry. Figure 3.6 reports the A_{cmin} distribution calculated according to Equation 3.10 versus s/H (green line) compared to the initial coolant passage area (blue line) that is constant through all the duct. For s/H $<$ 0.3 the cross-sectional area is lower than the minimum value required by Eq. 3.10 to keep the pressure margin higher than a target value of

1.03 (dotted black line). In order to demonstrate the effectiveness of the author's concept an insert was integrated into the vane leading edge cooling duct to improve the performance in this region and was used to cover the 7 holes closer to the coolant feeding side of rows S2, S1, P1 and P2, corresponding to s/H<0.3 as shown in Figure 3.7. The 3D CAD models were created with SolidWorks.

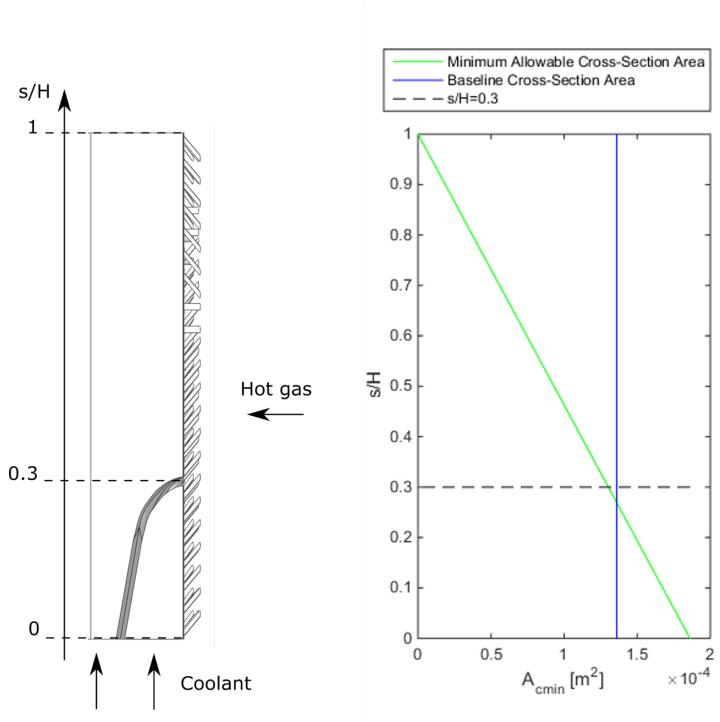


Figure 3.6: **Theoretical minimum allowable cross-sectional area distribution $A_{cmin}(s/H)$ for the baseline case calculated with Equation 3.10**

Equation 3.10 was used to calculate the theoretical minimum cross-sectional area required to feed the film cooling holes inside the insert, setting $\dot{m}_c(s/H = 0)$ as the coolant mass flow rate through these holes in the baseline case (black line in Figure 3.8). Starting from this theoretical distribution, six different geometries of leading edge channels were created (Figure 3.8): geometry A approximates the theoretical line, while from geometry B to F A_c is continuously increased.

As previously mentioned in Section 3.2, optimization of the diffuser performance is required to prevent backflow. The losses inside the diffuser cause the coolant

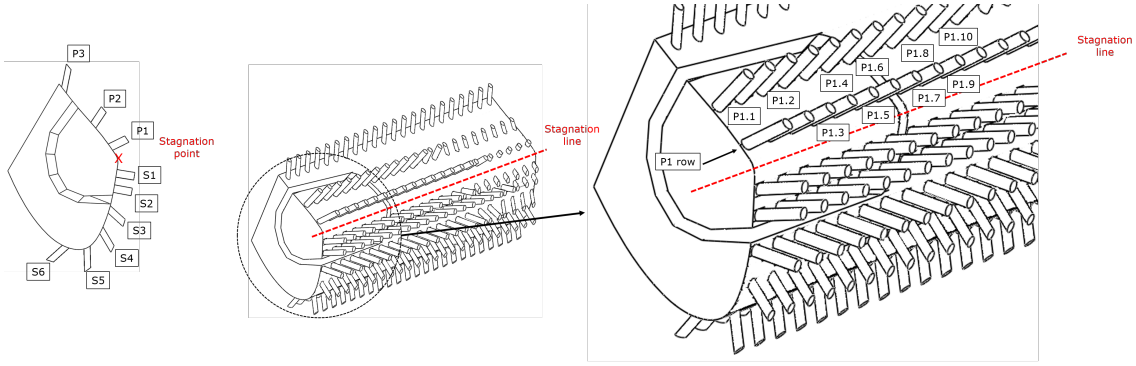


Figure 3.7: **Film cooling hole row nomenclature: top view (on the left), perspective view (in the centre) and enlargement of the insert (on the right). In the P1 row the holes from P1.1 to P1.7 are fed from the insert**

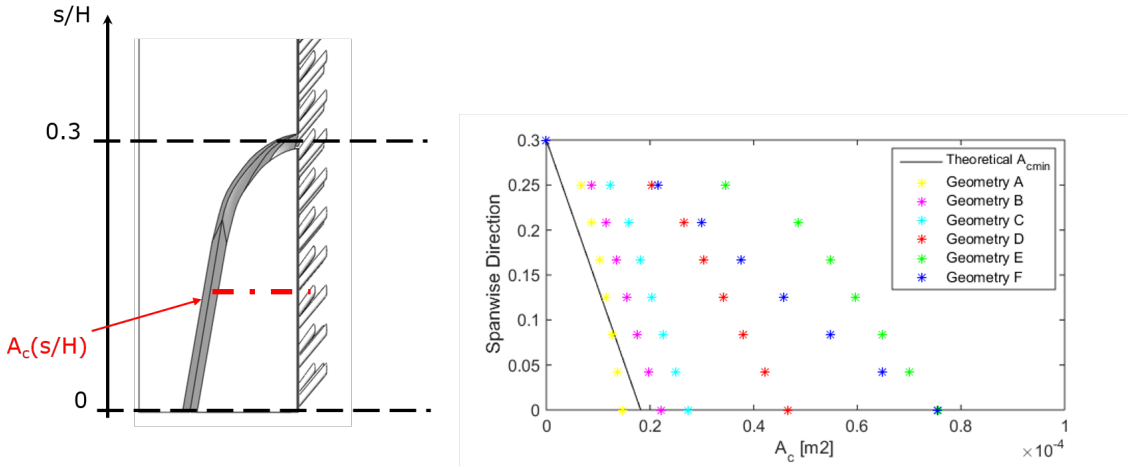


Figure 3.8: **Leading edge insert: Cross-sectional area distribution $\mathbf{A_c}$(s/H) for different geometries**

total pressure to drop inside the passage and this can increase the risk of hot gas ingestion downstream of the insert in the diffuser section and downstream, in the region highlighted in Figure 3.5.

The diffuser length set to s/H = 0.3 following the preliminary design considerations (Figure 3.6), the geometrical parameters that can be modified to optimise the system performance are the outlet-to-inlet area ratio A_o/A_i and the diffuser angle Θ (defined in Figure 3.9). Note that, in this case, A_o was fixed at the area of the

leading edge passage.

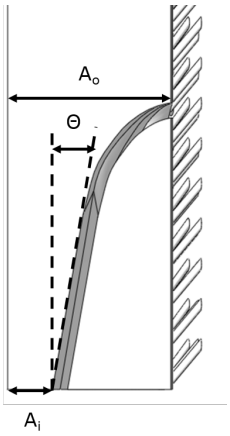


Figure 3.9: **Insert diffuser geometric parameters: A_i is the diffuser inlet area, A_o is the diffuser outlet area and Θ is the diffuser angle at the inlet section measured in the section plane perpendicular to the LE cooling duct.**

The values of A_o/A_i and Θ for the different studied configurations are reported in Table 3.1. The bottom view and four sections of each analysed geometry are shown in Figures 3.11, 3.12, 3.13, 3.14, 3.15, 3.10. The range of geometries from A to F were obtained through slight modifications of A_o/A_i and Θ, with the purpose of evaluating the effect of these parameters on the system performance.

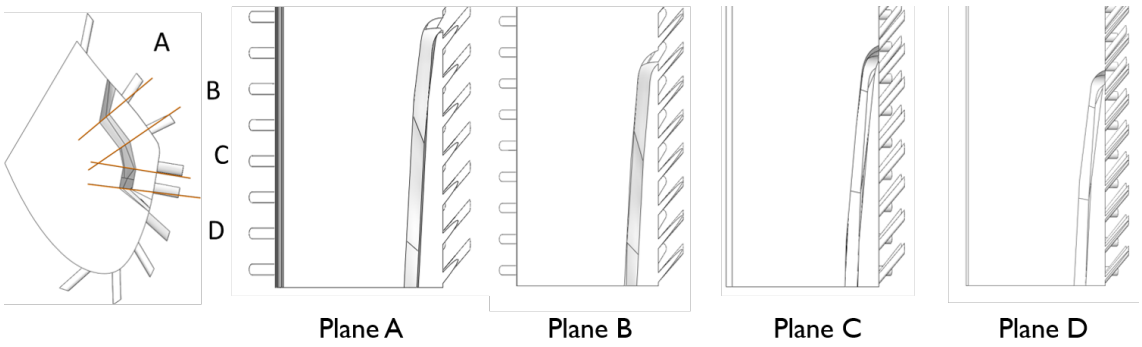


Figure 3.10: **Simulated leading edge geometries: Geometry A - Bottom view and plane sections**

	A_o/A_i	$\Theta[^\circ]$
Geometry A	1.2	3
Geometry B	1.3	7
Geometry C	1.4	7
Geometry D	1.8	10
Geometry E	3.3	10
Geometry F	3.3	20

Table 3.1: **Simulated leading edge geometries: diffuser geometric parameters. The different geometries were chosen to explore the effect of A_o/A_i and Θ on the insert and diffuser performance**

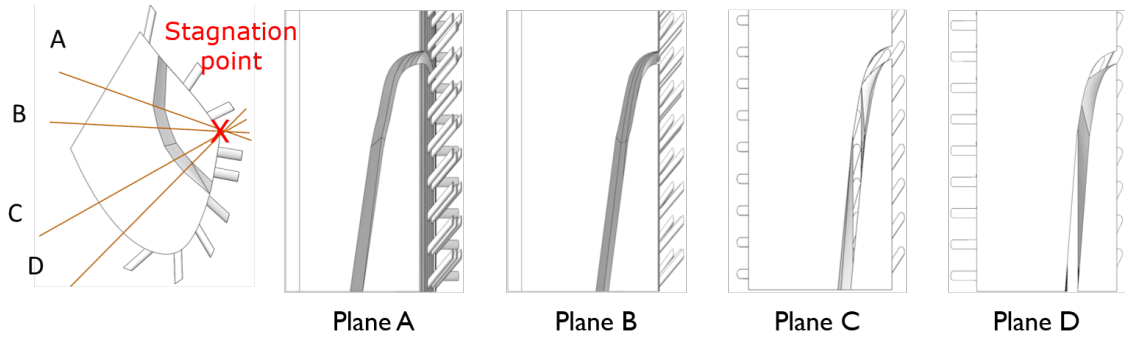


Figure 3.11: **Simulated leading edge geometries: Geometry B - Bottom view and plane sections**

The insert concept can be further developed to more advanced designs. Two examples are shown in Figure 3.16. The use of two inserts, as in Figure 3.16 (a), would allow the coolant temperature increase to be contained and feed the holes with colder air. The model in Figure 3.16 (b) is fed from both endwalls and, with three inserts, avoids a pressure margin decrease downstream of the inner inserts, maximizing the design flexibility.

These concepts have not been further studied because the author decided it was more important to determine the fundamental functional of a single piece insert before studying multi-piece inserts.

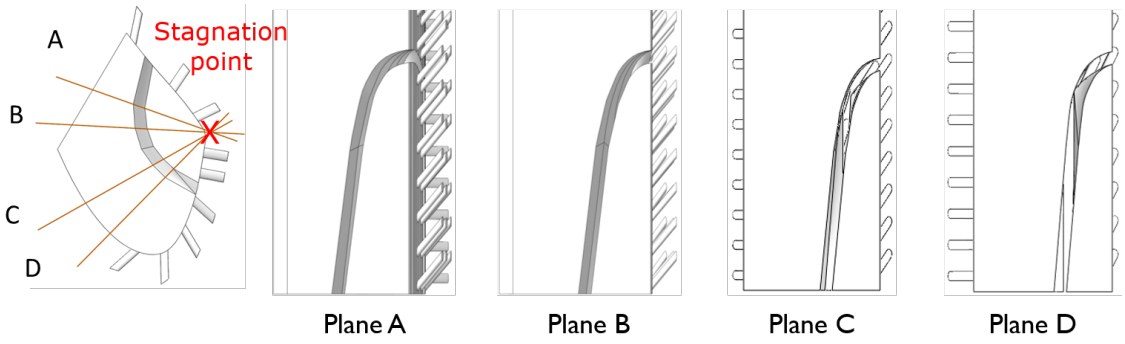


Figure 3.12: **Simulated leading edge geometries: Geometry C - Bottom view and plane sections**

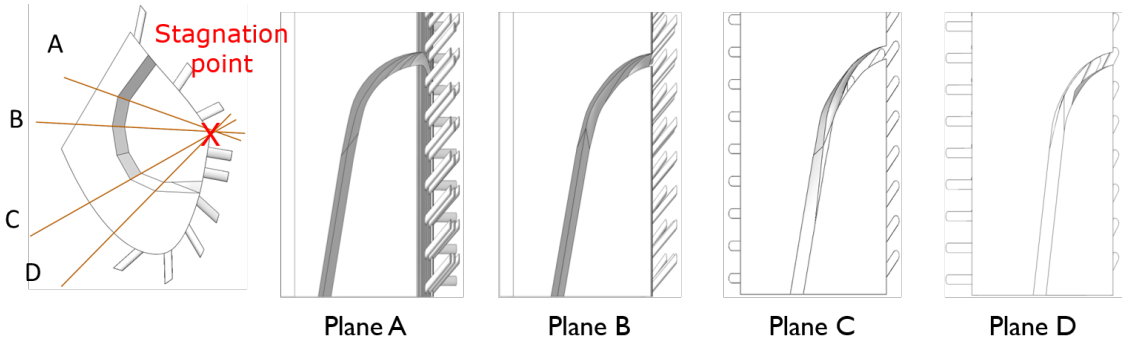


Figure 3.13: **Simulated leading edge geometries: Geometry D - Bottom view and plane sections**

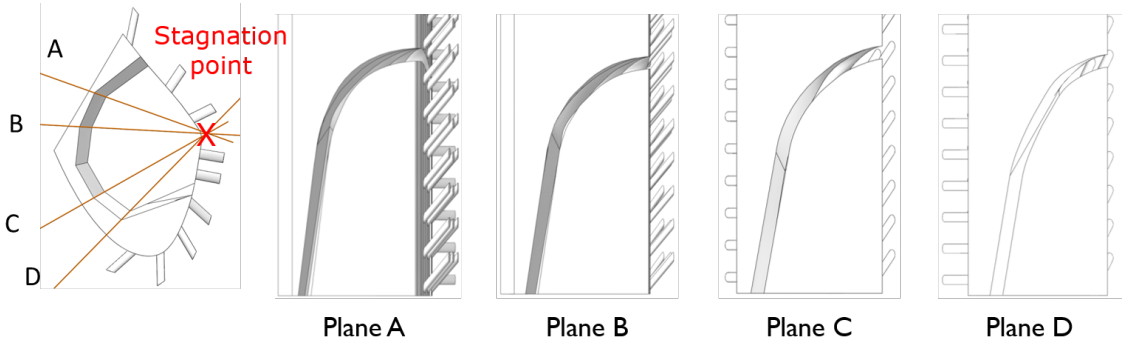


Figure 3.14: **Simulated leading edge geometries: Geometry E - Bottom view and plane sections**

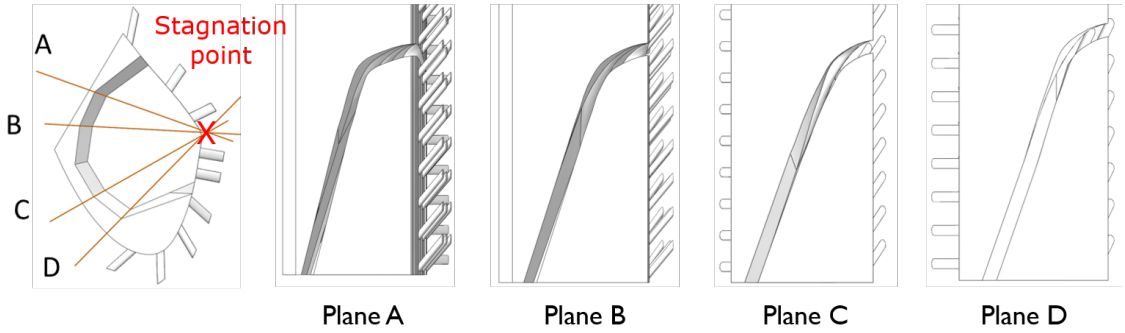


Figure 3.15: **Simulated leading edge geometries: Geometry F - Bottom view and plane sections**

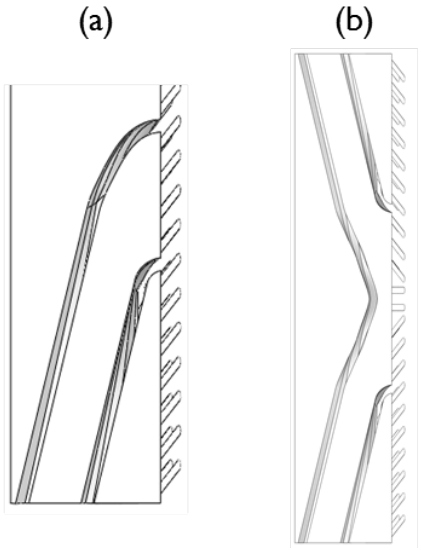


Figure 3.16: **Double insert configurations**

3.4 CFD simulations

A detailed CFD investigation was performed on the different cooling passage designs presented above. The unstructured tetrahedral meshes were generated with ANSYS ICEM 12.0 and typically contained around $5 \cdot 10^6$ elements used in the computation (Figure 3.17). The RANS simulations were performed with ANSYS Fluent 12.0. The turbulence was modeled using the realizable k-ε model with enhanced wall functions. The imposed boundary conditions were:

- Uniform total and static pressure distribution at the insert and main channel inlets.
- Uniform static pressure at each hole outlet (obtained from the mainflow Mach number distribution).
- Uniform wall temperature.

The boundary condition parameter values used for the simulations were engine-representative.

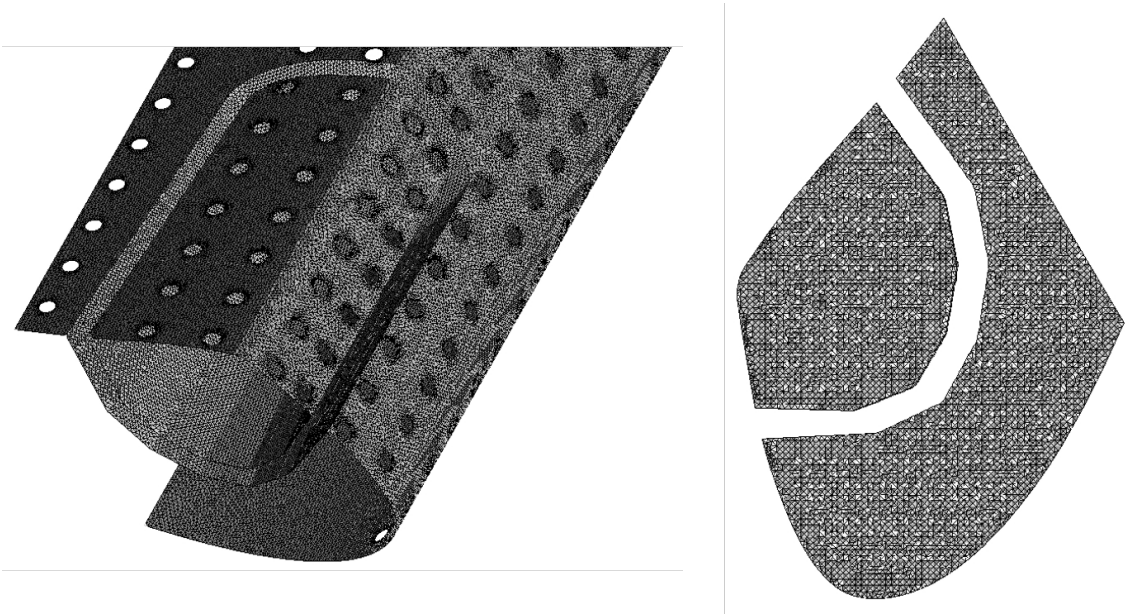


Figure 3.17: **Example of mesh used (Geometry D)**

3.5 CFD results

The results obtained from the simulation of the six geometries presented in Section 3.3 will be discussed in this section. The author will firstly evaluate the impact of the insert geometry to the diffuser performance and to the film cooling mass flow rate distribution and afterwards analyse the beneficial effect on the coolant static pressure distribution and the pressure margin across the film cooling holes.

The diffuser performance is assessed using two parameters defined by Miller [44] for a diffuser with a constant area section at the outlet: the loss coefficient K_d and the static pressure recovery coefficient C_{pr}

$$K_d = \frac{p_o(s/H=0) - p_0(s/H=0.3)}{1/2\rho u^2} \tag{3.11}$$

$$C_{pr} = 1 - \left(\frac{A(s/H=0)}{A(s/H=0.3)}\right)^2 - K_d \tag{3.12}$$

where s/H=0 corresponds to the diffuser inlet, s/H=0.3 to the section of the main channel just downstream the insert and u is the flow mean velocity at the diffuser inlet section. To estimate the total pressure loss inside the insert, the loss ratio defined by Miller [44] for a dividing manifold based only on geometrical parameters was calculated as follows:

$$K_{ins} = \left(\frac{\sum_{i=1}^{N} A_i}{A(s/H=0)}\right)^2 \tag{3.13}$$

where A_i is the area at the exit of the i-th hole and N is the number of holes fed by the insert.

Figures 3.18 and 3.20 compare the loss coefficients calculated from the author's CFD results for the selected geometries inside the insert and the diffuser. It can be seen that the diffuser loss coefficients show the opposite trend compared to the losses made up by the flow in the insert: an increase of the insert inlet cross-sectional area reduces the coolant velocity improving the insert performance, but this causes a decrease of the diffuser duct inlet cross-sectional area (the total inlet area is set by the space available in the leading edge) and a consequent increase of the diffusion ratio. This suggests that a compromise will be necessary in the selection of the insert geometry for design.

Miller [44] reports the static pressure recovery C_{pr} data in a chart as a function of the area ratio A_o/A_i and the non-dimensional length N/R_1, where N is the diffuser length and R_1 is half of the hydraulic diameter at the diffuser inlet. In Table 3.2

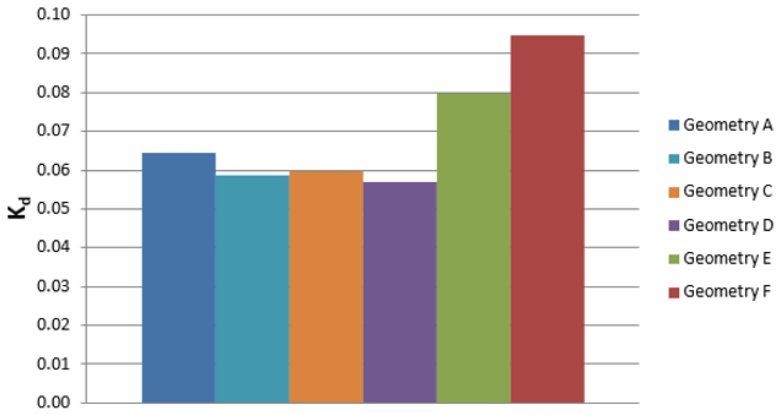


Figure 3.18: **Diffuser loss coefficient** $\mathbf{K_d = \frac{p_o(s/H=0) - p_0(s/H=0.3)}{1/2\rho u^2}}$

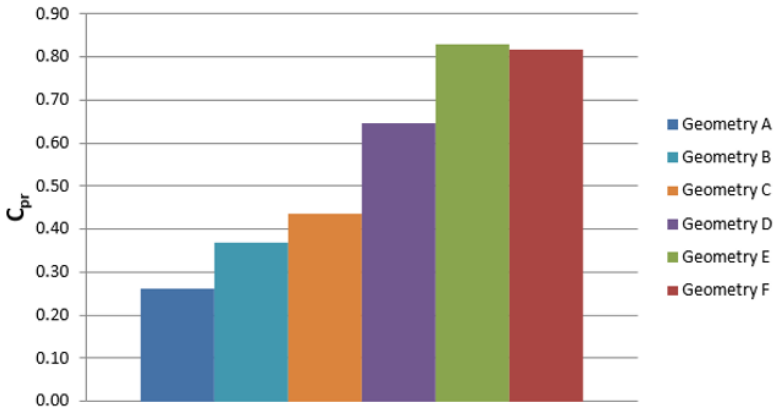


Figure 3.19: **Diffuser static pressure recovery coefficient** $\mathbf{C_{pr} = 1 - \left(\frac{A(s/H=0)}{A(s/H=0.3)}\right)^2 - K_d}$

the C_{pr} values extrapolated from Miller's diffuser performance chart are compared to the CFD calculations by the present author and it can be seen that there is a very good agreement.

A_o/A_i appears to be the parameter which most influences total pressure loss (Figures 3.21 and 3.23). The diffuser pressure losses starts to increase for $A_o/A_i \geq 1.8$. At high area ratio values, a lower Θ at the diffuser inlet helps to limit the pressure losses in the diffuser. An increase of A_o/A_i leads to an increase of static pressure recovery (Figure 3.22): this means that for geometries E and F the high value of K_d can be partially compensated by a higher recovery (Figure 3.19).

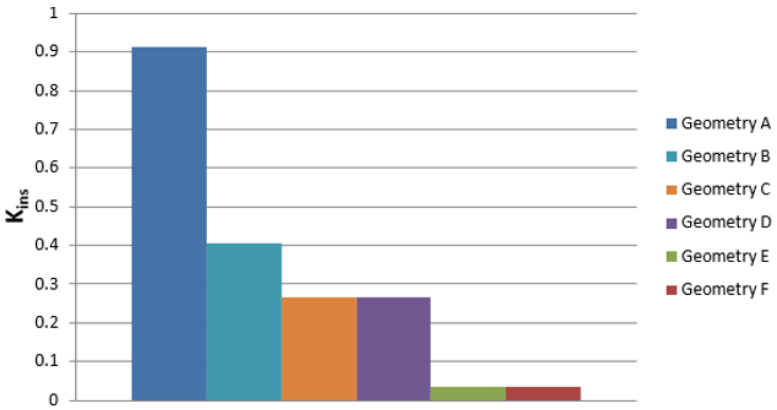


Figure 3.20: **Insert loss coefficient** $\mathbf{K_{ins} = \left(\frac{\sum_{i=1}^{N} A_i}{A(s/H=0)}\right)^2}$

	A_o/A_i	N/R_1	C_{pr} (Miller [44])	C_{pr} (CFD from Fig. 3.19)
Geometry A	1.2	4.1	≈0.3	0.26
Geometry B	1.3	4.4	0.3 - 0.4	0.37
Geometry C	1.4	4.8	0.4 - 0.5	0.43
Geometry D	1.8	6.7	0.6 - 0.7	0.65
Geometry E	3.3	13.5	>0.75	0.83
Geometry F	3.3	13.7	>0.75	0.82

Table 3.2: **Diffuser static pressure recovery coefficient C_{pr}: Comparison with Miller's [44] performance data for a diffuser with a constant area section at the outlet**

The presence of the insert decreases the total feed area and introduces further pressure losses which cause the total coolant mass flow rate to be lower than for the baseline case: the ratio between the total mass flow rate through each geometry and the baseline mass flow rate are plotted in Figure 3.24. The increase of $(A_i)_{insert}$ causes a continuous decrease in the total mass flow rate from geometry B to F: geometry A is the one less affected.

In order to better understand how the coolant is distributed through the system, the ratio between the mass flow rates through the diffuser and through the insert

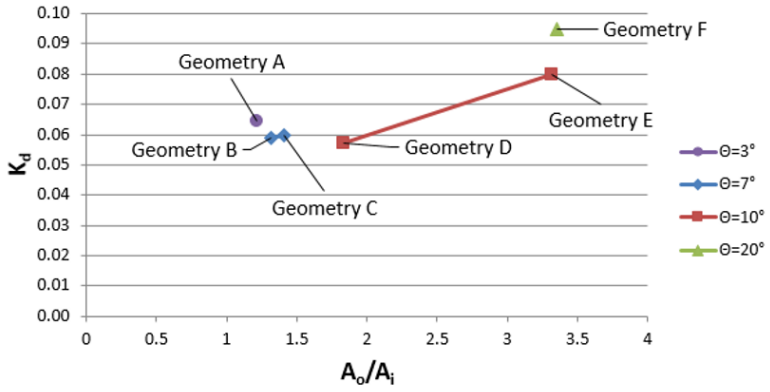


Figure 3.21: **Diffuser loss coefficient $K_d = \frac{p_o(s/H=0)-p_0(s/H=0.3)}{1/2\rho u^2}$ vs A_o/A_i for different Θ values**

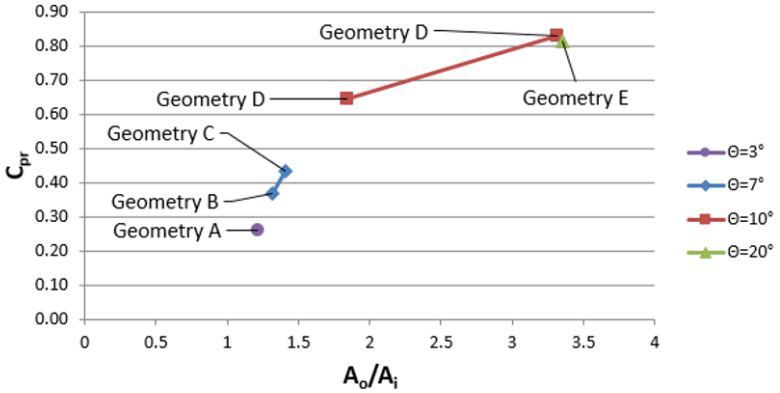


Figure 3.22: **Diffuser static pressure recovery coefficient $C_{pr} = 1 - \left(\frac{A(s/H=0)}{A(s/H=0.3)}\right)^2 - K_d$ vs A_o/A_i for different Θ values**

divided by the total coolant flowing through the LE coolant passage are shown in Figures 3.25 and 3.26. The differences in the diffuser mass flow rate are caused by the variation in the loss coefficient in the diffuser. The mass flow rate variation in the insert is lower and is significant only for $\Theta > 10°$.

The coolant mass flow rate through the first ten holes of row P1 (Fig. 3.7) for each geometry is compared to the baseline leading edge geometry in Figure 3.27, where the mass flow rate variation for the i-th hole is calculated as

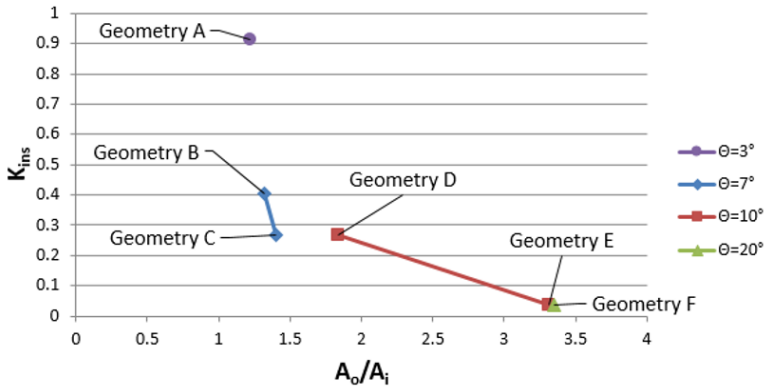


Figure 3.23: **Insert loss coefficient $\mathbf{K_{ins} = \left(\frac{\sum_{i=1}^{N} A_i}{A(s/H=0)}\right)^2}$ vs $\mathbf{A_o/A_i}$ for different $\mathbf{\Theta}$ values**

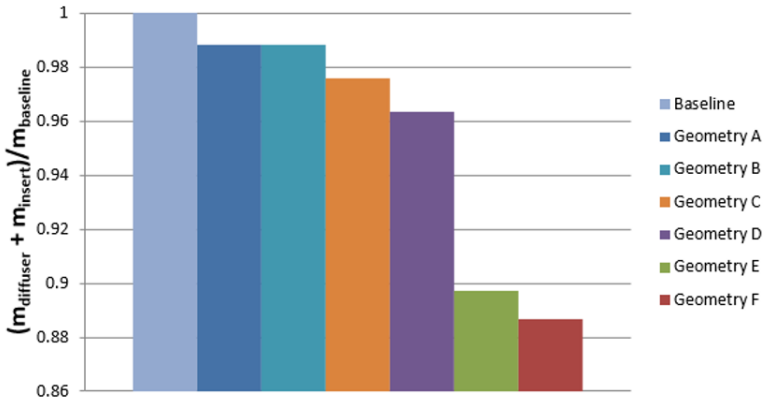


Figure 3.24: **Total coolant mass flow rate non-dimensionalized by the baseline case mass flow rate: Comparison between different geometries at fixed supply pressure**

$$\Delta\dot{m}_{Ci} = \frac{\dot{m}_{Ci} - (\sum_{i=1}^{N} \dot{m}_{Ci})/N}{(\sum_{i=1}^{N} \dot{m}_{Ci})/N} \tag{3.14}$$

where N=10 is the number of holes considered. The holes from 1 to 7 are inside the insert, the ones labeled from 8 to 10 are downstream of the insert (see Fig. 3.27).

As expected, without the insert the distribution is more uniform: the effect of an increase of both A_o/A_i and Θ is to decrease the uniformity of the coolant distribution through the holes in the spanwise direction. Geometries E and F are the cases with

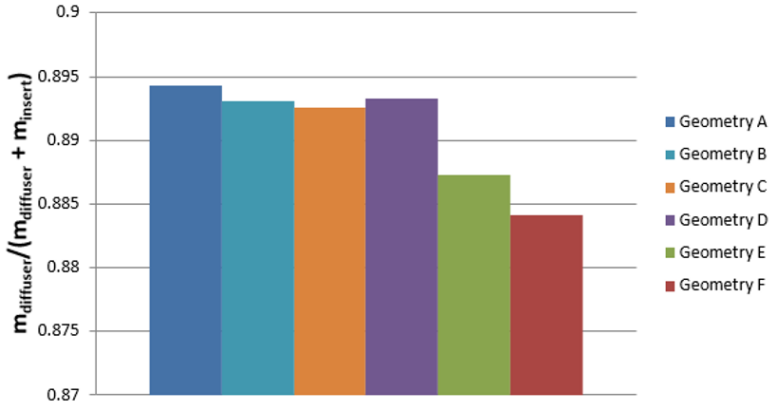


Figure 3.25: **Diffuser coolant mass flow rate non-dimensionalized by the total mass flow rate: Comparison between different geometries at fixed supply pressure**

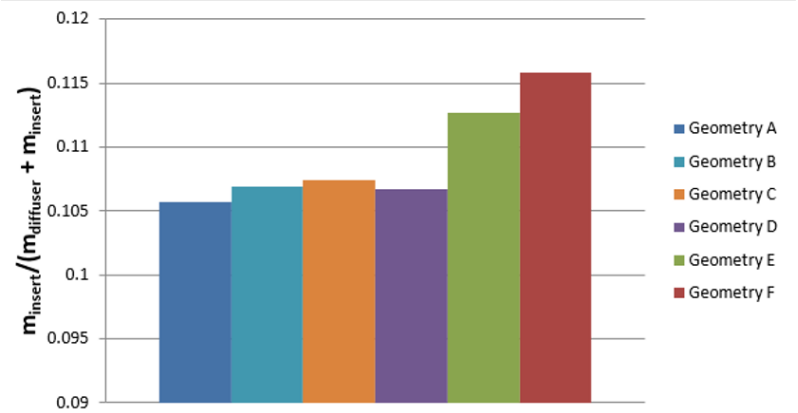


Figure 3.26: **Insert coolant mass flow rate non-dimensionalized by the total mass flow rate: Comparison between different geometries at fixed supply pressure**

the mass flow distribution which varies the most. These data indicate that the uniformity of the mass flow rate distribution decreases as the diffuser performance deteriorates.

To clarify the dependence of the film cooling hole mass flow uniformity on A_o/A_i, $\frac{max(m_{Ci})-min(m_{Ci})}{(\sum_{i=1}^{N} \dot{m}_{Ci})/N}$ for each case considered is plotted in Figure 3.28: this parameter gives a measure of the maximum spread between the mass flow rate through each

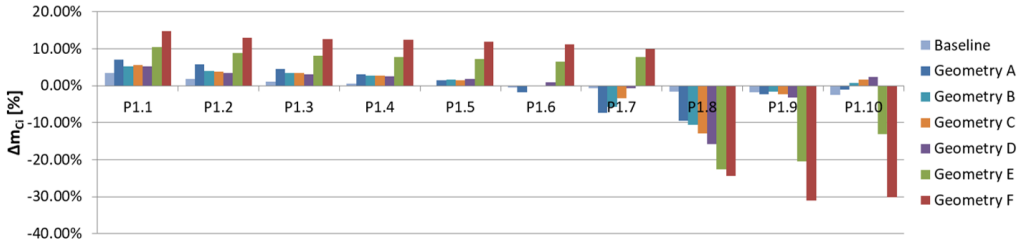


Figure 3.27: **Mass flow rate variation (as defined in Eq. 3.14) through each hole of row P1 – Comparison between different insert geometries**

hole between P1.1 and P1.10. Its value continuously increases when A_o/A_i increases indicating a constant reduction in mass flow uniformity, that would result in a reduced uniformity of the external film coverage in the spanwise direction.

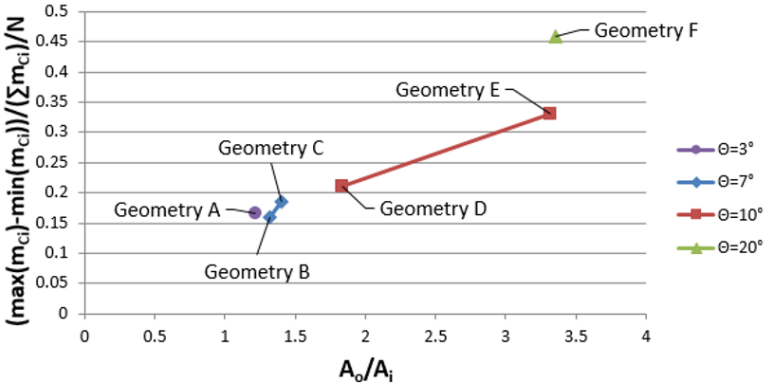


Figure 3.28: $\frac{\max(m_{ci})-\min(m_{ci})}{(\sum_{i=1}^{N}\dot{m}_{ci})/N}$ **vs** A_o/A_i **for different** Θ **values**

The effect is the same on the coolant distribution inside the insert between the different rows (Figure 3.29): geometry A is the case with the highest film cooling mass flow rate through rows P1, P2 and S2, but there is a drop for row S1. The insert design can be further optimised to modulate the mass flow rate (i.e. the film blowing ratio) through each row, but this is beyond the current intentions of the author.

Despite the impact on the film cooling mass flow distribution, this new concept can benefit the static pressure distribution inside the LE coolant passage and the

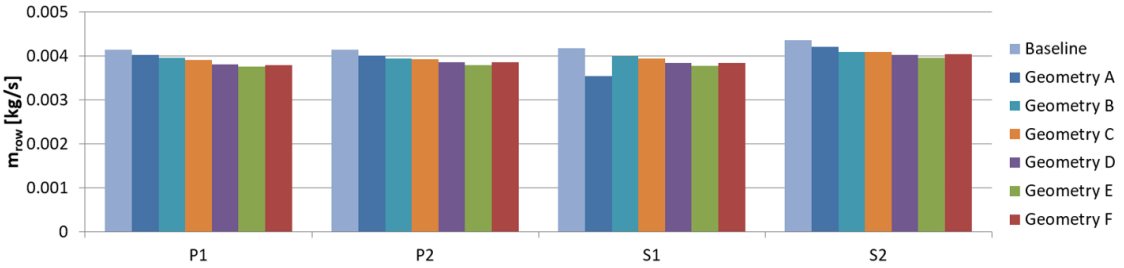


Figure 3.29: **Mass flow rate through rows P1, P2, S1 and S2 for holes inside the insert: Comparison between different insert geometries**

pressure margin across the films. The difference between the coolant static pressure p_{sc} in each insert geometry and in the baseline case non-dimensionalized with the dynamic head $1/2\rho v^2(s/H = 0)$, where $v(s/H = 0)$ is the averaged velocity at the insert inlet, is plotted versus s/H in Figure 3.30. The values of p_{sc} are calculated averaging the static pressure at each s/H position considered inside the insert for geometries from A to F and inside the entire cross-section for the baseline case. The results show that the presence of the insert increases the static pressure at each location ($p_{sc} - p_{sc_{Baseline}} > 0$ for all the cases). Increasing the insert inlet area (i.e. slowing down the flow) from geometry A to F, the static pressure continuously increases at any spanwise location, especially close to the coolant inlet (s/H=0).

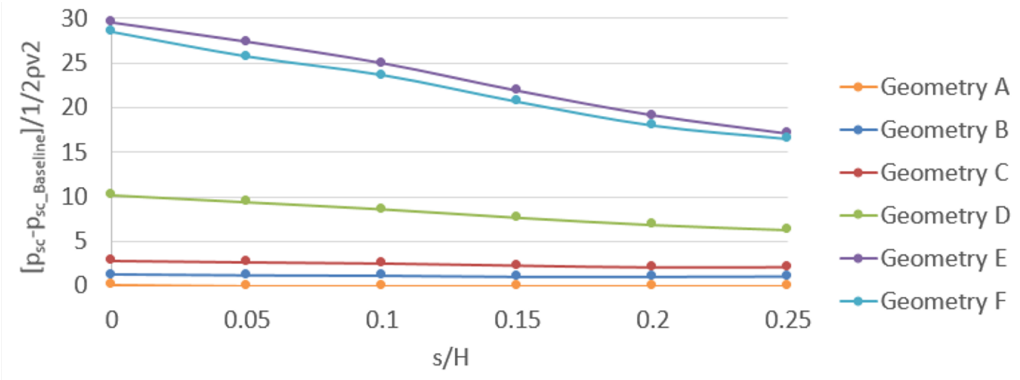


Figure 3.30: **Difference between coolant static pressure in each insert geometry and baseline case$[\mathbf{p_{sc} - p_{sc_{Baseline}}}]/\mathbf{1/2\rho v^2}(\mathbf{s/H = 0})$ inside the insert versus s/H**

Figure 3.31 shows the pressure difference between the coolant static pressure p_{sc} inside the insert and the maximum mainstream static pressure $max(p_{s\infty})$ (i.e. the stagnation pressure) non-dimensionalized with the dynamic head $1/2\rho v^2(s/H = 0)$, where $v(s/H = 0)$ is the averaged velocity at the insert inlet. The baseline and geometry A lines are almost coincident at the bottom of the graph. This plot shows again that the static pressure margin is higher with the new geometries and, in particular, it increases drastically with the increase of the insert inlet area: this proves to be the driving parameter affecting the insert performance.

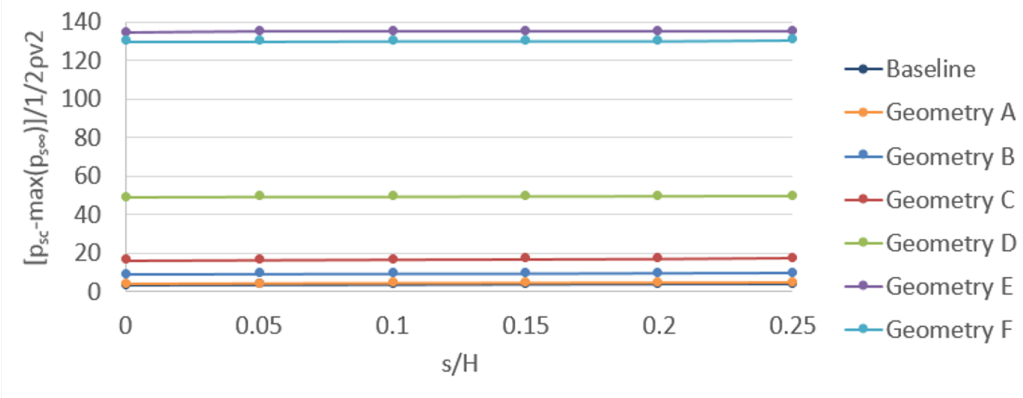


Figure 3.31: **Difference between coolant and mainstream static pressure $[\mathbf{p_{sc} - max(p_{s\infty})}]/\mathbf{1/2\rho v^2(s/H = 0)}$ inside the insert versus s/H**

The effect on the diffuser performance needs to be taken into account before any further analysis. Figure 3.32 shows the diffuser frame of reference: the insert covers up to s/H = 0.3 and for this reason it was decided to check the static pressure levels in the range 0.25 < s/H < 0.35 to understand the flow behaviour at the end of the diffusion process, where there is a risk of flow separating.

Figure 3.33 reports difference between the coolant static pressure p_{sc} in each insert geometry and in the baseline case non-dimensionalized with the dynamic head $1/2\rho v^2(s/H = 0)$, where $v(s/H = 0)$ is the averaged velocity at the diffuser inlet, plotted versus s/H at the diffuser outlet. In this case the values of p_{sc} are averaged at each considered s/H position outside the insert for geometries from A to F and inside the entire cross-section in the baseline case. Geometry A is the only

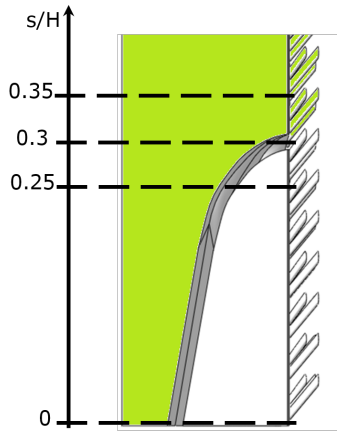


Figure 3.32: **Diffuser frame of reference (LE coolant passage section view)**

case where the flow diffuses slowly enough to improve the flow conditions compared to the baseline case ($p_{sc} - p_{sc_{Baseline}} > 0$). Geometries B and C show a small static pressure deficit at the the diffuser outlet that is recovered for s/H > 0.3. Geometry D (characterized by a slight increase of both A_o/A_i and Θ compared to geometries B and C) produces a static pressure drop that is not recovered as quickly as in geometries B and C. The diffusers in geometries E and F (characterized by a steep increase of both A_o/A_i and Θ) show very low performance and the static pressure is significantly lower than the other cases across the outlet. In geometries from B to E the static pressure stops increasing at the diffusion outlet because of the flow mixing and then it starts to increase again as the coolant velocity drops. Because of the very high diffusion angle value in geometry F ($\Theta = 20^o$) the static pressure decreases at the diffuser outlet ($0.3 <$ s/H < 0.35).

The pressure difference between the coolant static pressure p_{sc} at the diffuser outlet and the maximum mainstream static pressure $max(p_{s\infty})$ (i.e. the mainstream stagnation pressure) non-dimensionalized with the dynamic head $1/2\rho v^2(s/H = 0)$, where $v(s/H = 0)$ is the averaged velocity at the diffuser duct inlet, is plotted in Figure 3.34. This shows how the diffuser performance deteriorates when A_o/A_i and Θ are increased: a mild diffusion (such as in geometry A) allows an improvement of the pressure distribution downstream of the diffuser but limits the ability to increase

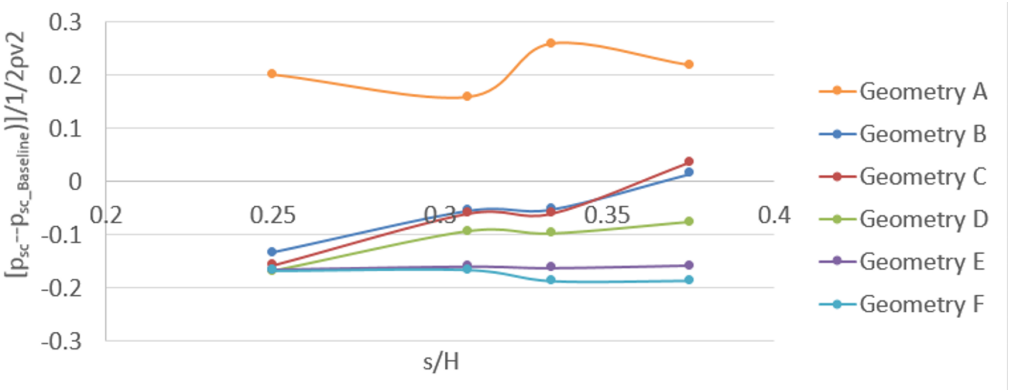


Figure 3.33: **Difference between coolant static pressure in each insert geometry and baseline case$[\mathbf{p_{sc}} - (\mathbf{p_{sc_{Baseline}}})]/\mathbf{1/2}\rho\mathbf{v^2}(\mathbf{s/H = 0})$ inside the diffuser versus s/H**

the pressure margin inside the insert (Figures 3.30 and 3.31).

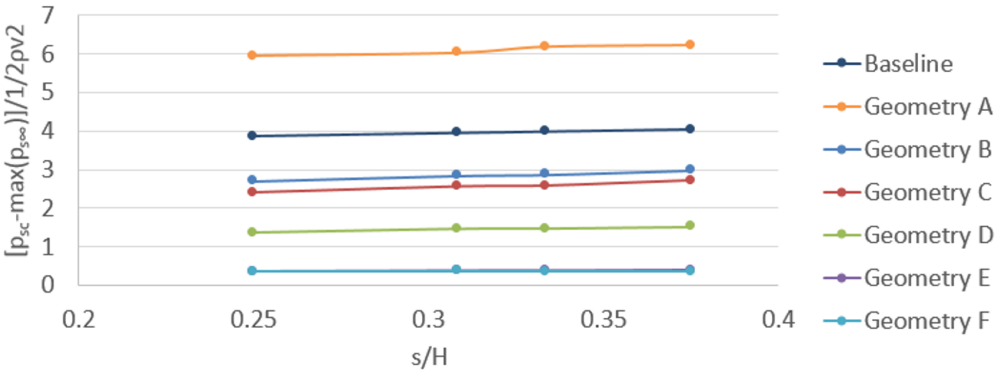


Figure 3.34: **Difference between coolant and mainstream static pressure $[\mathbf{p_{sc}} - \mathbf{max}(\mathbf{p_{s\infty}})]/\mathbf{1/2}\rho\mathbf{v^2}(\mathbf{s/H = 0})$ inside the diffuser versus s/H**

The data reported in this section reveal the challenge of balancing the need to increase the static pressure inside the insert and the necessity to avoid any risk of a pressure drop downstream of the diffuser sufficient to increase the chances of ingestion downstream of the insert. The design purpose is therefore to reach a sufficient pressure margin increase for $s/H < 0.3$ keeping the diffusion losses to acceptable levels.

3.5.1 Stewart plot

The Stewart plot is used in industry to illustrate the ingestion risk between different engines. The X axis is the reciprocal of the Q function. Q is a parameter proportional to the mass flow rate fed to the cooling system and dependent on the Mach number, total-to-static temperature ratio and total-to-static pressure ratio. Q is defined

$$Q = \frac{\dot{m}\sqrt{T_0}}{Ap_0} \tag{3.15}$$

which can be rearranged to

$$Q = \sqrt{\frac{\gamma}{R}} Ma \sqrt{\frac{T_0}{T_s}} \frac{p_s}{p_0} \tag{3.16}$$

For an isentropic flow, the following relationships exist

$$\frac{p_s}{p_0} = \left(1 + \frac{\gamma - 1}{2} Ma^2\right)^{\frac{-\gamma}{\gamma - 1}} \tag{3.17}$$

$$\frac{T_s}{T_0} = \left(1 + \frac{\gamma - 1}{2} Ma^2\right)^{-1} \tag{3.18}$$

This means that Q is a unique function of the Mach number

$$Q = \sqrt{\frac{\gamma}{R}} Ma \left(1 + \frac{\gamma - 1}{2} Ma^2\right)^{-1/[2(\gamma - 1)]} \tag{3.19}$$

The ordinate for a Stewart plot is the maximum total pressure difference between coolant and hot gas, defined as

$$\frac{p_{0c} - p_{40}}{p_{0c}} \tag{3.20}$$

where p_{40} is the hot gas total pressure at the NGV inlet plane.

$(p_{0c} - p_{40})/p_{0c}$ can be rewritten as a function of the pressure margin

$$\frac{p_{0c} - p_{40}}{p_{0c}} = 1 - \frac{p_{40}}{p_{0c}} = 1 - \frac{p_{40}}{p_{sc}} \times \frac{p_{sc}}{p_{0c}} \tag{3.21}$$

and after defining the pressure margin according to Eq. 3.1

$$PM = \frac{p_{sc}}{p_{40}} \tag{3.22}$$

it is possible to write that

$$\frac{p_{0c} - p_{40}}{p_{0c}} = 1 - 1/PM \times \frac{p_{sc}}{p_{0c}} \tag{3.23}$$

Following Eq. 3.17, p_{sc}/p_{0c} can be written as a function of the Mach number

$$\frac{p_{0c} - p_{40}}{p_{0c}} = 1 - 1/PM \times \left(1 + \frac{\gamma - 1}{2} Ma^2\right)^{\frac{-\gamma}{\gamma - 1}} \tag{3.24}$$

Therefore, once coolant Mach number and desired pressure margin are set, it is possible to calculate Q and $(p_{0c} - p_{40})/p_{0c}$:

$$\begin{cases} Q = \sqrt{\frac{\gamma}{R}} Ma \left(1 + \frac{\gamma-1}{2} Ma^2\right)^{-1/[2(\gamma-1)]} \\ \frac{p_{0c}-p_{40}}{p_{0c}} = 1 - 1/PM \times \left(1 + \frac{\gamma-1}{2} Ma^2\right)^{\frac{-\gamma}{\gamma-1}} \end{cases} \tag{3.25}$$

The isolines of PM (which is equal to p_{sc}/p_{40}) are included on the Stewart plot to help compare different LE coolant passage performance. The dimensionless total pressure difference (the ordinate) and the value of 1/Q (the abscissa) are known for many cooling systems. The lines of constant PM are indicative of the levels of pressure margin under the assumption of isentropic flow.

An ideal cooling system design would be able to achieve a high pressure margin for a small value Q and hence high value of 1/Q. As 1/Q increases, the Mach number drops and the coolant static pressure gets closer to the total pressure. In other words, there is less chance of ingestion if the flow is moving slowly, which means that the required coolant pressure tohot gas pressure ratio gets lower for a given PM. The chart enables the design engineers to assess the risk of flow reversal in the flm cooling holes.

Figure 3.35 compares the different geometries on a Stewart plot for conditions at the insert inlet. $\frac{p_{0c}-p_{40}}{p_{0c}}$ is constant and equal to 3% for all the cases because the pressure boundary conditions are the same for all the simulations, while 1/Q

decreases when the air flow velocity increases (i.e. the static pressure decreases). It is evident that the insert concept works: while the baseline vane has a pressure margin lower than 1.025, the vanes with insert can reach a pressure margin higher than 1.03. The cases with a higher insert inlet area, for example geometries E and F, have lower air velocity at the insert inlet which produces a higher static pressure margin.

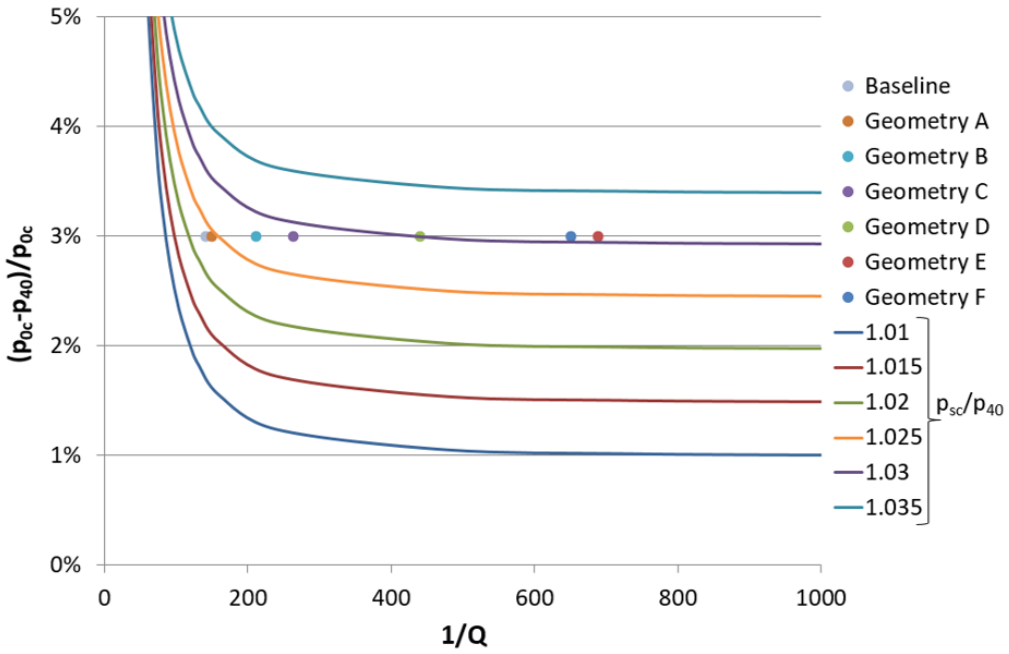


Figure 3.35: **Stewart plot: Insert inlet**

Figures 3.33 and 3.34 showed a decrease of static pressure at the diffuser outlet (s/H = 0.3) where A_o/A_i and Θ increase. For this reason, it is important to quantify how much this drop affects the pressure margin downstream of the insert and the data at s/H = 0.3 are reported on the Stewart plot in Figure 3.36. The geometries with the best insert performance (like E and F) are the ones with the highest diffuser losses: this is because an increase of the insert inlet area is beneficial for the insert performance, but causes an increase in $(A_o/A_i)_{diffuser}$ that has been shown to be detrimental to the diffuser performance (Figure 3.18). The presence of the diffuser causes a reduction of the pressure margin downstream of the insert compared to

the baseline case in the same location. Geometry A, which shows no improvement from the baseline case inside the insert, is the only one with better performance downstream of the insert.

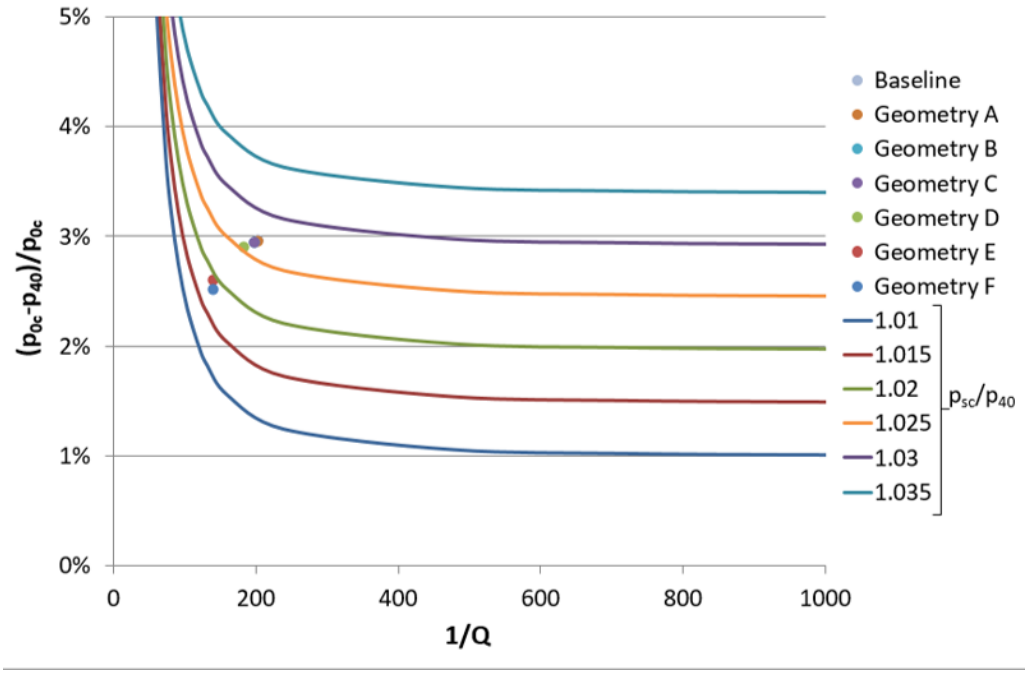


Figure 3.36: **Stewart plot: Downstream of the insert (s/H=0.3)**

It is important to notice that at the insert inlet the data are very spread (Figure 3.35), while downstream of the insert the performance variation is more moderate (Figure 3.36). That means that is possible to get improvements inside the insert without compromising the performance downstream, obtaining a general benefit for the vane working conditions over the baseline case. Table 3.3 reports the pressure margin for each case at the insert inlet (s/H = 0) and downstream of the insert (s/H = 0.3) and their percentage variation from the baseline case. The pressure margin increases continuously from geometry A to F at the insert inlet, while the decrease downstream of the insert becomes relevant for geometries E and F.

	PM insert inlet (s/H=0)	PM downstream of insert (s/H=0.3)	PM variation compared to baseline case (s/H=0)	PM variation compared to baseline case (s/H=0.3)
Baseline	1.0234	1.0269		
Geometry A	1.0242	1.0268	+0.07%	-0.01%
Geometry B	1.0276	1.0265	+0.41%	-0.03%
Geometry C	1.0288	1.0265	+0.52%	-0.04%
Geometry D	1.0301	1.0255	+0.65%	-0.14%
Geometry E	1.0306	1.0192	+0.70%	-0.75%
Geometry F	1.0306	1.0183	+0.70%	-0.69%

Table 3.3: **Pressure margin comparison**

3.5.2 Average film cooling effectiveness

To evaluate the implications of the new LE coolant passage design on film cooling performance, the effect of the changes in mass flow distribution through each film cooling hole row (Figure 3.29) on the average film cooling effectiveness was estimated. The average film effectiveness data from engine design conditions were scaled to different mass flow rates for each row according to the following equation from Kirollos and Povey [32]

$$\eta_{eff_{new}} = \eta_{eff_{old}} \cdot \frac{1}{\left(1 - \frac{\dot{m}_{old}}{\dot{m}_{new}}\right) \eta_{eff_{old}} + \frac{\dot{m}_{old}}{\dot{m}_{new}}} \tag{3.26}$$

The total average effectiveness was then calculated using Sellers' superposition model [60]

$$\eta_{eff_{tot}}(x) = 1 - \prod_{i=1}^{n} (1 - \eta_{eff_i}(x)) \tag{3.27}$$

These equations allow the different designs to be directly compared. The results for the different geometries on the suction and pressure side are shown in Figures

3.37 and 3.38. In both cases the baseline is the geometry with the highest coverage and this is due to the higher total coolant mass flow rate flowing through the LE coolant duct (Figure 3.24). Then the geometries with a lower coolant mass flow rate (i.e. geometries E and F) have lower film effectiveness. The worsening of the film performance is stronger on the pressure side, where the decrease in η is up to 6%, while on the suction side the variations are below 3%.

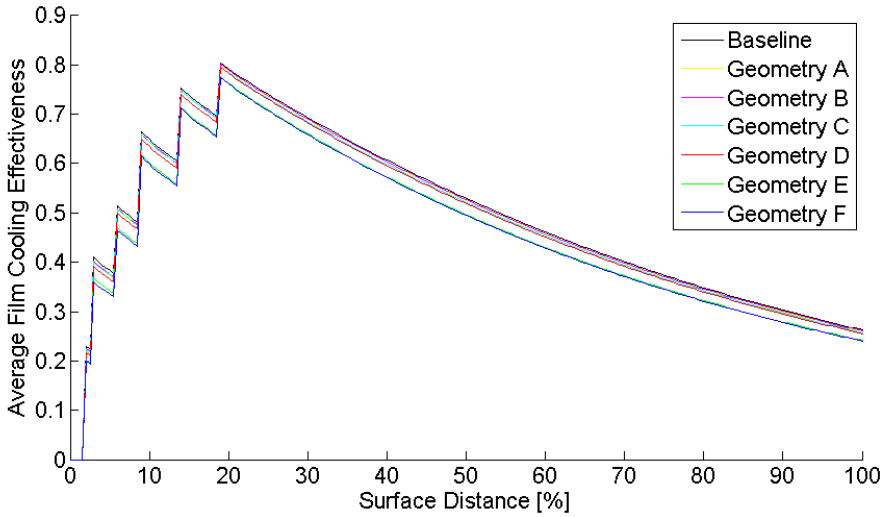


Figure 3.37: **Average film cooling effectiveness: Suction side**

3.6 Methods of improving diffuser performance

As evident from the results previously shown, diffusers are devices that are very sensitive to boundary conditions and geometry. Gad-el-Hak and Bushenell [22] wrote a review on separation control techniques. In a viscous flow, the fluid particles are slowed down by the wall friction: when subject to an adverse pressure gradient (as in a diffuser) the low momentum fluid near the wall can reverse direction. This flow reversal is the basis of flow separation. When separation occurs the rotational flow region next to the wall abruptly thickens and the boundary layer approximations are no longer valid: large energy losses are associated with boundary layer disruption.

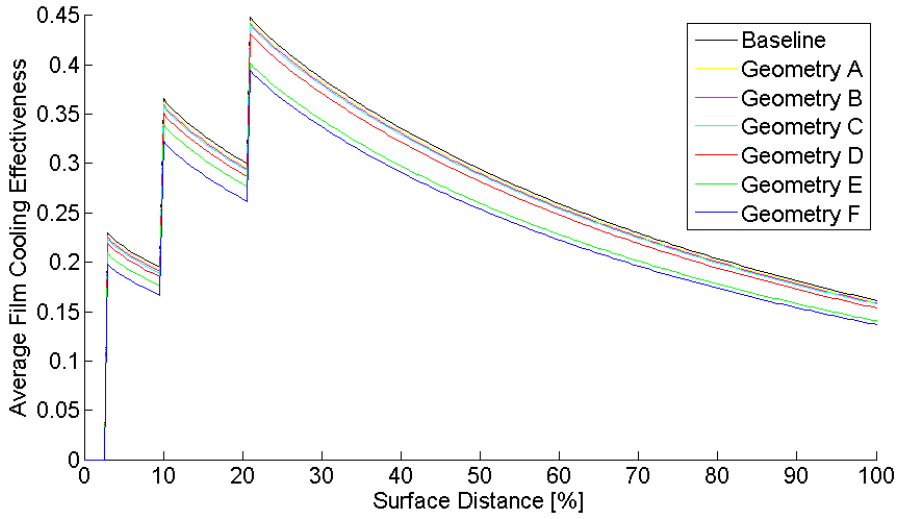


Figure 3.38: **Average film cooling effectiveness: Pressure side**

According to Miller [44], diffuser performance can be improved with one of the following four methods:

- Low energy near-wall flow can be removed by suction (Figure 3.39 (a));
- Boundary layer can be re-energized by air blowing (Figure 3.39 (b));
- Vortex generators can be placed inside the diffuser to promote high-energy flow in the boundary layers;
- Vanes can be installed to guide the internal flow.

Inside the leading edge passage, as the coolant flows around the insert and through the diffuser, there is a danger of flow separation. Once practical constraints are considered, the most promising approach to prevent separation of the boundary layer inside the LE passage is the inclusion of holes in the surface of the insert to allow flow to bleed from the insert cavity into the diffuser stream where the static pressure is lower, thus energising the boundary layer and delaying the flow separation.

For this reason, holes were added to the insert of geometries D and E at different

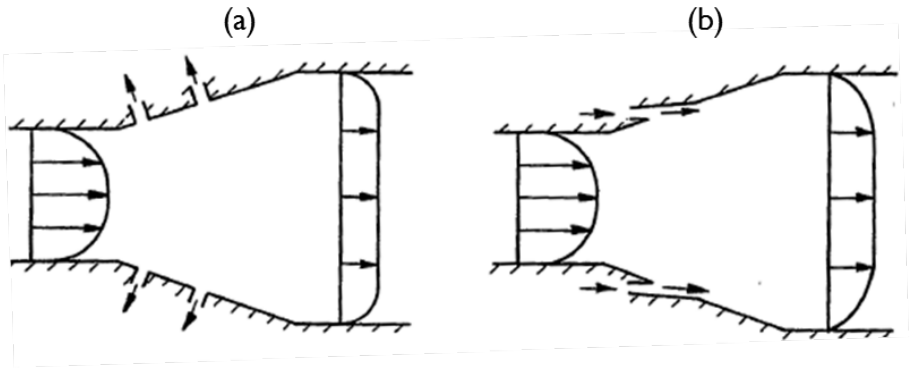


Figure 3.39: **(a) Removal or (b) re-energizing of low-energy boundary layer**

spanwise positions. Geometry D was chosen because the pressure margin increase inside the insert is obtained at the expense of a very moderate decrease of pressure margin downstream of the diffuser (Table 3.3). In geometry E the pressure margin decrease compared to the baseline case is the highest (Table 3.3) and so it was thought that this case could benefit from improved diffusion.

The predictions for the modified cases based on geometry D are reported in Table 3.4 and shown in Figure 3.43. The diffuser loss and pressure recovery coefficients (defined in Eq. 3.11 and 3.12) for cases D.1, D.2 and D.3 are shown in Figure 3.41: the improvement in results are negligible. The Stewart plot in Figure **??** is almost unaffected by the presence of the bleed holes in the insert.

	s/H	No holes
Geometry D.1	0.27	4
Geometry D.2	0.30	3
Geometry D.3	0.30	4

Table 3.4: **Simulated leading edge geometries D with holes: hole position and number of holes**

The cases studied for the modified geometry E are summarized in Table 3.5 and Figure 3.43. Figure 3.44 shows the diffuser loss and pressure recovery coefficients: in E.1 and E.2 the holes are positioned too upstream and are too perpendicular with

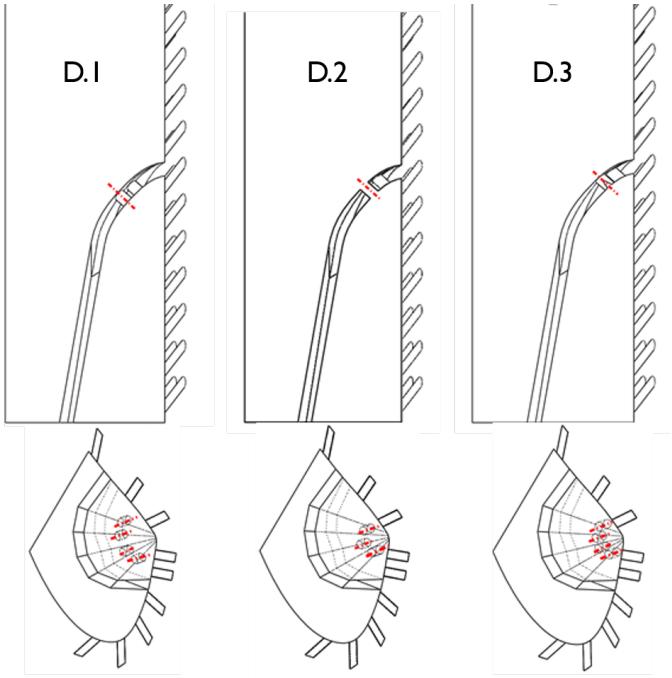


Figure 3.40: **Geometry D - Diffuser with blowing holes (hole axis in red)**

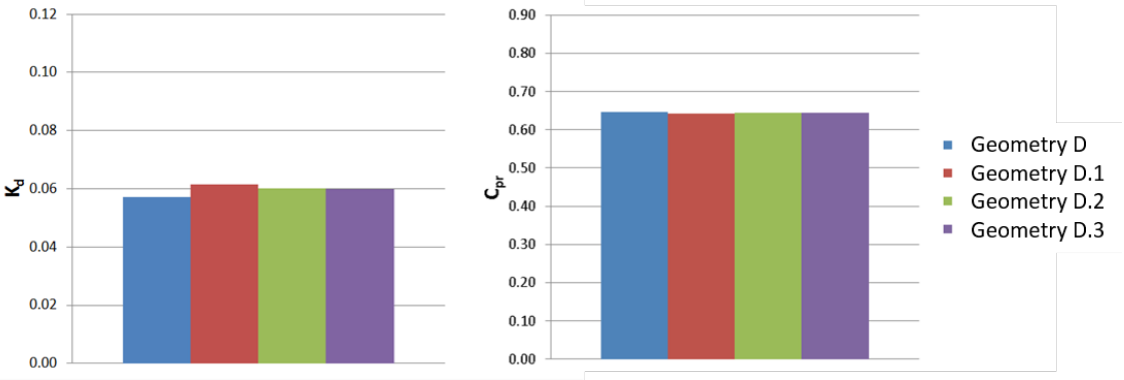


Figure 3.41: **Geometry D with blowing holes - Diffuser loss coefficient K_d on the left and static pressure recovery coefficient C_{pr}**

respect to the coolant stream thereby causing the performance to worse compared to geometry E. Moving the holes downstream instead appears beneficial. Geometry E.3 has the lowest K_d and highest C_{pr} even if the improvement is limited. Despite the encouraging benefits in the diffuser performance for geometry E, the Stewart plot in Figure 3.45 shows that the pressure margin increase is very limited.

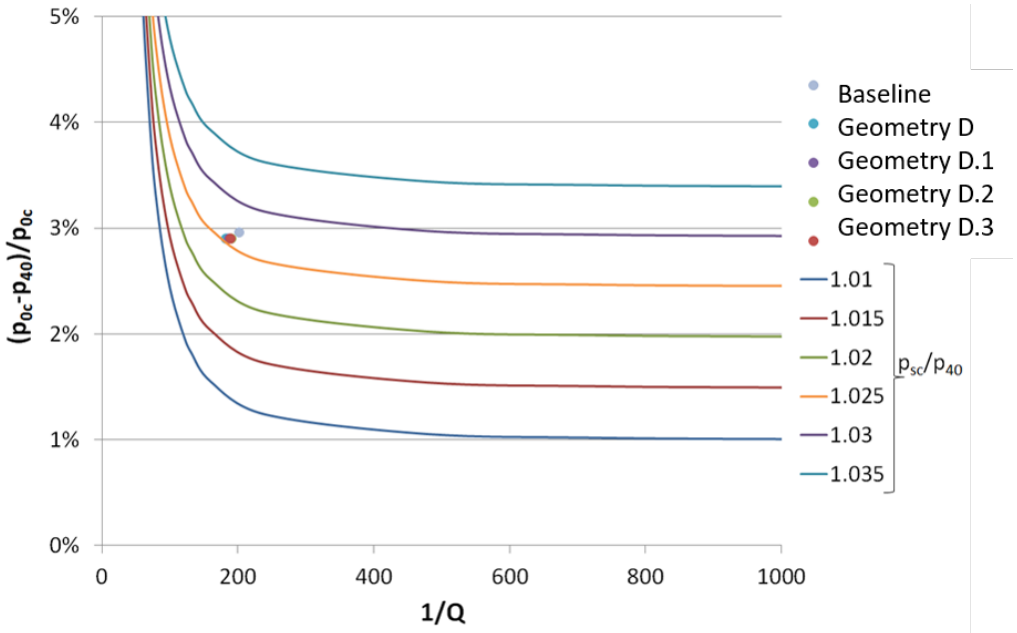


Figure 3.42: **Geometry D with blowing holes - Stewart plot: Downstream the inlet (s/H=0.3)**

These numerical results show that the increase in design and manufacturing complexity due to the addition of holes in the insert are not compensated by a relevant improvement in the system performance. For this reason this concept has not been studied any further in this thesis. Anyway, because of the complicated physical environment, the bleed jet behaviour could not be accurately predicted by RANS simulations and an experimental validation is suggested for future work.

	s/H	No holes
Geometry E.1	0.11	4
Geometry E.2	0.19	4
Geometry E.3	0.27	4
Geometry E.4	0.28	4

Table 3.5: **Simulated leading edge geometries E with holes: hole position and number of holes**

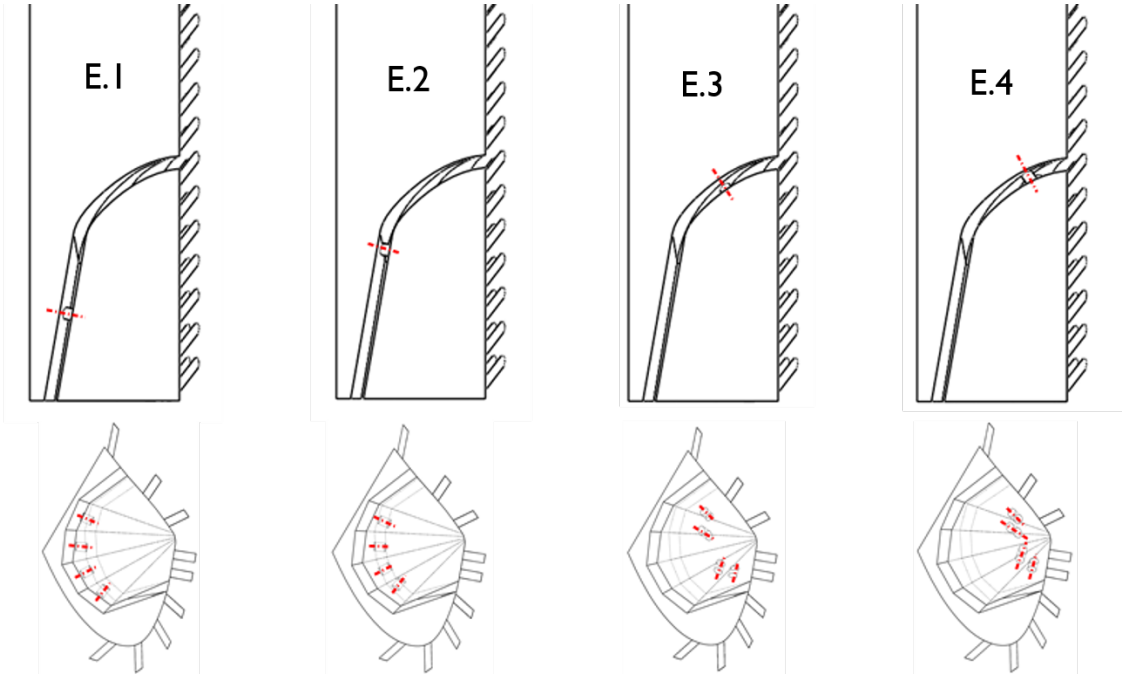


Figure 3.43: **Geometry E - Diffuser with blowing holes (hole axis in red)**

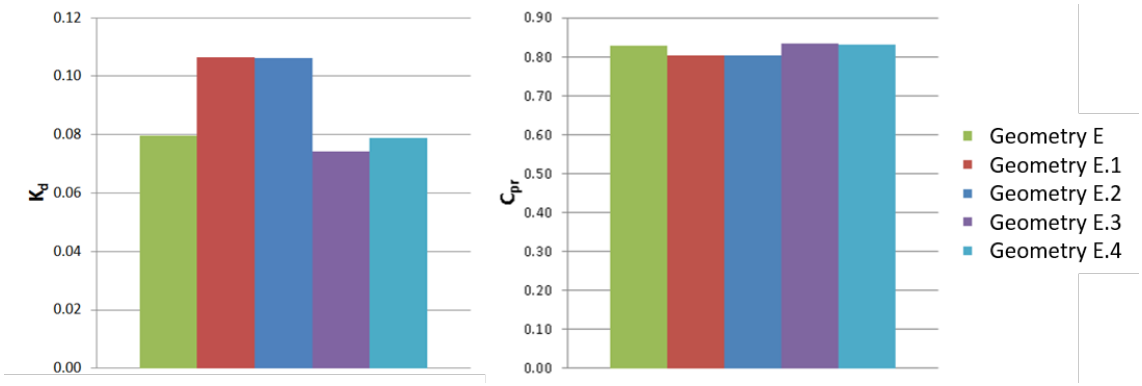


Figure 3.44: **Geometry E with blowing holes - Diffuser loss coefficient K_d on the left and diffuser static pressure recovery coefficient C_{pr}**

3.7 Numerical uncertainty

Roache [56] points out the importance to quantify the uncertainty of a CFD simulation to uniformly report the results of numerical calculations. For this reason in this section the Grid-Convergence Index was calculated for the simulations reported in this chapter.

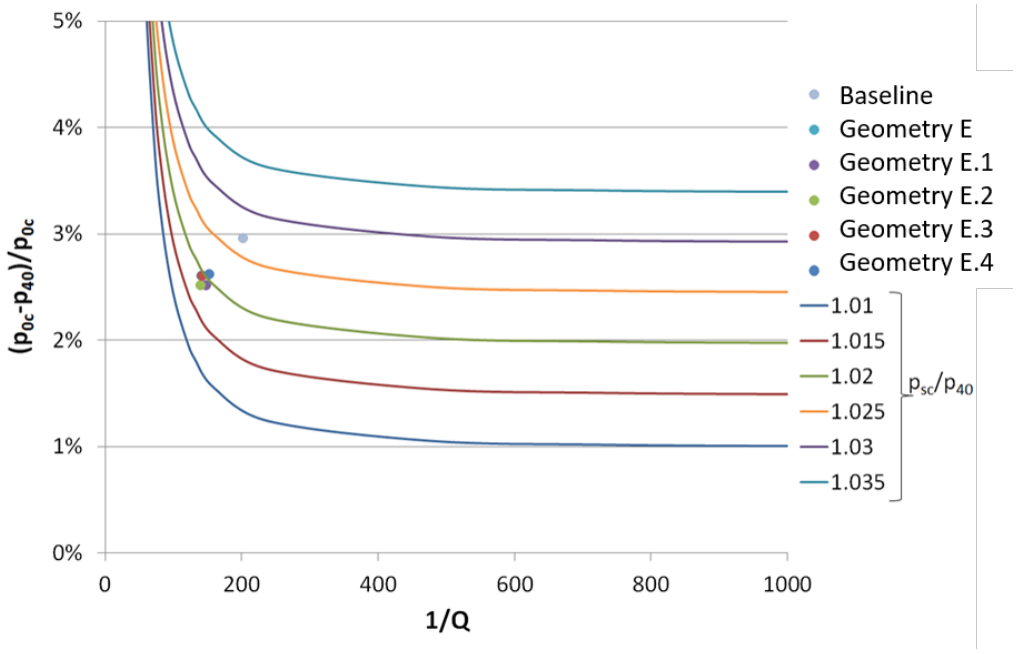


Figure 3.45: **Geometry E with blowing holes - Stewart plot: Downstream the inlet (s/H=0.3)**

3.7.1 The Grid-Convergence Index (GCI)

The GCI is a method described by Roache [56] for uniform reporting of grid-convergence studies, based on the generalized Richardson Extrapolation involving the comparison of the discrete solutions at two different grid spacings.
A fine-grid Richardson error estimator is defined as

$$E_R = \frac{f_2 - f_1}{1 - r^p} \tag{3.28}$$

where

- f_1 is the fine-grid numerical solution obtained with grid spacing h_1
- f_2 is the coarse-grid numerical solution obtained with grid spacing h_2
- $r = h_2/h_1 > 1$ is the refinement factor between the coarse and the fine grid
- p is the formal order of accuracy of the algorithm

and the GCI can be calculated as

$$GCI = F_s|E_R| \tag{3.29}$$

where F_s is a safety factor. Roache [56] recommends a conservative value of 3.

3.7.2 Vane leading edge

The sensitivity of the baseline leading edge mesh was controlled calculating the GCI for the following variables:

- Total pressure inside the coolant passage at s/H = 0.3 (downstream the insert) to total pressure at s/H = 0 (at the insert feeding inlet);
- Coolant-to-mainstream pressure margin at s/H = 0;
- Coolant-to-mainstream pressure margin at s/H = 0.3.

The results are reported in Table 3.6:

Variable	GCI
$p_0(s/H = 0.3)/p_0(s/H = 0)$	0.00004
$PM(s/H = 0)$	0.0017
$PM(s/H = 0.3)$	0.0010

Table 3.6: **Vane leading edge study: Grid-Convergence Index (GCI)**

3.8 Summary

A new LE coolant passage feeding system was designed with the intent of managing the pressure margin across the film cooling holes. The region with the highest risk of hot gas ingestion was identified in the area around the stagnation point close

to the endwall and an insert was fitted inside the coolant passage to increase the static pressure in this zone by locally slowing down the flow.

Through the use of some general preliminary design guide lines different geometries were modeled and numerically simulated at engine conditions for a set coolant feeding total pressure. The numerical results were used to compare the performance sensitivity to different geometrical parameters, such as the diffuser outlet-to-inlet area ratio and angle. The effects due to the presence of the insert on the coolant flow downstream of it were taken into account and analysed.

This new concept proves to be able to sensibly increase the pressure margin in the critical region, slowing down the coolant and increasing its static pressure. This provides a potential increase to either the cycle efficiency or the vane reliability.

Following the reported analysis geometry D showed to be the best compromise and for this reason it was the geometry chosen to be tested experimentally to validate the numerical analysis.

Chapter 4

Experimental apparatus - Combustor-Turbine Interaction Rig

A large-scale low-speed linear cascade for high spatial resolution investigation of NGV leading edge films was designed and commissioned by the author. The engine representative combustor simulator and the engine Reynolds number at the passage throat are key aspects of this facility. Two different test sections were designed to allow measurements of the flow field downstream of the combustor simulator before testing the vanes. The overall purpose of the Combustor-Turbine Interaction (CTI) test facility is to study film cooling performance with a particular emphasis on researching the NGV LE coolant passage at engine representative conditions.

4.1 Rig overview

The wind tunnel is capable of 100 m/s at the vane throat (3.2 kg/s through the test section) and is fitted with a 150 kW heater mesh ahead of the test section [24]. The geometrical scaling factor from engine dimensions was around 4.45. A primary air flow replicates the mainstream gas flow and a secondary air path is available to

reproduce the coolant path.

The mainstream air enters the CTI rig combustor simulator with a uniform velocity profile, achieved using a contraction upstream. A heater mesh (400x500 mm^2 with 38% open area) provides a step rise in the inlet temperature of up to 50 K. This heating strategy was chosen because of the short heat-up time, the uniform heating of the flow and the available expertise with this technique, which has been widely used and tested in the Osney Laboratory [24] [30]. A DC power supply with airflow control and heater voltage detection was installed: the power supply cannot be turned on if the airflow is below a minimum value (in this case set to 1 kg/s at the rig inlet) and an external LED is fitted to indicate when voltage is applied. The coolant flow is injected into the mainflow through a combustor simulator that was designed to create engine representative conditions at the NGV inlet plane (see Sec. 4.2). The coolant stream is provided by a blower and passes through four different pipes that feed four separate plenums: one feeds the outer dilution ports, one the inner dilution ports, one the RIDN and one the RODN (see Sec. 4.4). Each air flow can be individually controlled and monitored allowing considerable flexibility in the test set-up. Two test sections were fitted in the rig as shown in Figure 4.1 (see Sec. 4.3). In the first configuration, at the top of Figure 4.1, a 267x500 mm^2 straight duct is placed downstream of the combustor simulator to allow detailed flow field measurements at the combustor simulator outlet. In the arrangement shown at the bottom of Figure 4.1 three large scale vanes, with a cooled central LE, were integrated. Diffuser ducts with internal straightening bars and sheets connect the test section to the suction fan (see Sec. 4.3).

4.2 Combustor simulator

A combustor simulator was designed with the goal of obtaining engine representative flow conditions at the vane inlet: in particular, the leading target was to achieve realistic dimensionless velocity, turbulence and dimensionless temperature



Figure 4.1: **CTI rig: Test section without vanes (on top) and with vanes (on the bottom)**

coefficient distributions.

The combustor simulator CAD model and its major features are shown in Figure 4.2. Downstream of the inlet contraction the mainstream passes through a heater mesh that allows the test engineer to set the required temperature at the combustor inlet. The dilution flow is injected through opposing ports and where it mixes with the heated gas. Following a contraction further coolant is injected through RIDN and RODN holes upstream of the NGV inlet plane to cool down the endwall. In the CTI rig, the dilution ports, RIDN and RODN geometries are engine representative (Mitra et al. [66]) and the main geometrical parameters (non-dimensionalized with the combustor inlet height H and the hole diameters D) are reported in Table 4.1.

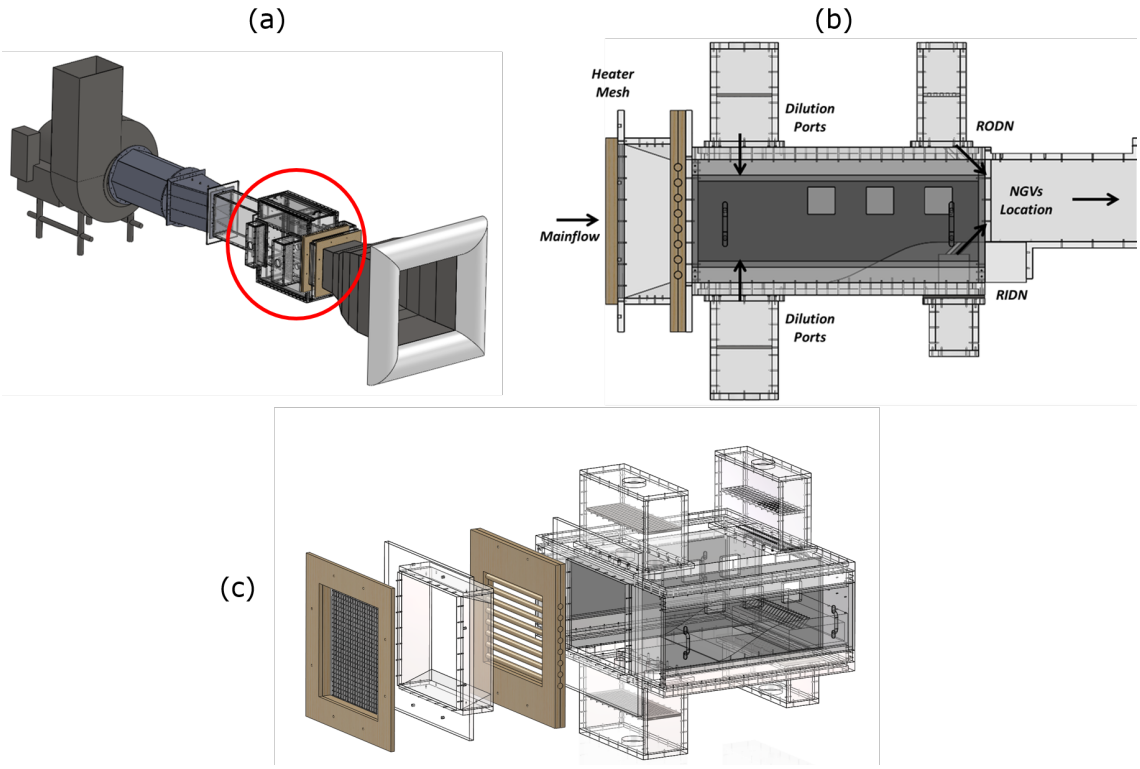


Figure 4.2: **Combustor simulator: Flowpaths (on the top) and exploded view (on the bottom)**

	D [mm]	D/H	Inclination [^{o}]	p [mm]	p/D
Inner wall big dilution ports	71	0.18	90	250	3.5
Inner wall small dilution ports	44.5	0.11	90	250	5.6
Outer wall big dilution ports	80	0.20	90	250	3.1
Outer wall small dilution ports	53.5	0.13	90	250	4.7
RIDN	9	0.03	90	21.6	2.4
RODN	9	0.03	90	18	2

Table 4.1: **Combustor simulator - Geometrical dimensions [66]**

4.2.1 Engine - rig matching

Because the main target of the combustor simulator design is to achieve engine representative conditions for the mainstream at the NGV inlet plane, the key parameters that need to be matched are the Reynolds number based on the vane chord and the coolant-to-mainstream momentum flux ratio.

Fan performance curves for the relationship between the static pressure difference across the fan and the volume flow rate were used to design the installation. The intersection between the fan curve and the system resistance curve (i.e. the sum of all the pressure losses across the rig) sets the wind tunnel operating point (Figure 4.3). The design volume rate in the CTI rig was estimated to be around 2.8 m^3/s. The Reynolds number based on the vane chord, C, and the flow velocity at the passage throat, u_t, is defined as

$$Re_C = \frac{\rho u_t C}{\mu} \tag{4.1}$$

For the calculated mass flow rate of 3.2 kg/s $Re_C = 2{\cdot}10^5$, which is approximately engine representative.

One of the fundamental requirements necessary to achieve a satisfactory dimensionless temperature distribution at the turbine inlet is is the need for adequate

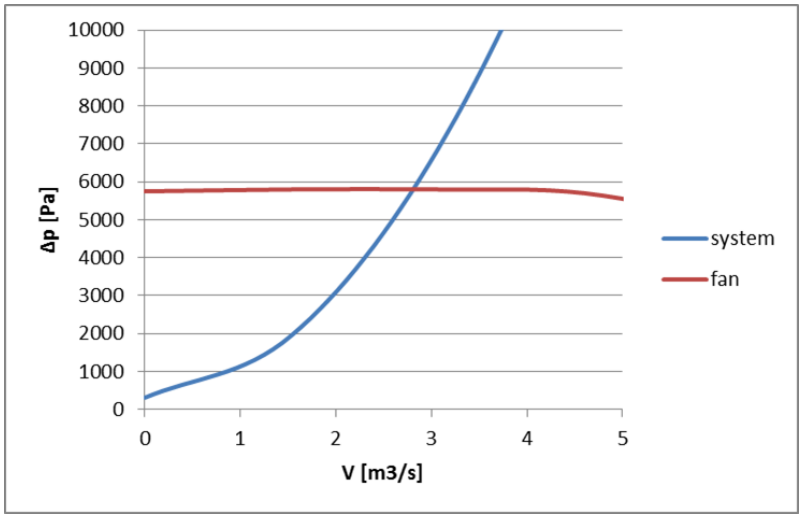


Figure 4.3: **Operating point (Static pressure vs. Volume flow rate). The fan line is from the manufacturer (see Section 4.4).**

penetration of the dilution air jets [34]. The jet-to-mainstream momentum flux ratio

$$J = \rho_j u_j^2 / \rho_\infty u_\infty^2 \tag{4.2}$$

and the jet diameter D_j are the most significant factors affecting the jet penetration and mixing in a combustor liner [34], [74]. A geometrical scaling factor of about 4 was used to obtain the diameter of dilution ports, RIDN and RODN, while the coolant mass flow rates were scaled according to the J values reported in Table 4.2.

Reynolds number		$^1Re_C = 2 \cdot 10^5$
Jet-to-mainstream momentum flux ratio	Dilution ports	$J = 9$
	RIDN	$J = 11$
	RODN	$J = 6$

Table 4.2: **Typical flow conditions present in an engine combustion chamber [65]**

In order to obtain a high-resolution quantification of the flow approaching the

turbine NGVs, velocity, turbulence and temperature were measured in the CTI rig and compared to RANS simulation predictions.

The Radial Temperature Distribution Factor (RTDF) was calculated from the measured data according to the definition given by Cha et al. [8]:

$$RTDF = \frac{\langle T \rangle(r) - \langle\langle T \rangle\rangle}{\langle\langle T \rangle\rangle - T_\infty} \tag{4.3}$$

where

- $\langle T \rangle(r)$ is the temperature averaged with respect to the circumferential coordinate for each radial position;
- $\langle\langle T \rangle\rangle$ is the temperature averaged with the respect to both the circumferential and the radial coordinates;
- T_∞ is a constant reference temperature, that for the work reported in this thesis was chosen to be the mainflow temperature measured at the combustor simulator inlet downstream of the heater mesh location.

4.2.2 Sensitivity studies

To facilitate the understanding of the operation of the combustor simulator rig, numerical simulations were run to check the sensitivity of the flow field at the NGV inlet plane to specific parameters.

First of all, two calculations at different combustor inlet boundary turbulence intensity values (15% and 20%) were run. The profiles of velocity magnitude and turbulence intensity non-dimensionalized with the mainstream value and the RTDF for the two cases are plotted in Figure 4.4. They show that the predicted sensitivity to the turbulence intensity value chosen at the inlet boundary is very low: the maximum variation in the velocity magnitude is lower than 0.5%, for the turbulence intensity is less than 2% and the effect on RTDF around 1%.

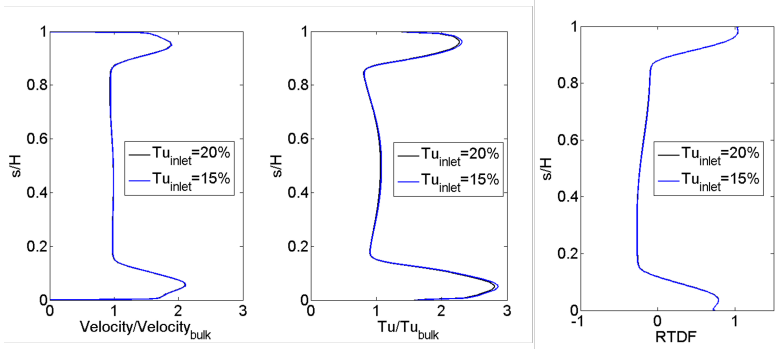


Figure 4.4: **Mainflow inlet turbulence: Velocity, turbulence intensity and RTDF at the NGV inlet plane**

In the real engine the dilution flow enters the combustor at an angle with respect to the combustor side wall and this angle depends on the geometry of the secondary air system (Figure 4.5). For this reason a sensitivity study to the angle Θ (defined according to Figure 4.6) was performed: simulations with Θ varying between 0 and 45 degrees were run and the resulting profiles are shown in Figure 4.7. For $\Theta = 45^o$ the maximum velocity variation (compared to the $\Theta = 0^o$ case) close to the wall is +3.3% and in the bulk flow is +7.8% and variations of the same order are noticed in the turbulence levels and in the RTDF (-5.4% close to the wall and +13% in the bulk flow).

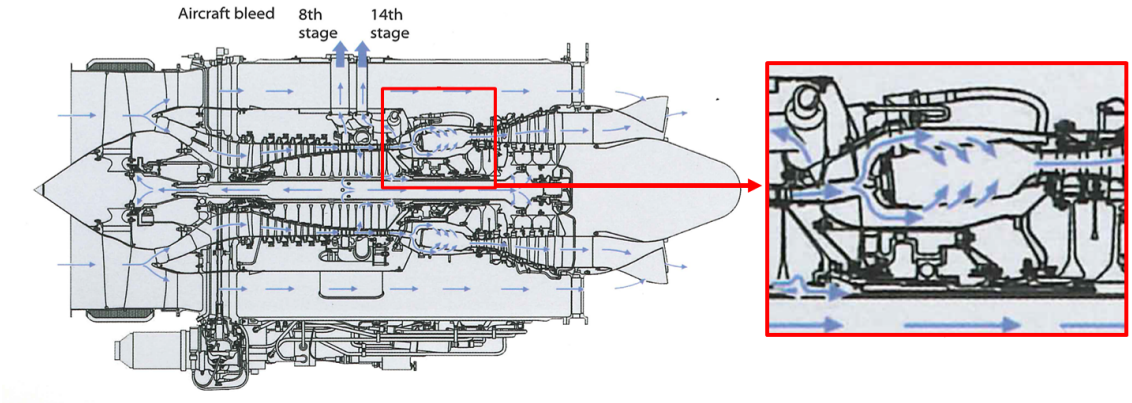


Figure 4.5: **General arrangement and flowpaths of the internal air system of the AE 3007 engine [52]**

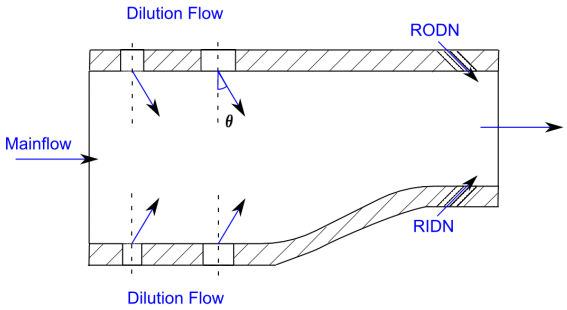


Figure 4.6: **Dilution ports: Inlet angle nomenclature**

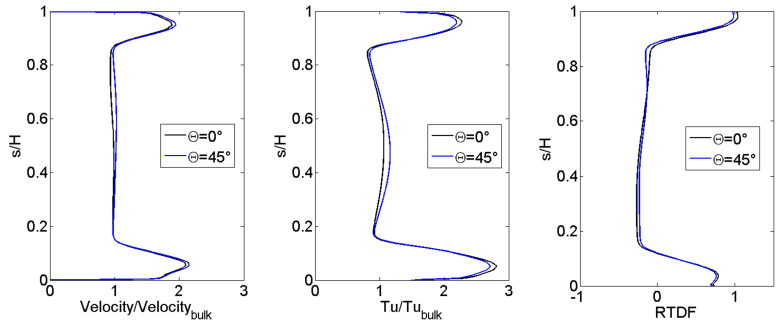


Figure 4.7: **Dilution inlet angle: Velocity, turbulence intensity and RTDF at the NGV inlet plane**

Another difference between the combustor simulator installed in the CTI rig and a real annular combustor is the presence of the side walls. In order to quantify the effect of the side walls, CFD simulations with side walls and lateral periodic boundaries were run and compared (Figure 4.8): their influence on the considered variable results was found to be negligible .

4.3 Test section and outlet ducts

Two different test sections were manufactured for the CTI rig. The first one (Figure 4.9) is a 267x500 mm^2 straight duct used to take measurements downstream of the combustor simulator. A traverse mechanism designed by the author was installed to fully characterize the mainflow conditions before testing the vanes and

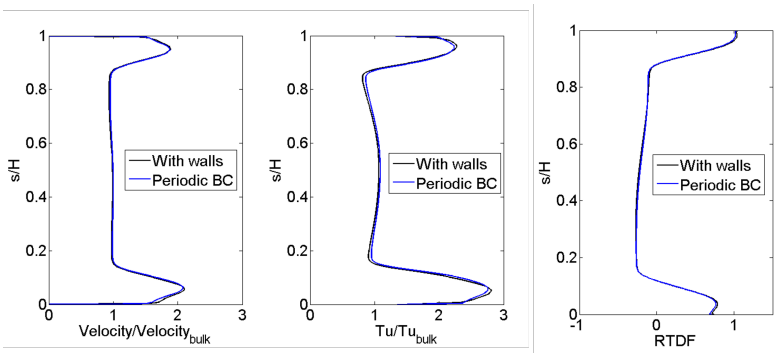


Figure 4.8: **Side wall effect: Velocity, turbulence intensity and RTDF at the NGV inlet plane**

to validate the CFD results reported in Chapter 3.

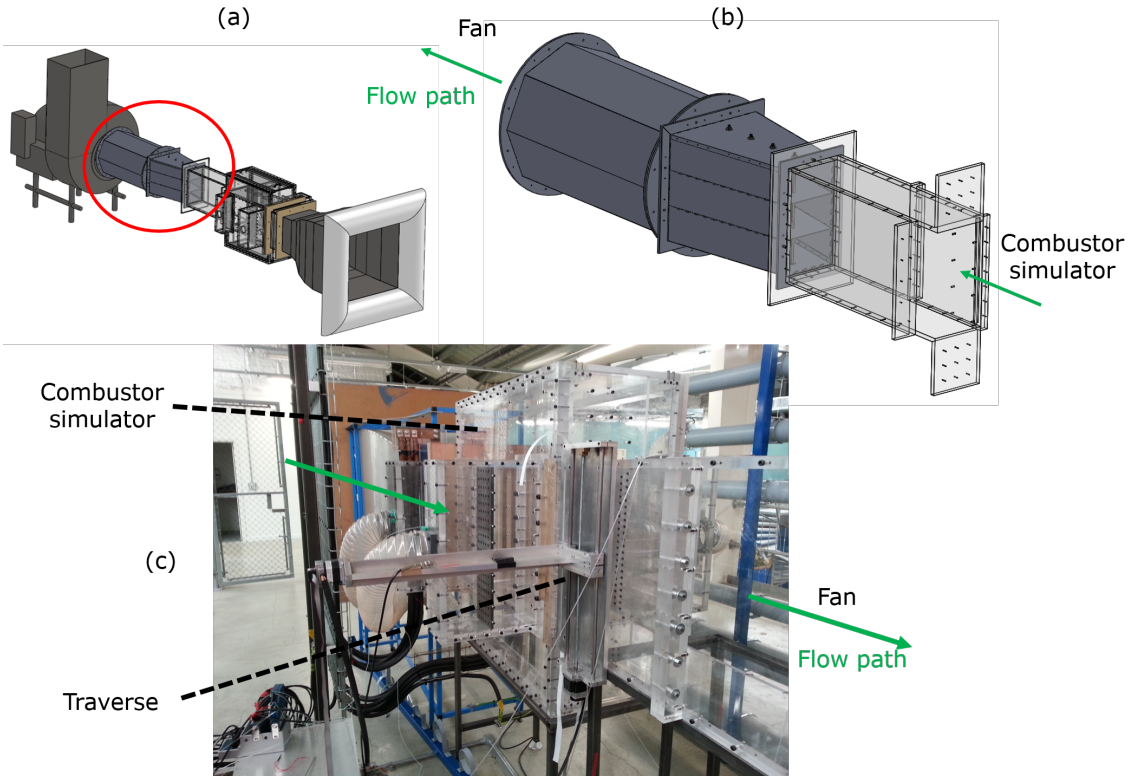


Figure 4.9: **CTI Rig – Test section without vanes: (a) test section in the CTI rig, (b) CAD of test section and outlet ducts, (c) installed test section with traverse mechanism**

The second test section in Figure 4.10 includes three large-scale 263 mm-chord

prismatic vanes giving two mainstream flow passages. Figure 4.11 gives an exploded overview of the vane section, that includes:

- Two solid vanes;
- One vane with a replaceable cooled Leading Edge (LE);
- Two Rohacell plates at the endwall;
- A profiled endwall that produces a representative contraction upstream of the vanes.

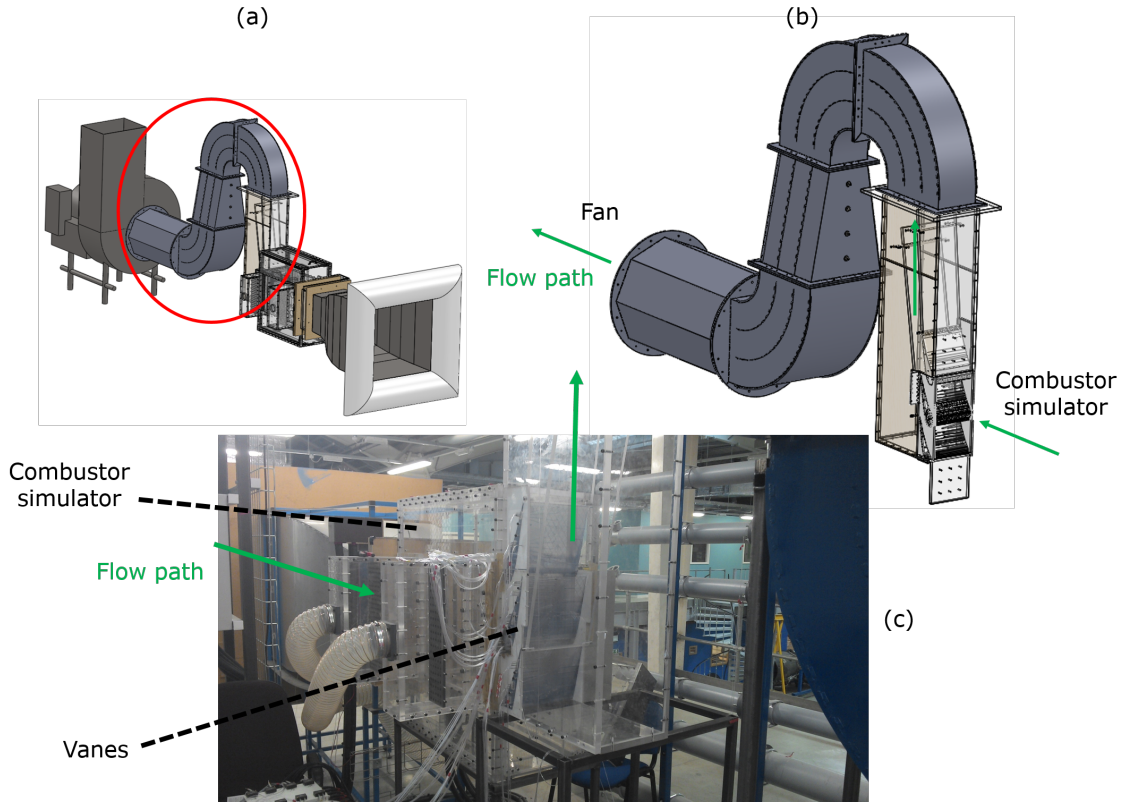


Figure 4.10: **CTI Rig – Test section with vanes: (a) test section in the CTI rig, (b) test section and outlet ducts CAD, (c) installed test section with vanes**

The three vanes are instrumented with a total of 54 pressure tappings along the midspan to enable the mainflow periodicity to be measured (Figure 4.12). The

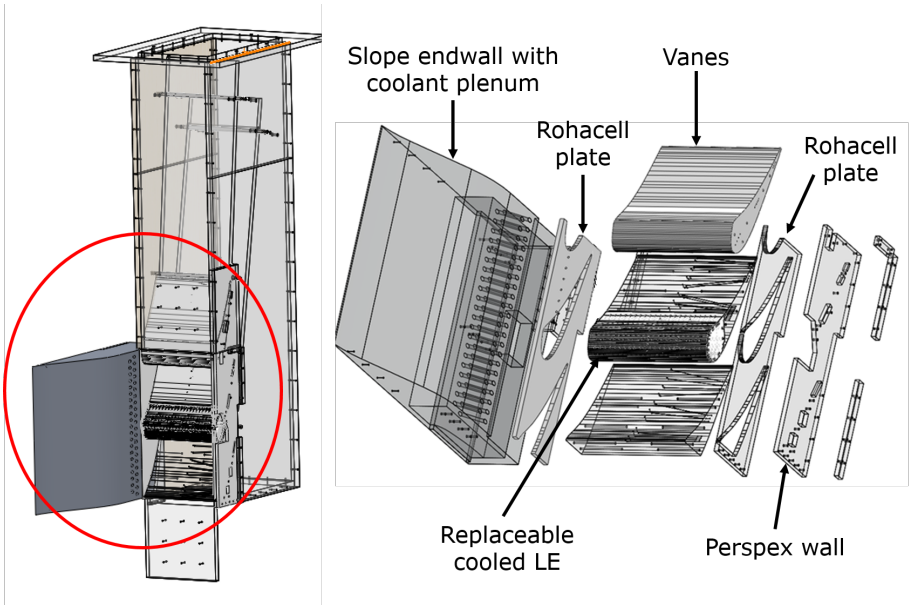


Figure 4.11: **CTI Rig – Vane Section: Exploded view**

central vane has a separate replaceable cooled LE shown in Figure 4.13 which is instrumented with 24 pressure tappings on the mainstream side and 20 on the coolant side. The components were manufactured by stereolithography in the Rolls-Royce Rapid Prototyping Facility in Bristol.

Following the numerical analysis reported in Chapter 3 a LE insert reproducing geometry D (Figure 3.13) was 3D printed and attached with silicone rubber to the baseline LE vane (Figures 4.14 and 4.15).

The outlet ducts were designed with the main purpose of minimizing the pressure losses between the vanes and the fan. Internal strengthening bars and plates were used to sustain the ducts during rig operation (Figure 4.16). Note that commercially available duct work was not able to withstand the low gauge pressure encountered here.

4.3.1 Vane LE coolant passage discharge coefficient

The coolant required by the RIDN and the vane LE is fed through the plenum located inside the slope endwall shown in Figure 4.17. The coolant entering the

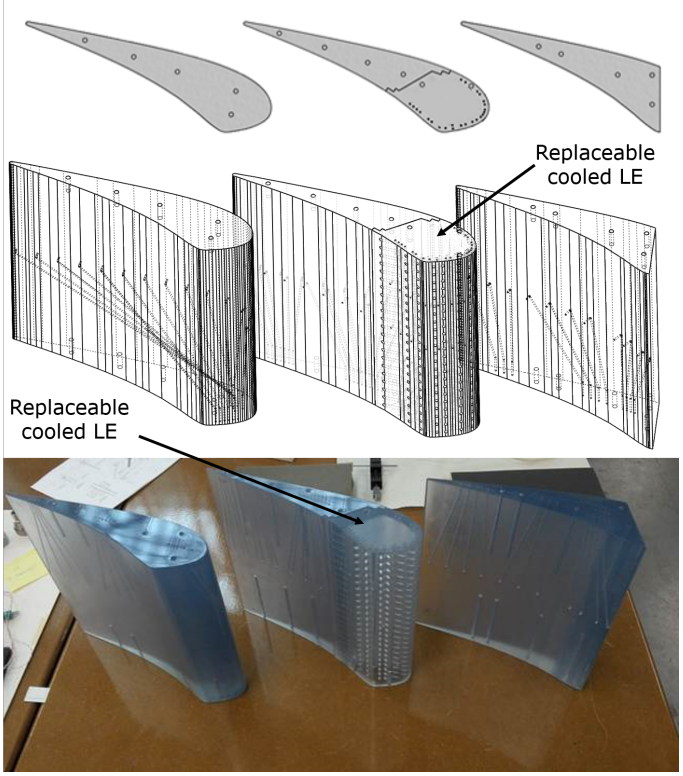


Figure 4.12: **CTI Rig – Baseline vanes: CAD top view (on the top), CAD instrumentation (in the centre) and SLA manufactured components (on the bottom)**

plenum is separated into two flows: one stream cools the endwall and the other feeds the vane LE passage.

The pressure losses inside the plenum needed to be adjusted to obtain the correct flow distribution between LE passage and RIDN. For this reason two different perforated plates were inserted at the LE vane inlet: their location is highlighted in red in Figure 4.17. Two different mesh size plates were used: "Plate A" is coarser and "Plate B" is finer (Figure 4.18). Four cases were tested and they are listed in Table 4.3.

The discharge coefficient C_d was defined as

$$C_d A = \frac{\dot{m}}{\sqrt{2\rho(p_0 - p_s)}} \tag{4.4}$$

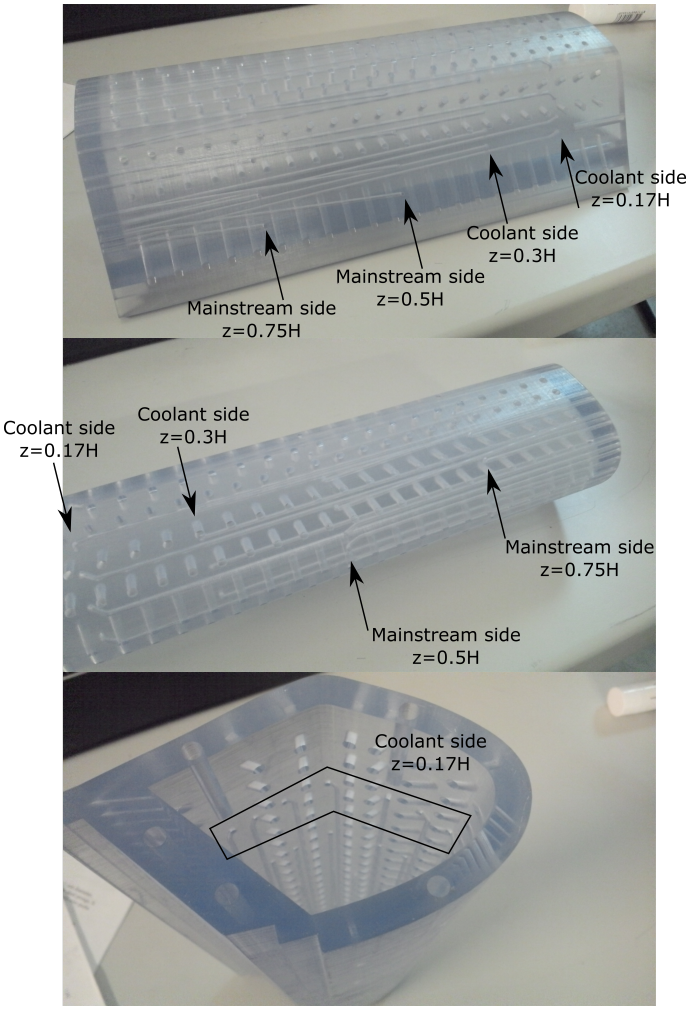


Figure 4.13: **CTI Rig – Baseline vanes: cooled LE pressure tapping close-up**

Case	LE geometry	Perforated plate configuration
0	Baseline	No plate
1	Baseline	Plate A
2	Baseline	Plate B
3a	Baseline	Plate A + Plate B
3b	Geometry D	Plate A + Plate B

Table 4.3: **Perforated plates at LE vane inlet: Experimentally tested cases with different perforated plates**

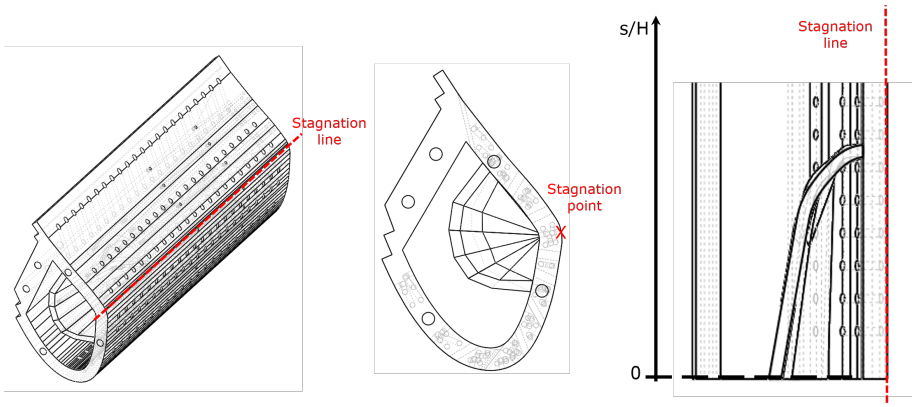


Figure 4.14: **CTI Rig – Vane with insert - LE geometry D: CAD section view (on the left), bottom view (in the centre), perspective view (on the right)**

where A is the inlet LE coolant passage cross-sectional area, p_0 the total pressure inside the plenum and p_s the static pressure inside the LE channel. C_d was experimentally measured for the different configurations at different mass flow rates. The results for the two different LE geometries are plotted in Figure 4.19. Case 3a was initially chosen for the baseline configuration because it was designed to obtain a jet-to-mainstream momentum flux ratio of 10.3 at the RIDN and 8% of the throat vane mass flow rate at the LE passage inlet: theses values are considered to be engine representative.

From the measured data a best-fit second order polynomial equation was obtained to correlate the discharge coefficient for the baseline case to the coolant mass flow rate over the range of interest:

$$(C_d)_{Baseline} = -0.00999717\dot{m}^2 + 0.00589971\dot{m} + 0.00173227 \tag{4.5}$$

Then the same configuration was tested for the LE with insert and the measured discharge coefficient was correlated by the following equation:

$$(C_d)_{GeometryD} = -0.00575850\dot{m}^2 + 0.00385707\dot{m} + 0.00140137 \tag{4.6}$$

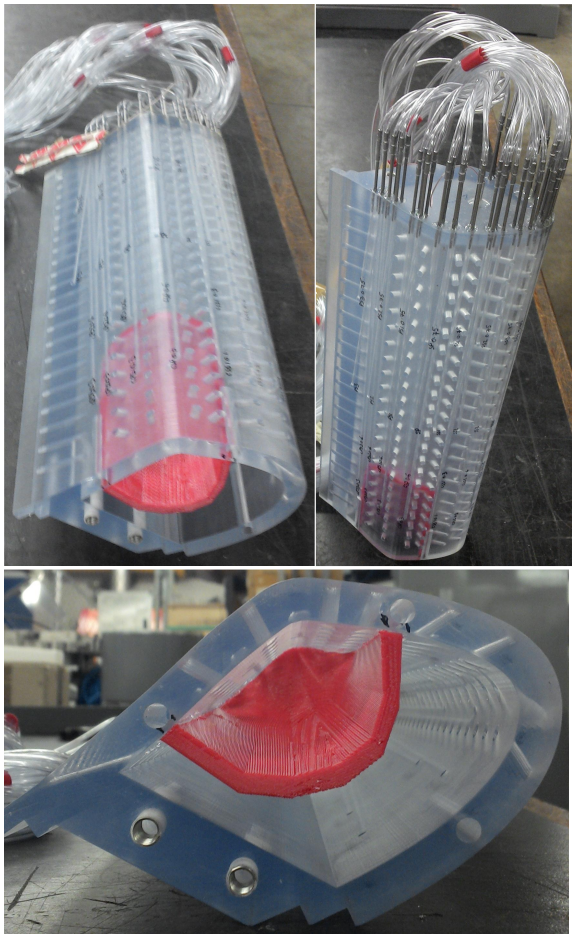


Figure 4.15: **CTI Rig – Vane with insert - LE geometry D. The component has been instrumented with 44 static tappings**

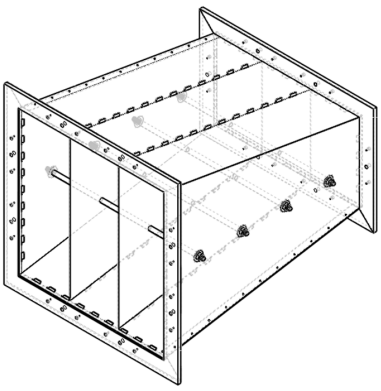


Figure 4.16: **CTI Rig – Diffuser with straighteners**

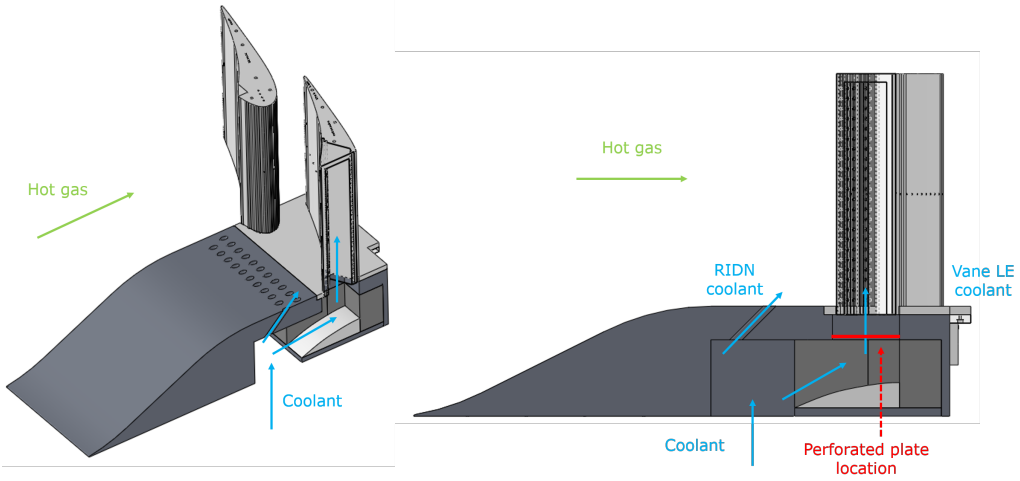


Figure 4.17: **CTI Rig – Vane section: LE passage feeding section**

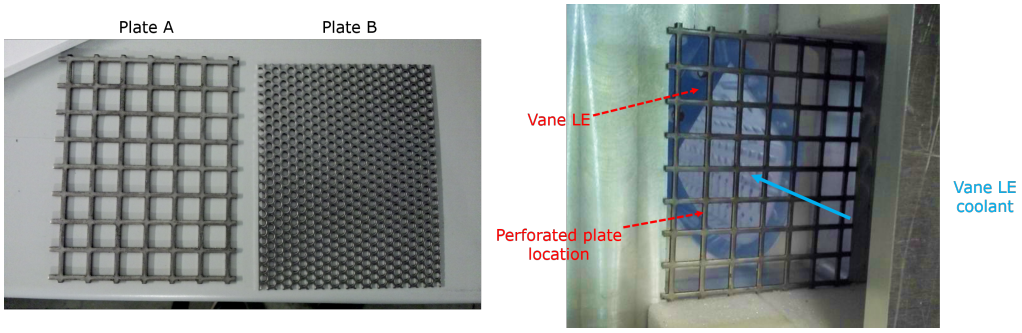


Figure 4.18: **Perforated plates at LE vane inlet: tested geometries (on the left) and plate installed in the CTI rig (on the right)**

The C_d values obtained from these correlations were used to evaluate the coolant air flowing through the LE passage for the cases reported in Chapter 9.

4.4 Suction fan and blower

The mainstream suction fan was manufactured by Woodcock & Wilson LTD [1] and it is a BFN SISW centrifugal fan with a diameter of 630 mm. The secondary coolant blower was manufactured by B.O.B. Stevenson LTD [2] and it is an ALCOVA

[1] Woodcock & Wilson LTD, Airstream Works, Huddersfield, HD7 7AA, UK
[2] B.O.B. Stevenson LTD, Coleman Street, Derby, DE2 8NN, UK

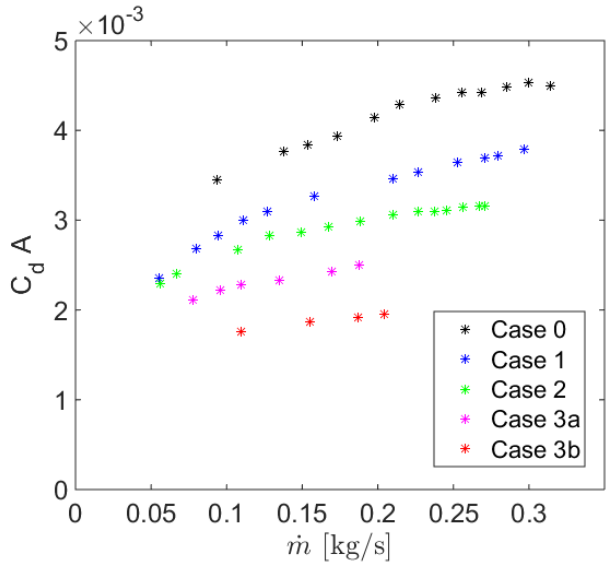


Figure 4.19: **Vane discharge coefficient C_d for different configurations at different mass flow rates**

RBJ centrifugal fan with a diameter of 710 mm. The performance curves of both fans are shown in Figure 4.20.

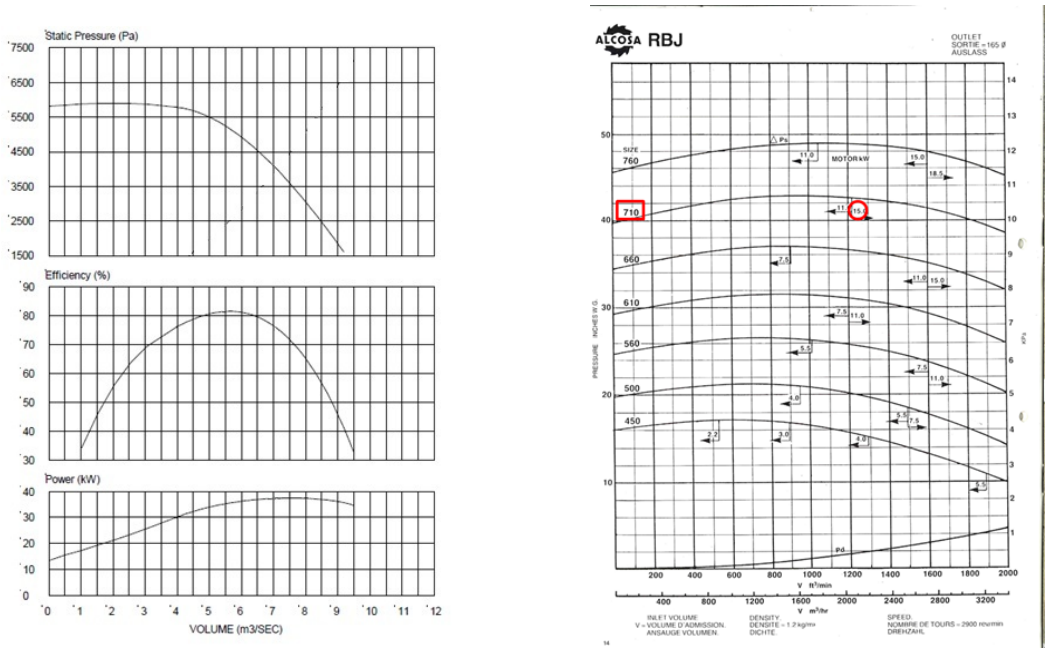


Figure 4.20: **Performance curves of the Woodcock and Wilson LTD fan (on the left) and of the B.O.B. Stevenson LTD blower (on the right)**

4.5 Coolant pipes

All the PVCu push-fit pipes and fittings were supplied by Marley Plumbing and Drainage [3]. The fan is connected to six pipes as shown diagrammatically in Figure 4.21:

- Pipe A feeds the dilution ports on the outer side;
- Pipe B feeds the dilution ports on the inner side;
- Pipe C feeds the RODN (Rear Outer Discharge Nozzle);
- Pipe D feeds the RIDN (Rear Inner Discharge Nozzle);
- Pipe E is a spare pipe that could be used in the future to feed the NGVs also from the outer wall;
- Pipe F is a bleeding pipe used to regulate the coolant air flow.

The choice of using separate pipes allows a considerable flexibility in the test set-up. The mass flow rate through each pipe is measured with orifice meters designed according to ISO 5167-22003.

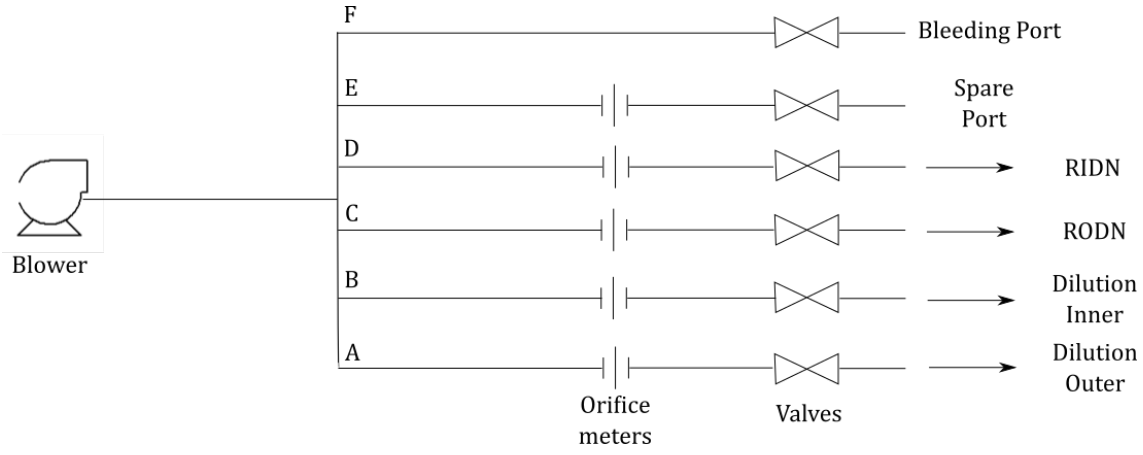


Figure 4.21: **Coolant delivery system**

[3]Marley Plumbing and Drainage, Lenham, Maidstone, Kent, ME17 2DE, England

4.6 Summary of Chapter 4

A large-scale low-speed linear cascade facility was designed, assembled and commissioned with the target of allowing high resolution measurement of the film cooling around a HP vane LE at engine representative conditions. Particular attention was given to the combustor simulator in order to obtain flow and dimensionless temperature fields as close as possible to engine conditions at the NGV inlet plane (Section 4.2). Two different test sections were used and described in Section 4.3:

- One without vanes was fitted with a two-dimensional traverse system to get complete access downstream of the combustor simulator and obtain measurements in the entire plane;
- One with vanes was installed to test the LE coolant passage design described in Chapter 3.

Chapter 5

Instrumentation

A detailed measurement campaign was undertaken at the inlet plane to the nozzle guide vanes (see Figure 4.9), in order to obtain a complete overview of the flowfield at the combustor simulator outlet: a traverse mechanism (designed by the author) was installed at the NGV inlet plane and different probes were used to obtain velocity and temperature (both time mean and unsteady) data. Once this was completed the vanes were installed (Figure 4.10) and static pressure measurements of both the mainstream flow around the vanes and inside the leading edge cooling passage were acquired.

5.1 Test section without vanes

The installation of a straight duct downstream of the combustor simulator allowed easy access for the instrumentation. A photo of the test section with the traverse system is included in Figure 4.9.

5.1.1 Traverse mechanism

A two-axis computer-controlled traverse system moved a probe across the NGV inlet plane. The traverse system comprises two Mclennan [1] 23HSX202CI500L stepper motors connected to two ST5-Q-NN stepper drivers and controlled with a NI-PCI6220 card [2]. Three slots in the wall enabled the traverse position in the streamwise direction to be changed. The mean velocity and temperature maps were measured with a four-hole pressure probe and with a K-type thermocouple. Turbulence information was acquired using a Dantec Dynamics 55P11 miniature single wire sensor (Table 5.1) and a Dantec Dynamics StreamLine Pro CTA (Constant Temperature Anemometer) system. Data of temperature fluctuations were obtained with K-type 12.7μm thermocouple inserted in a ceramic shield and mounted on a metallic probe.

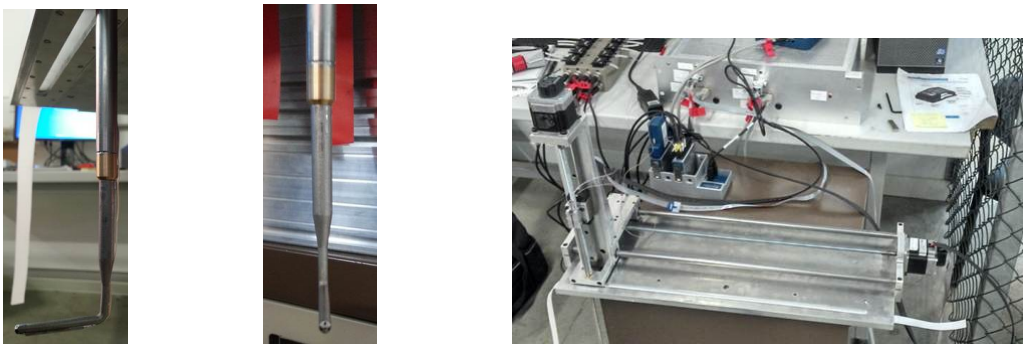


Figure 5.1: **Four-hole probe and traverse mechanism**

5.1.2 Velocity measurements

Four-hole probe

There are several techniques that can be used to study a three-dimensional velocity field (Main et al. [41], Tsang [68], Goodman [25]). A four-hole pressure probe

[1] Mclennan Servo Supplies Limited. Unit 1, The Royston Centre, Lynchford Lane, Ash Vale, GU12 5PQ, England

[2] National Instruments, http://uk.ni.com/

		55P11
Sensor material		Platinum-plated tungsten
Sensor dimensions	D	5 μm
	l	1.25 mm
Sensor resistance		3.5 Ω
Temperature coefficient of resistance		0.36%/^{o}C
Frequency limit		400 kHz (CTA mode)

Table 5.1: **Dantec wire sensor 55P11: technical data**

was chosen because it provides the minimum instrumentation required to characterize the flow keeping the set-up simple, low-cost and robust. The flow velocity and angles are calculated from the pressure differences between the four holes at the probe tip. The variation of the velocity components in the plane perpendicular to the probe stem is measured by the yaw angle α, while the component in the plane perpendicular to former plane are dependent on the pitch angle γ (Figure 5.2). There are two possible operational modes [2]: either the probe is rotated to balance the pressure difference across the tappings B, C and D in Figure 5.2 ($p_B = p_C = p_D$) or the probe remains in a fixed position and the flow velocity is calculated by means of calibration curves, that link the variation of pitch and yaw angles and dynamic head with specific coefficients (Figure 5.3 shows an example calibration). For practical reasons the latter procedure was used for the measurements reported in this thesis. The probe was calibrated by Forsyth et al. [19] following the strategy used by Telisinghe and Gillespie [63], who describe an adaptation to low Mach number flows of the process described by Main et al. [41]. The coefficients used in the calibration are calculated as follows:

$$C_{pitch} = \frac{p_B - 1/2(p_C + p_D)}{P_A - \overline{p}} \tag{5.1}$$

$$C_{yaw} = \frac{p_C - p_D}{P_A - \overline{p}} \tag{5.2}$$

$$C_{dyn} = \frac{p_{dyn}}{P_A - \overline{p}} \tag{5.3}$$

$$\overline{p} = \frac{p_B + p_C + p_D}{3} \tag{5.4}$$

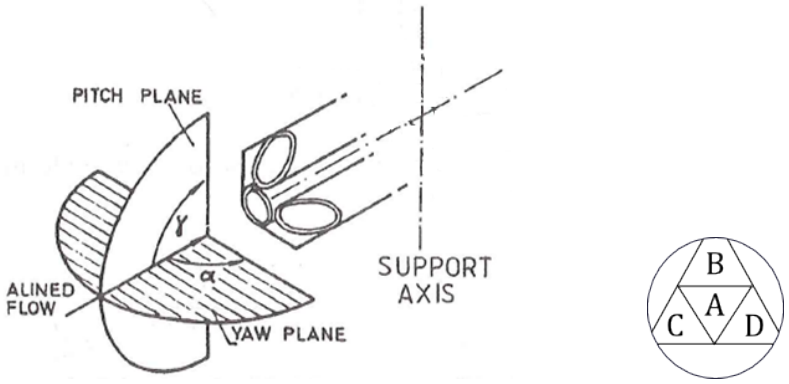


Figure 5.2: **Four-hole probe: Definition of pitch and yaw angles [2] (on the left) and tapping nomenclature [63] (on the right)**

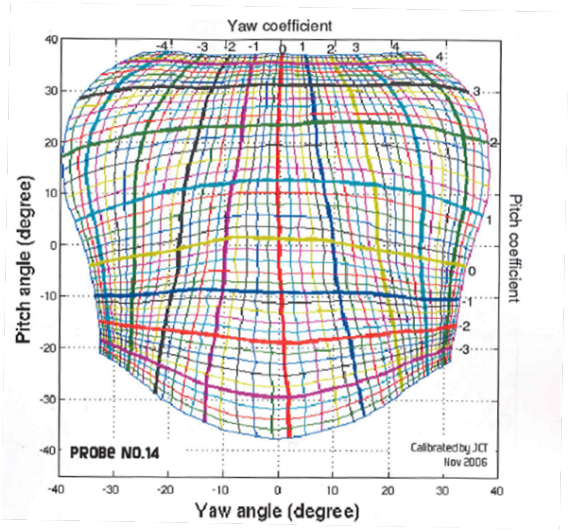


Figure 5.3: **Four-hole probe: Calibration map - Example [63]**

Hot-wire and Constant Temperature Anemometry

The hot-wire anemometer is able to measure fluid velocity at high bandwidth which enables time mean and unsteady velocity to be measured [2]. The hot-wire

anemometer consists of a very fine heated wire sensor placed in the fluid and an electronic equipment, that is an integral part of the measuring system (Figure 5.4).

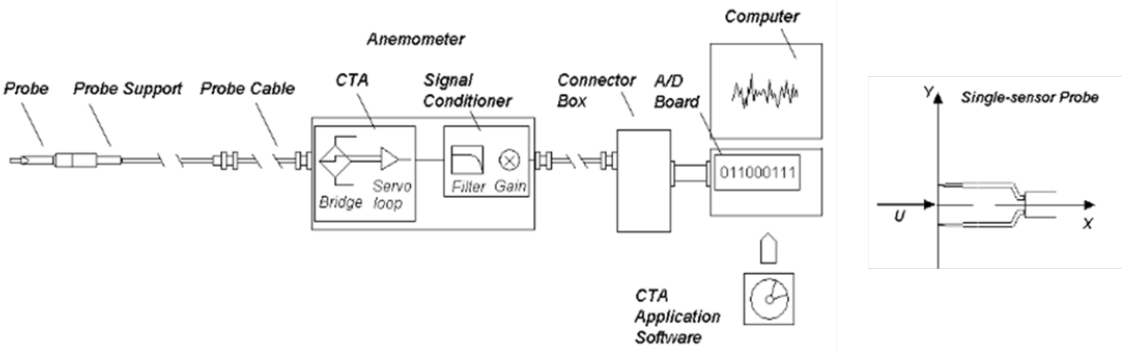


Figure 5.4: **Hot-wire anemometry: Measurement chain (on the left) and single sensor probe (on the right) [31]**

The convective heat transferred from the sensor to the surrounding fluid is related to the flow velocity. When the system is controlled with the constant temperature method, the electronic circuit maintains the sensor temperature constant, letting the heat transfer varying. The probe is connected to one of the arms of a Wheatstone bridge, the opposite arm being connected to a variable resistance controlling the overheat factor (Figure 5.5). An amplifier controls the bridge current to maintain the bridge balance. The instantaneous unbalance voltage of the bridge determines an instantaneous value of velocity pulsation.

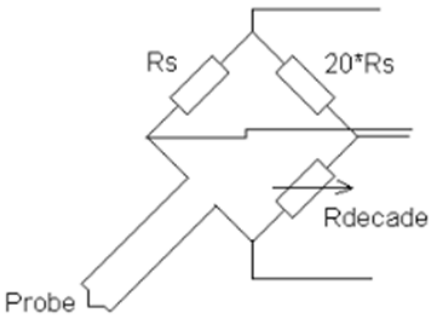


Figure 5.5: **Hot-wire anemometry: Wheatstone bridge [31]**

Hot-wire probes need to be calibrated before and after each measurement. The

calibration curve is non-linear because the rate of heat transfer to the fluid is equal to the electrical power supplied to the sensor [2]:

$$Supply = E^2/R_{hw} = \pi D_{hw} l_{hw} h(T_{hw} - T_a) = Dissipation \tag{5.5}$$

where E is the voltage across the sensor, R_{hw} is the wire operating resistance at T_{hw}, D_{hw} and l_{hw} are the wire dimensions and h is the heat transfer coefficient. The King's power law is derived from the analytical solution for the heat transfer for an infinite cylinder in an incompressible low Reynolds number flow and it proves to give a good fit to data [31]:

$$E^2 = A + BU_{hw}^n \tag{5.6}$$

where U_{hw} is the fluid velocity measured by the hot-wire, n=0.45 for Re=0.02-44, A and B are constants that need to be obtained by calibration. The hot-wire was calibrated according to King's law (Figure 5.6) in situ before each test fitting the voltage output to that measured by a Pitot probe installed in the wind tunnel.

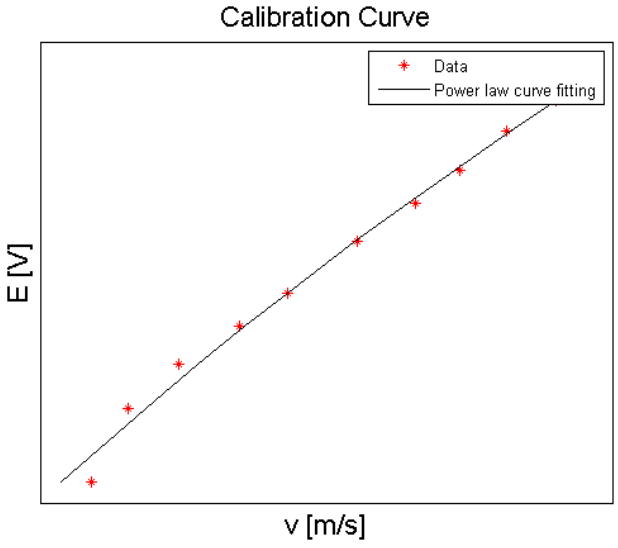


Figure 5.6: **Hot-wire anemometry: Calibration curve - Example**

Turbulence

J.O. Hinze [26] defines turbulence as follows: "Turbulent fluid motion is an irregular condition of flow in which the various quantities show a random variation with time and space coordinates, so that statistically distinct average values can be discerned". While the instantaneous pattern is random because of the flow unstable nature (Fig. 5.7), the turbulent motion shows a distinct pattern that repeats in time if it is processed by means of statistical tools. These characteristics of turbulence can be the result of the motion of periodic structures of different dimensions at various frequencies superposed to produce a complex flow field. These features are usually described introducing the concept of "scales of turbulence": their magnitude is determined by the dimensions and velocities of eddies moving in the turbulent flow. The maximum length scale is typically determined by the dimensions of the apparatus, the minimum by viscosity effects (the smaller the eddy, the greater the velocity gradient, the greater the viscous shear stresses): the first kind of eddies corresponds to low frequencies in the turbulent motion, the latter to the highest frequencies.

A turbulent flow field can be described through averaged quantities (i.e. mean value, quantity intensities etc.) and time-domain statistics (i.e. auto-correlation coefficient, integral scales, power spectrum etc.).

Time-averaged analysis

The ergodic hypothesis states that a time averaged series converges to a mean value as the averaging time becomes large, meaning that random variables must become uncorrelated after a certain amount of time and that an integral scale exists and measures the time needed to lose correlation [23]. It is clear that defining how large the average time should be is not straightforward. The minimum (or Nyquist) sampling rate, to avoid errors due to aliasing from digitalization

$$f_s = 2f_{max} \tag{5.7}$$

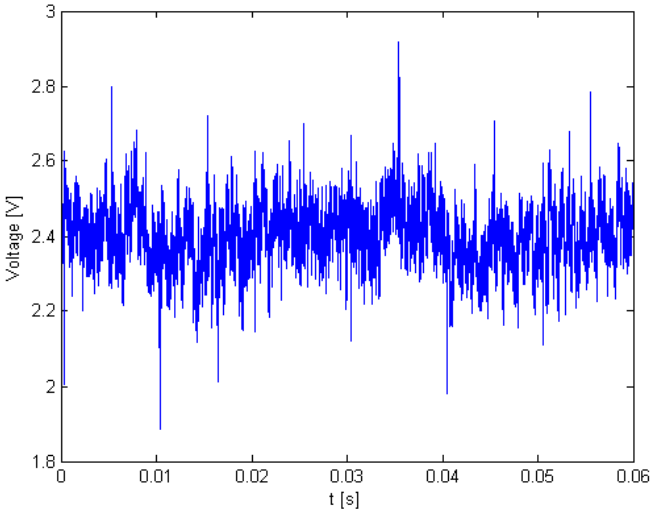


Figure 5.7: **Hot-wire anemometry: Random signal - Example**

where f_{max} is the frequency of the highest spectral component of the measured quantity. Practically f_{max} is equal to the analogue cut-off frequency f_c that is set by the user to different values for the hot-wire and the thermocouple measurements. From a single time series of the quantity q it is possible to calculate the flow mean value $\overline{q}$:

$$\overline{q} = \frac{1}{N} \sum_{i=1}^{N} q_i \tag{5.8}$$

where N is the number of samples.

Time spectral analysis

In turbulence studies it is common to assume the validity of the Taylor's hypothesis, for $u'/\overline{u} << 1$ and Tu<30% [26], which states:

$$\frac{\partial}{\partial t} = -\overline{u}\frac{\partial}{\partial x_i} \tag{5.9}$$

This is equivalent to considering the turbulent structures to be frozen, i.e. it is as the mean flow advects the eddies across the sensor, the fundamental properties remain unchanged. Under this assumption it is possible to calculate the correlation

between the value of a fluctuating quantity (such as velocity and temperature) at a fixed point at two different instants t and $(t+\tau)$:

$$R_{qq}(\tau) = \frac{\overline{q_i'(t)q_i'(t+\tau)}}{q_i'^2} \tag{5.10}$$

From R_{qq} it is possible to calculate the integral time and length scales of the turbulent flow. The integral time scale

$$T = \int_0^\infty R_{qq}(\tau)\ d\tau \tag{5.11}$$

is a measure of the average time scale associate with the energy containing eddies in the flow. Assuming Taylor's hypothesis the integral length scale (Fig. 5.8) at a fixed point can be calculated as

$$\Lambda = \overline{q}T \tag{5.12}$$

The power spectrum density (Fig. 5.8) shows how the power of the signal (either velocity or temperature) is distributed among eddies of different wavenumbers, and hence sizes: $PSD(k)dk$ is the energy contained by eddies with wavenumbers between k and $(k+dk)$ and for the results presented in this thesis it was evaluated using Welch's method [42]. Kolmogorov's theory [26] states the existence, in turbulent flows with sufficiently high Reynolds number, of a region of the kinetic energy spectrum where the statistics of the small scale motions have a universal form, uniquely determined by the turbulent dissipation rate ε and the kinematic viscosity ν. Within this region the theory identifies the existence of an inertial subrange where the effect of ν is negligible and the spectrum follows the -5/3 power law (explained below). This relation holds only if there is no direct effect of the energy-containing eddies, i.e. only if no parameter other than ε and ν affects the turbulence in this region and the spectrum is thereby independent of its conditions of formation. Figure 5.9 summarizes the general behaviour of the power spectrum density in the entire wavenumber range:

- The low k range is characterized by the largest eddies dependent on their condition of formation;
- The mid k range comprises mainly the range of energy-containing eddies;
- The high k range is the universal equilibrium range:
  - The lower inertial subrange includes the k range until eddies start dissipating.

The root mean square of the turbulent fluctuation q'_{rms} is obtained by integrating the PSD with respect to k and the fluctuating quantity intensity is calculated as

$$Tu = \frac{q'_{rms}}{\overline{q}} \tag{5.13}$$

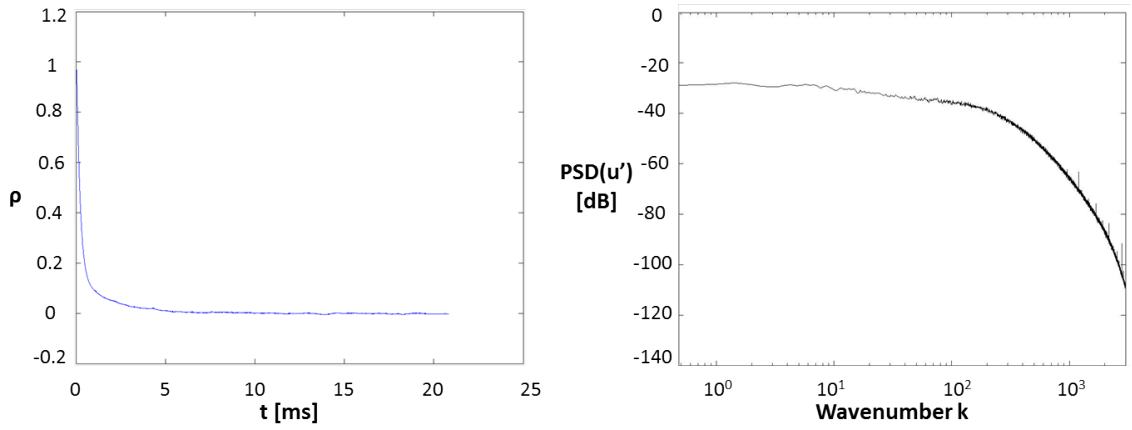


Figure 5.8: **Examples of autocorrelation function R_{uu} (left) and power spectrum density (right) plots from the CTI rig**

5.1.3 Temperature measurements

As previously described for the velocity measurements, a distinction was made between time-averaged and time-resolved measurements. For the first set of data a 75 μm wire diameter K-type (chromal/alumel) thermocouples was used, while for the latter a 12.7 μm K-type thermocouple was calibrated and employed.

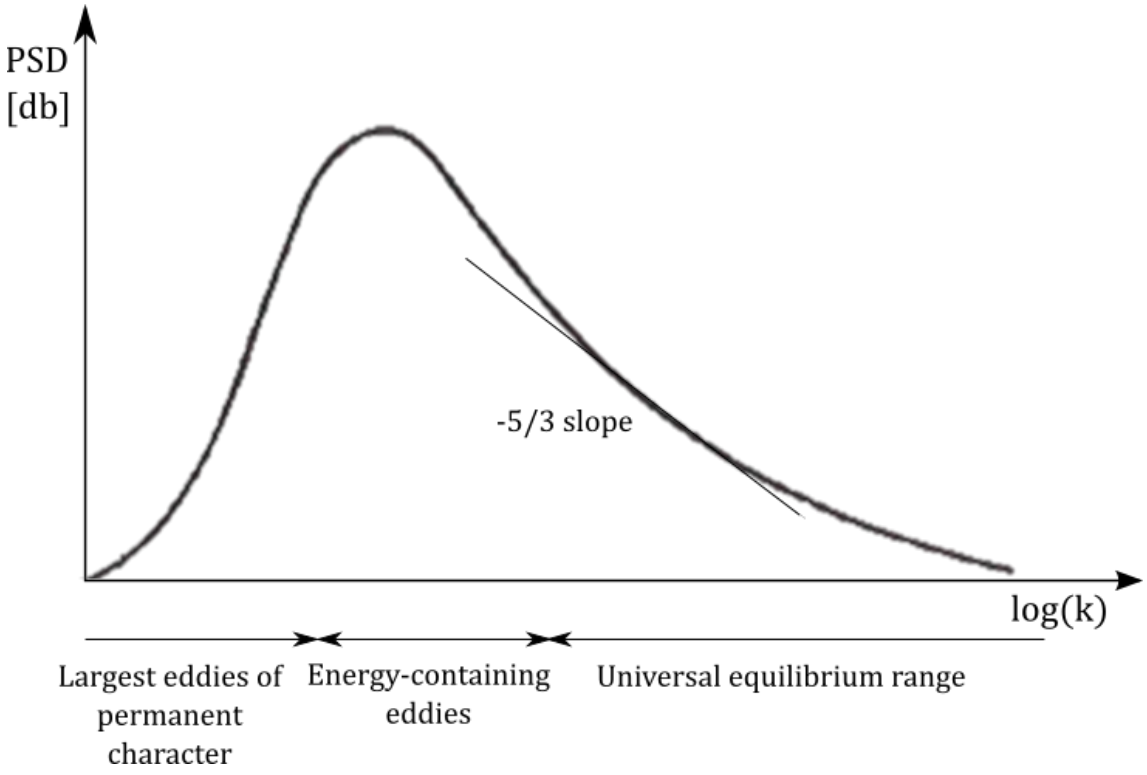


Figure 5.9: **Form of power spectrum density in the various wavenumber ranges**

Thermocouple

A 75 μm wire diameter K-type chromal/alumel thermocouple was inserted downstream of the heater mesh to get a reference temperature that was used to non-dimensionalize the temperature at the test section and keep the measurements independent of the lab ambient conditions. Four other thermocouples were used to acquire the coolant temperatures inside the four plenums.

Another K-type thermocouple was installed in the probe and swept through the NGV inlet plane with the traverse mechanism and was used to get mean temperature values across the plane. 200 samples were acquired at 100 Hz and were used to ensure a statistically independent data set. The thermocouple voltage outputs were acquired with the NI 9214 module [3].

[3]National Instruments, http://uk.ni.com/

Fine thermocouple

In order to measure temperature fluctuations at the required frequency a sensor of dimensions of the order of μm is required. Fine wire resistance thermometers operating in a constant current circuit with a wire diameter $\approx 1\mu m$ give a very high frequency response [5] but they are very fragile and this limits their usage. The implementation of a cold wire system was firstly attempted by the author, but this try failed because of troubles with the constant current power supply: in switching it on a pulse of higher current was enough to burn the sensor. Coarser thermocouples are more robust but because of the typically bigger dimensions the main problem emerged in their application is excessive thermal inertia, so either electrical or digital compensation is required.

In the present work a 12.7 μm wire chromal/alumel thermocouple inserted in a ceramic shield and mounted on a metallic probe was manufactured, as previously used by Lockwood and Moneib [40], who took fluctuating temperature measurements downstream of a heated jet. The tip geometry of the thermocouple probe is shown in Figure 5.10. Note that the wire protrudes from the ceramic holder by approximately $150D_w$ so conduction effects between stem and housing are negligible.

The thermocouple voltage output was amplified with a Michigan Scientific Corporation[4] MicroTC-D amplifier.

The thermocouple response to a temperature change can be mathematically modeled as a first-order system and its time constant τ determines the rate at which the probe response approaches the final value, i.e., for a temperature sensor, the time that is needed for it to reach the 63% of the fluid temperature variation ΔT.

The rate at which the wire exchanges heat with the fluid must equal the rate of change of the sensor internal energy

[4]Michigan Scientific Corporation, 8500 Ance Road, Charlevoix, MI 49720, USA, http://www.michsci.com/

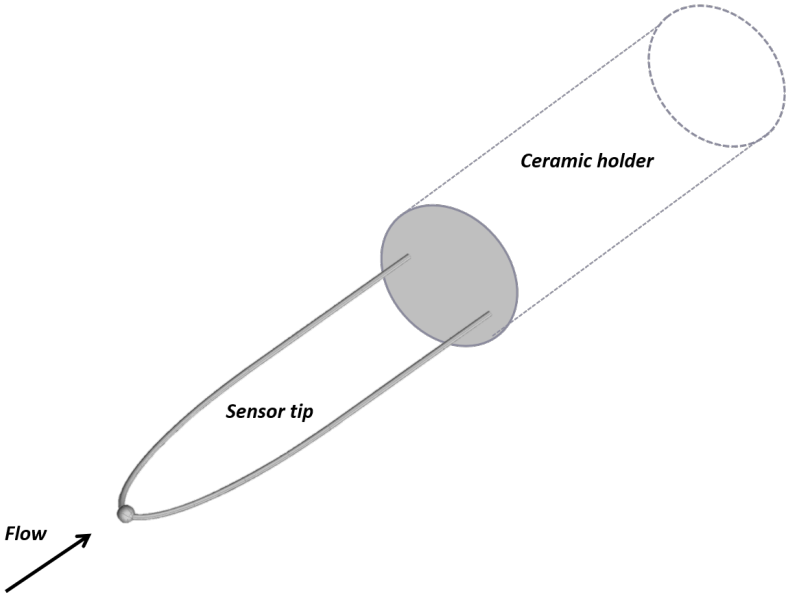


Figure 5.10: **Sketch of the fine thermocouple model drawn approximately to scale. Note that the wire protrudes from the ceramic holder by approximately 2mm.**

$$hA(T_\infty - T_{TC}) = mc\frac{dT_{TC}}{dt} \tag{5.14}$$

This means that it is possible to account for the thermocouple time constant by including a term that multiplies the time derivative of the measured signal by the time constant

$$T_\infty = \left[1 + \tau_{TC}\frac{d}{dt}\right] T_{TC} \tag{5.15}$$

where

$$\tau_{TC} = \frac{mc}{hA} \tag{5.16}$$

It is clear from the above that an accurate evaluation of τ_{TC} is required to correct the acquired temperature data: its experimental estimate in the velocity range of interest is reported in Chapter 6.

5.2 Test section with vanes

After the installation of the vanes pressure measurements were acquired to control the mainstream flow periodicity on the pressure and suction side of the cooled vane and to measure the pressure distribution inside the leading edge coolant passage. These measurements are presented and discussed in Chapter 9.

5.2.1 Pressure measurements

The vanes were instrumented with a total of 86 pressure tappings:

- The right vane has 11 pressure tappings on the pressure side (Figure 5.11) at s=0.5H (i.e. midspan);
- The left vane has 14 pressure tappings on the suction side (Figure 5.12) at s=0.5H (i.e. midspan);
- The cooled vane has
  - 29 pressure tappings (Figure 5.13) at s=0.5H (i.e. midspan);
  - 12 pressure tappings in the cooled LE part at s=0.75H;
  - 20 pressure tappings inside the coolant passage
    - 10 pressure tappings at s=0.17H;
    - 10 pressure tappings at s=0.3H.

The pressure was measured with signal conditioned pressure transducers from SensorTechnics [5] HSX series and the data were acquire with NI 9220 [6] analogue input module.

[5] FirstSensor, http://www.first-sensor.com/en/

[6] National Instruments, http://uk.ni.com/



Figure 5.11: **Pressure tappings: right vane**

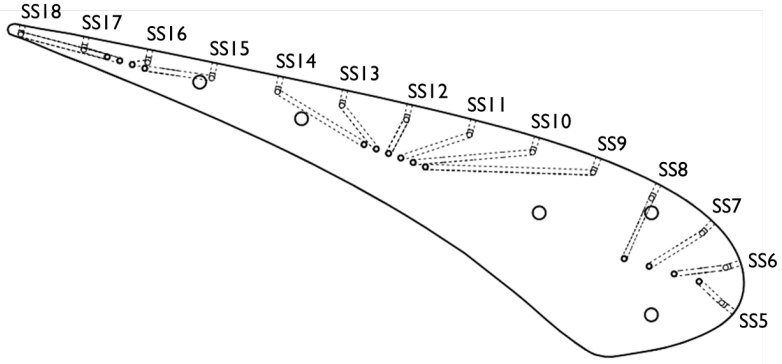


Figure 5.12: **Pressure tappings: left vane**

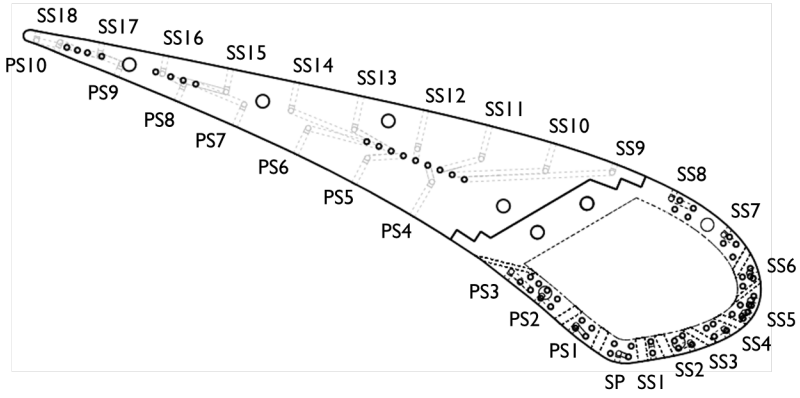


Figure 5.13: **Pressure tappings: cooled vane**

5.3 Uncertainty analysis of experimental data

The quantification of experimental and numerical uncertainty is required to guarantee a correct interpretation of presented data by researchers and to improve the uniformity of them for the users. This is possible only if there is uniformity in the definition and interpretation of what is the uncertainty analysis [45].

Moffat [45] states that if the the flow field quantity q is dependent on N different independent variables X_i it can be written as follows

$$q = q(X_1, X_2, ..., X_N) \tag{5.17}$$

and its uncertainty can be estimated with good accuracy using a root-mean square combination of the effect of each individual variable

$$\delta q = \left[\sum_{i=1}^{N} \left(\frac{\partial q}{\partial X_i} \delta X_i \right)^2 \right]^{1/2} \tag{5.18}$$

5.3.1 Orifice meter: Mass flow

When q involves operations that are difficult to differentiate, Moffat [45] suggests to sequentially perturb the inputs to determine the effect of each term ∂X_i on q. This method was used to calculate the uncertainty on the mass flow rate calculation, that was defined according to the standard ISO 5167-2

$$\dot{m} = \frac{C_d}{\sqrt{1-\beta^4}} \varepsilon \frac{\pi}{4} D^2 \sqrt{2\rho\Delta p} \tag{5.19}$$

where

- C_d is the orifice discharge coefficient (which is a function of the Reynolds number, i.e. a function of $\dot{m}$, and that means it needs to be obtained by iteration);
- β is the orifice-to-pipe diameter ratio;

- ε is the expansibility factor (which is a function of the orifice upstream-to-downstream pressure ratio);
- D is the orifice diameter;
- Δp is the pressure drop across the orifice;
- ρ is the fluid density.

The values of Δp and ρ were perturbed and the maximum evaluated uncertainty was lower than 6%.

5.3.2 Four-hole probe: Velocity

The flow velocity is calculated from the four-hole probe pressure measurements through the coefficients reported in Section5.1.2:

$$v = \sqrt{\frac{2}{3} C_{dyn} \frac{RT}{p} (2p_A - p_B - p_C)} \tag{5.20}$$

The overall uncertainty is obtained from the following equation derived by Eq.5.18

$$\delta v = \left[\left(\frac{\partial v}{\partial C_{dyn}} \delta C_{dyn} \right)^2 + \left(\frac{\partial v}{\partial T} \delta T \right)^2 + \left(\frac{\partial v}{\partial p} \delta p \right)^2 + \left(\frac{\partial v}{\partial p_A} \delta p_A \right)^2 + \left(\frac{\partial v}{\partial p_B} \delta p_B \right)^2 + \left(\frac{\partial v}{\partial p_C} \delta p_C \right)^2 \right]^{1/2}$$

For the experimental data obtained with the four-hole probe presented in this thesis the maximum uncertainty is around 6%.

5.3.3 Hot-wire: Velocity and turbulence

Yavuzkurt wrote a guide to calculate the uncertainty for hot-wire data [71]. That considers the following sources of error:

- Calibration;

- Reduction of calibration data;
- Approximation for a horizontal wire.

The total maximum uncertainty on the mean velocity value in the reported measurements is lower than 5% and that one on the fluctuation value varies between 5 and 6% depending on the magnitude of the velocity fluctuations in the spanwise and lateral direction.

5.3.4 Thermocouple: Temperature

The maximum error for the time-averaged temperature values acquired with the NI 9274 module is approximately 1.5 K: in the measurement range this gives a maximum error of 7% on the plotted normalized temperature $\frac{T-T_c}{T_\infty-T_c}$. The maximum temperature error obtained with the thermocouple amplifier MicroTC-D, used in the time-resolved measurements, is 3 K.

Chapter 6

Fine Thermocouple Time Response Study

The main problem that emerged in using a thermocouple to acquire time-resolved measurements is that their thermal inertia needs to be correctly evaluated and taken into account to correct the acquired temperature values. Various experimental techniques have been developed to measure τ and thus correct the measured signal: usually internal and external heating techniques are employed [50]. For this study a low-speed wind tunnel in the Osney Thermo-Fluids Laboratory was used where the fine thermocouple described in Section 5.1.3 was installed downstream of a heater mesh that provided the temperature change.

The work reported in this chapter was published in the proceedings of the International Gas Turbine Congress, held in Tokyo in November 2015 [13].

6.1 Experimental time constant estimation

The thermocouple time response calibration was performed in a low-speed wind tunnel previously used by Moss [46]. The sampling rate was chosen according to the Nyquist criterion to be higher than twice the system cut-off frequency that was set at 1kHz. The number of samples was 10k per data point. The heater mesh

is installed downstream of an intake and the thermocouple downstream of a flow contraction ($u_{TC} = 2u_m$), as shown in Figures 6.1 and 6.2.

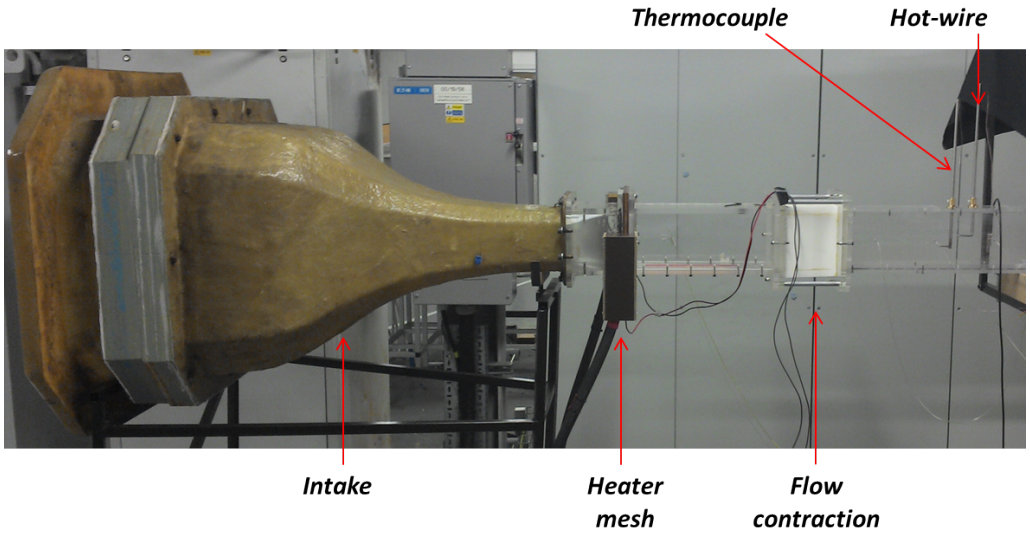


Figure 6.1: **Calibration low-speed wind tunnel**

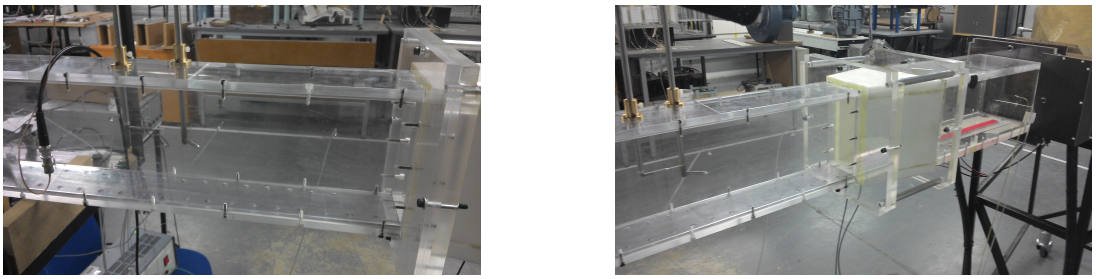


Figure 6.2: **Calibration low-speed wind tunnel test section: side view (left) and upstream view (right)**

The flow was subjected to a first-order gas temperature change when the heater mesh was turned on that can be mathematically modeled as

$$T_\infty(t) = T_\infty(t=\infty) + (T_\infty(t=0) - T_\infty(t=\infty))e^{(-t/\tau_m)} \tag{6.1}$$

where τ_m is the heater mesh time constant.

Combining Eq. 5.14 and 6.1 and solving the resulting differential equation, the temperature measured by the thermocouple can be modeled by the following formula

$$T_{TC}(t) = T_\infty(t=\infty) + (T_\infty(t=0) - T_\infty(t=\infty)) \left[\left(1 - \frac{\tau_m}{\tau_m - \tau_{TC}}\right) e^{(-t/\tau_{TC})} + \frac{\tau_m}{\tau_m - \tau_{TC}} e^{(-t/\tau_m)}\right] \tag{6.2}$$

To obtain τ_m a hot wire was installed next to the thermocouple (Fig.6.2) to measure the thermal transient as described by Gillespie [24] (Fig.6.2). The hot-wire voltage response, E, follows the equation

$$\frac{E^2(t)}{R_{hw}} = \frac{E^2(t=\infty)}{R_{hw}} + \left[\frac{E^2(t=0) - E^2(t=\infty)}{R_{hw}}\right] e^{(-t/\tau_m)} \tag{6.3}$$

Examples of the comparison between experimental measurements and Eq. 6.2 and 6.3 are presented in Figure 6.3. The value of τ_m was obtained by minimizing the least square difference between the right hand side of Eq. 6.3 and the hot wire output. τ_{TC} was then determined from the least square regression of Eq.6.2 to the measured thermocouple signal.

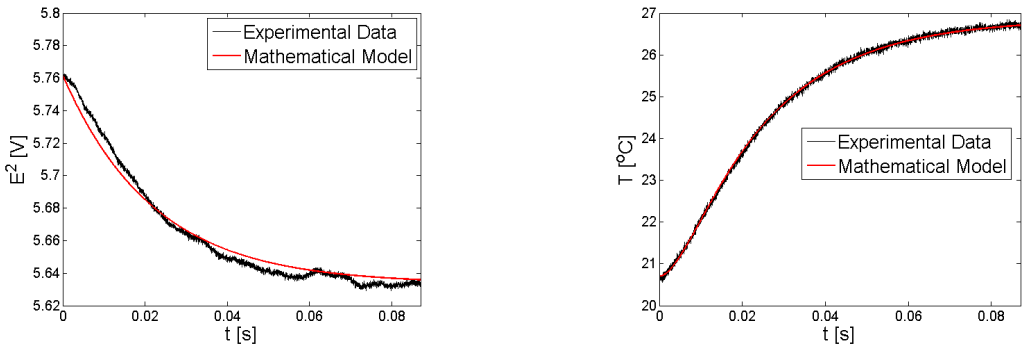


Figure 6.3: **Comparison between experimental data and mathematical models: Hot wire voltage squared (left) and thermocouple (right) output**

A Pitot probe was also installed adjacent to the thermocouple during the calibration to record the flow speed during heating. These measurements confirmed that the flow speed remained constant during the calibration. The heater mesh time constant versus flow velocity is plotted in Figure 6.4 and the results can be correlated as $\tau_m = 0.082 * v_{flow}^{-0.505}$ for fixed supplied power.

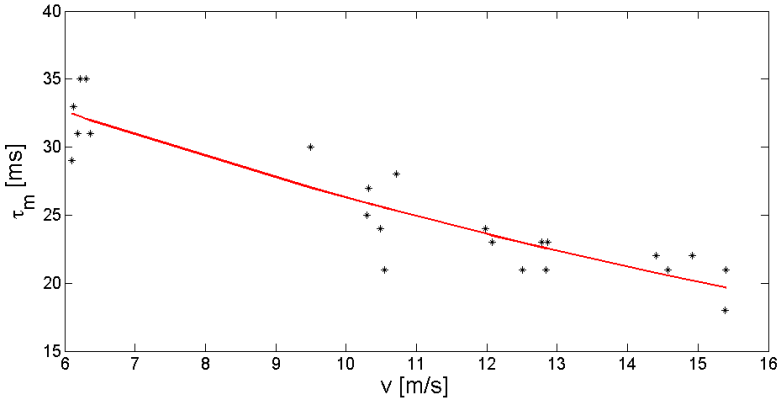


Figure 6.4: **Heater mesh response: τ_m vs. flow velocity**

6.2 Earlier analytical studies

Yule [72] analytically studied the response characteristics of an unshielded fine-wire thermocouple idealizing its geometry as a spherical bead connected to an infinitely long cylindrical wire as shown in Figure 6.5. The main heat transfer mechanisms that take place in this case are:

- Direct heat exchange between the bead and the gas $\dot{Q}(gas - bead)$;
- Heat conduction from the bead along the wire $\dot{Q}(bead - wire)$;
- Direct heat exchange between the wire and the gas $\dot{Q}(gas - wire)$;
- Heat conduction from the wire to the support $\dot{Q}(wire - support)$ (that is assumed negligible in this case).

The wire time constant τ_w can be estimated using the correlation for heat transfer coefficient for a cylinder, with radius r_w, in crossflow

$$\tau_w = \frac{\rho_w c_w r_w^2}{k_g N u_w} \tag{6.4}$$

assuming $Nu_w = 0.24 + 0.56 Re_w^{0.45}$ [10].
Approximating the bead as a truncated sphere with radius r_b, its time constant τ_b can be obtained from

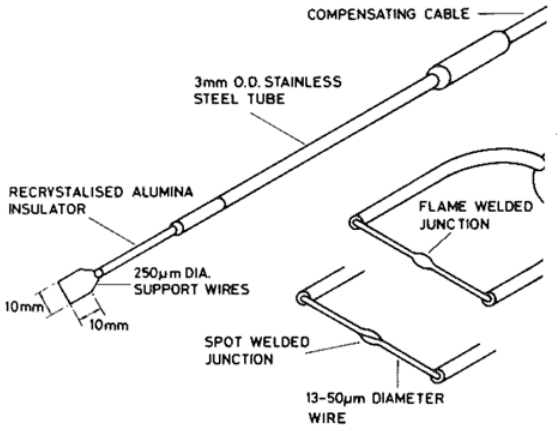


Fig. 1 Design of fine-wire thermocouple probe.

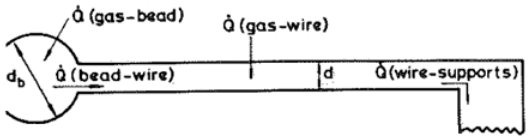


Figure 6.5: **Fine-wire thermocouple sketch from Yule [72]**

$$\tau_b = \frac{(2/3)r_b^2 \rho_b c_b (1 + 1/2(r_w/r_b)^2)}{k_g N u_b} \tag{6.5}$$

assuming $Nu_b = 2 + 0.6 Pr^{0.33} Re^{0.5}$ (where $Pr = 0.73$).

The real response of the thermocouple to a transient change in gas temperature of a thermocouple is between two limiting cases:

a For a bead diameter D_b much larger than the wire diameter D_w the heat transfer from the bead is dominated by convection with the gas, i.e. $\dot{Q}(gas - bead) >> \dot{Q}(bead - wire)$ and $\tau_{TC} = \tau_b$;

b For a bead diameter D_b very close to the wire diameter D_w the thermocouple behaviour can be modeled as an infinite wire and $\tau_{TC} = \tau_w$.

6.3 CFD simulations

In order to check the ability of RANS simulations to predict such a device time response and increase the number of variables controlled compared to the experiments (such as sensor angle with respect to the flow direction and bead diameter), different numerical models were produced by the author.

Two different numerical models of the thermocouple were created and are shown in Figure 6.6: one idealizes the thermocouple geometry as a spherical bead connected to a transverse wire, as this is the geometry analytical studied by Yule et al. [72], while the second represents the actual thermocouple geometry (Figure 5.10). The unstructured meshes in Figure 6.7 were generated with ANSYS ICEM 12.0 and contain around $2 \cdot 10^6$ elements with prism layers on the bead and wire surfaces. RANS simulations were performed using Fluent 12.0. The simulated cases are reported in Table 6.1 in accordance to the nomenclature and the flow reference system shown in Figure 6.8.

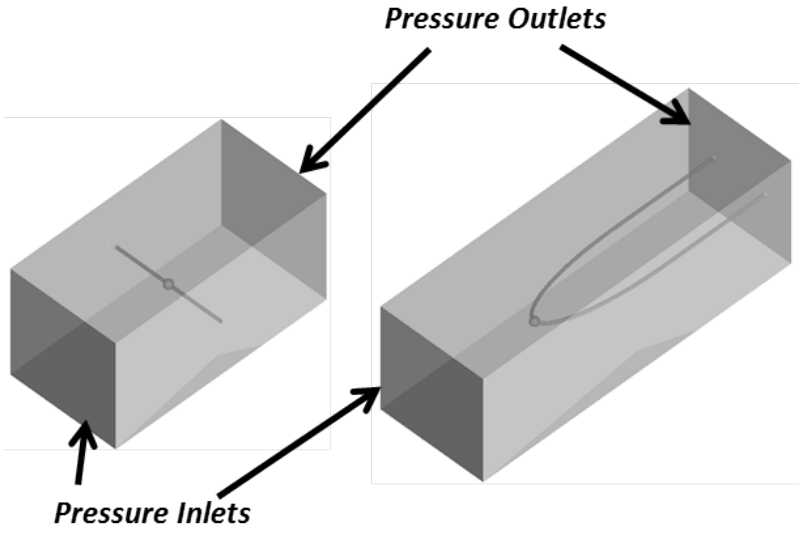


Figure 6.6: **Thermocouple computational model: Yule's geometry (left) and real geometry (right)**

The heat transfer coefficient h was calculated for each considered case and used

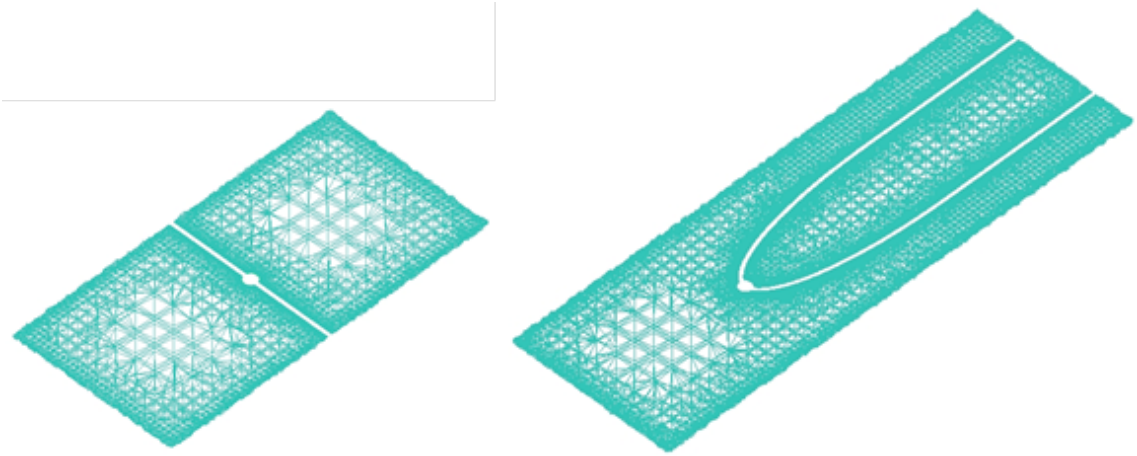


Figure 6.7: **Thermocouple computational model: Yule's geometry (left) and real geometry (right)**

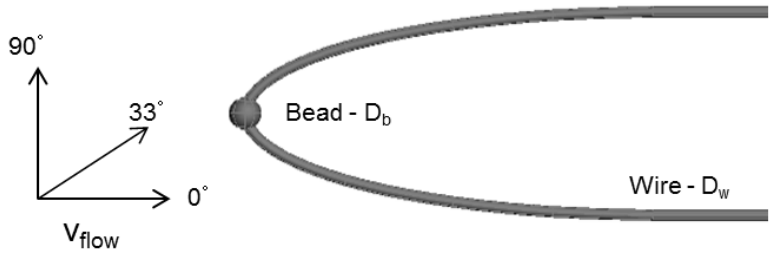


Figure 6.8: **Thermocouple nomenclature and coordinate system**

to estimate the Nusselt number for the wire

$$Nu_w = \frac{h_w d_w}{k} \tag{6.6}$$

and for the bead

$$Nu_b = \frac{h_b d_b}{k} \tag{6.7}$$

The time constant values were then obtained using Equations 6.4 and 6.5.

	Geometry	D_b	Flow angle [^{o}]
Case A	Yule [1978] [72]	$3D_w$	0
Case AA	Yule [1978] [72]	$2D_w$	0
Case B1	Cresci [2015] [13]	$3D_w$	0
Case B2	Cresci [2015] [13]	$3D_w$	33
Case B3	Cresci [2015] [13]	$3D_w$	90
Case BB1	Cresci [2015]	$2D_w$	0
Case BB2	Cresci [2015]	$2D_w$	33
Case BB3	Cresci [2015]	$2D_w$	90

Table 6.1: **Thermocouple CFD cases**

6.3.1 Uncertainty analysis

Following the GCI method described in Section 3.7 three different mesh "Coarse", "Standard" and "Fine" were tested for the study in Chapter 6: their details are reported in Table 6.2.

Mesh	Scale factor	No elements
Coarse	1.5	$\approx 10^6$
Standard	1	$\approx 2 * 10^6$
Fine	1.5	$\approx 8 * 10^6$

Table 6.2: **Fine thermocouple study: Tested mesh**

The "Coarse" mesh gave some numerical instability issue, so it was considered not suitable for this application. The GCI was calculated comparing the heat transfer coefficient of the bead and wire surfaces obtained with the "Standard" and "Fine" mesh the results are listed in Table 6.3.

Case (Table 6.1)	Variable	GCI
Case A	$h_{w_{Standard}}/h_{w_{Fine}}$	0.004
	$h_{b_{Standard}}/h_{b_{Fine}}$	0.001
Case B1	$h_{w_{Standard}}/h_{w_{Fine}}$	<0.001
	$h_{b_{Standard}}/h_{b_{Fine}}$	0.003

Table 6.3: **Fine thermocouple study: Grid-Convergence Index (GCI)**

6.4 Results and comparison

Figure 6.9 compares the CFD calculations and analytical predictions from Yule et al. [72].

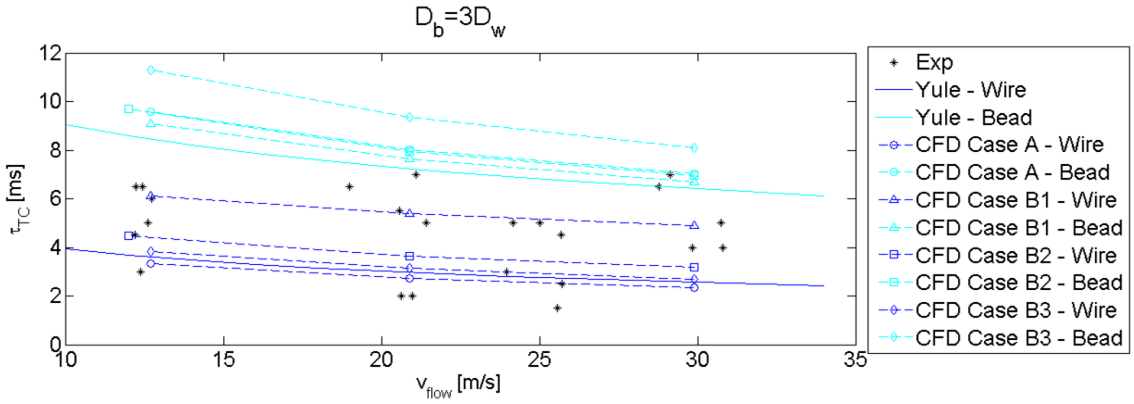


Figure 6.9: **Thermocouple time constant: comparison of present measurements (" Exp") with the CFD predictions and correlations from Yule et al. [72]. Note that these measurements were made at approximately 1 bar and 20-25^{o}C.**

Firstly, Yule's equations give results very close to those predicted by CFD on geometry A: the difference on τ_b is around 1 ms, while on τ_w is 0.5 ms. The curve slopes are the same. The real geometry simulated with CFD with perpendicular flow (Case B1) shows a much narrower range compared to Yule et al.'s geometry, because, while the bead heat transfer coefficient is essentially the same, the wire heat transfer decreases sensibly. Increasing the flow incidence (Cases B2 and B3)

significantly affects the way in which the flow approaches the wire and increases the heat transfer coefficient thereby decreases the time constant; the opposite happens at the bead where its time constant increases. The net result is that increasing the angle with which the flow approaches the thermocouple increases the difference between τ_b and τ_w, thereby τ_{TC} range increases. The experimental data were acquired with the thermocouple inclined of 33^o respect to the flow direction because of facility constrains. Comparing them to geometry B2 it is possible to see that almost all the acquired values fall inside the area delimited by the predicted τ_b and τ_w.

The effect of the bead diameter was investigated using Yule's equations and CFD simulations and the results are reported in Figure 6.10. A reduction of the bead diameter decreases the thermocouple time response because of a decrease of the thermocouple thermal inertia. In addition, the difference between wire and bead time constant reduces to values around 1 ms in the considered velocity range for the cases with flow perpendicular to the thermocouple.

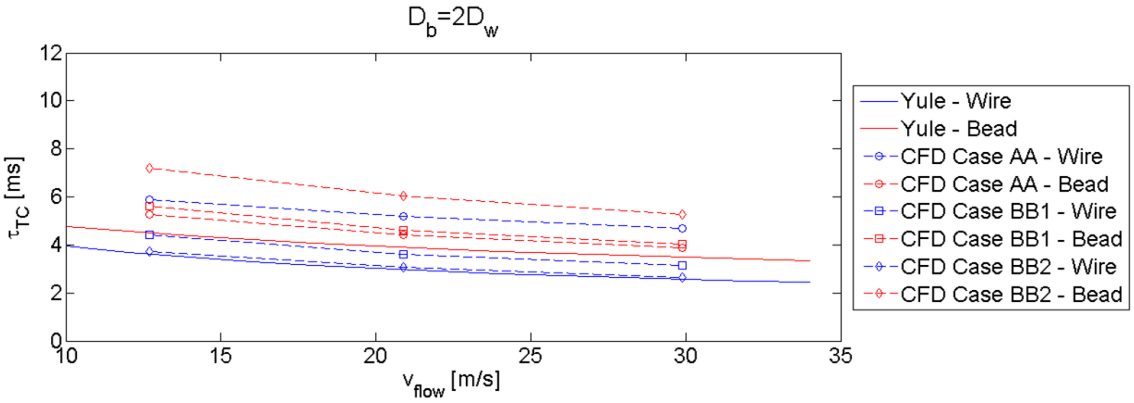


Figure 6.10: **Thermocouple time constant:** $D_b = 2D_w$

6.5 Summary

- The time constant of a fine thermocouple (12.7 μm diameter wire) was experimentally estimated:

  - The facility used for the calibration was described and the thermocouple time response mathematical model reported;
  - Yule's analytical approach [72] was employed to obtain a range of time constant for the fine thermocouple;
  - CFD simulations were run to to check the ability of predicting the probe time response and increase the number of parameters controlled compared to the experiments (i.e. sensitivity to flow direction and to bead diameter).

- The above experimental measurements, analytical evaluation and numerical simulations gave the author high confidence in their ability to correctly compensate for the thermocouple thermal inertia.

- For a 12-30 m/s flow velocity range the experimentally measured time constant varies averagely between 6 and 5 ms, with a variation of ± 3 ms. The numerical simulations predict a variation of around ± 2 ms with the flow angle changing from 0 to 90^o and around -3 ms when the bead diameter decreases from 3 to 2 times the wire diameter.

- Values of time constant between 5 and 6 ms (depending on the data point velocity) were used to correct the measurements presented in Chapter 7.

Chapter 7

CTI Rig: Combustor Simulator Flow and Temperature Study

The flow at the combustor-turbine interaction plane is complex and, up to now, has frequently been idealized as a uniform field in both experimental set-ups and CFD simulations. This simplification has been shown to limit the accuracy of the experimental simulation of flow through a turbine cascade [1].

The principal goal of the work presented in this chapter is to reproduce the main flow features present downstream of a Rich-Burn, Quick-Mix, Lean-Burn (RQL) combustor in a low speed linear cascade and quantify the main parameters describing the flow approaching the HP NGVs.

The work reported in this chapter was partially presented at the European Turbomachinery Conference [12], held in Madrid in March 2015, and partially at the International Gas Turbine Congress [13], held in Tokyo in November 2015.

7.1 CFD simulations

CFD simulations of the combustor simulator at the rig operating conditions were performed to support understanding of the flow at the combustor turbine interaction plane.

7.1.1 Computational domain

An overview of the combustor simulator was illustrated in Section 4.2. It includes two rows of dilution ports with different diameters at the inner and outer walls followed downstream by two rows of RIDN and RODN (Fig. 7.1). The main geometrical parameters are reported in Table 4.1.

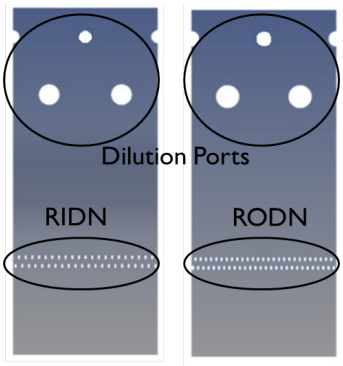


Figure 7.1: **Dilution ports and film cooling holes configuration on the endwalls (inner wall on the left, outer wall on the right)**

The combustor model has five different inlets (one for the mainstream, one for the outer dilution port plenum, one for the inner dilution port plenum, one for the RODN plenum, one for the RIDN plenum) and one outlet downstream of the NGV inlet plane: these planes are highlighted in Figure 7.2 .

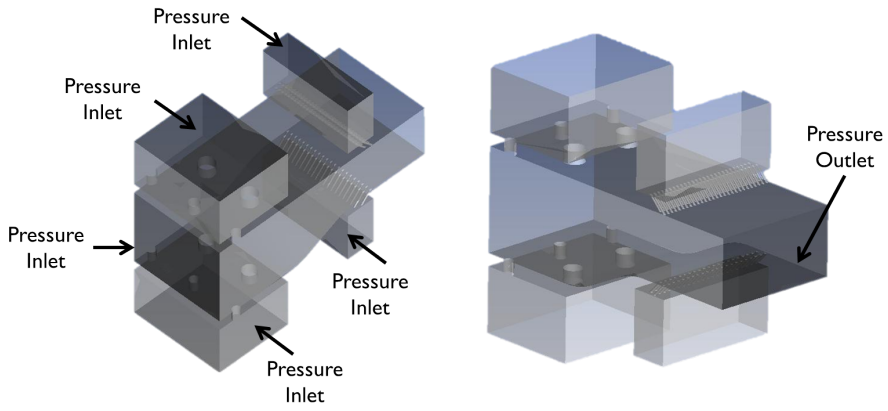


Figure 7.2: **Computational model: Boundary planes**

7.1.2 Mesh

The unstructured computational mesh was generated with ANSYS ICEM 12.0 and contained around 10^7 elements. Prism layers were used at the walls achieving $y^+ < 20$. Figure 7.3 shows a view of the mesh shells on the region around the dilution ports on the inner wall and of RODN holes. A section through the core flow mesh is shown in Figure 7.4.

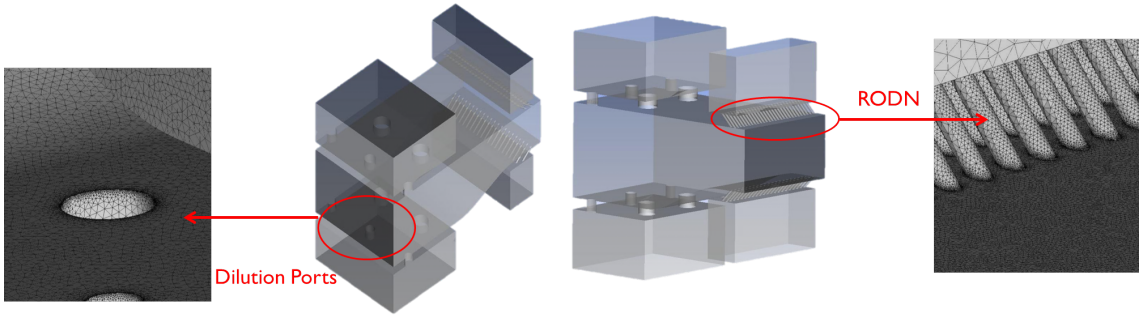


Figure 7.3: **Computational model: dilution port and RODN detail**

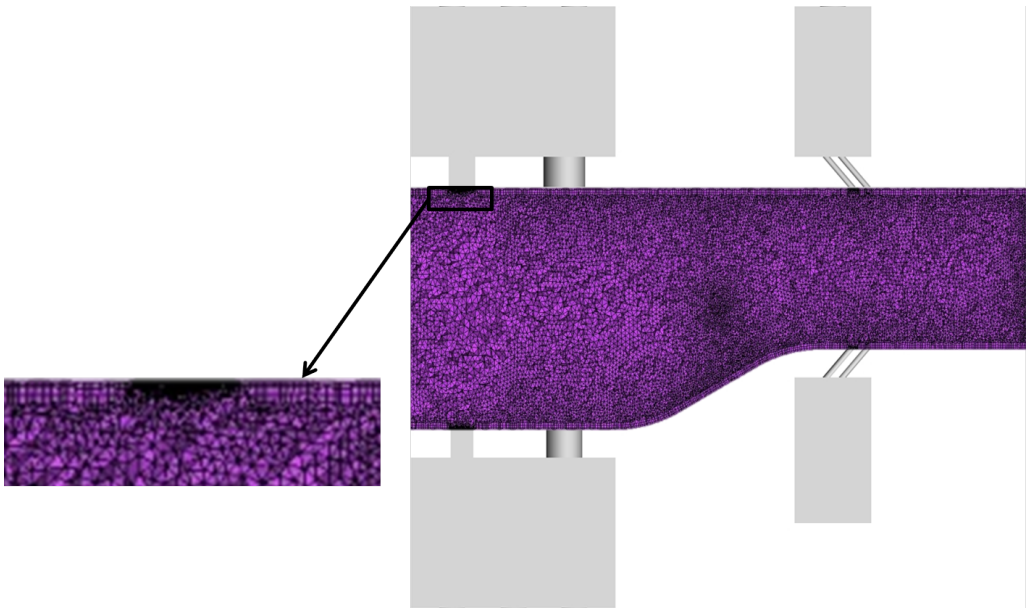


Figure 7.4: **Computational model: mesh section and enlargement**

In the centre of Figure 7.5 the location of the section planes at which CFD data were extracted is presented: plane A is downstream of the dilution flow injection

and upstream of the cross-section reduction; plane B is inside the contraction; plane C is downstream of it; plane D is between the first and the second nozzle row and plane E coincides with the NGV inlet and the experimental measurement plane.

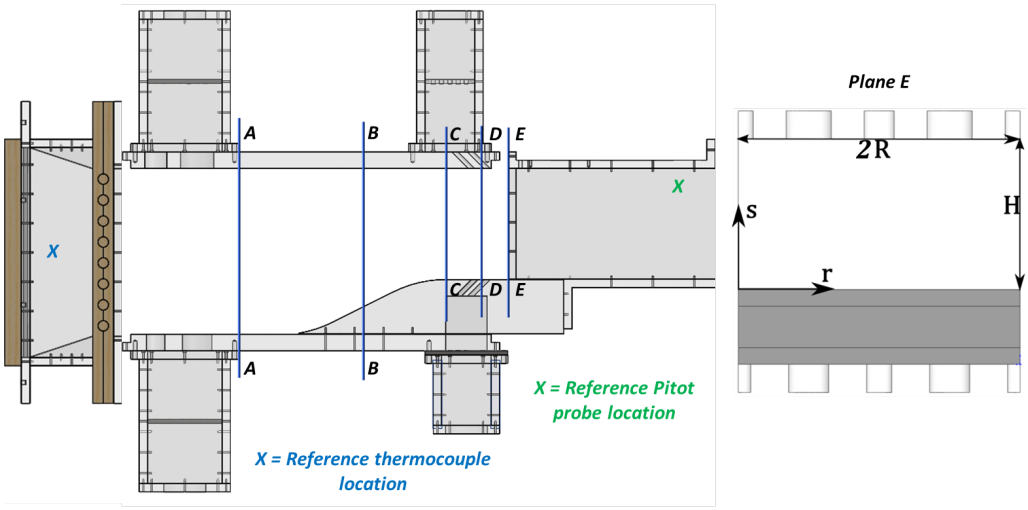


Figure 7.5: **Section plane locations from the side (on the left) and coordinate system at plane E upstream view (on the right)**

7.1.3 Boundary conditions

RANS simulations were performed using ANSYS Fluent 12.0. The turbulence was modeled using the realizable k-ε model with enhanced wall treatment, in accordance to the previous study from Cha et al. [8]. A comparison with other turbulence models is reported in Appendix C. All the inlet total pressure boundaries were set at rig conditions with turbulence levels at 20% [8]. It is important to note that the choice of the inlet turbulence value had little effect on turbulence intensity at the exit plane: simulations showed that a variation of 5% of inlet turbulence intensity causes a maximum variation of 0.1% on the turbulence intensity at the outlet plane in Figure **??**, confirming that the turbulence levels at the NGV inlet plane are dictated by the dilution jets configuration (Figure 7.6) and not the turbulence level at inlet to the plenums. The coolant inlet conditions were applied at the plenum inlets, so the computational mesh is extended into the plenums, as suggested by

Walters and Leylek [70]. A uniform static pressure boundary condition was applied at the outlet section. The inlet temperature was set to be uniform at all the boundaries and matched the reference values experimentally measured downstream of the heater mesh (mainstream inlet) and inside the coolant plenum (see Section 5.1.3). Wall boundaries were set on the side walls to match the computational domain with the experimental facility. The wall boundary conditions were set at a constant external temperature with wall thickness and properties set according to rig conditions (20 mm Perspex wall). Convergence was determined by monitoring mass flow rate, temperature and turbulent kinetic energy residuals at the outlet section.

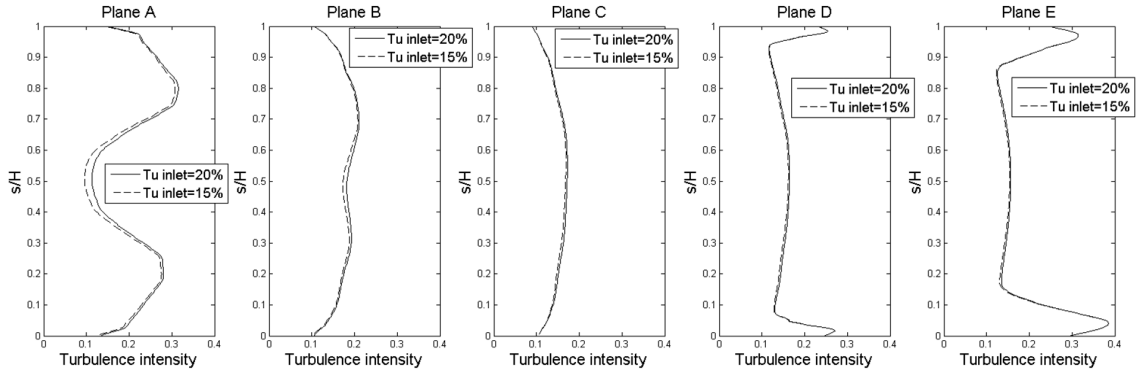


Figure 7.6: **CFD predictions of turbulence intensity profile averaged in the radial direction: inlet turbulence intensity effect**

7.1.4 Numerical uncertainty

The sensitivity of the numerical simulation results for the combustor simulator to a decrease in the mesh size to 0.75 times the original dimension was checked on the main parameters of interests:

- Velocity magnitude non-dimensionalized by the average bulk velocity;
- Turbulence intensity non-dimensionalized by the average bulk turbulence intensity;

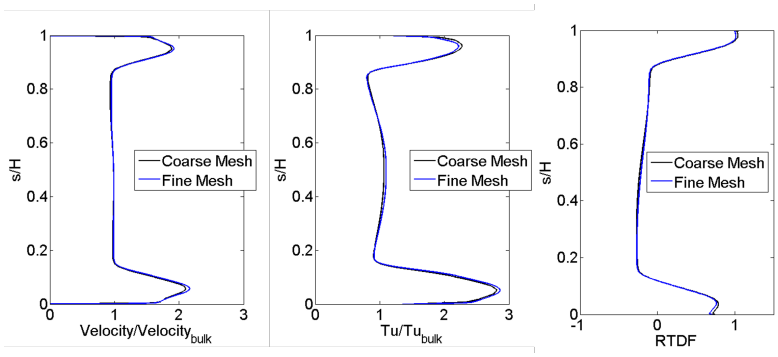


Figure 7.7: **Mesh sensitivity: Velocity, turbulence intensity and RTDF**

- RTDF.

The comparison of the averaged values in the lateral direction plotted along the spanwise direction is shown in Figure 7.7. The GCI (Section 3.7) based on the maximum value of $(f_2 - f_1)$ in Eq.3.28 was calculated for the three variables and the results are reported in Table 7.1.

Variable	GCI
V/V_{bulk}	0.023
Tu/Tu_{bulk}	0.872
RTDF	0.073

Table 7.1: **Combustor simulator study: Grid-Convergence Index (GCI)**

7.2 Comparison of experiment and CFD

In this section the CFD predictions and the acquired measurements are presented and discussed. The results are obtained at the typical engine flow conditions reported in Table 4.2.

7.2.1 Velocity field

In this section the time-averaged and time-resolved velocity fields are presented and reviewed. The hot-wire measurements were taken at iso-thermal conditions.

Time-averaged field

A complete overview of the flowfield inside and downstream of the combustor simulator is provided through CFD simulations of the entire combustor simulator domain and experimental measurements at the NGV inlet plane. The time-averaged velocity field was acquired by means of a four-hole probe (see Section 5.1.2).

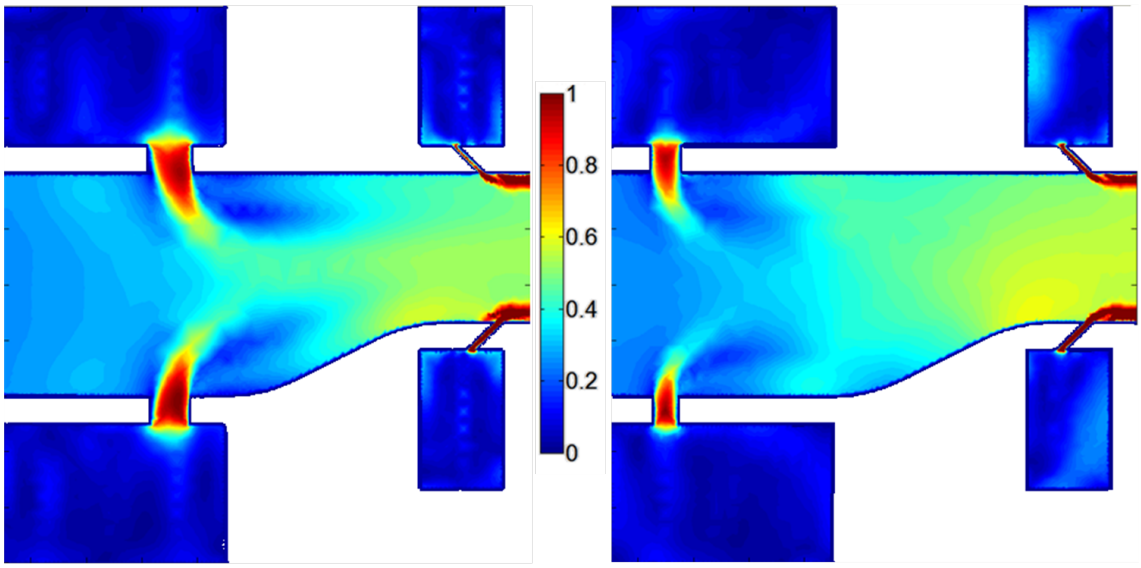


Figure 7.8: **CFD predictions of normalized velocity v/v_{max} at r/R=0.5 (on the left) and at r/R=1 (on the right)**

In Figure 7.8 the flow velocity distribution predicted by the CFD simulation at two different streamwise planes is normalized by the maximum jet velocity: r/R=0.5 bisects the secondary larger dilution ports and r/R=1 bisects the primary small dilution ports (Figure 7.5). A noticeable low-velocity region is visible downstream of each jet injection, as previously reported by Vakil and Thole [69]. An upstream acceleration of flow near the inner inclined wall is also evident. The jet streamlines

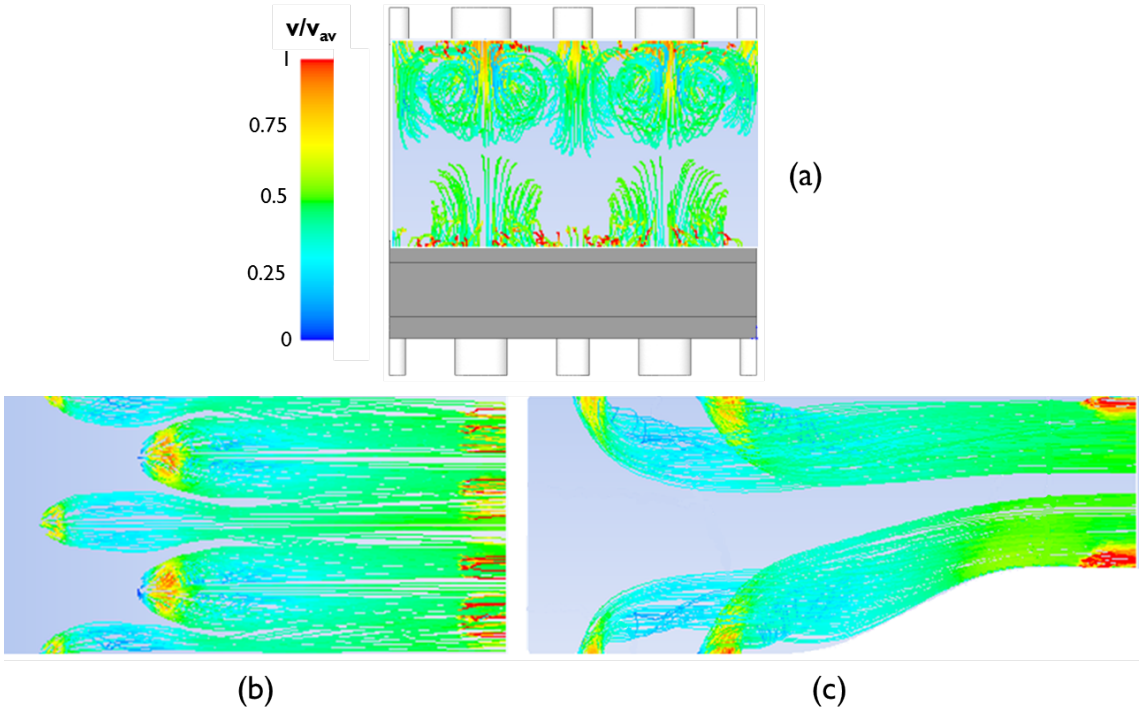


Figure 7.9: **CFD predictions of dilution jet streamlines colored with normalized velocity v/v_{max} (a) view from downstream, (b) view from the outer wall, (c) view from the side wall**

in Figure 7.9 show the jet development in the computational domain: the dilution jet dissipation increases close to the bottom wall due to the acceleration caused by the slope.

Figure 7.10 shows the flow velocity non-dimensionalized with the plane area-averaged velocity on the NGV inlet plane (plane E in figure 7.5) predicted by CFD and measured experimentally in the CTI rig. The flow is mostly uniform away from walls with velocity variations within 3% due to the blockage caused by the big dilution jets from the top wall (Fig. 7.9). The high velocity flow close to the inner and outer walls has been injected through the RIDN and RODN. The sidewall effects (at r=0 and r=2R) is very small. The level of agreement between CFD and measurements is very high, even if the realizable k-ε model seems to underestimate the jet diffusion near the walls.

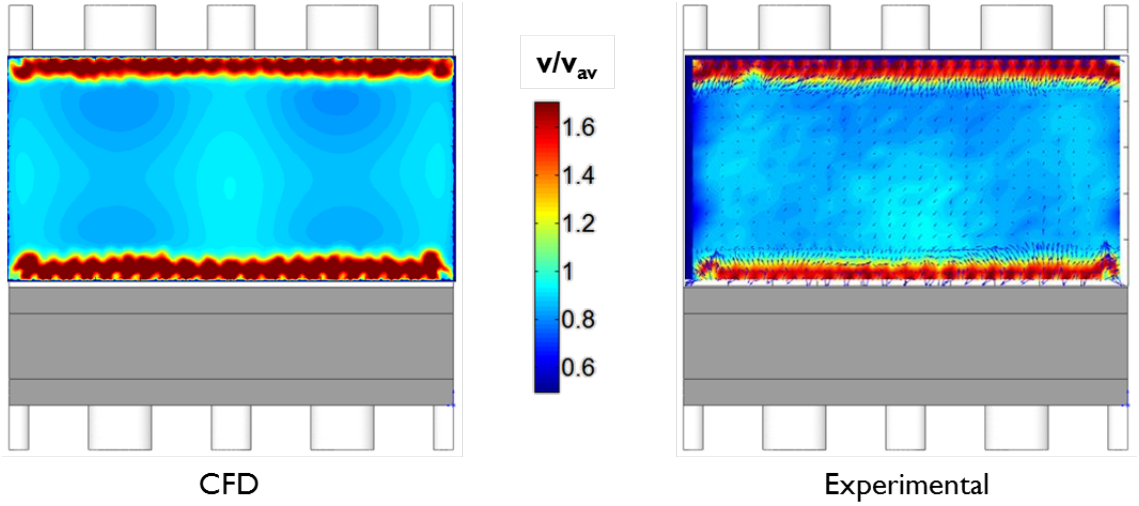


Figure 7.10: **CFD predictions (left) and experimental measurements (right) of normalized velocity** v/v_{av}

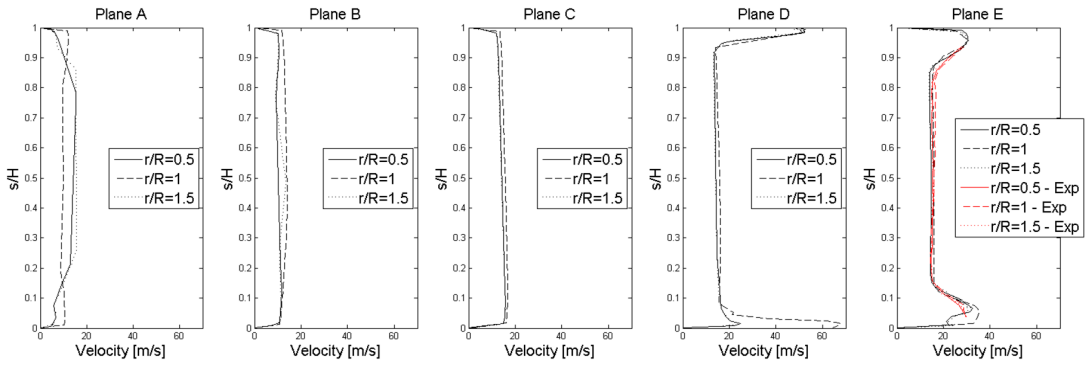


Figure 7.11: **CFD predictions and experimental measurements of velocity profiles at r/R=0.5 - 1 - 1.5**

Figure 7.11 shows the velocity profiles across the system as predicted by CFD: from these profiles, the boundary layer development along the simulator can be observed. The velocity peaks due to the dilution jets evident at plane A fade away as the flow accelerates which means the flow becomes much more uniform across the whole span in plane B. In plane C the flow near the bottom wall is faster because of the asymmetric contraction. The cooling injection results in a momentum surplus near the endwalls (planes D and E). The mainstream velocity does not change from

plane C to plane E as there is no change in cross-sectional area. The differences along the radial direction are relevant at plane A but decrease moving downstream: the differences between the velocity profile at off-centerline planes (r/R=0.5 and r/R=1.5) and the centerline plane (r/R=1) are below 2% in the bulk flow for both numerical and experimental data. The agreement between CFD and experiments is very good, with velocity discrepancies below 1%.

Time spectral analysis

High frequency velocity measurements were acquired with a single hot wire (Section 5.1.2) at the locations shown in Figure 7.12 and defined in Table 7.2. The hot-wire calibration was performed in situ using the Pitot tube located at the position marked with a green X in Figure 7.5. For the work presented in this section the number of acquired samples was 1 million per data point. The cut-off frequency of the CTA low-pass frequency filter was set at 10kHz (so that for a flow velocity of 30 m/s this enables information for wavelengths as small as 3 mm to be resolved). The ensemble-averaging of 50 blocks of 1 million samples were used to ensure a statistically independent data set of the sample number.

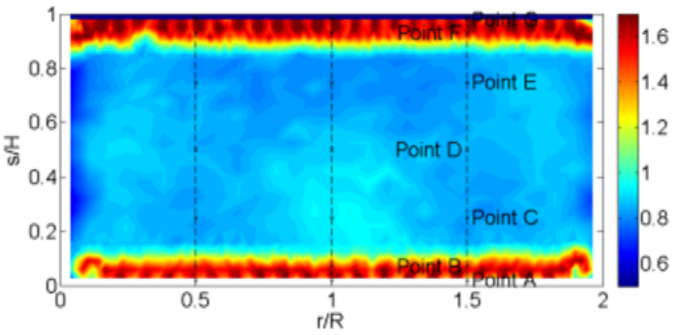


Figure 7.12: **Hot-wire measurement locations (experimental measurements of normalized velocity v/v_{av})**

Following Eq.5.10, R_{uu} was calculated as

Point	s/H	r/R
A	0.02	0.5 - 1 -1.5
B	0.07	0.5 - 1 -1.5
C	0.25	0.5 - 1 -1.5
D	0.5	0.5 - 1 -1.5
E	0.75	0.5 - 1 -1.5
F	0.93	0.5 - 1 -1.5
G	0.98	0.5 - 1 -1.5

Table 7.2: **Hot-wire measurement locations**

$$R_{uu}(\tau) = \frac{\overline{u_i'(t)u_i'(t+\tau)}}{u_i'^2} \tag{7.1}$$

In Figure 7.13 R_{uu} at points A, B and C is plotted. Because the trends are very similar, R_{uu} at the other locations is not shown. As expected, the coherence of the flow structures lasts longer in the mainflow (point C) than close to the wall and downstream of the coolant injection (points A and B).

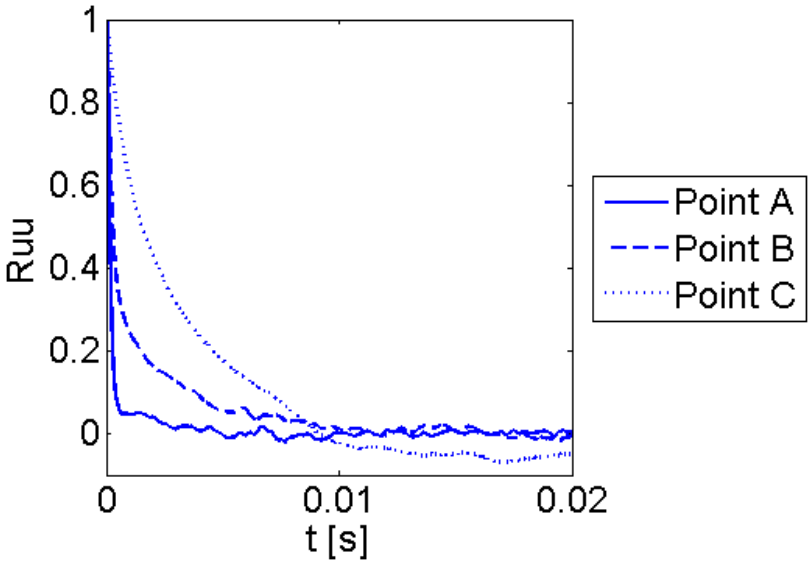


Figure 7.13: **Autocorrelation function** R_{uu}

From R_{uu} it is possible to calculate the integral length scales of the turbulent flow, as defined in Eq.5.12. The Λ distribution (Fig. 7.14) is symmetrical in the spanwise direction and shows large coherent structures in the bulk flow and smaller structures near the endwalls. The larger eddies are generated by the dilution jets, while the near-wall small-scale ones are created by the RIDN and RODN. The length scale values vary in the spanwise direction but the trend is constant. An approximate estimate of the integral length scales is calculated using an equation suggested by Sikes et al.[62] for a round, turbulent jet injected normal to a uniform stream:

$$\Lambda = 0.25D + 0.025r' \tag{7.2}$$

where r' is the distance measured from the dilution port with diameter D. This equation was used to predict the levels in Fig. 7.14 in the bulk flow: the range boundaries correspond to $\Lambda(D = 44.5mm)$ and $\Lambda(D = 80mm)$, respectively the smallest and the biggest dilution port diameter (Table 4.1).

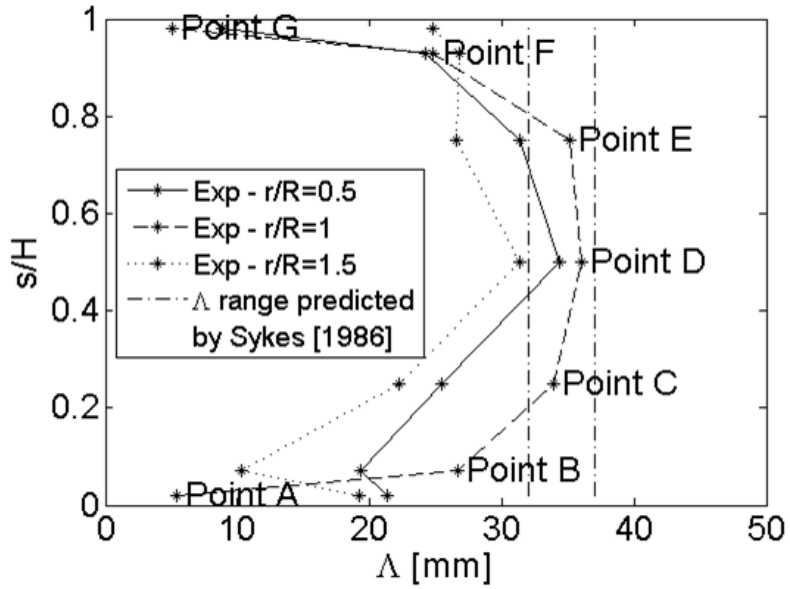


Figure 7.14: **Integral length scale** Λ

The integral length scale-to-diameter ratio at points A and C is reported in Table 7.3. These results are in accordance with the values reported by Barringer et al. [3]

and they show, once more, that the turbulence length scale is a strong function of the hole size that has generated the jet.

(r/R=1)	Λ [mm]
A	$\approx 0.65 D_{RDN}$
C	$\approx 0.8 D_{dil}$

Table 7.3: **Integral length scales Λ at Points A and C**

As previously mentioned for R_{uu}, the PSD is plotted only for points A, B and C to avoid data redundancy (Figure 7.15). The flow close to the walls (points A and B) is strongly energized by the film injection and has significant kinetic energy at high wavenumber $k = \frac{2\pi f}{\overline{u}}$ (corresponding to small wavelength) compared to the mainstream flow. The PSDs calculated by the author are compared to the Kolmogorov's power law (Section 5.1.2): a good correspondence is evident over a wide wavenumber range inside the bulk flow where the PSD plots are tangential to the straight lines with slope -5/3. The inertial subrange is narrower downstream of the film jets: this is because in this region the endwall coolant is still in the mixing process and the turbulence has not settled down. At higher k the slope of the curve changes and the energy contained in the eddies quickly dissipates at a rate depending on both ε and ν.

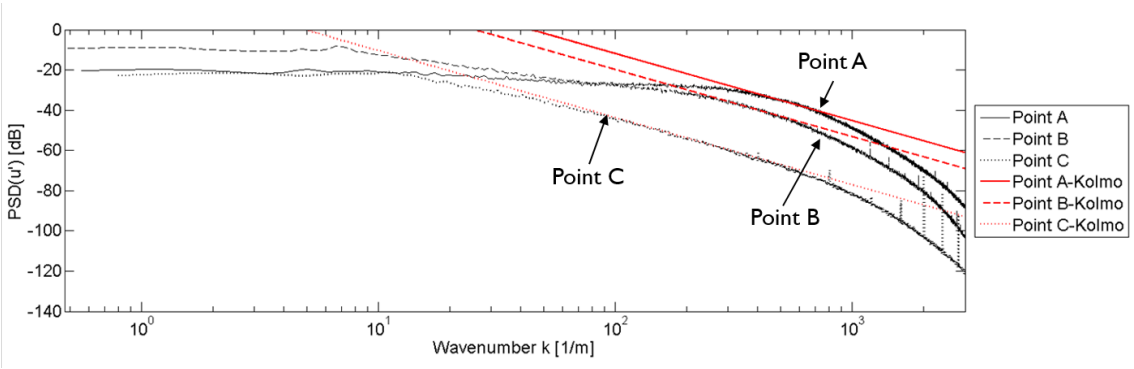


Figure 7.15: **Power density spectrum PSD(k) with Kolmogorov's -5/3 power law slope**

Figure 7.16 shows the PSD plotted versus the eddy wavelength

$$\lambda = \frac{2\pi}{k} \tag{7.3}$$

On the same plot, lines of constant Λ are reported as measured at locations A, B and C. According to Kolmogorov's theory these values are an estimate of the length scale of the larger eddies: indeed at both points C and B, Λ coincides with the upper limit of the inertial subrange. On the other hand, Λ_A is well below the intersection between the spectrum and the -5/3 power law curve: that is again because the turbulence in this region has not full developed.

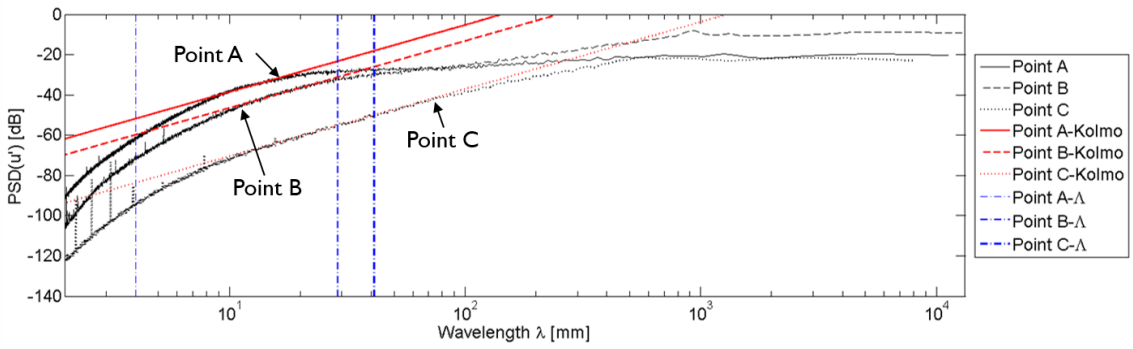


Figure 7.16: **Power density spectrum PSD(λ) with Kolmogorov's -5/3 slope and Λ**

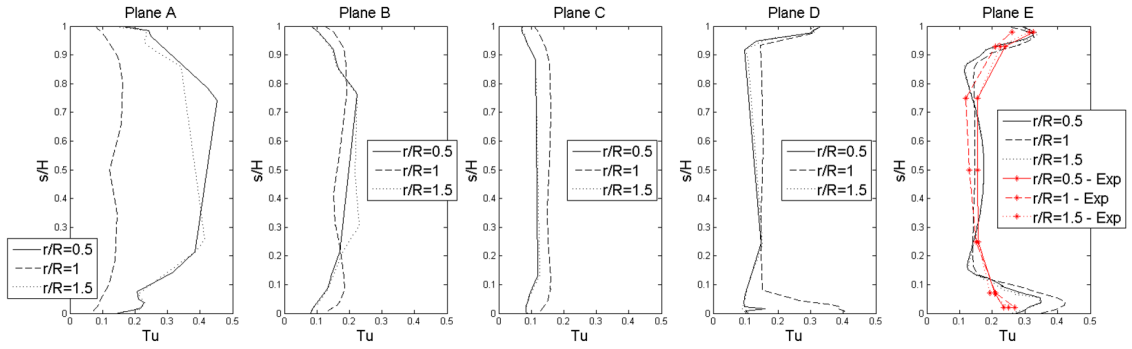


Figure 7.17: **CFD predictions and experimental measurements of turbulence intensity profiles at r/R=0.5 - 1 - 1.5**

The profile development of turbulence intensity (Eq.5.13) along the measurement planes is shown in Figure 7.17. At plane A the dilution jets strongly affect the profile, but their influence decreases moving in the streamwise direction as the flow accelerates (plane B), becoming progressively more uniform at plane C. Also the radial uniformity increases moving downstream: the maximum difference at plane E between the profiles at the planes at r/R=0.5 - 1 -1.5 is around 3% in the bulk flow for both CFD and experimental data. The endwall cooling injection causes an increase in turbulence levels near the walls: this enhancement is overestimated by the realizable k-ε model compared to the experimental data and this problem is discussed in detail in Chapter 8. Good agreement is reached in the bulk flow with differences within 3%.

7.2.2 Temperature field

This section reports the measurements obtained using the fine thermocouple, whose calibration is presented and discussed in Chapter 6. The mainflow reference temperature T_∞ was measured just downstream of the heater mesh, in the location indicated in blue in Figure 7.5.

Time-averaged field

The dimensionless temperature field at the NGV inlet plane is shown in Figure 7.18. The post-processing of the measured data took into account the change of temperature in the lab during the data acquisition. The temperature in the bulk flow is more uniform than the velocity field and always lower than the combustor inlet temperature (i.e. T_∞): the dilution jet footprint is no longer distinguishable. The top and bottom walls are cooler due to the RIDN and RODN injections. The numerical predictions shows features that are not evident in the experimental results, but the agreement between CFD predictions and experiments on the temperature levels is generally good.

The RTDF profile was calculated according to the definition given by Eq.4.3

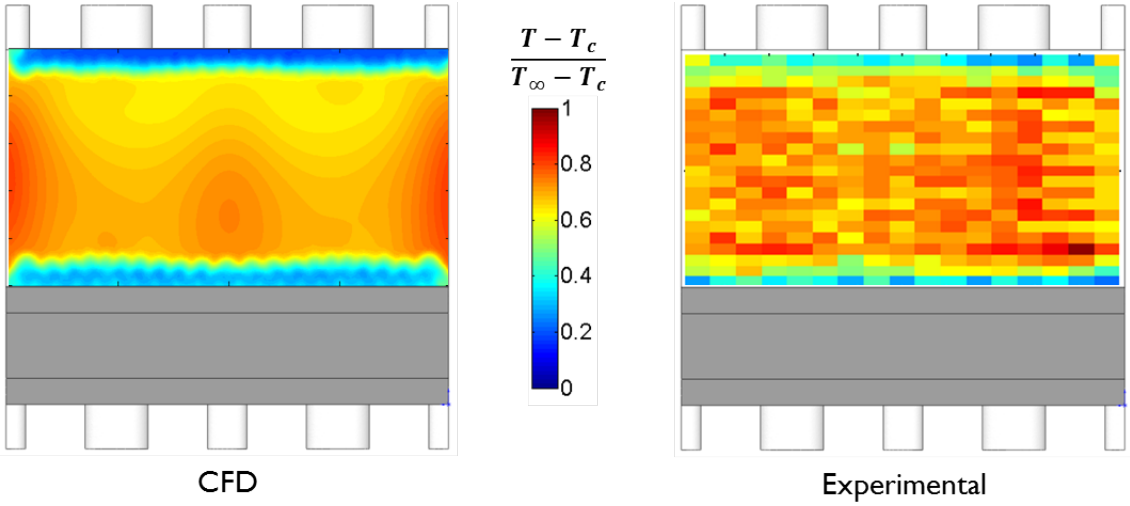


Figure 7.18: **CFD predictions (left) and experimental measurements (right) of normalized temperature** $\frac{T-T_{cin}}{T_{\infty in}-T_{cin}}$

from experimental and numerical data and the results are shown in Figure 7.19. The temperature distribution is far from uniform in the radial direction and the coolant effect at the endwall is very evident. The agreement between CFD and experiments is good, with differences in dimensionless temperature difference lower than 20%.

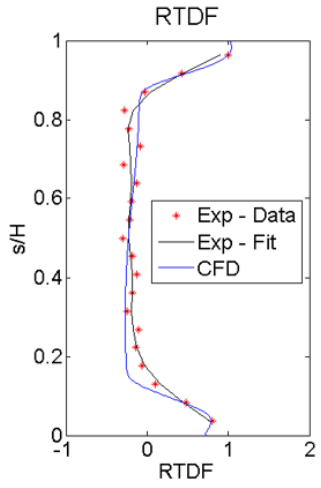


Figure 7.19: **CFD predictions and experimental measurements of RTDF at plane E**

Further measurements were taken close to the wall downstream of the coolant injection. The hole system of reference is shown in Figure 7.20. The temperature was normalized using the coolant temperature T_c and T_∞ measured downstream of the heater mesh at the combustor inlet (Figure 7.21). The distance from the wall was non-dimensionalized with the hole diameter D and the lateral distance with the pitch $P = 2D$. The lateral distribution of the coolant is very uniform and there are no traces of the individual jets. The coolant film is very compact and the temperature value is almost constant up to 2D away from the wall.

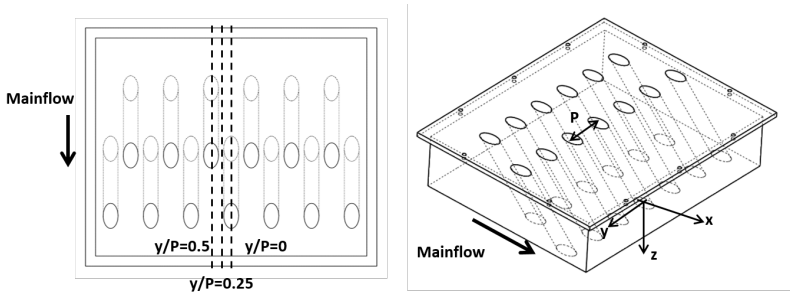


Figure 7.20: **RODN: coordinate system and details**

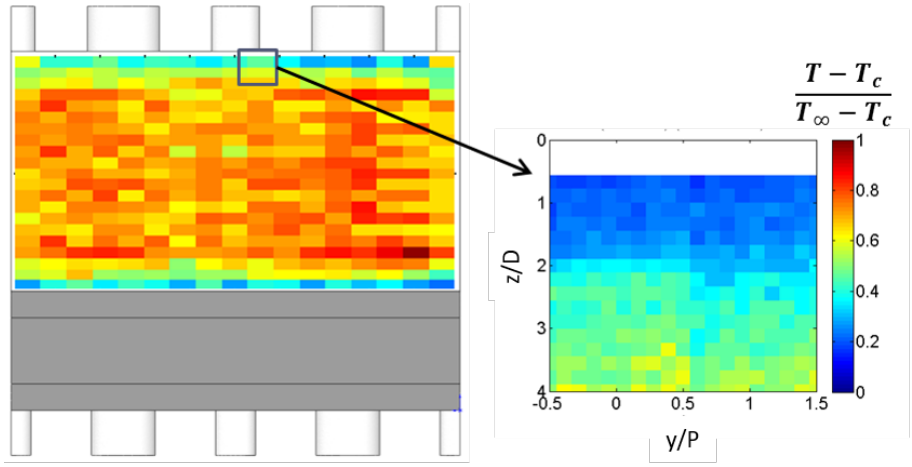


Figure 7.21: **Experimental measurements of normalized temperature $\frac{T-T_c}{T_\infty-T_c}$ downstream of the endwall coolant injection**

In order to compare these results to CFD the temperature difference coefficient values were laterally averaged and plotted against z/D (Figure 7.22). Note that the

difference between the temperature T and the coolant temperature T_c is normalised by the value at $z/D = 10$. The agreement is very good with differences below 10%: the dimensionless temperature difference continuously increases up to 4D from the wall and then reaches the mainstream value.

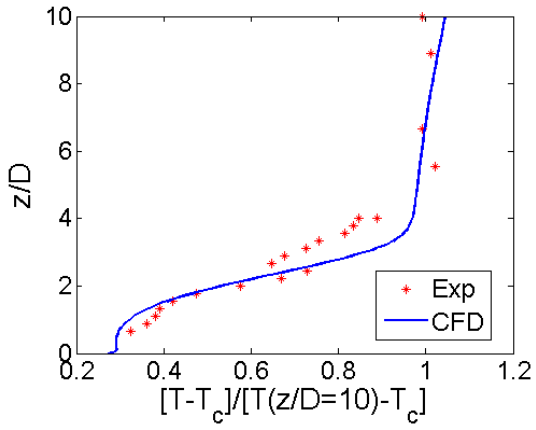


Figure 7.22: **CFD predictions and experimental measurements of averaged laterally normalized temperature** $\frac{T-T_c}{T(z/D=10)-T_c}$

Time spectral analysis

When the temperature variation is small enough to not affect the flow dynamics, flow temperature is commonly mathematically modeled as a passive scalar simply transported by turbulent mixing and diffused by molecular effect [36]. The turbulent energy linear-cascade assumption assumes that the rate at which the scalar cascade proceeds is governed by the local velocity gradients. Obukhov [48] and Corrsin [11] have independently proposed the existence of an inertial-convective range where the velocity is inertial (i.e. motion is determined by inertial effects and the viscosity influence is negligible) and the scalar is convective (i.e. it is simply transported by the velocity field) and the temperature spectrum correlates with $k^{-5/3}$, where k is the wavenumber. But Lesieur and Rogallo [37] showed that the temperature cascades toward small scales faster than the kinetic energy with a slope following k^{-1} at low wavenumbers and discovered an anomalous logarithmic rise of the eddy

conductivity in the same k range. Lesieur [36] states that this anomalous behaviour of the passive scalar spectrum might be due to the direct shearing of the velocity fluctuations by the large-scale velocity gradients.

The characteristics of the thermocouple time constant reported in Chapter 6 enabled the author to quantify the fluctuations in the combustor simulator. The temperature fluctuation spectrum is initially evaluated at points A, B, C (Table 7.2) to allow a direct comparison to the velocity fluctuation spectra previously reported. That measurements had proved that the turbulent kinetic energy is fed at scales that are comparable to geometric features.

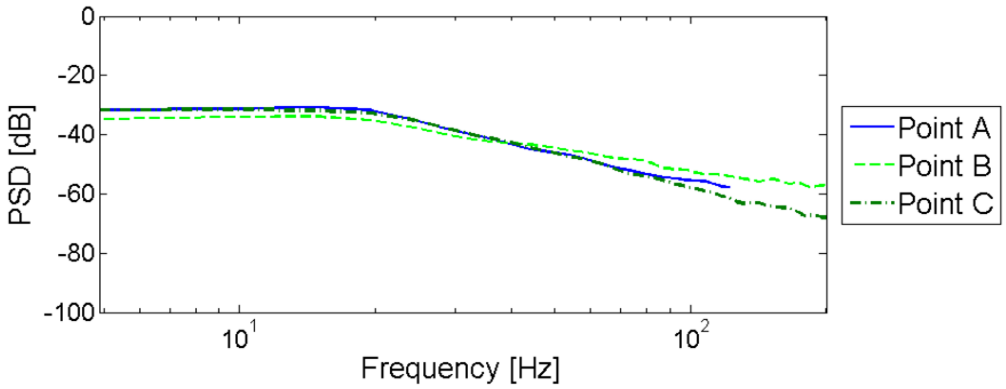


Figure 7.23: **Temperature power spectrum - PSD(f)**

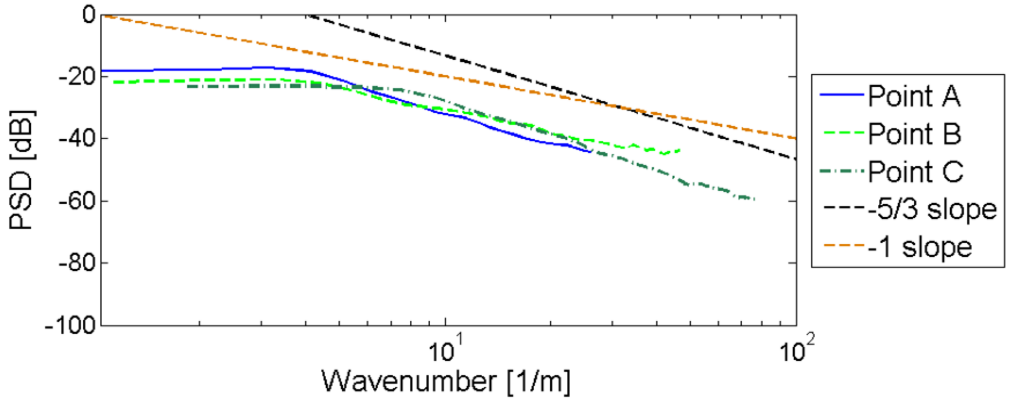


Figure 7.24: **Temperature power spectrum - PSD(k)**

The measured temperature power density spectra are plotted in Figure 7.23 as

a function of frequency. The spectra are normalized such that $\int_0^\infty PSD(f)df = 1$, following Lockwood's work [40]. For all three points the spectrum is flat up to 20 Hz and then starts decreasing. The spectra are truncated at 200 Hz, i.e. at a timescale of 5 ms corresponding to the thermocouple time constant (Chapter 6). Figure 7.24 shows the PSD versus the wavenumber k: the spectra are compared with the $-5/3$ slope predicted by Obukhov [48] and Corrsin [11] for the inertial-convective range and the -1 slope forecasted by Lesieur and Rogallo [37]: all three spectra decrease with a slope between these two values. Note that, since $k = \frac{2\pi f}{\bar{u}}$, when plotting the spectrum against k the distribution at higher velocity values at locations A and B shifts towards lower wavenumbers relative to data from point C.

Figure 7.25 shows the spectra plotted against the wavelength λ: the significant rig geometrical dimensions (combustor depth H, maximum and minimum dilution port diameters and RIDN and RODN diameter) are included as well to help understand the geometric features. The finite thermocouple bandwidth does not allow any measurement below a scale of 10^2 mm. This graph shows how the spectrum decay starts at very large wavelengths ($\approx 4H$) and does not show correlation to any geometrical dimension.

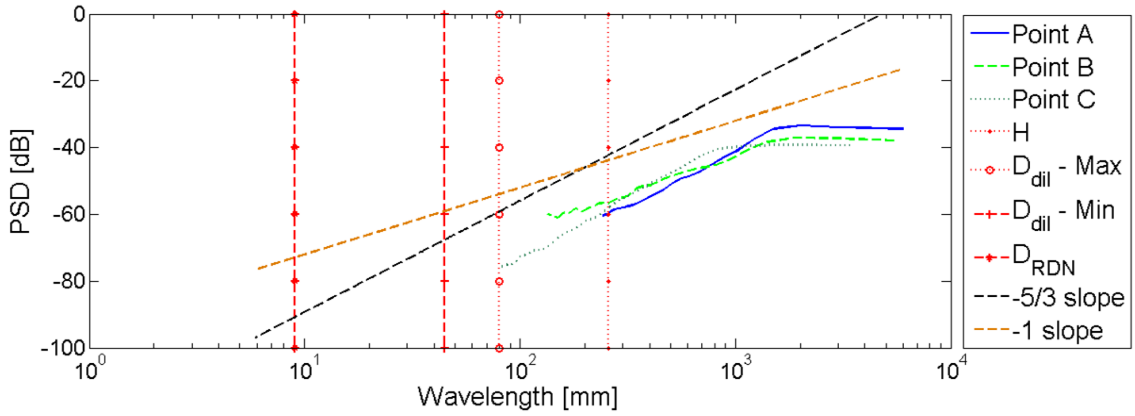


Figure 7.25: **Temperature power spectrum - PSD(λ)**

In order to show the repeatability of the present data, more measurements were performed moving the thermocouple in the vicinity of point A to the coordinates

listed in Table 7.4. The resulting spectra are visible in Figure 7.26 and they demonstrate the low sensitivity of the measurements to the exact location of the probe.

Point	s/H	r/R
A	0.02	1
A1	0.02 + D	1
A2	0.02	1 + D
A3	0.02	1 + 2D

Table 7.4: **Fine thermocouple: Sensitivity study**

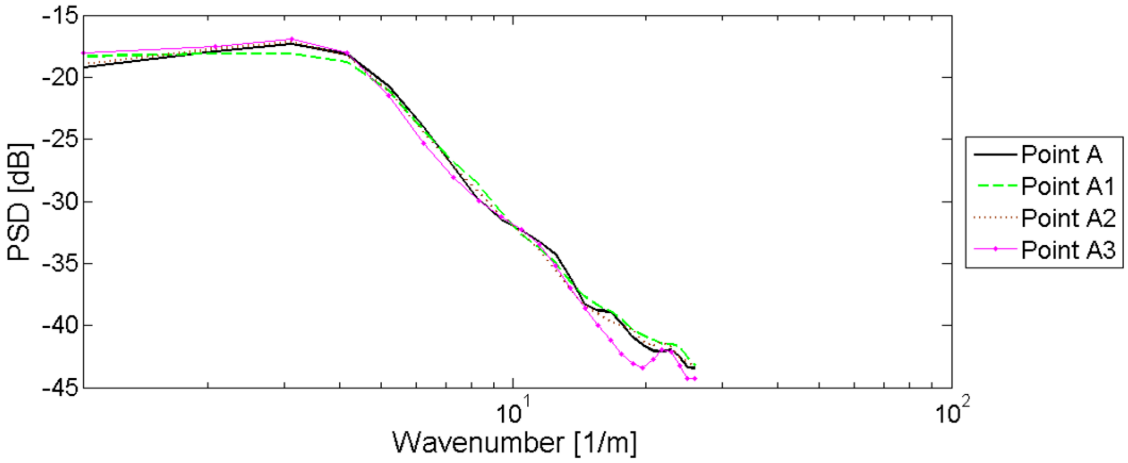


Figure 7.26: **Temperature power spectra at Point A: Study of sensitivity to position**

Figures 7.27, 7.28 and 7.29 compare the velocity and temperature spectra at Points A, B and C.

The temperature spectra were again plotted against the wavelength λ with the previously reported velocity spectra in Figure 7.30: the comparison confirms how the velocity spectra are strictly linked to the facility dimensions, but this is not the case for the thermal fluctuation field.

Further temperature measurements were taken along r/R=1 to evaluate the variation of the temperature fluctuation spectrum in the spanwise direction. Figure 7.31

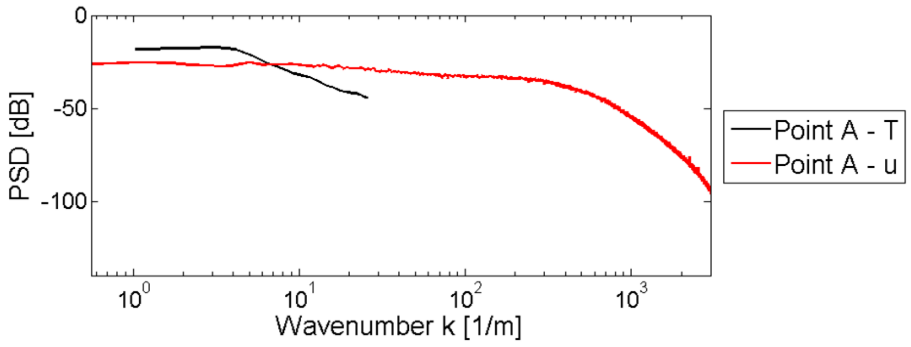


Figure 7.27: **Temperature and streamwise velocity power spectra - Point A**

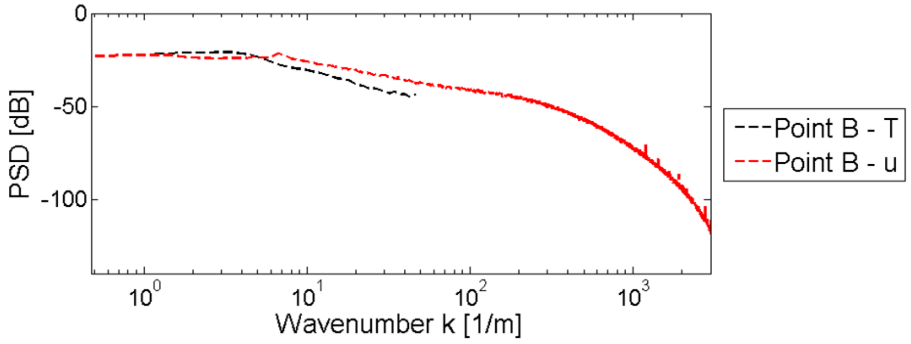


Figure 7.28: **Temperature and streamwise velocity power spectra - Point B**

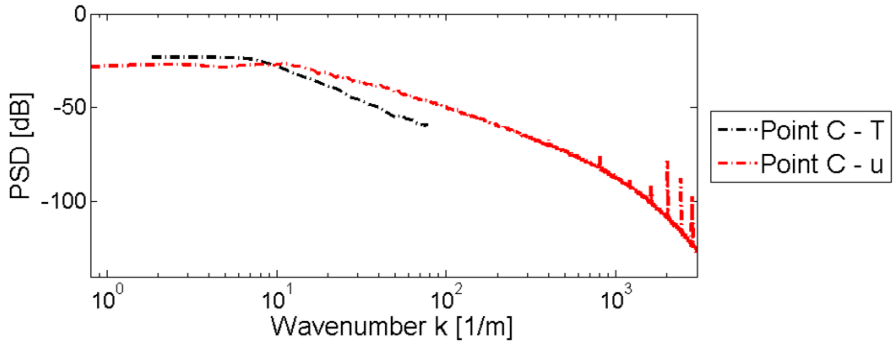


Figure 7.29: **Temperature and streamwise velocity power spectra - Point C**

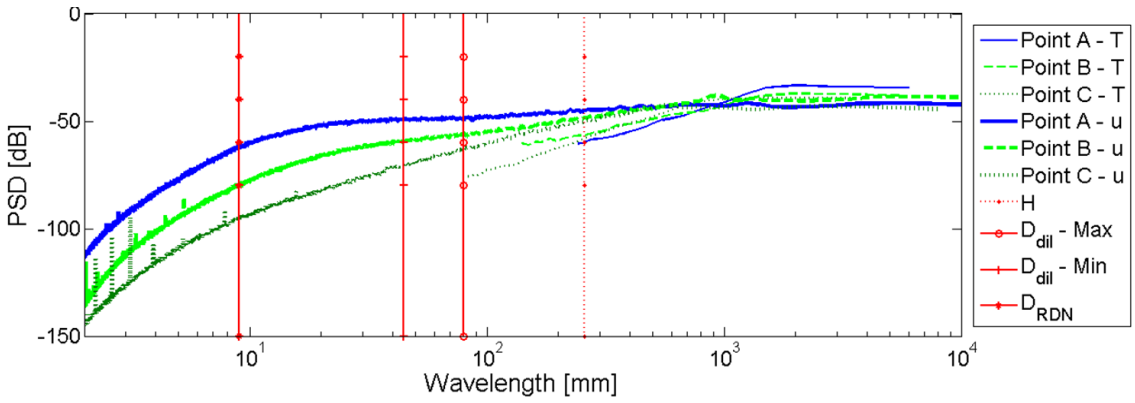


Figure 7.30: **Temperature and streamwise velocity power spectra - PSD(λ)**

shows that the spectrum distribution versus frequency is almost unchanged for all the considered locations and in particular the turbulent thermal energy content starts decreasing at around 20 Hz and independently of the measurement position. The wavenumber distribution changes because of the velocity profile and the wavelength value at which the spectrum starts decaying, λ_1, is plotted in Figure 7.32: it is noticeable once more that λ_1 is much larger than any geometric dimension inside the experimental apparatus.

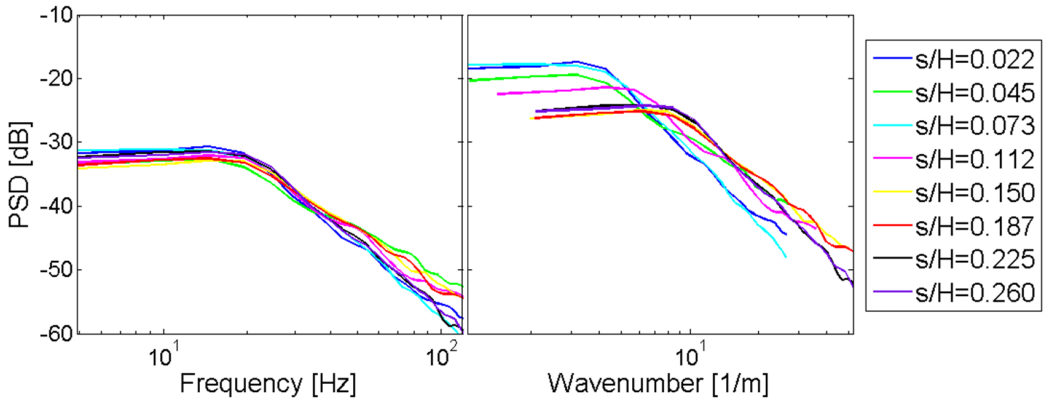


Figure 7.31: **Temperature power spectrum at different locations along r/R=1**

Schlichting [59] states that the mechanisms for the transfer of momentum and heat are not identical: the reported experimental measurements in free turbulent

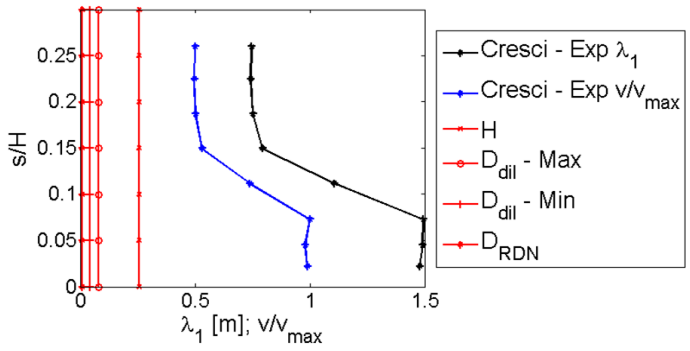


Figure 7.32: λ_1 **and** v/v_{max} **at different locations along r/R=1**

flows prove that the temperature profile is wider than the velocity profile because of the temperature higher diffusion rate. That means that in a jet the temperature profile becomes flatter earlier than the velocity profile so that it mixes earlier with the mainstream. This could explain why in Figure 7.21 there is no trace of the individual jets, while the velocity field in Figure 7.10 shows the footprint of each endwall jet. If the turbulent Prandtl number is less than 1 (the work from Lesieur and Rogallo [37] reports a turbulent Prandtl number varying between 0.2 and 0.8 in the frequency spectrum) that could explain the temperature spectrum behaviour reported in this chapter.

Certainly the reason for this spectrum behaviour requires further investigations to fully understand the fundamental mechanism governing this phenomenon.

7.3 Summary

- The work reported in this chapter shows the strong influence of the near-wall jets and a lower, but still significant, effect of the dilution jets on velocity, turbulence and temperature distribution downstream of a rich-burn combustor, in accordance with prior research work reported in literature.

- The kinetic PSD plots exhibit good agreement with Kolmogorov's theory and the inertial subrange is evident.

- The integral length scales obtained from the velocity field show that the turbulent kinetic energy is fed at scales corresponding to geometric features. This means that the turbulence nature differs depending on the plane location, causing different turbulence intensity levels and showing an important connection between the turbulence and the jet injection that has generated it.

- In the present temperature measurements the thermal energy cascade begins at scales larger than the CTI rig geometrical features. This lack of connection between geometric features and the scale of temperature fluctuations was unexpected but has been observed before by Lesieur and Rogallo [37]. This could be a symptom of a straining mechanism dominating the temperature spectrum at low wavenumbers and evidence of a non-unity turbulent Prandtl number.

Chapter 8

Rear Outer Discharge Nozzle (RODN)

In this chapter different configurations of a double row of staggered film cooling cylindrical holes at the endwall downstream of the engine representative combustor simulator are experimentally and numerically analysed. The endwall coolant develops long reach films by using coolant-to-mainstream momentum flux ratios in excess of 6 and arranged in a staggered double row configuration. High pressure margin intersecting holes, previously developed by Fletcher [18] and Nowlin [47] for the leading edge of turbine airfoils, were also studied for the first time for this specific application. The goal of the present work is to provide velocity and turbulence measurements downstream of different endwall film cooling hole arrangements at engine representative geometrical and flow field conditions [65]. These data were compared with RANS calculations run at the same rig conditions and passive film effectiveness by prediction.

The work reported in this chapter was published in the proceedings of the ASME Turbo Expo, held in Montreal in June 2015 [14].

P/D	Θ	J	x/P	y/P	z/P
2	-	6	[4.2, 9.2, 14.2]	[-0.5, -0.25, 0 0.25, 0,.5]	[0.7, 1.1, 1.5, 1.9]
3	-	6	[4.2, 9.2, 14.2]	[-0.5, -0.25, 0, 0.25, 0,.5]	[0.7, 1.1, 1.5, 1.9]
6	-	6	[4.2, 9.2, 14.2]	[-0.5, -0.25, 0, 0.25, 0,.5]	[0.7, 1.1, 1.5, 1.9]
6.3	90^o	6	[4.2, 9.2, 14.2]	[0, 0.25, 0.75]	[0.7, 1.7, 2.7, 3.7, 4.7]

Table 8.1: **RODN: Cases experimentally tested**

8.1 Test section

The experimental tests were run with three cylindrical hole configurations at different pitch-to-diameter ratios (Figure 8.1) and one intersecting hole geometry (Figure 8.2): the cases tested are reported in Table 8.1. The jet-to-mainstream momentum flux ratio J was kept constant in the different tests. Measurements were taken at three different locations x/D downstream of the injection point at different y/P positions: y/P = 0 corresponds to the centre of the hole in the second row, y/P = -0.25 and 0.25 are between two adjacent holes of the first and second row, y/P = -0.5 and 0.5 are the centres of the holes in the first row. For the intersecting hole arrangement y/P = 0.75 is downstream of the first row hole.

Because of the geometrical symmetry of the system, the measurements at y/P=-0.25 and -0.5 are not reported in this chapter but are shown in Appendix D.

8.2 CFD simulations

The computational model described in Section 7.1 was modified to run the simulations reported in Table 8.2: the jet-to-mainstream momentum flux ratio J was kept constant for all the simulations, in agreement with the experimental tests. The numerical results were used to support the physical understanding of the jet

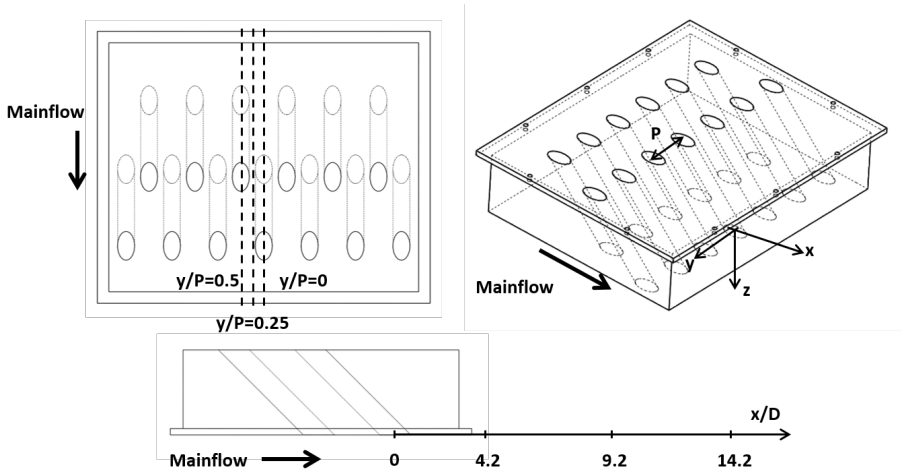


Figure 8.1: **Cylindrical holes: Frame of reference and geometric details**

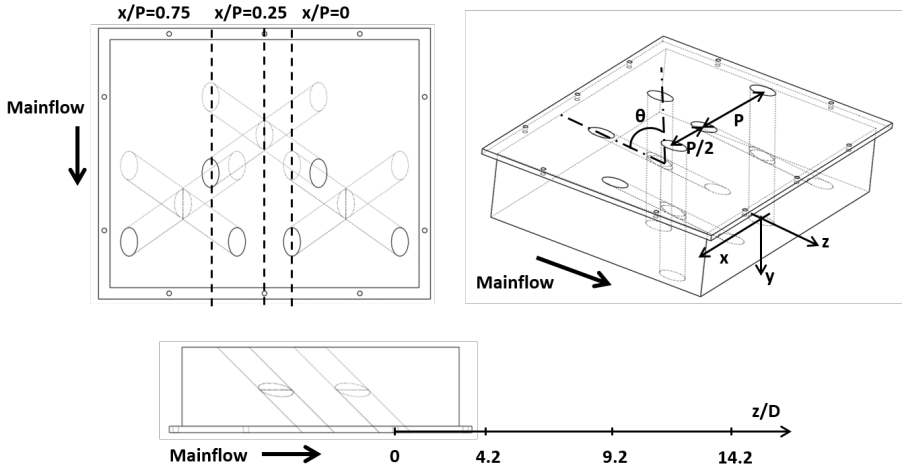


Figure 8.2: **Intersecting holes: Frame of reference and geometric details**

behaviour.

8.2.1 Passive-scalar tracking method

The adiabatic cooling effectiveness can be defined as follows [65]:

$$\eta_{eff} = \frac{T_{0,\infty} - T_{aw}}{T_{0,\infty} - T_{0,c}} \tag{8.1}$$

and is commonly used to characterize the film performance. η_{eff} is typically equal

P/D	Θ	J
2	-	6
3	-	6
6	-	6
6.3	90^o	6
2.6	45^o	6
1.7	30^o	6

Table 8.2: **RODN: Numerically simulated cases**

to 1 at the exit of the hole, where $T_{aw} = T_{0,c}$ and then decreases progressively downstream due to turbulent dispersion of the coolant jet.

Cooling effectiveness can be numerically estimated by means of the passive-scalar tracking method described by Thomas [65]. The method involves evaluating the concentration of a passive scalar released at the cooling hole inlet. Once the momentum and continuity equations are solved for the velocity field, it is possible to model the steady-state transport of a passive scalar by the advection equation [29]

$$\frac{\partial}{\partial x_i}\left(\rho U_i \Phi_k - \Gamma \frac{\partial \Phi_k}{\partial x_i}\right) = S_{\Phi_k} \tag{8.2}$$

where Γ is the diffusion coefficient and S_{Phi_k} is the source term supplied for each of the N scalar equations. In this case $S_{Phi_k} = 0$ and Γ can be calculated from the effective thermal conductivity k_{eff}

$$\Gamma = \frac{1}{\rho c_p} k_{eff} = \frac{1}{\rho c_p}\left[k + \left(\frac{c_p \mu_T}{Pr_T}\right)\right] \tag{8.3}$$

where μ_T is the turbulent viscosity and Pr_T is the turbulent Prandtl number (whose default value in Fluent is 0.85).

When setting $\Phi = 1$ as a boundary condition at the inlet cooling holes and $\Phi = 0$ at any other inlet (Fig.8.3), then it is possible to prove that

$$\eta_{eff} = \sum_{i=1}^{N} \Phi_k \tag{8.4}$$

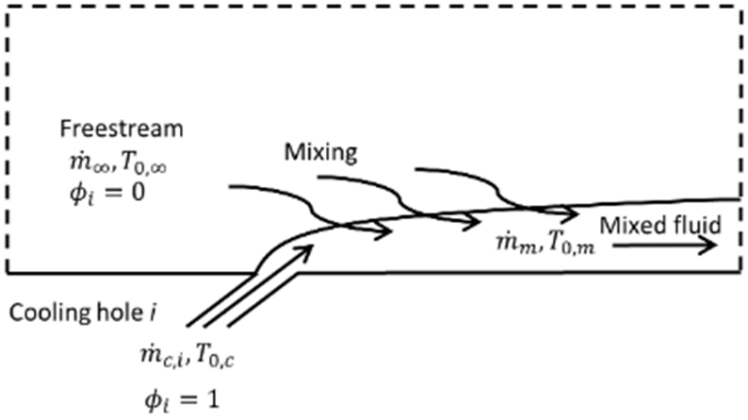


Figure 8.3: **Control volume for the passive-scalar tracking method [65]**

For more information on the method and its implementation in Fluent the reader is referred to Thomas's thesis [65].

8.3 Results: Cylindrical holes - Pitch effect

The flow just downstream of the injection point has a strong spanwise component w which decreases moving downstream (Fig. 8.4): for the P/D = 3 case w is around 10% of the streamwise component u at z/D = 4.2, lower than 2% at z/D = 9.2 and less than 1% at z/D = 14.2. With a single-wire probe the vertical velocity component is not measured, but at the measurement planes chosen, the flow is sufficiently uni-directional to allow us to consider this limitation acceptable: the use of a double-wire probe would be required for measurements closer to the injection point. The application of a single wire sensor is consistent with the work of Porter et al. [53].

The crossflow-to-mainstream momentum flux ratio J, i.e. the coolant velocity magnitude, is kept constant in the CTI rig to reproduce the engine conditions, where

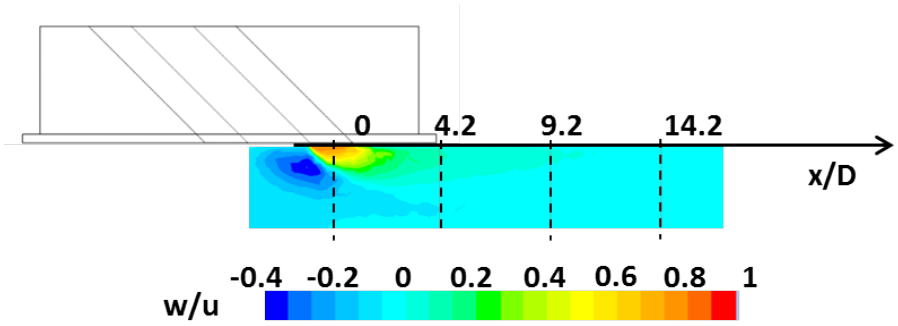


Figure 8.4: **Spanwise-to-streamwise velocity ratio w/u downstream of a jet (P/D=3 case - CFD)**

the pressure ratio across the holes is a boundary condition given by the engine cycle. This means that the coolant air flowing through the RODN changes for different total hole cross-sectional area values. The coolant mass flow rates $\dot{m}_c$ for the cases tested are reported in Table 8.3 as a percentage of the mainstream mass flow rate $\dot{m}_\infty$.

P/D	$\dot{m}_c/\dot{m}_\infty$	J
2	6%	6
3	4%	6
6	2%	6

Table 8.3: **Cylindrical holes: Coolant mass flow rate comparison**

8.3.1 Velocity field

CFD allows us to give a general overview of the jet trajectory development at different hole spacing (Fig. 8.5). It can be seen that, for the smaller hole spacing configurations, the jet velocity decrease rate in the streamwise direction is slower compared to cases with larger pitch where the jets are less protected from the main-flow and spread laterally. A better coverage can be expected for closer spacing as shown in the film cooling effectiveness data from Ligrani et al. [39]. Another

important aspect affecting the film performance [38] is that, for small hole pitch values, the jets stay attached to the wall, while for P/D = 6 the jet lift-off after the injection point is evident. This phenomenon is caused by the different boundary layer approaching the second row of holes that affects the incident crossflow velocity (Figure 8.6): for P/D = 6 the flow upstream of the second row is a fully developed turbulent layer and the cross-flow velocity relevant to the jet trajectory is that of the undisturbed bulk flow, while for P/D = 2 the upstream flow is strongly affected by the close injection of the first row and the maximum velocity at around z/D = 2 is 50% higher than the bulk flow velocity (25% in the case with P/D = 3). This suggests that, for the small pitch case the local coolant-to-mainflow momentum flux ratio for the second row is effectively lower than for the upstream row, and this keeps the jet closer to the wall and helps prevent the film from lifting off from the surface.

The velocity profiles downstream of the film injection are non-dimensionalized with the mainstream velocity and reported in Figure 8.7. Data obtained with the four-hole probe were available only for P/D = 2 at x/D = 4.2. All three cases show two gradients, one very steep near the wall and another one in the shear layer. Despite the fact that the blowing ratio is kept constant, the position of the latter moves further from wall when increasing the hole spacing, in agreement with the jet trajectories predicted by CFD. When P/D = 2 the measurements record a velocity increase up to z/D $\approx$ 1.5-2. In the case with P/D = 3 an increase of velocity is noticeable for z/D = 1.9. For P/D = 6 the velocity is very close to the mainstream value up to z/D $\approx$ 2. In all the cases the profiles become flatter moving downstream, even if for the closer-spaced configurations the film velocity is still higher than the mainstream flow. This long lasting near-wall momentum surplus is expected to dominate the flow field in presence of the vane secondary flows and ensure film coverage for the entire domain despite the vane pressure secondary flow (see Section 2.2.2), avoiding the lift-off issue reported by Zhang and Jaiswal [73]. The agreement with CFD is generally good for x/D $>$ 9, with differences between the 20%. A

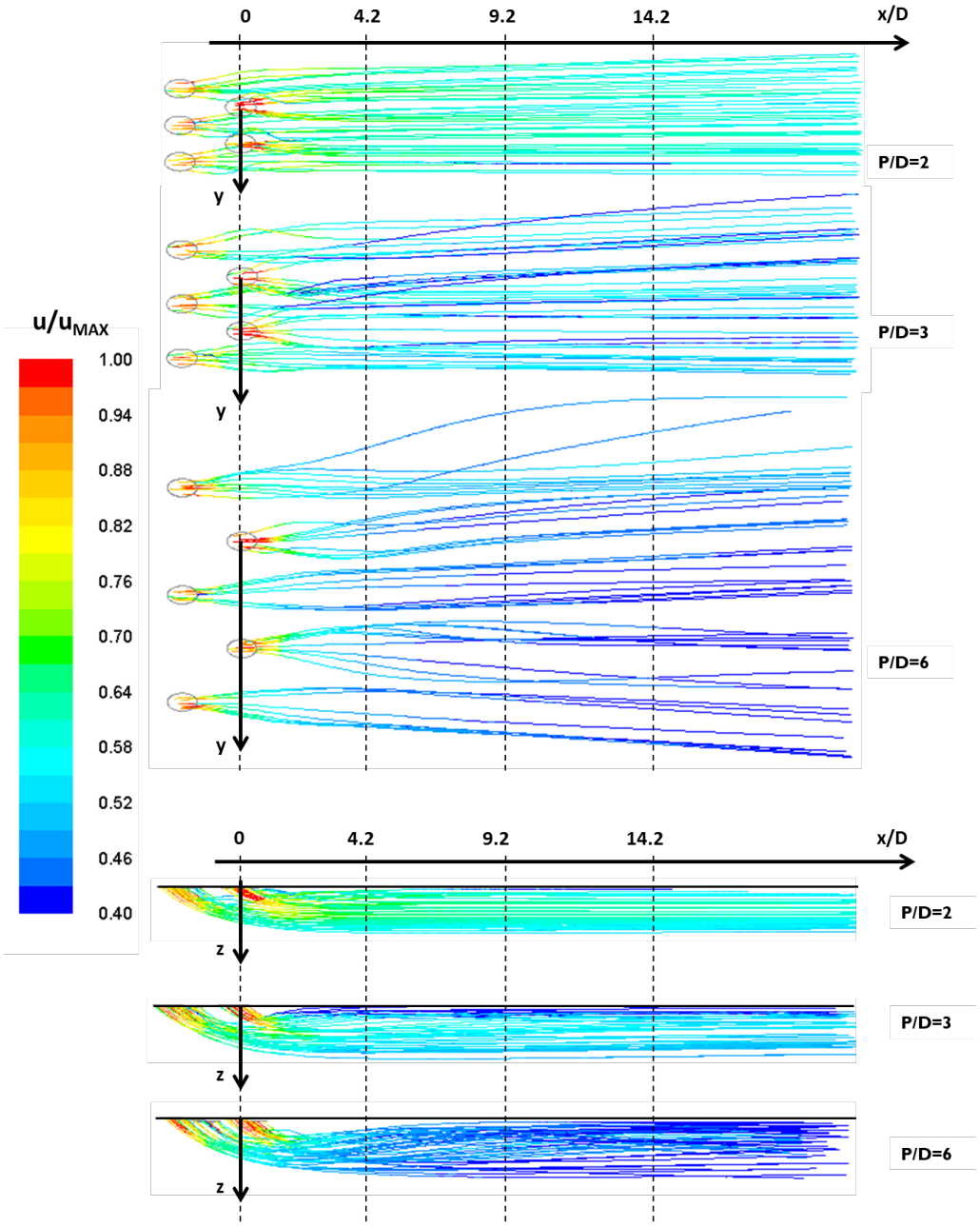


Figure 8.5: **Jet trajectory (CFD)**

stronger mismatch (up to 50%) is reported closer to the injection point: that could be due CFD limitations to predict the jet trajectories, but more measurements for z/D >2 would be required to prove that.

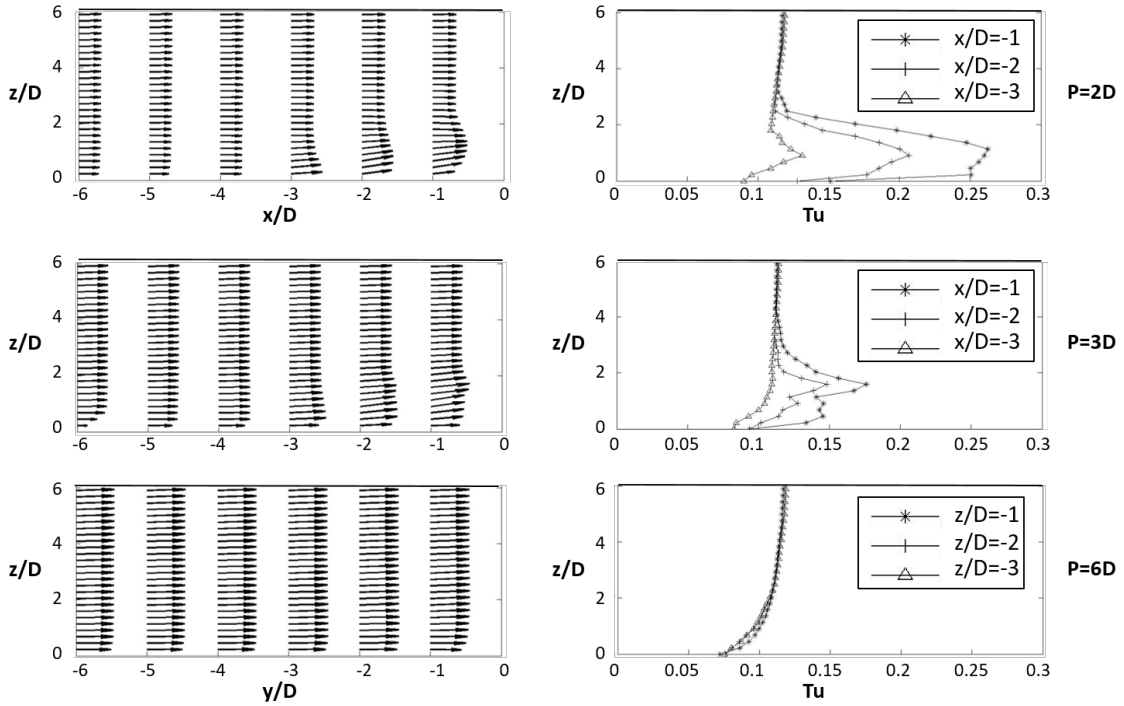


Figure 8.6: **Boundary layer approaching the second hole row (CFD)**

8.3.2 Time spectral analysis

The turbulence intensity and integral length scale development of the film is reported in Figure 8.8. Starting from the measurements at y/P = 0 and x/D = 4.2 it is quite evident that the turbulence peak moves further from the wall when the pitch increases: the peak moves with the maximum velocity gradient in agreement with Pietrzyk's [51] experimental data, obtained with the same pitch. The turbulence levels decrease moving downstream: in the closest-spaced case a higher turbulent energy dissipation causes a stronger decrease of turbulence levels at x/D = 9.2 and 14.2, while increasing the spacing the energy contained in the flow decreases more slowly. Considering the turbulence model intrinsic limitations, only a qualitative analysis of RANS predictions was possible. The location at x/D = 4.2 is where the three configurations differ the most with differences up to 100%: this is due in part to the more complex flow physics (film separation and reattachment) and in part to the fact that CFD considers the velocity fluctuations of every component, while the

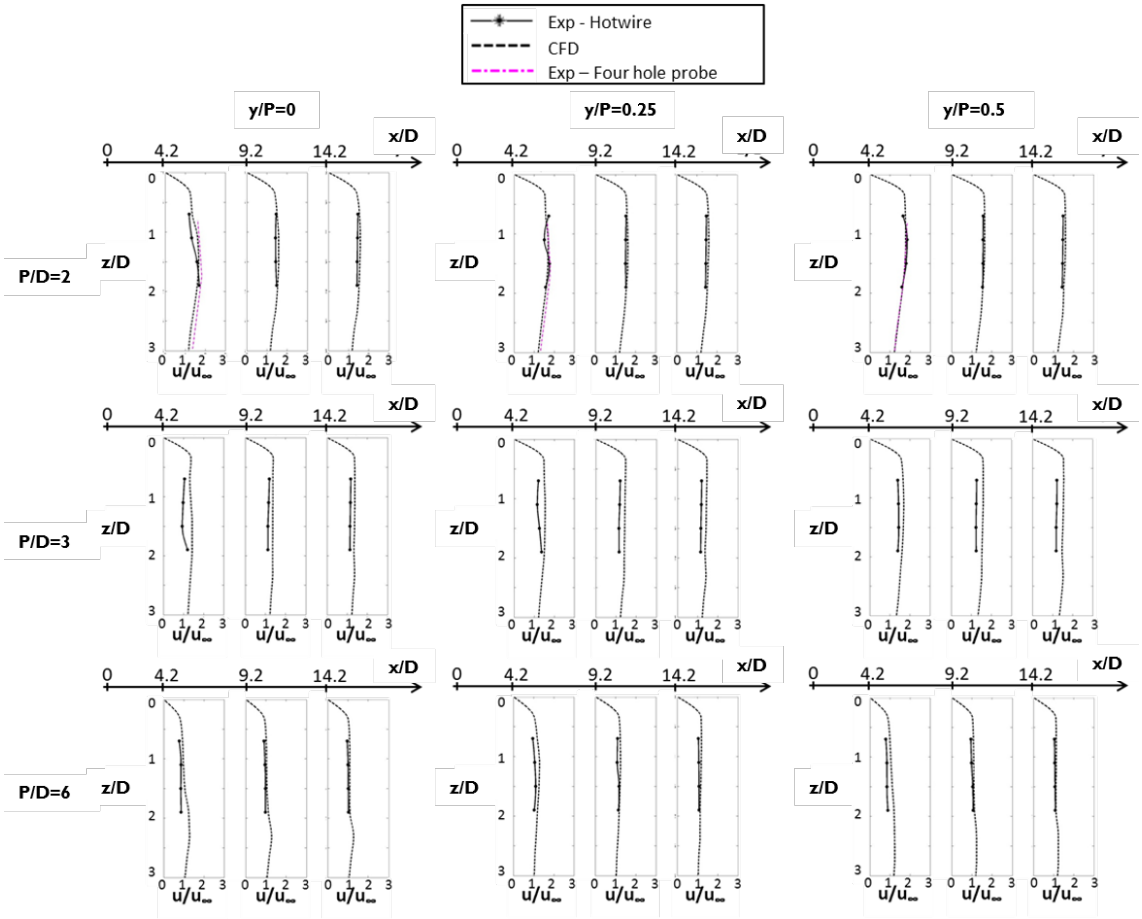


Figure 8.7: **Velocity non-dimensionalized with the mainstream value u_∞ at y/P=0 (downstream of a jet of the second row), y/P=0.25 (between jets) and y/P=0.5 (downstream of a jet of the first row)**

experiments predominantly measure velocity fluctuations normal to the single-wire sensor. Either measurements of all three flow components or LES would be required to get better agreement in this area. The agreement increases moving downstream, where the film is attached and the fluctuations in spanwise and lateral velocity components are damped. The case with P/D = 3 shows very good agreement between CFD and experiments, with differences less than 15% for x/D>9. For smaller spacing computational results tend to overpredict the turbulence levels of 30%, while for the larger-spaced geometry an underprediction of up to -80% is noticed. RANS is not able to reproduce the increase of turbulent energy dissipation

with the pitch decrease that is found in measurements.

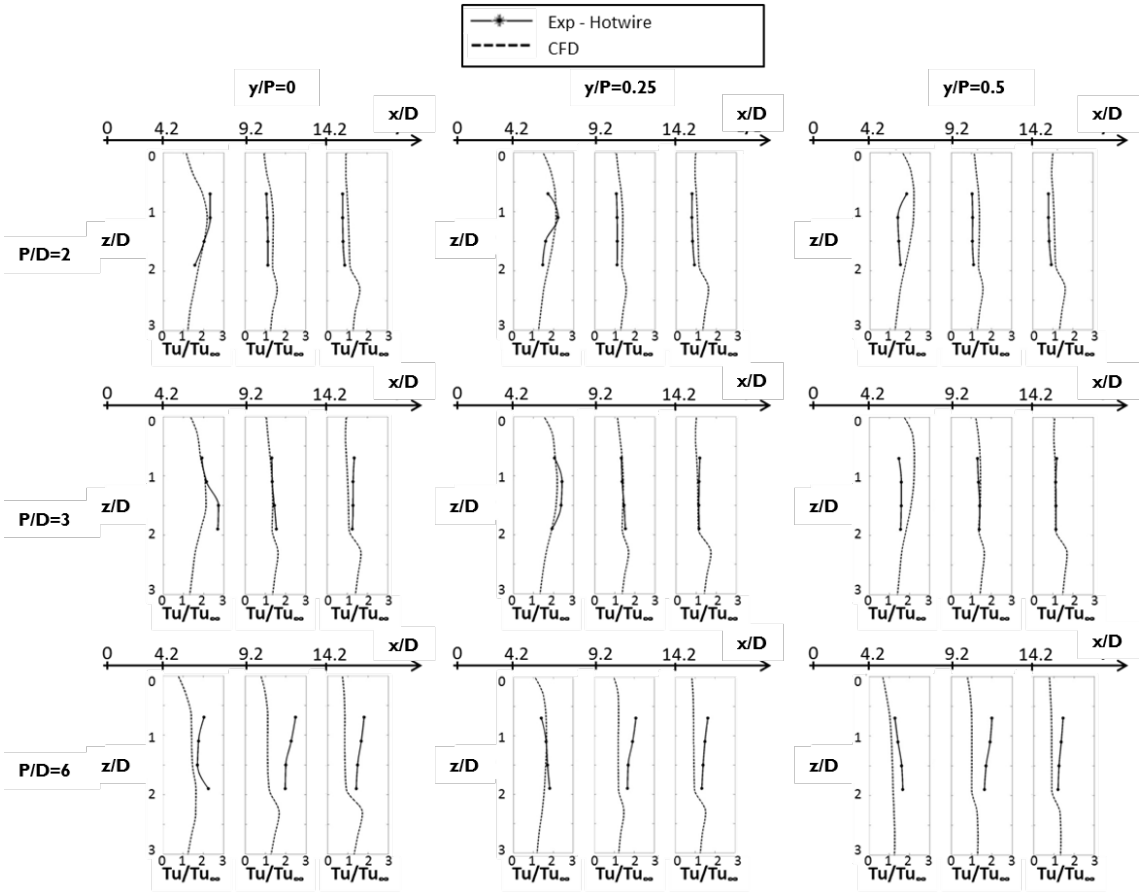


Figure 8.8: **Turbulence intensity non-dimensionalized with the mainstream value Tu_∞ at y/P=0 (downstream of a jet of the second row), y/P=0.25 (between jets) and y/P=0.5 (downstream of a jet of the first row)**

From the length scale plots in Figure 8.9 a general growth in the size of eddies moving downstream is noticeable which increase from a dimension close to the hole diameter to a magnitude of the order of the pitch. This means that for the more largely-spaced cases, the eddies have more space to grow. Another interesting point is that the length scale increases very close to the wall at P/D = 3 - 6: this could be due to the fact that the turbulent energy is not replenished so that the short length scale eddies die away. For P/D = 3 at x/P = 0 and x/D = 4.2, i.e. close to the injection, turbulence levels close to the wall are high and the length scale is smaller close to the wall and increases moving further away: this confirms that a lack of

near-wall turbulence downstream is the cause of the bigger length scales. For closer spaced holes, the distribution remains more uniform.

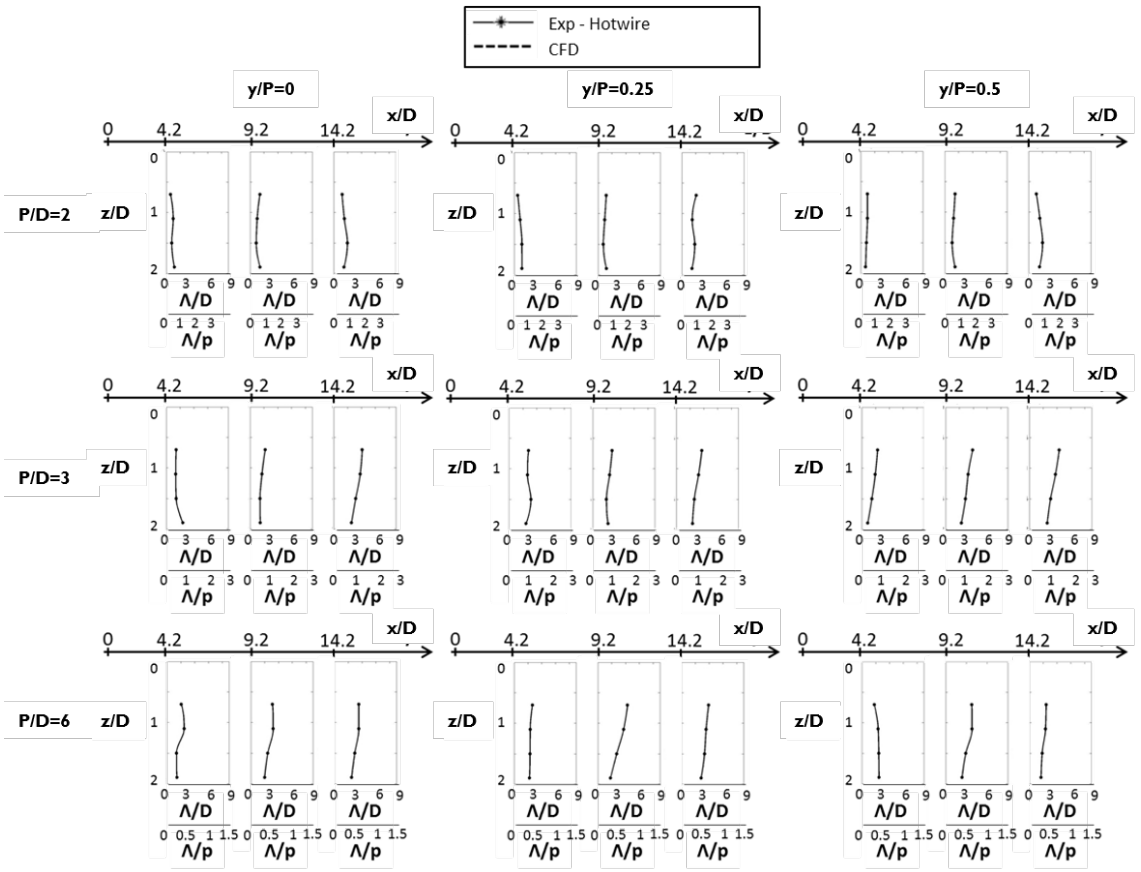


Figure 8.9: **Integral length scale Λ non-dimensionalized with the hole diameter D and the pitch p at y/P=0 (downstream of a jet of the second row), y/P=0.25 (between jets) and y/P=0.5 (downstream of a jet of the first row)**

8.3.3 Film effectiveness

Using the method described in Section 8.2.1, the passive scalar concentration Φ released from the RODN inlet was calculated with Fluent and the film effectiveness was plotted (Figure 8.10). As expected from the flow field analysis, the film effectiveness shows a substantial decrease with an increase in the hole spacing. With P/D = 2 the effectiveness is very uniform at the wall and its value reaches approxi-

mately $\eta_{eff} \approx 0.5$ just downstream of the second row of holes and from x/D ≈ 2 its value is consistently higher than 0.6 over the entire downstream domain. Increasing the pitch, the lift-off region (Figure 8.5), and so the area of the wall where the film is actually effective ($\eta_{eff} > 0$), increases. At P/D = 3 the coverage becomes uniform for x/D > 5 and $\eta_{eff} \approx 0.4$. For P/D = 6 the film never becomes uniform, the film lift-off causes a very low effectiveness until x/D ≈ 5 and the maximum coverage is only reached for x/D > 10 where η_{eff} is around 0.2.

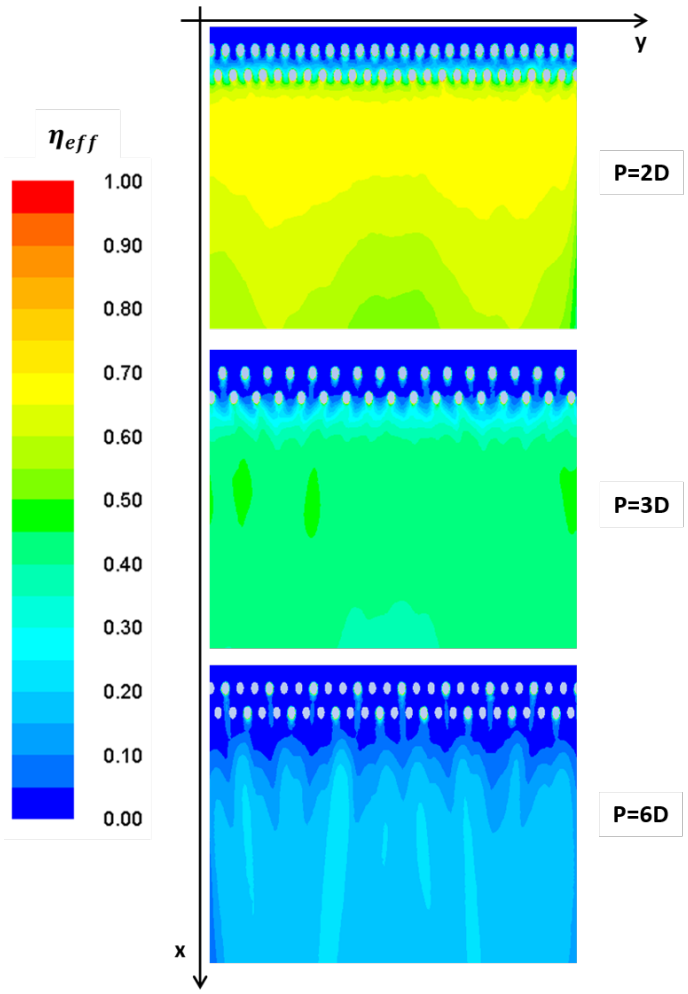


Figure 8.10: **Film effectiveness for cylindrical holes at different pitch-to-diameter ratios (CFD predictions)**

Figure 8.11 reports the film effectiveness averaged along the lateral direction y. The film effectiveness shows a first peak immediately downstream of the first

row hole center and a second peak immediately downstream of the second row hole center (x/D =0). Because of the mixing of the jets, the film becomes more uniform moving in the x direction, as shown in Figure 8.10, and that increases the averaged effectiveness: the effect becomes stronger with decreasing the hole pitch value.

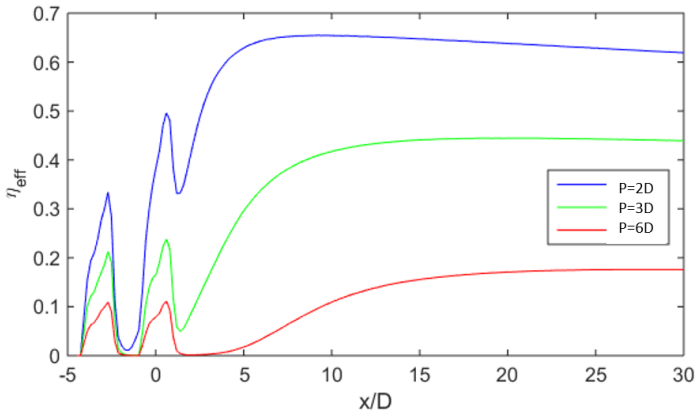


Figure 8.11: **Lateral-averaged film effectiveness for cylindrical holes at different pitch-to-diameter ratios (CFD predictions)**

8.4 Results: Intersecting holes - Investigation of the effect of intersecting angle

Numerical simulations of the combustor simulator with intersecting holes at the outer wall were run for $\Theta = 30^o - 45^o - 90^o$ (Table 8.2) and experiments were tested with $\Theta = 90^o$ (Table 8.1).

The coolant mass flow rates $\dot{m}_c$ for the cases tested are reported in Table 8.4 as a percentage of the mainstream mass flow rate $\dot{m}_\infty$. Increasing the value of Θ the number of holes increased, i.e. the total hole cross-sectional area, and this explains the increase of coolant mass flow rate. It would be possible to keep both J and the area, i.e. the number of holes (the hole diameter does not change in the different geometries), constant, but that would compromise the spreading of the film coolant in the lateral direction.

P/D	Θ	$\dot{m}_c/\dot{m}_\infty$	J
6.3	90^o	2%	6
2.6	45^o	5%	6
1.7	30^o	7%	6

Table 8.4: **Intersecting holes: Coolant mass flow rate comparison (CFD predictions)**

8.4.1 Velocity field: $\Theta = 90^o$

The flow downstream of the intersecting holes is strongly three-dimensional: at the x/D = 4.2 plane the spanwise velocity component w is up to 60% of the streamwise velocity u, while the lateral component v maximum is the 20% of u, at x/D = 9.2 $(v/u)_{max}$ drops to 40% and at x/D = 14.2 $(v/u)_{max} \approx 20\%$. The use of a single hot-wire means that the authors are only able to report measurements of the streamwise velocity component.

Because of the compound angle, the jets emerging from adjacent holes mix forming a new row of jets with spacing p' (Figure 8.12). The behaviour of the trajectories is very similar to that observed for large-spaced holes in the previous section: the jets tend to spread laterally, the velocity rapidly decreases and the coolant lifts from the wall, in this case without reattaching.

Figure 8.13 shows velocity and turbulence intensity profiles. The velocity profile is generally very flat at every location. The agreement with CFD is very good with a maximum overprediction lower than 30% at y/P = 0.25 and x/D = 4.2. At y/P = 0.25 the streamwise measured turbulence near wall is around the same value as the mainstream turbulence levels. The highest turbulence levels are measured at y/P = 0.25: turbulence increases in the streamwise direction from x/D = 4.2 to x/D = 9.2 where $Tu \approx 2Tu_\infty$ and then decreases moving further to x/D = 14.2; the profile is very uniform up to z/D $\approx$ 4 and then starts decreasing. CFD shows up to 100% higher turbulence levels close to wall: the fact that only the streamwise component was measured helps to explain the high mismatch at x/D = 4.2, where

the fluctuations in the other directions are not negligible. The agreement improves moving downstream, even if the modeled turbulent dissipation is too high and the levels are underpredict up to -80% at y/P = 0.25 and x/D = 9.2. At y/P = 14.2 the turbulence levels are quite uniform in the y direction and the CFD underprection is lower than -50%.

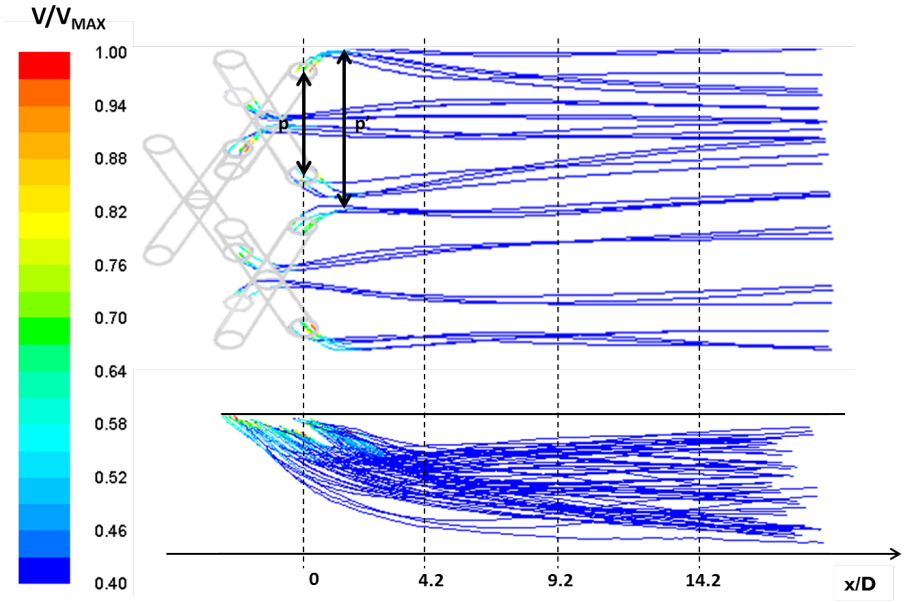


Figure 8.12: **90^o intersecting holes: jet trajectory (CFD)**

8.4.2 Velocity field: $\Theta = 30^o - 45^o$

Because of the low performance of the $\Theta = 90^o$ intersecting hole geometry, the value of Θ was decreased in order to reduce the hole spacing. Figure 8.14 compares the trajectory downstream of straight holes at P/D =2 to that downstream of the holes with an intersecting angle of 45^o (P/D = 2.6) and 30^o (P/D = 1.7): the calculations were run keeping the blowing ratio constant. The case with $\Theta = 45^o$ performs better than the geometry with $\Theta = 90^o$ (Figure 8.12), but the jets still tend to mix causing a lack of film coverage in relatively wide areas. Decreasing Θ to 30^o helps overcome this problem: the trajectory is similar to the one of the straight

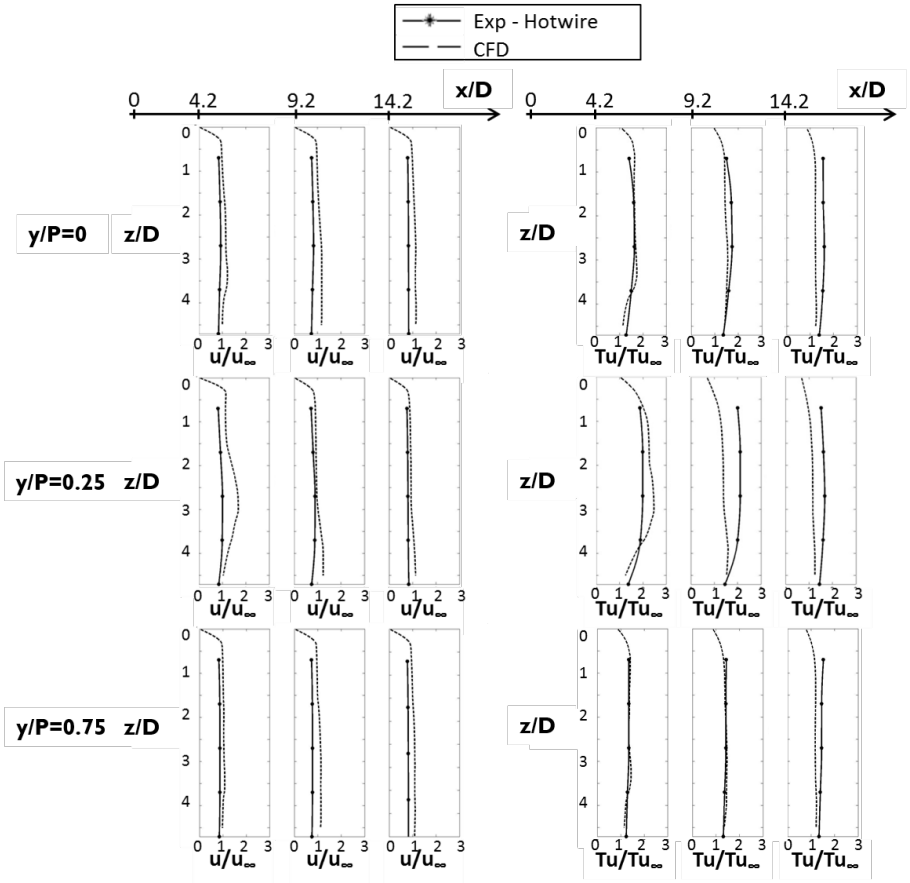


Figure 8.13: **Velocity (on the left) and turbulence intensity (on the right) non-dimensionalized with the mainstream values u_∞ and Tu_∞ downstream of 90^o intersecting holes**

holes (P/D = 2). The 45^o intersected holes deliver 14% less flow to area per unit of area of the straight hole configuration; the 90^o case 9% less. That could enable the design engineer, whilst keeping the same feed pressure, to either decrease the coolant mass flow rate for the same total hole area or to keep the same mass flow but with an increase of total area: in the second case the coolant velocity, i.e. momentum flux ratio, is decreased and the coolant is spread over a greater area.

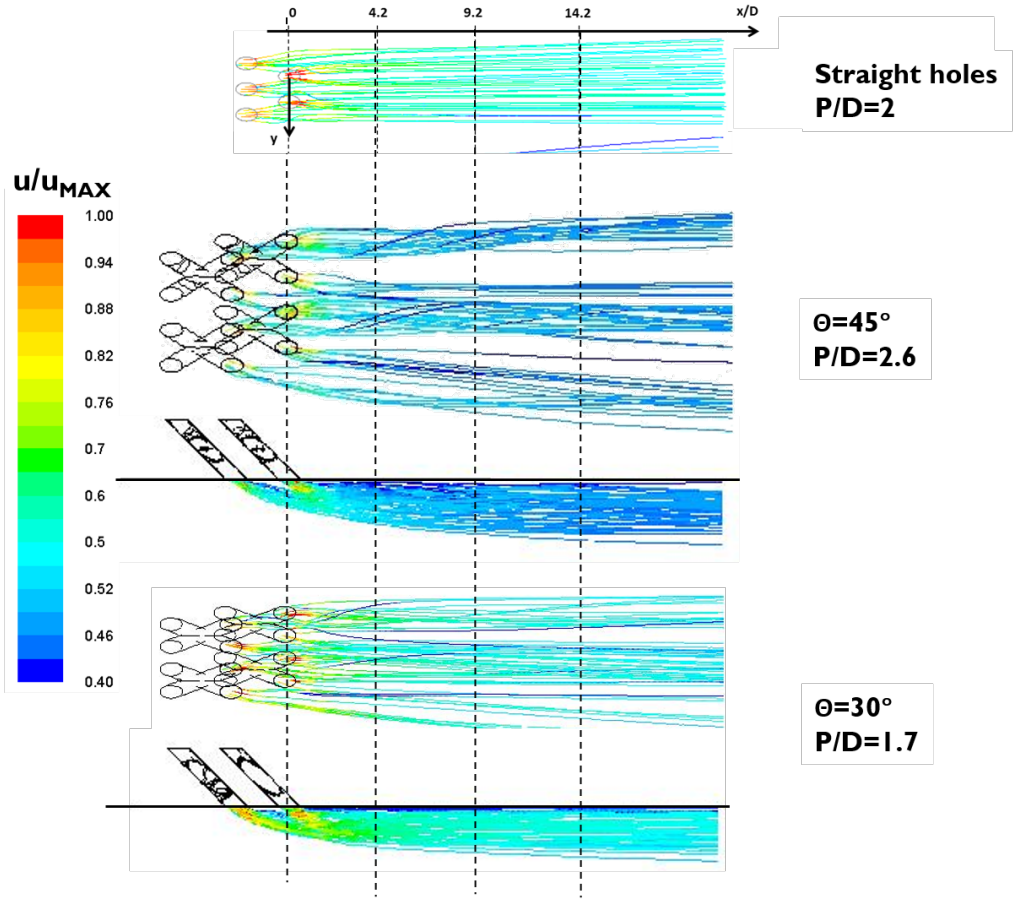


Figure 8.14: **Jet trajectory comparison (CFD): straight holes and P = 2D (on top) - 45^o intersecting holes and P = 2.6D (in the centre) - 30^o intersecting holes and P = 1.7D (on the bottom)**

8.4.3 Film effectiveness

The film effectiveness distributions obtained with the passive-scalar method are plotted in Figure 8.15 for the different intersecting angles: the study of the film coverage completes the analysis reported for the velocity field. The case with $\Theta = 30^o$ shows a high non-uniformity, with high peaks where the adjacent jets mix, but η_{eff} < 0.15 in the rest of the wall: this lack of coverage is due to the jet lift-off previously discussed. When $\Theta = 45^o$ the effectiveness levels increase to approximately $\eta_{eff} \approx$ 0.3 and the film uniformity increases. For $\Theta = 30^o$ the levels when the film has reached its maximum coverage are in the range $0.5 < \eta_{eff} < 0.7$.

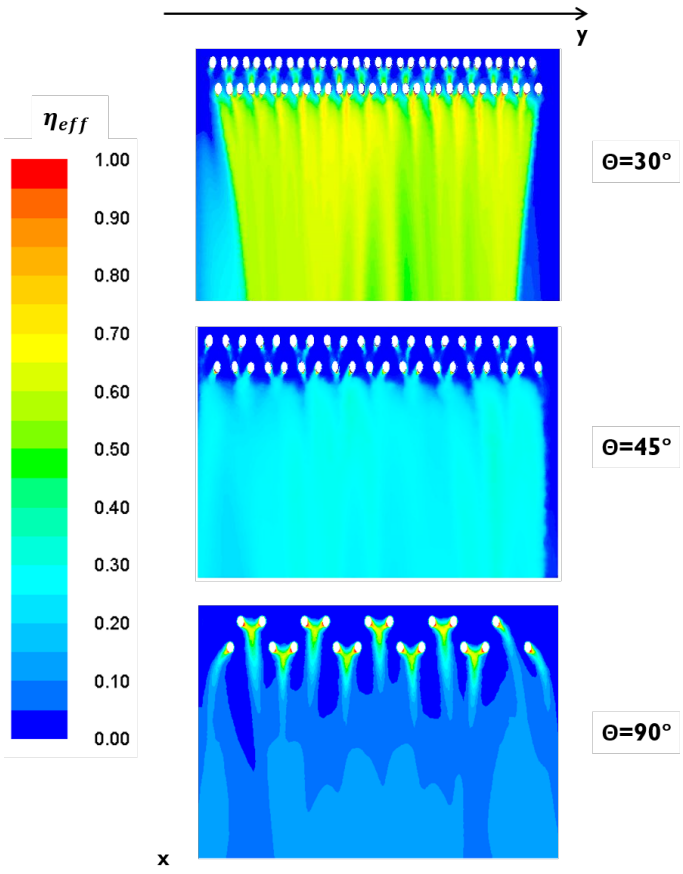


Figure 8.15: **Film effectiveness for intersecting holes at different intersecting angles (CFD predictions)**

The film effectiveness averaged in the lateral direction y is plotted in Figure 8.16 for the different values of Θ. As in the case with cylindrical holes (Figure 8.11), the effectiveness plots show two peaks just downstream of the two hole rows for all the geometries. The $\Theta = 30^o$ case has a trend very similar to the cylindrical holes and for $x/D > 4$ the effectiveness reaches a value of approximately 0.55, that decreases very slowing moving downstream. When $\Theta = 45^o$ the film behaviour is very similar to the geometry with $\Theta = 30^o$, but the effectiveness settles around a value of 0.25 and stays constant until x/D = 30. The film effectiveness trend changes drastically increasing the intersecting angle to $\Theta = 90^o$: downstream of the second hole row (i.e. x/D > 0) the averaged effectiveness decreases and settle to a value lower than 0.1.

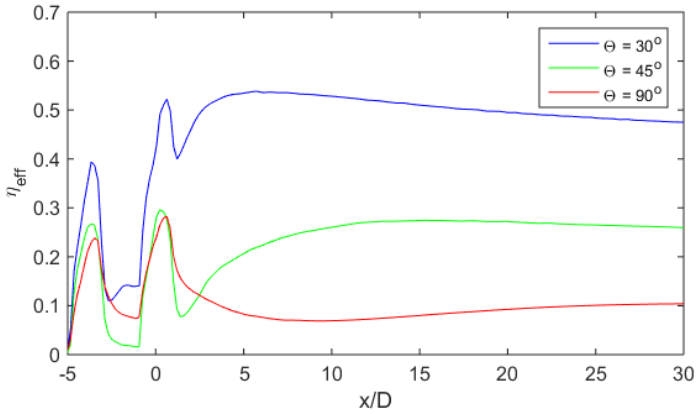


Figure 8.16: **Lateral-averaged film effectiveness for intersecting holes at different intersecting angles (CFD predictions)**

8.5 Summary

- The research reported in this chapter confirms the strong influence of the near-wall jets on the velocity and turbulence profiles downstream of a combustor and extends the dataset presented in Chapter 7, giving a better insight to the flow behaviour and development close to the endwall.

- The hole spacing is proved to be a key parameter to manage the film development: close holes have significantly more effect downstream.

- The arrangement with a pitch-to-diameter ratio of 2 is shown to produce an effective film, without jet lift-off, a lower streamwise velocity gradient and lower turbulence levels.

- The predicted film effectiveness demonstrates that a closer-spaced configuration guarantees a more uniform and long-lasting coverage. This agrees with the film effectiveness data trend from Ligrani et al. for different hole spacing [39].

- The integral length scales are of the order of the hole diameter close to the injection point but they keep increasing moving downstream tending to the

pitch dimension.

- RANS equations and realizable k-ε model with enhanced wall treatment show a good agreement with the experimental velocity data and the measurement trends but prove a lack of capability in predicting the entity of turbulence dissipation for different hole spacing configurations. CFD results are satisfying from a qualitative point of view in the turbulence prediction and even quantitatively in predicting velocity.

- Intersecting holes can potentially reduce the amount of coolant required from the endwall.

  - Adjacent jets mix creating a row of jets with larger spacing and this decreases the downstream film coverage.

  - The film performance is strongly affected by the jet lift-off: the possible benefits are considered to be too small to overcome the increase of manufacturing complexity and that is the reason why this work was not continued any further.

Chapter 9

Nozzle Guide Vanes (NGVs)

The CTI rig was designed to enable the Leading Edge (LE) film cooling performance in a High Pressure (HP) Nozzle Guide Vane (NGV) to be researched. For this purpose the vanes described in Chapter 4.3 were instrumented with pressure tappings on both the mainstream (external) surface and inside the LE coolant passage, as reported in Section 5.2.

The pressure measurements and the CFD simulations of the mainstream flow field are reported in this chapter, followed by the data obtained inside the LE channel at different coolant mass flow rates for the baseline case (Figure 4.12) and the insert case, reproducing Geometry D discussed in Chapter 3 (Figures 4.14 and 4.15).

9.1 Tests without LE film cooling injection

The mainstream flow around the vanes is strongly dependent on the conditions downstream: because of the absence of a blade row, tailboards are needed in order to obtain representative exit flow conditions. The position at which the tailboard achieves flow periodicity is not known a priori: for this reason adjustable boards were installed to enable the best exit geometry to be determined experimentally (Figure 9.1).

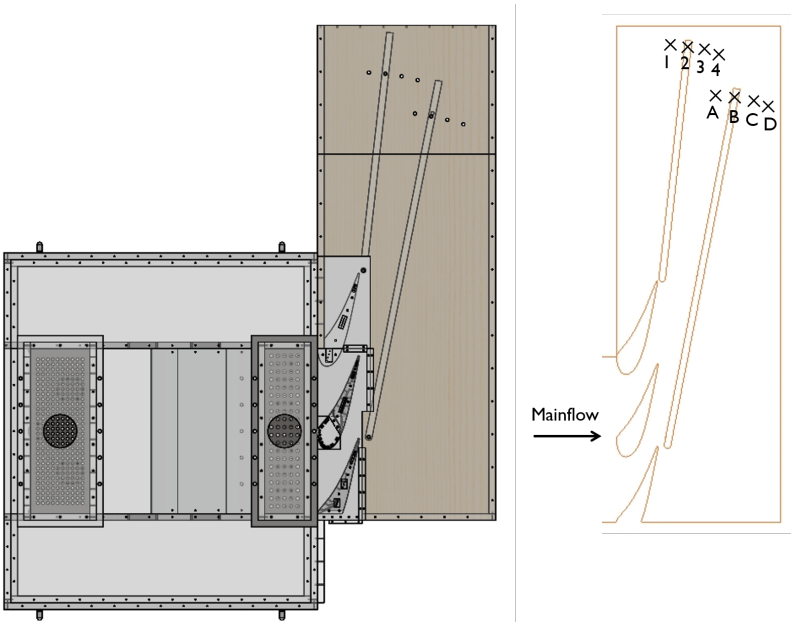


Figure 9.1: **CAD geometry of CTI rig (left) and adjustable tailboards setting positions (right).**

9.1.1 CFD simulations

CFD simulations of the test section with vanes installed at the rig operating conditions were performed with ANSYS Fluent. The computational model is shown in Figure 9.2 and it contains the combustor simulator (including dilution ports, RIDN and RODN), the vanes and the tailboards: the LE coolant passage was not simulated. Different models were created with different tailboard positions.

The unstructured computational meshes were generated with ANSYS ICEM 12.0 and contain around 10^7 elements (Figure 9.3). Prism layers were used at the vane walls as shown in Figure 9.4.

The strategy adopted used these CFD simulations as a design tool to narrow down the range of tailboard positions to be experimentally tested: the cases that were run are summarised in Table 9.1. In the results reported in this chapter the turbulence was modeled with the Spalart-Allmaras (SA) turbulence model. Figure 9.5 shows a comparison between the pressure distribution around the vanes for the B2 tailboard configuration obtained with SA and k-ε models: the differences are

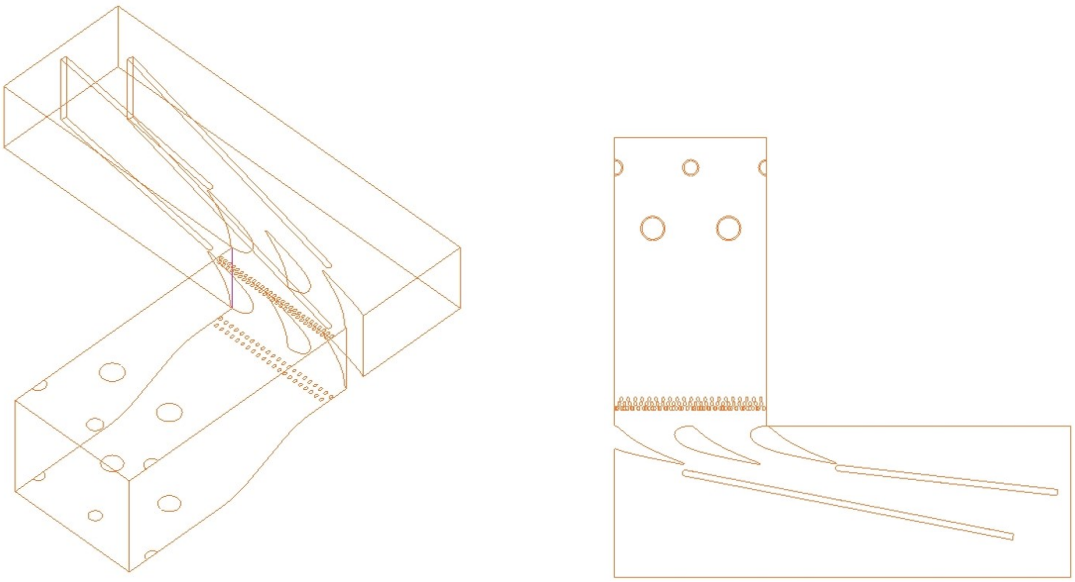


Figure 9.2: **Computational model of the cascade passage: Isometric view (on the left) and top view (on the right)**

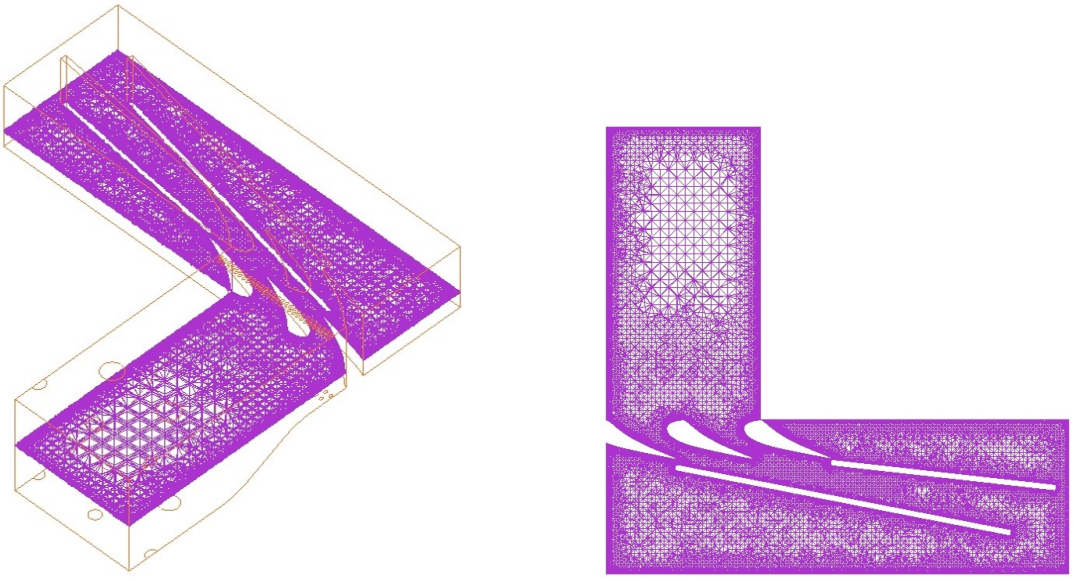


Figure 9.3: **Computational mesh of the cascade passage: Isometric view (on the left) and top view (on the right)**

less than 1% and therefore are considered negligible by the author.

Thomas [65] defines the pressure coefficient as

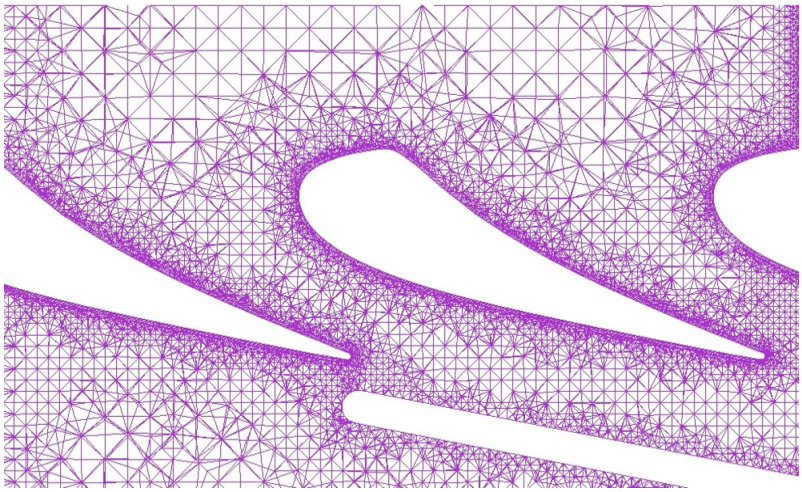


Figure 9.4: **Computational mesh of the cascade passage: enlargement around the central vane.**

Tailboard position	1	2	3	4
A				
B	✓	✓	✓	
C	✓	✓	✓	✓
D				

Table 9.1: **Numerically tested tailboard positions. Note that positions A and D were not required.**

$$C_p = \frac{p - p_{SP}}{p_{SP}} \tag{9.1}$$

where the stagnation pressure p_{SP} is replaced with the highest value from the pressure tapping readings. Note that gauge pressures were measured.

Equation 9.1 was used to compare the numerical simulations run on the CTI rig to Thomas' pressure profile measured at the midspan of the same vane geometry in another low-speed cascade facility in the Osney laboratory: for this reason his results are used as a datum profile. Thomas measured the gauge pressures referred

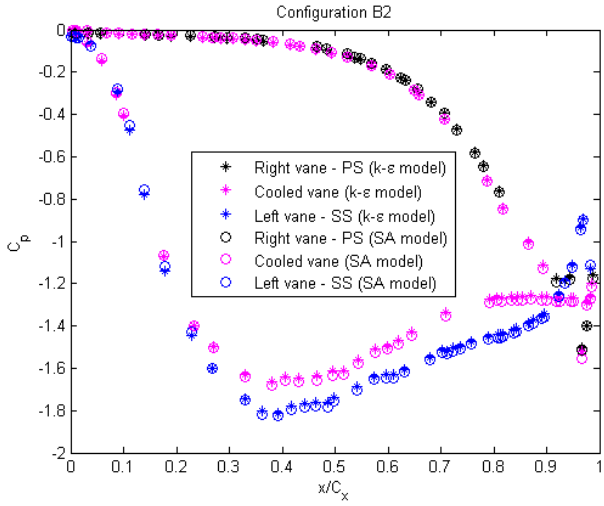


Figure 9.5: **Pressure coefficient C_p vs x/C_x: CFD predictions for the B2 tailboard position)**

to ambient pressure, which was coincident with the vane outlet pressure for his experimental facility. Because the CTI rig is a suckdown tunnel, the vane discharge static pressure is below atmosphere: in order to be able to compare the two sets of data the gauge pressures for the results concerning the CTI rig are referred to a static pressure tapping positioned downstream of the tailboards, as reported in Figure 9.6.

The predicted C_p profiles are shown in Figure 9.7. The data labeled "Cooled vane" correspond to the measurements around the central vane (according to the definitions in Section 5.2): interest is mainly focused on this vane because it is the vane with the cooled leading edge and where the measurements reported later in this chapter are located. The vanes either side (labeled as "Right vane - PS" and "Left vane - SS" vanes, see Section 5.2) are used to check the flow periodicity inside the two passages on the Pressure and Suction Sides ('PS' and 'SS'). The data marked as "Thomas [2014]" are the measurements reported by Thomas [65].

The increase of flow area in the passage between the tailboards downstream of the vane (in particular in configurations B1 and C2) causes a decrease of pressure around the vanes, especially around the SS, increasing the vane loading and reducing

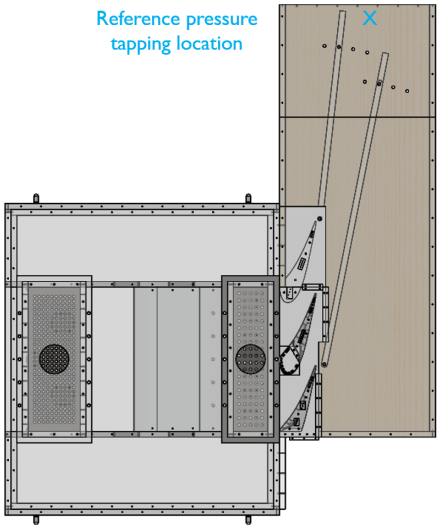


Figure 9.6: **CTI rig: Mainstream reference pressure tapping location**

the pressure coefficient on the suction surface. The effect is highlighted by the C_p definition choice: because the denominator is a gauge pressure it changes with the reference pressure, that decreases when the flow velocity at tailboard exit increases. The opposite trend is noticed when the cross-sectional area is reduced, moving the tailboards to configurations B3 and C4: the pressure levels upstream increase and, because this effect is stronger on the SS, the vane loading decreases. It appears that the SS results are more sensitive to the position of the tailboards than the PS results. An excessive narrowing of the passage area downstream of the vane passages is detrimental for the flow periodicity: in configurations B3 and C4 the flow around the cooled vane tends to accelerate much more on the SS compared to the left vane. Configuration B2 shows the best agreement with Thomas' data and a good periodicity: for these reasons this was the configuration chosen to be experimentally tested in the CTI rig.

The pressure coefficient distributions for the B2 configuration at the spanwise positions $s = 0.1H$, $s = 0.25H$, $s = 0.5H$, $s = 0.75H$ and $s = 0.9H$ are plotted in Figure 9.8. The flow periodicity is very good at every location and the variations of the C_p profile between $s = 0.25H$ and $s = 0.75H$ are very small because the vanes

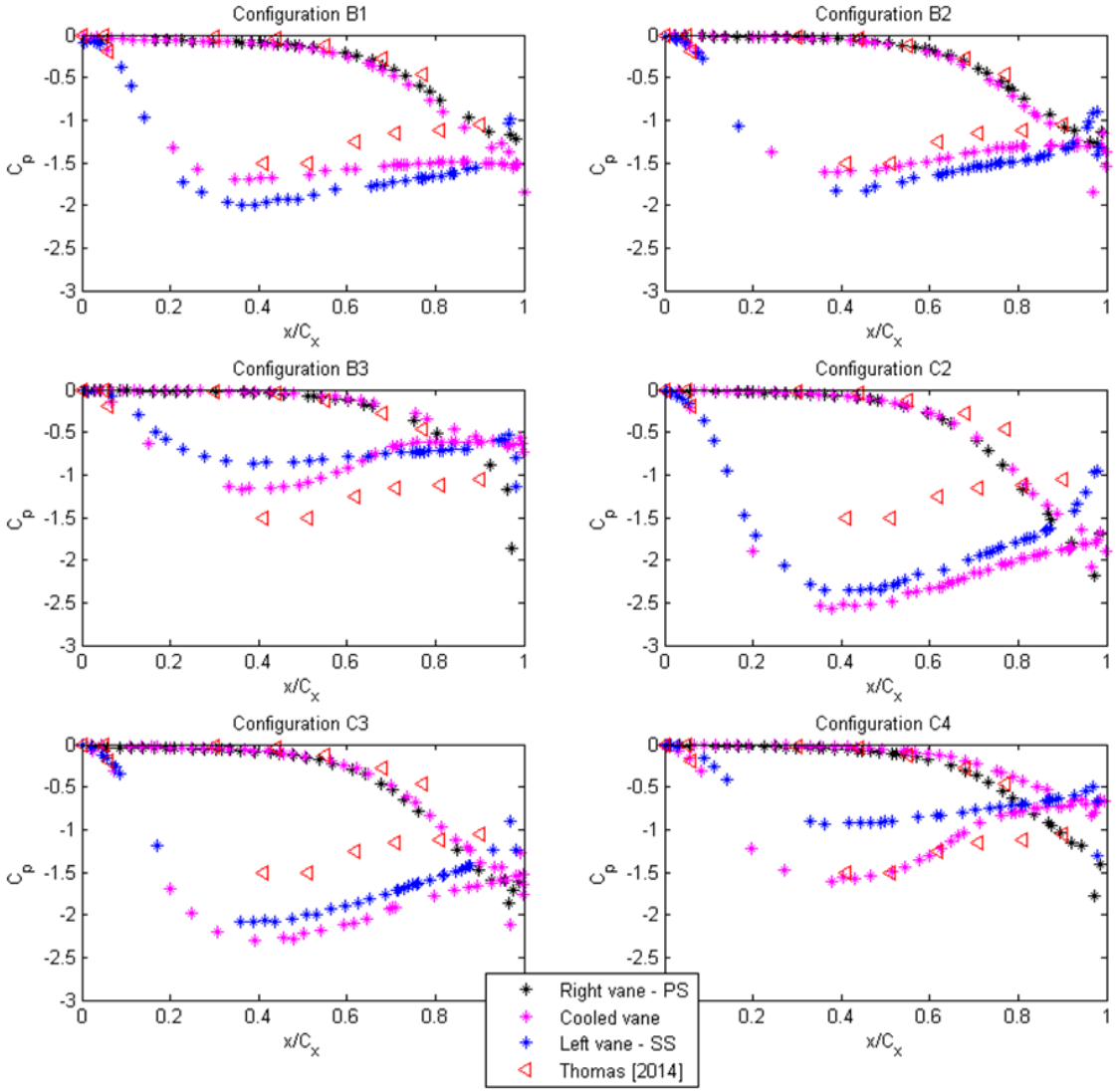


Figure 9.7: **Pressure coefficient C_p vs x/C_x at $s = 0.5H$: CFD predictions for different tailboard positions (Table 9.1). Note that the "cooled vane" predictions correspond to the central vane (see Section 5.2).**

are prismatic, i.e. the vane section is unvaried along the spanwise direction, and the approaching mainflow is very uniform (as shown in Figure 7.10). The near-wall flow is faster and this affects the pressure distribution around the vane close to the endwall. Figure 9.9 shows a decrease of up to 7% of C_p on the suction side in the range $0.1 < x/C_x < 0.5$. The lower mainstream static pressure would certainly affect the LE film cooling performance, but because this faster flow is the coolant

injected from the RIDN and RODN, this is not a source of concern for the LE vane integrity. For this reason this effect has not been further investigated.

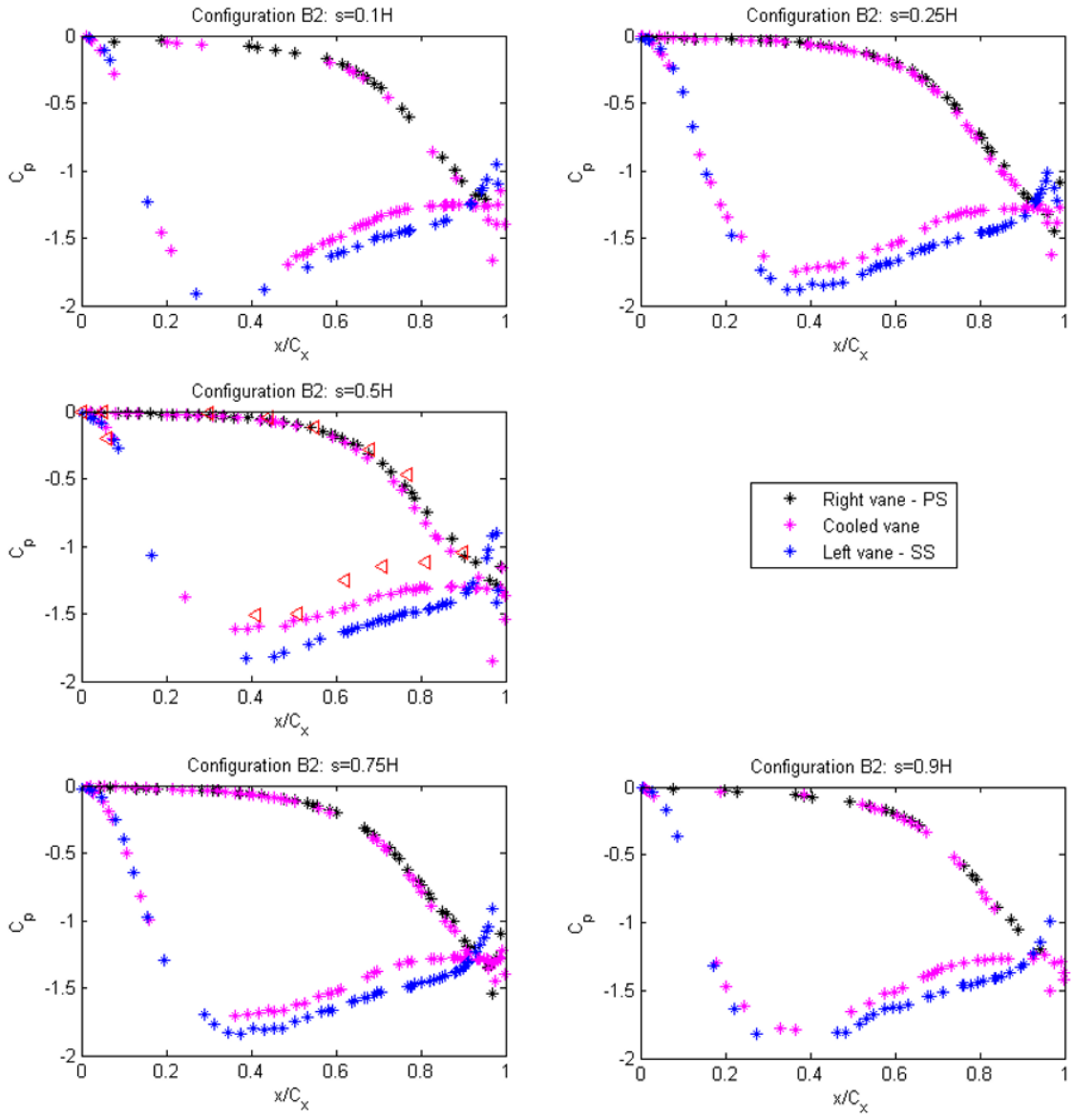


Figure 9.8: **Pressure coefficient C_p vs x/C_x: CFD predictions for the B2 tailboard position at $s = 0.1H$, $s = 0.25H$, $s = 0.5H$, $s = 0.75H$ and $s = 0.9H$**

9.1.2 Experimental measurements

The purpose of this test campaign was to match the pressure field around the central vane in the CTI rig with the results reported in Thomas' thesis [65] and

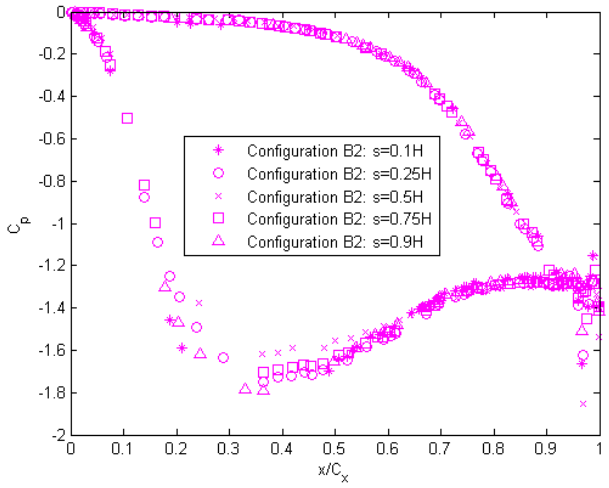


Figure 9.9: **Pressure coefficient C_p vs x/C_x: CFD predictions for the B2 tailboard position at $s = 0.1H$, $s = 0.25H$, $s = 0.5H$, $s = 0.75H$ and $s = 0.9H$**

optimize the flow periodicity inside the two vane passages.

Following the CFD preliminary results the tailboard positions B2 were chosen as a starting point and then the tailboards were adjusted to cover the cases reported in Table 9.2.

Tailboard position	1	2	3	4
A		✓		
B	✓	✓	✓	
C		✓		
D				

Table 9.2: **Experimentally tested tailboard positions**

In Figure 9.10, C_p was calculated from the static pressure measured around the CTI vanes and compared to Thomas' data. For these measurements no LE coolant was injected at this stage. The effect of moving the tailboards from the location B2 to A2 or B3 is to reduce the flow area downstream of the vane passages and this increases the pressure coefficient levels around the vanes. The opposite happens on moving the tailboards from B2 to C2 or B1: the passage area increases and

that reduces the pressure levels upstream. The trends are in agreement with the results predicted by CFD for the cooled vane and the Suction Side (SS) results being particularly sensitive to the position of the tailboards.

As for the periodicity, experimental measurements report a different development of the flow around the SS of the left vane compared to the cooled one: in particular, the profile around the left vane shows a minimum at $x/C_x = 1.6$. This is caused by the presence of the upstream side wall that causes the flow to separate and shifts the stagnation point towards the SS, as visible in the CFD static pressure and velocity contours shown in Figure 9.11.

In agreement with the CFD predictions, the B2 configuration provides the closest pressure distribution to Thomas' data with the best periodicity. For these reasons, B2 was the tailboard location chosen for the measurements with the LE coolant injection.

In order to check the pressure distribution along the spanwise direction around the LE, some pressure tappings were installed also at s = 0.75H. The C_p values measured at this position are compared to the data obtained at s = 0.5H in Figure 9.12. The agreement between the profiles is excellent and this further validates the numerical results.

9.2 Tests with LE film cooling injection

The data presented in this section were acquired in the CTI rig at different LE internal passage coolant mass flow rates: the coolant mass flow rate is reported as a percentage value of the mainstream mass flow rate evaluated at the vane throat. The cases tested are reported in Table 9.3 for both the baseline and the coolant insert cases.

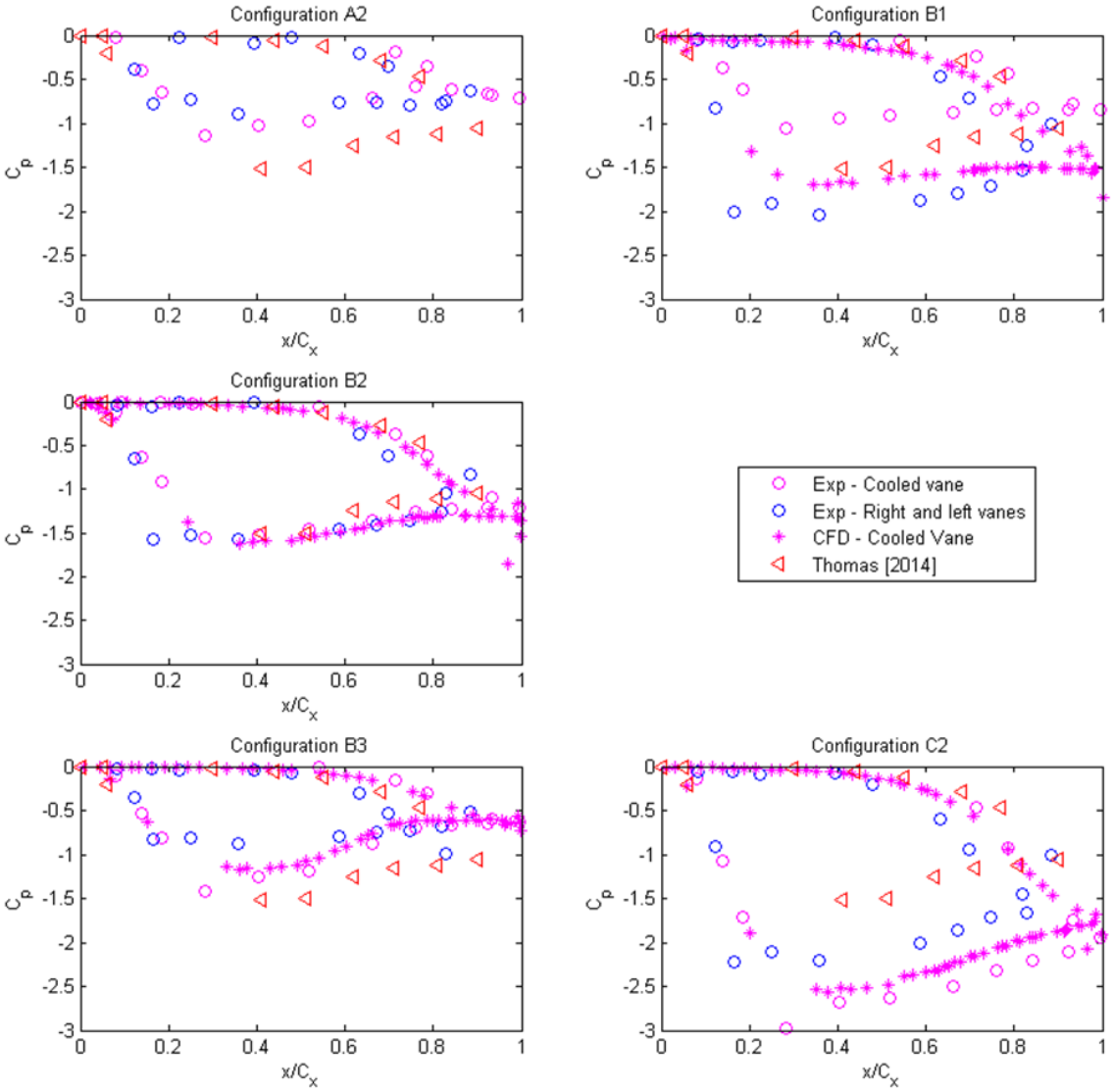


Figure 9.10: **Pressure coefficient C_p vs x/C_x: Experimental measurements and CFD predictions for different tailboard positions (Table 9.2)**

9.2.1 Mainstream

First of all, the effect of film cooling ejection on the mainstream pressure profile was analysed comparing the pressure coefficient C_p distribution around the vane midspan for the different baseline test cases: the measured distributions are plotted in Figure 9.13. It is evident that, while the effect of the film injection is negligible for $x/C_x > 0.4$, the coolant presence cannot be ignored around the leading edge, where the increase of coolant mass flow rate causes a decrease of static pressure around the

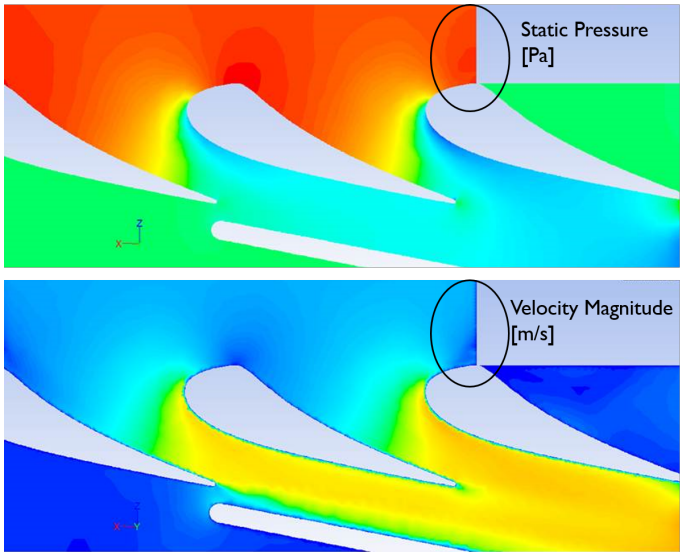


Figure 9.11: **Flow separation upstream of the left vane - CFD predictions at the midspan: Static pressure contours on the top and velocity contours on the bottom.**

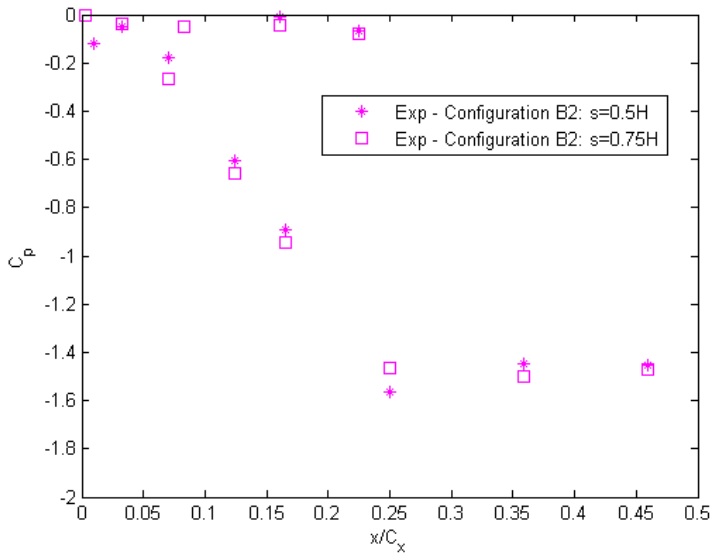


Figure 9.12: **Pressure coefficient C_p vs x/C_x - Tailboard position B2: s = 0.5H and s = 0.75H**

vane. The SS is more sensitive to the film injection and near the stagnation point C_p can drop to up to 3 time its value with the increase of coolant mass flow rate.

Tailboard position	$\dot{m}_c$ [%] Baseline case	$\dot{m}_c$ [%] Insert case
B2	0	–
B2	6.8	6.9
B2	8	7.8
B2	8.9	9.1
B2	10.5	9.7
B2	11.3	10.1

Table 9.3: **Experimentally tested cases at different coolant mass flow rates (percentage values of the mainstream mass flow rate at the vane throat)**

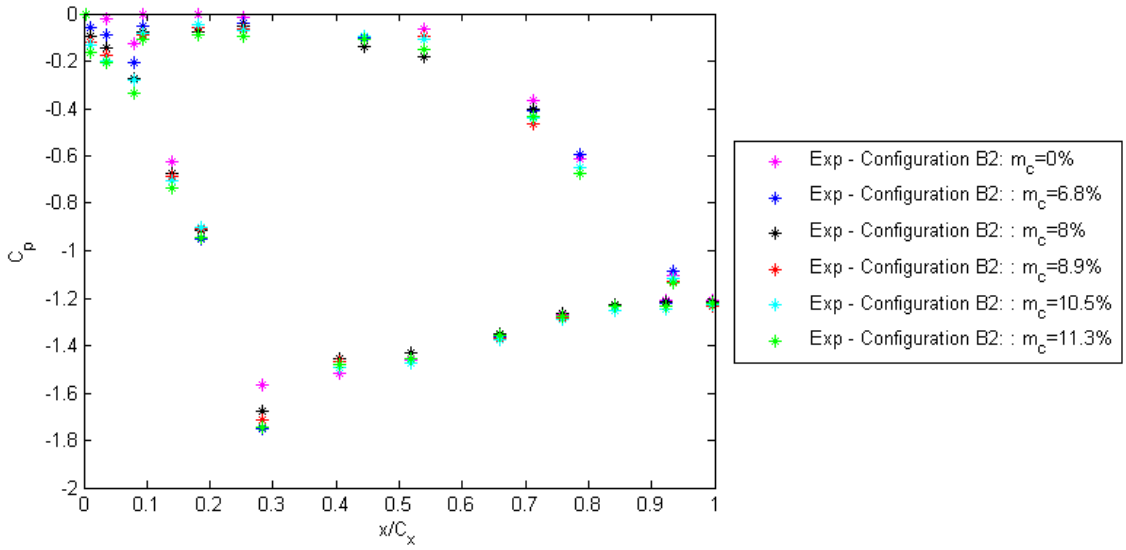


Figure 9.13: **Pressure coefficient C_p vs x/C_x for different coolant mass flow rates (percentage values of the mainstream mass flow rate at the vane throat)**

9.2.2 LE coolant passage - Static pressure measurements

The pressure tappings inside the LE coolant passage are positioned at two different spanwise locations, s/H = 0.17 and s/H = 0.3 (see Section 5.2): these locations

enable measurements to be made both inside and downstream of the insert. The data acquired inside the baseline LE at s/H = 0.17 at different coolant mass flow rates are reported in Figure 9.14. On the pressure side the pressure is approximately uniform and can be seen to increase with the increase in mass flow rate, while on the suction side the data are more variable: in particular a minimum at $x/C_x = 0.09$ and a peak at $x/C_x = 0.12$ are evident and this is due to the close film cooling holes sucking air from the passage and creating localized strong pressure variations. This effect is also shown in the CFD predictions obtained from the simulations run at engine conditions and reported in Chapter 3: a screenshot of the static pressure contours at s/H = 0.17 is shown in Figure 9.15 where the measurement locations are highlighted. The pressure tapping at $x/C_x = 0.12$ falls in the peak pressure region just next to a film cooling hole. The pressure acquired at s/H = 0.3 (Figure 9.16) because of the different location of the measurement plane compared to the film cooling holes: the data values are more homogeneous.

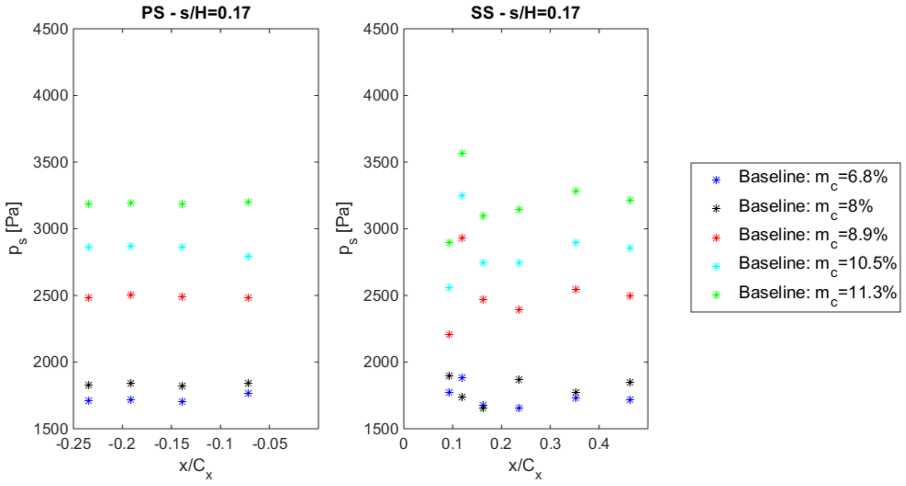


Figure 9.14: **Pressure measurements inside the LE coolant passage (Baseline case) at s/H = 0.17: PS on the left and SS on the right**

The LE passage design with the insert described in Section 4.3 corresponding to Geometry D (Figure 3.13) was tested and the results are shown in Figures 9.17 and 9.18. At s/H = 0.17 the region on the PS $-0.2 < x/C_x < 0$ is covered by the insert:

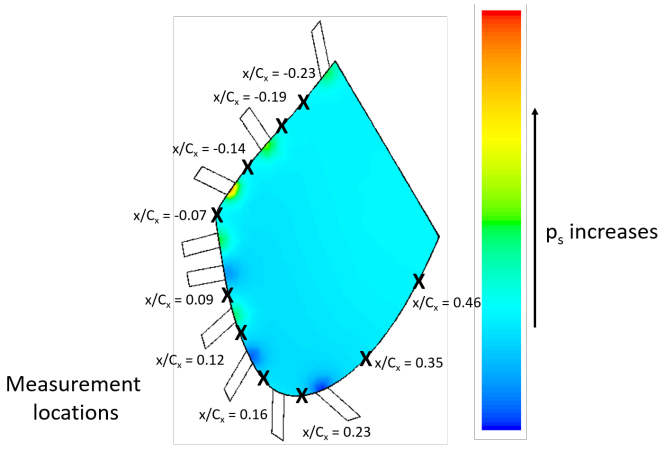


Figure 9.15: **CFD pressure predictions inside the LE coolant passage (Baseline case) at s/H = 0.17**

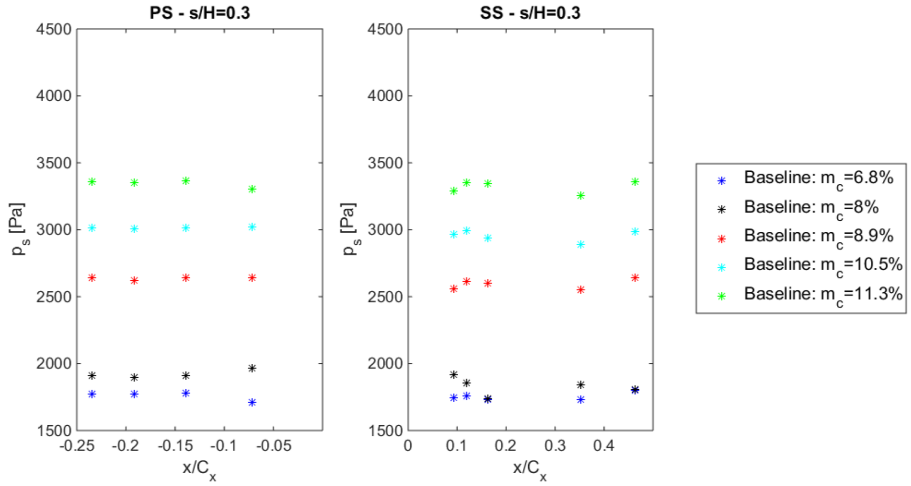


Figure 9.16: **Pressure measurements inside the LE coolant passage (Baseline case) at s/H = 0.3: PS on the left and SS on the right**

in this zone, a significant increase in static pressure can be seen at all coolant mass flow rates. At s/H = 0.3 the static pressure is uniform in the axial direction on the PS. The SS has a more homogeneous static pressure distribution with the insert without the peak detected inside the baseline LE at s/H = 0.17. The pressure field predicted by CFD shows in Figure 9.19 that the presence of the insert reduces the static pressure around the pressure tapping at $x/C_x = 0.12$.

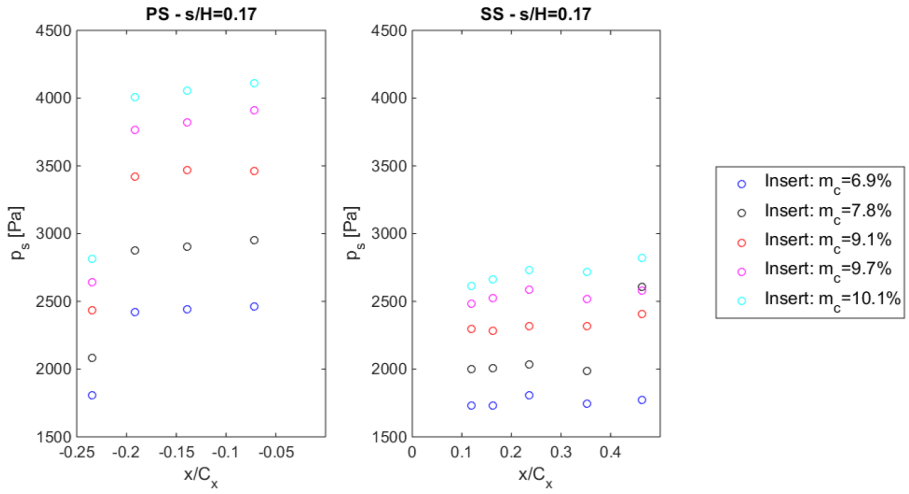


Figure 9.17: **Pressure measurements inside the LE coolant passage (Insert case) at s/H = 0.17: PS on the left and SS on the right**

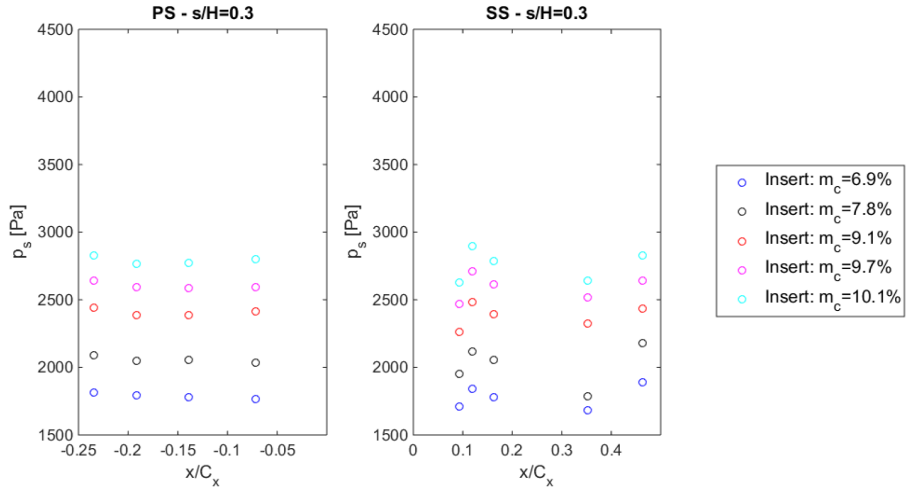


Figure 9.18: **Pressure measurements inside the LE coolant passage (Insert case) at s/H = 0.3: PS on the left and SS on the right**

Figures 9.20 and 9.21 show a direct comparison between the measurements obtained for the baseline case and with the insert. At s/H = 0.17 when $-0.2 < x/C_x < 0$ on the PS (i.e. inside the insert) the increase of static pressure varies between +25% and +60% depending on the coolant mass flow rate. It is interesting to note that the improvement is higher for relatively low coolant mass flow rate (i.e.

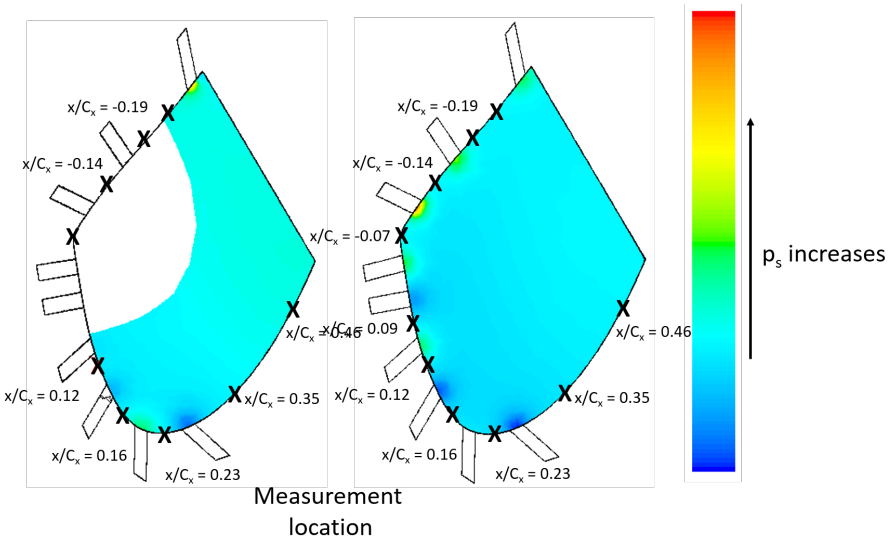


Figure 9.19: **CFD pressure predictions inside the LE coolant passage (Insert case on the left vs. Baseline case on the right) at s/H = 0.17**

lower static pressure working conditions inside the passage): this is relevant because the advantage of the insert increases when the LE coolant flow, and hence pressure margin, are lower. At the same spanwise location but outside the insert the pressure differences between the two cases are mostly due to the mass flow rate variations and so any variation due to the presence of the insert is found to be modest.

Moving downstream (s/H = 0.3) the case with $\dot{m}_c \approx 7\%$ does not show appreciable variations, while at higher mass flow rates the static pressure inside the LE with the insert decreases between -8% and -17%.

The pressure drop of an incompressible flow inside a duct depends on the mean flow speed according to

$$\Delta p = K_L 1/2 \rho v^2 \tag{9.2}$$

where K_L is a loss coefficient that includes all the relevant loss mechanisms.

Figure 9.22 reports the mean static pressure difference between the values measured inside the channel and the mainstream pressure plotted versus the square of

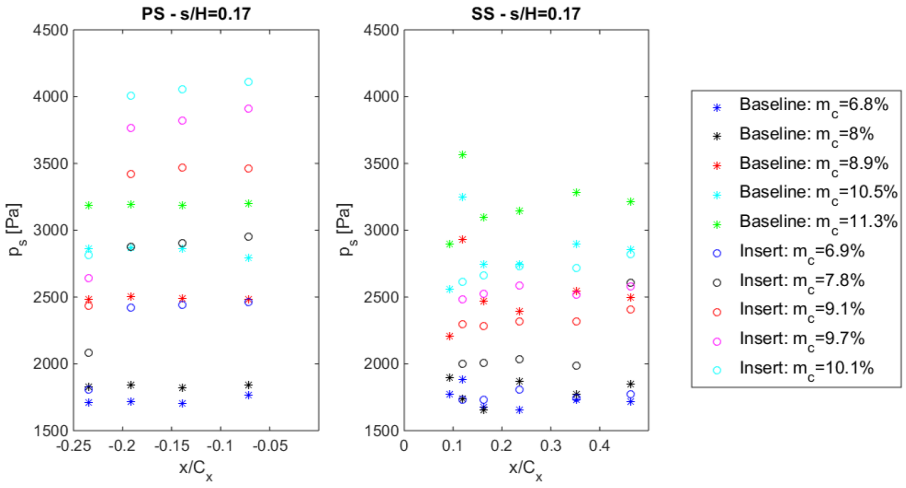


Figure 9.20: **Pressure measurements inside the LE coolant passage (Baseline case vs. Insert case) at s/H=0.17: PS on the left and SS on the right**

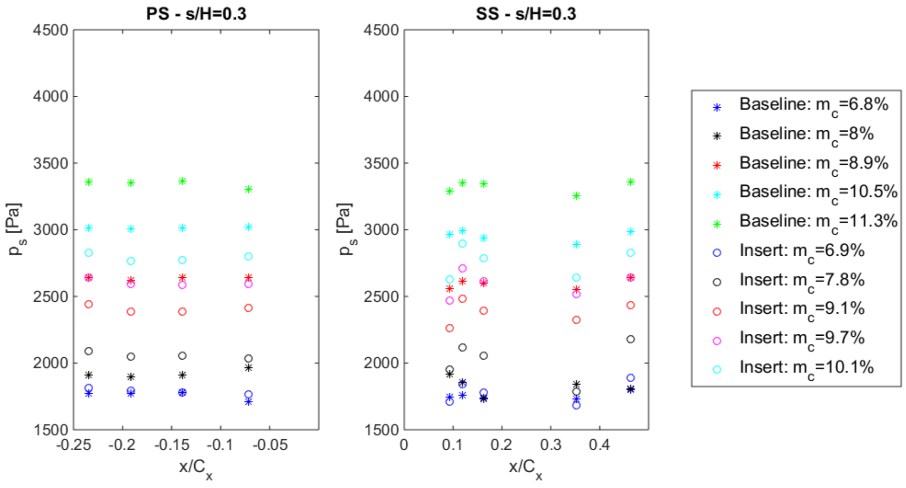


Figure 9.21: **Pressure measurements inside the LE coolant passage (Baseline case vs. Insert case) at s/H=0.3: PS on the left and SS on the right**

the velocity at the LE coolant passage inlet at the two measurement sections s/H = 0.17 and s/H = 0.3 for the baseline and the insert case: the straight line fits are added to show trends. Firstly, it can be seen that the lines do not intersect the coordinate system origin (i.e. $p_{sc} - p_{s\infty} = 0$ at $v_c = 0$): that is due to the presence

of losses that need to be overcome to allow the air to start flowing inside the LE channel. At s/H = 0.17, the channel with the insert provides a higher p_{sc} compared to the baseline case at a set coolant mass flow rate and the difference is higher at lower mass flow rates. This means that, firstly, the geometry with the insert is able to provide a higher static pressure at lower mass flow rates and, secondly, the change in static pressure inside the LE with the insert is a weaker function of coolant mass flow rate, avoiding sudden drops if the coolant amount decreases. At s/H = 0.3 the static pressure in the baseline case increases because of the decrease of mass flow along the spanwise direction (i.e. decrease of dynamic head): the static pressure difference between the two sections increases with the total coolant mass flow rate. On the other hand in the insert case the section-averaged static pressure decreases downstream of the insert because of the increase of the pressure losses inside the diffuser: the pressure losses inside the diffuser increase with v_c^2 so the difference between the two cases at s/H = 0.3 increases from around 7% at the lowest coolant mass flow rates to up to 20% moving towards higher coolant velocity.

Figure 9.22 shows the average trends but does not reveal the local behaviour of the flow. Figures 9.23 and 9.24 show the local pressure difference between the LE coolant passage and the mainstream for the baseline case: it is evident that, firstly, the static pressure decreases when coolant mass flow rate increases and, secondly, the region at $-0.25 < x/C_x < 0.1$ has the lowest pressure margin. The pressure margin increases moving downstream as previously shown in Figure 9.22 because of the dynamic head decrease, but the distribution is practically unvaried.

Figures 9.25 and 9.26 show a strong increase in pressure margin in the region covered by the insert (at s/H = 0.17, $-0.2 < x/C_x < 0$), but a general decrease outside this region is visible.

Figures 9.27 and 9.28 compare the pressure margin for the two different configurations. Inside the insert (at s/H = 0.17, $-0.2 < x/C_x < 0$) the increase is up to +150% at low mass flow rates and around +80% at higher mass flow rates. Around the insert at s/H = 0.17 the pressure margin is uniform: attention needs to

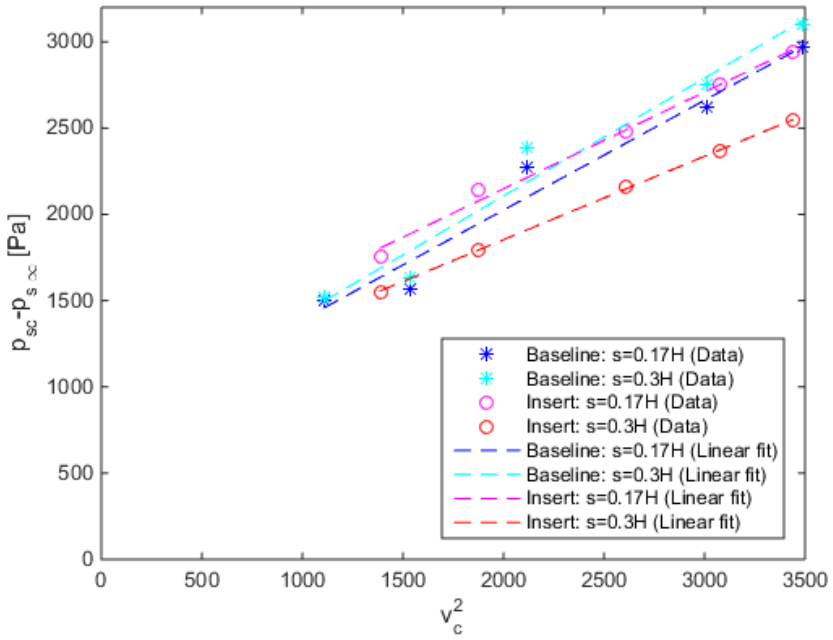


Figure 9.22: **Section-averaged static pressure difference between the LE coolant passage and the mainstream plotted versus the square of the coolant passage inlet velocity**

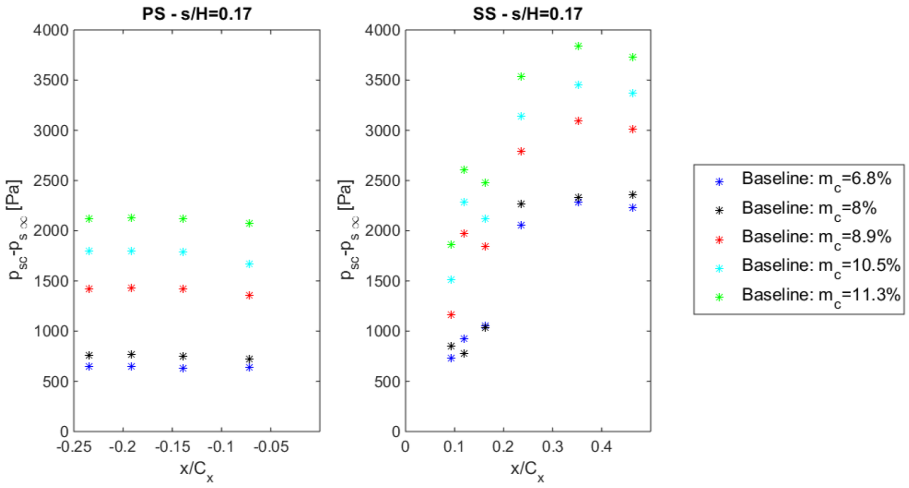


Figure 9.23: **Difference between the local static pressure in the LE coolant passage and the local external static pressure mainstream (Baseline case) at s/H = 0.17: PS on the left and SS on the right**

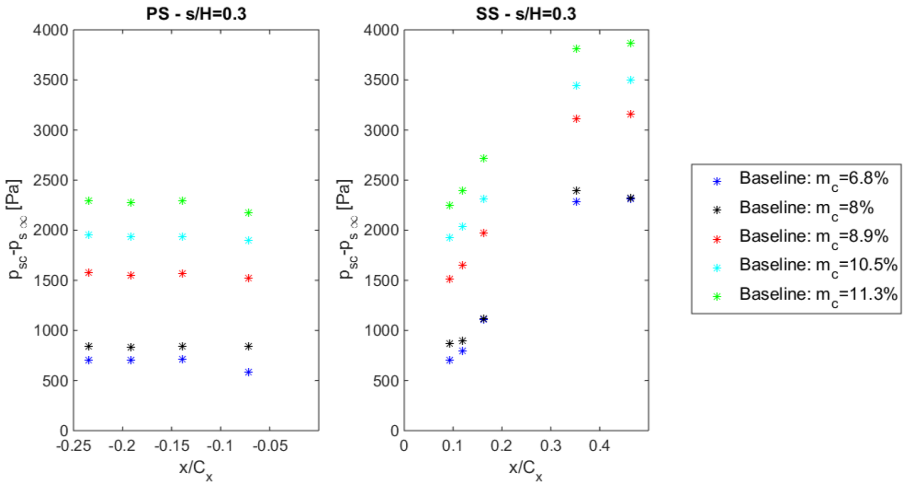


Figure 9.24: **Difference between the local static pressure in the LE coolant passage and the local external static pressure mainstream (Baseline case) at s/H = 0.3: PS on the left and SS on the right**

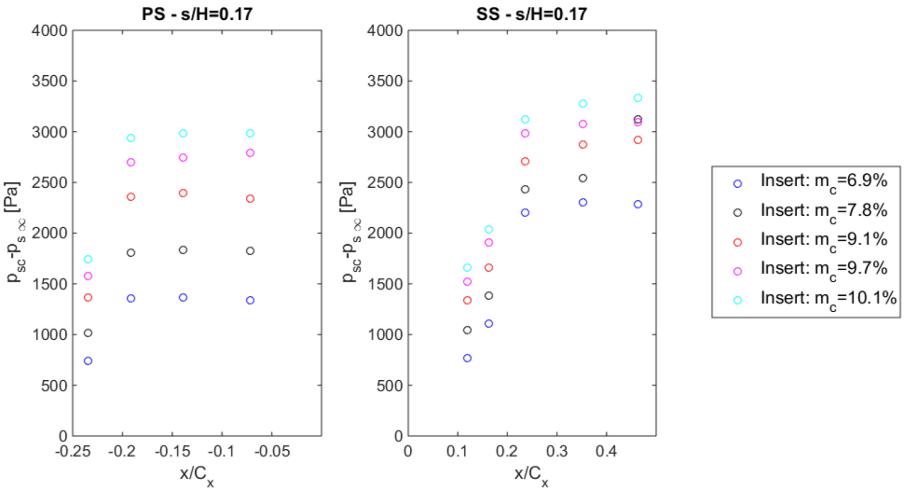


Figure 9.25: **Difference between the local static pressure in the LE coolant passage and the local external static pressure mainstream (Insert case) at s/H = 0.17: PS on the left and SS on the right**

be given in the region for $0 < x/C_x < 0.15$ where even smaller changes can cause the pressure margin to fall under the safety range: it is highly recommended for future work to test a wider insert covering also this area. For higher x/C_x the pressure

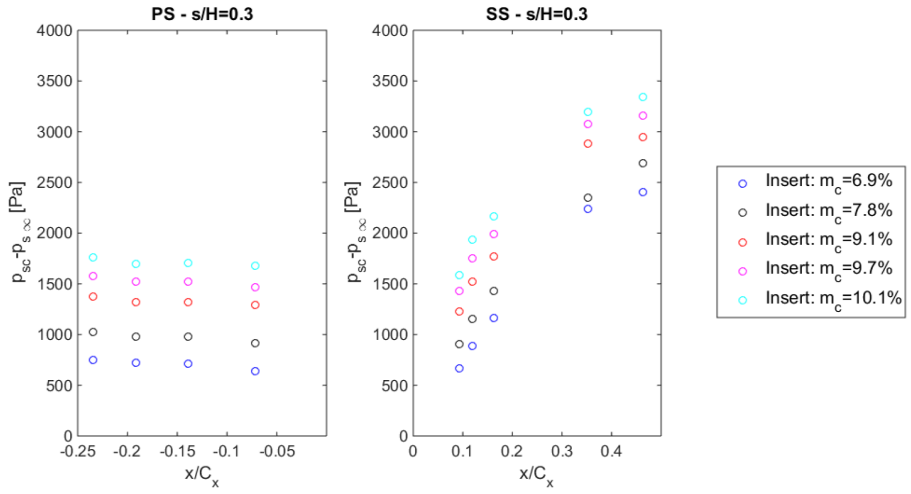


Figure 9.26: **Difference between the local static pressure in the LE coolant passage and the local external static pressure mainstream (Insert case) at s/H = 0.3: PS on the left and SS on the right**

margin increase and the ingestion risk is limited. At s/H = 0.3 there is a decrease of pressure margin of around -10% for $\dot{m}_c \approx$ 9-10% due to the increase of pressure losses inside the diffuser, while the reduction in benefit at lower mass flow rates is smaller.

Thereafter, the pressure margin was non-dimensionalized with the dynamic head calculated at the LE coolant passage inlet ($v_c(s = 0)$) and the results plotted in Figures 9.29 and 9.30 for the baseline case. The pressure differences between coolant and mainstream at s/H = 0.17 tend to collapse when normalised by the dynamic head along the pressure side and around the stagnation region: there is still a variation with the mass coolant rate but the values are all approximately 1. Moving along the suction side, on the other hand, the data spread increases: at higher mass flow rates the variation along the chord is lower and the maximum change is around +100%, while at lower mass flow rates the increase is up to +200%. The dynamic head at the passage inlet is not able to scale the pressure margin along the suction surface and this is because the pressure on the external surface of the suction surface also depends on the dynamic head of the mainstream flow around the vane. At s/H

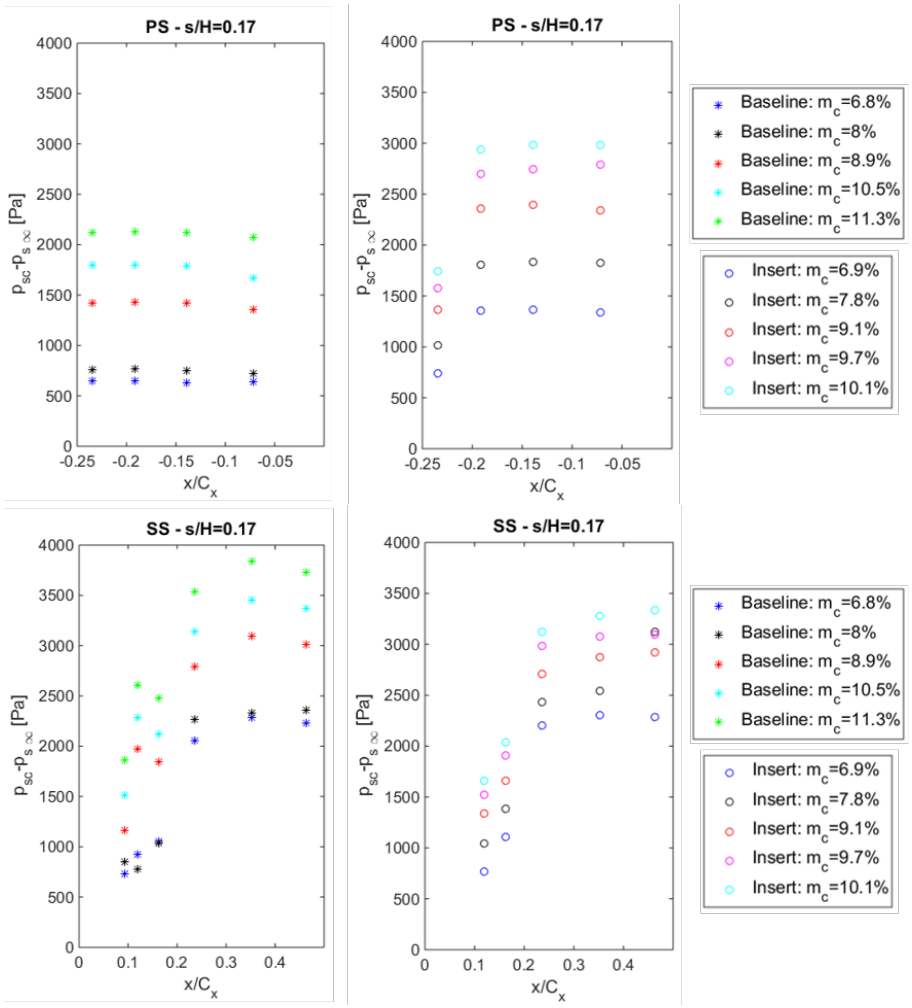


Figure 9.27: **Difference between the local static pressure in the LE coolant passage and the local external static pressure mainstream (Baseline case vs. Insert case) at s/H = 0.17: PS on the top and SS on the bottom**

= 0.3 the trends are very similar.

The flow inside the insert (Figure 9.31) collapses using the dynamic head at the inlet: because the only experimental data available were the total coolant mass flow rate for each test, these values were used to calculate the average coolant velocity at the inlet $v_c(s/H = 0)$ using the passage inlet area (smaller than in the baseline case because of the presence of the insert). $(p_{sc} - p_{s\infty})/1/2\rho v_c^2$ is 50% higher inside the insert compared to the nearby outside. The trend for the suction side results is the same as reported above for the baseline case and also the variations along the

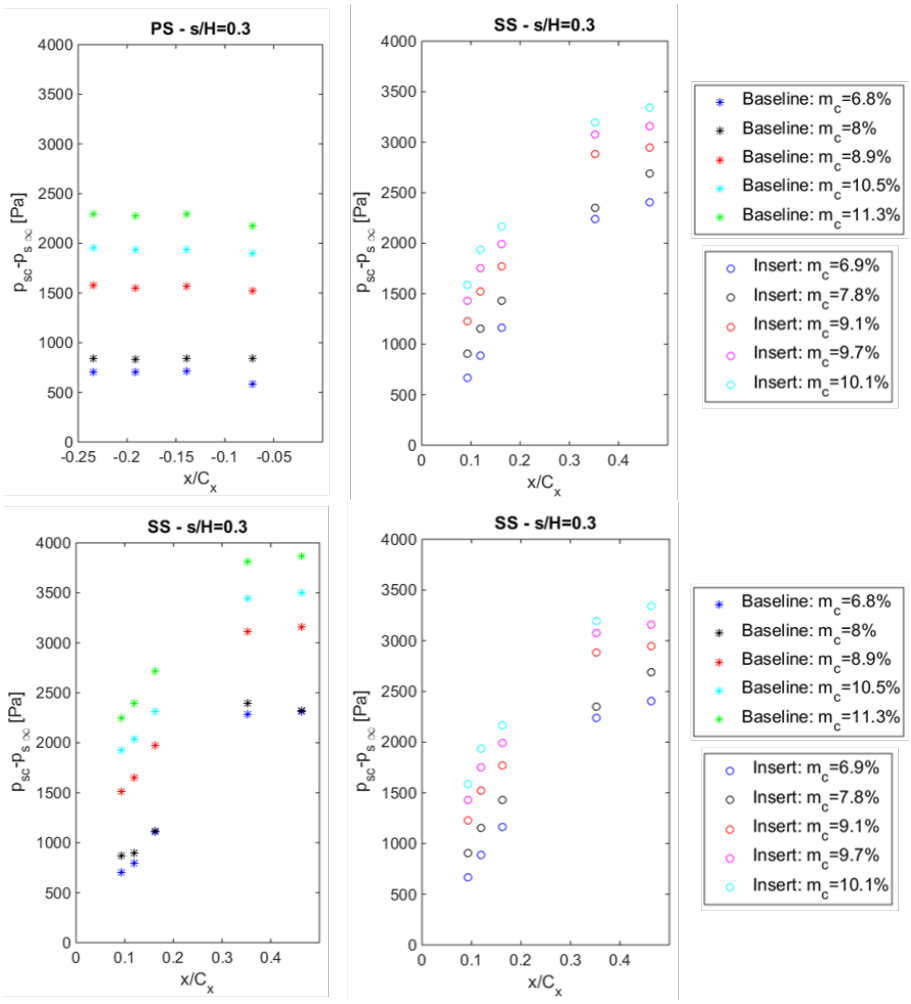


Figure 9.28: **Difference between the local static pressure in the LE coolant passage and the local external static pressure mainstream (Baseline case vs. Insert case) at s/H = 0.3: PS on the top and SS on the bottom**

chord (between +100 and +200%) are consistent. Similar observations can be made for the measurements at s/H = 0.3 (Figure 9.32).

Comparing the two different geometries in Figures 9.33 and 9.34, the inlet dynamic head appears to be more able to collapse the pressure margin inside the insert than in the baseline case. $(p_{sc} - p_{s\infty})/1/2\rho v_c^2$ is 50% higher inside the insert and approximately 20 - 30% lower along the suction side.

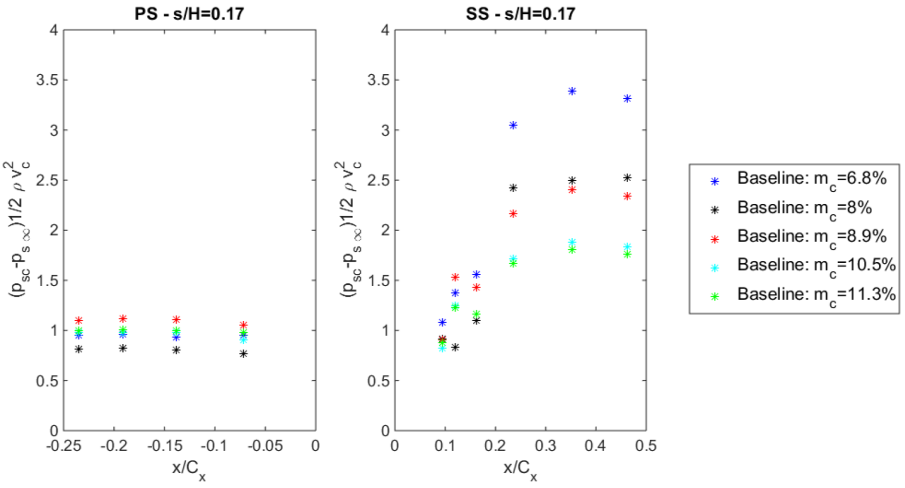


Figure 9.29: $(p_{sc} - p_{s\infty})/1/2\rho v_c^2$ **(Baseline case) at s/H = 0.17: PS on the left and SS on the right**

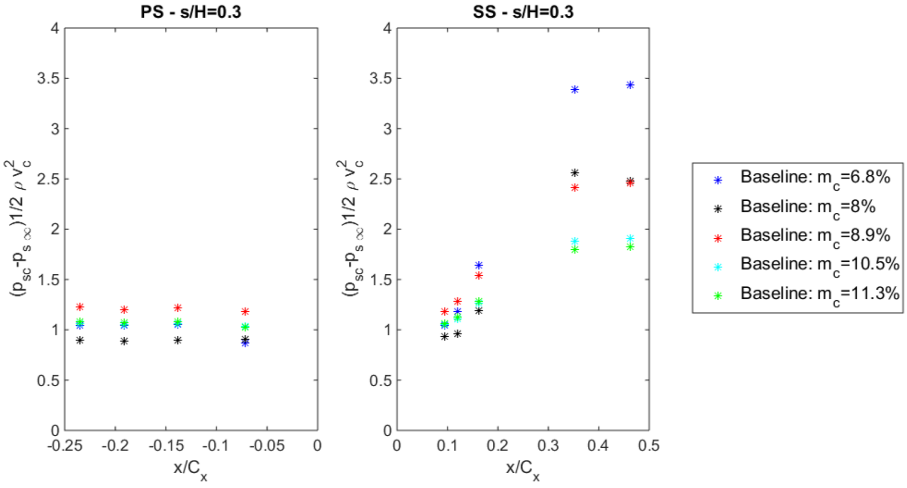


Figure 9.30: $(p_{sc} - p_{s\infty})/1/2\rho v_c^2$ **(Baseline case) at s/H = 0.3: PS on the left and SS on the right**

9.2.3 LE coolant passage - Stewart plot

The Stewart plot, previously described in Section 3.5.1, is used to compare different vane designs to evaluate the pressure margin at various operating conditions. The difference between coolant and mainstream total pressure over coolant total pressure is plotted on the Y-axis, the inverse of the Q function (which decreases

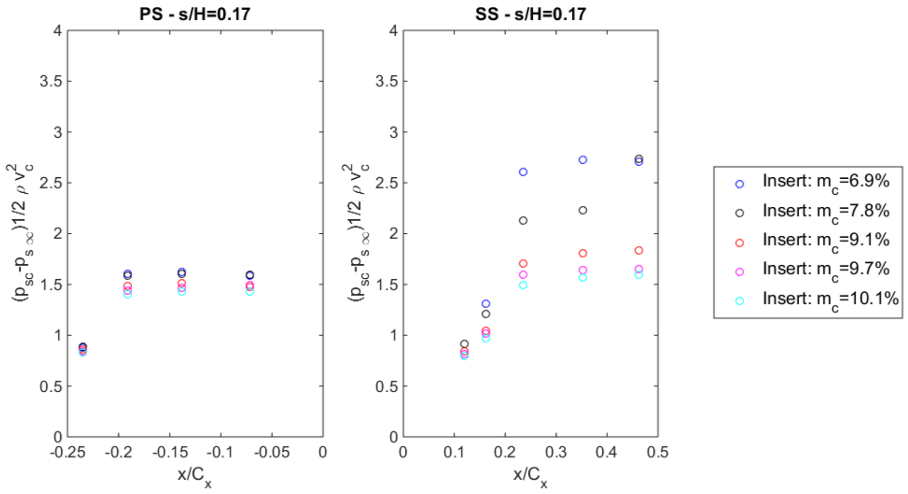


Figure 9.31: $(p_{sc} - p_{s\infty})/1/2\rho v_c^2$ **(Insert case) at s/H = 0.17: PS on the left and SS on the right**

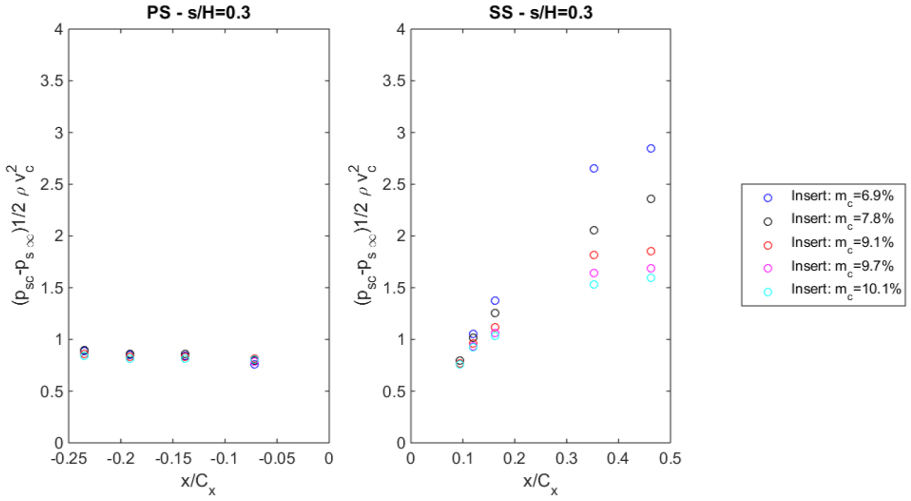


Figure 9.32: $(p_{sc} - p_{s\infty})/1/2\rho v_c^2$ **(Insert case) at s/H = 0.3: PS on the left and SS on the right**

with the Mach number, i.e. the flow velocity, according to the definition Eq.3.19) on the X-axis and the coolant-to-mainstream static pressure as constant pressure margin lines.

In order to relate the rig measurements to engine conditions a loss coefficient K_L was defined as follows

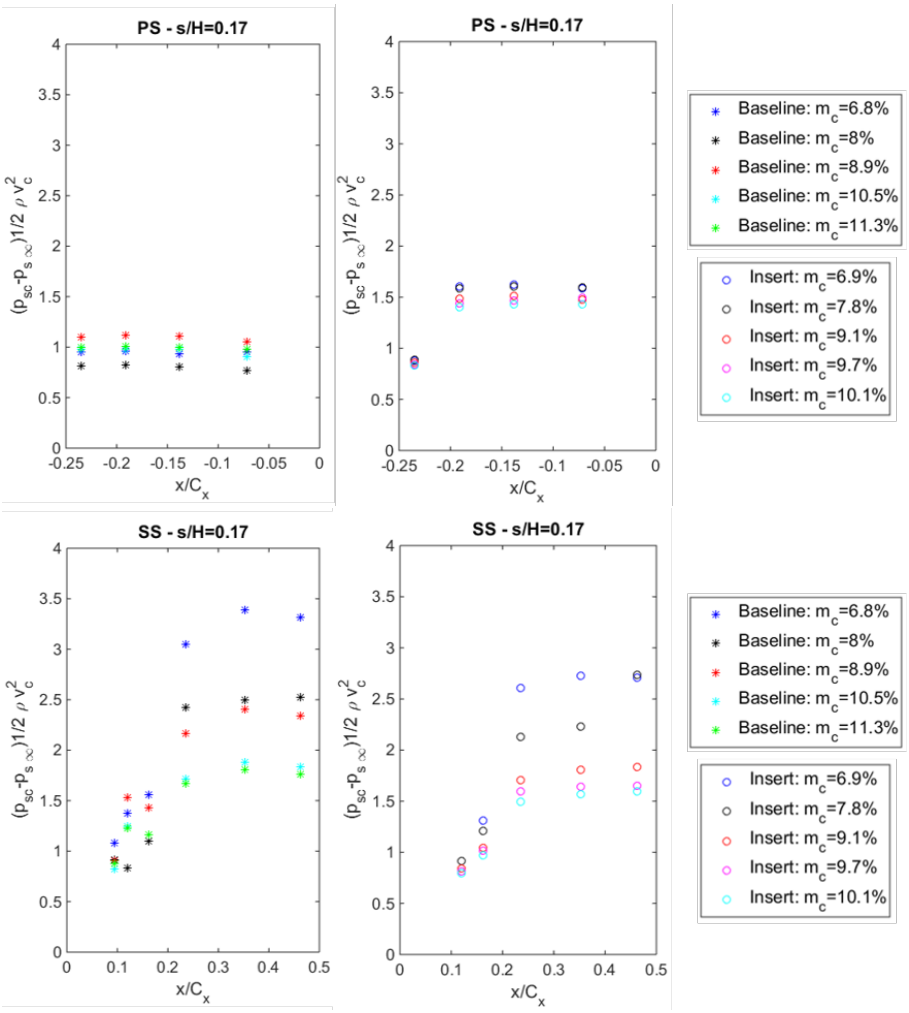


Figure 9.33: $(p_{sc} - p_{s\infty})/1/2\rho v_c^2$ **(Baseline case vs. Insert case) at s/H = 0.17: PS on the top and SS on the bottom**

$$K_L = \frac{p_{0c} - p_{0\infty}}{1/2\rho v_c^2} \tag{9.3}$$

The value of K_L was initially calculated from the experimental data at rig conditions and was then used to obtain an estimate of p_{0c} at engine conditions

$$(p_{0c})_{engine} = (p_{0\infty})_{engine} + K_L(1/2\rho v_c^2)_{engine} \tag{9.4}$$

p_{0c} in the rig was available only inside the plenum upstream of the perforated plate: for this reason the experimental data plotted on the Stewart plot cannot be compared to the CFD simulations (where the plenum is not part of the numerical

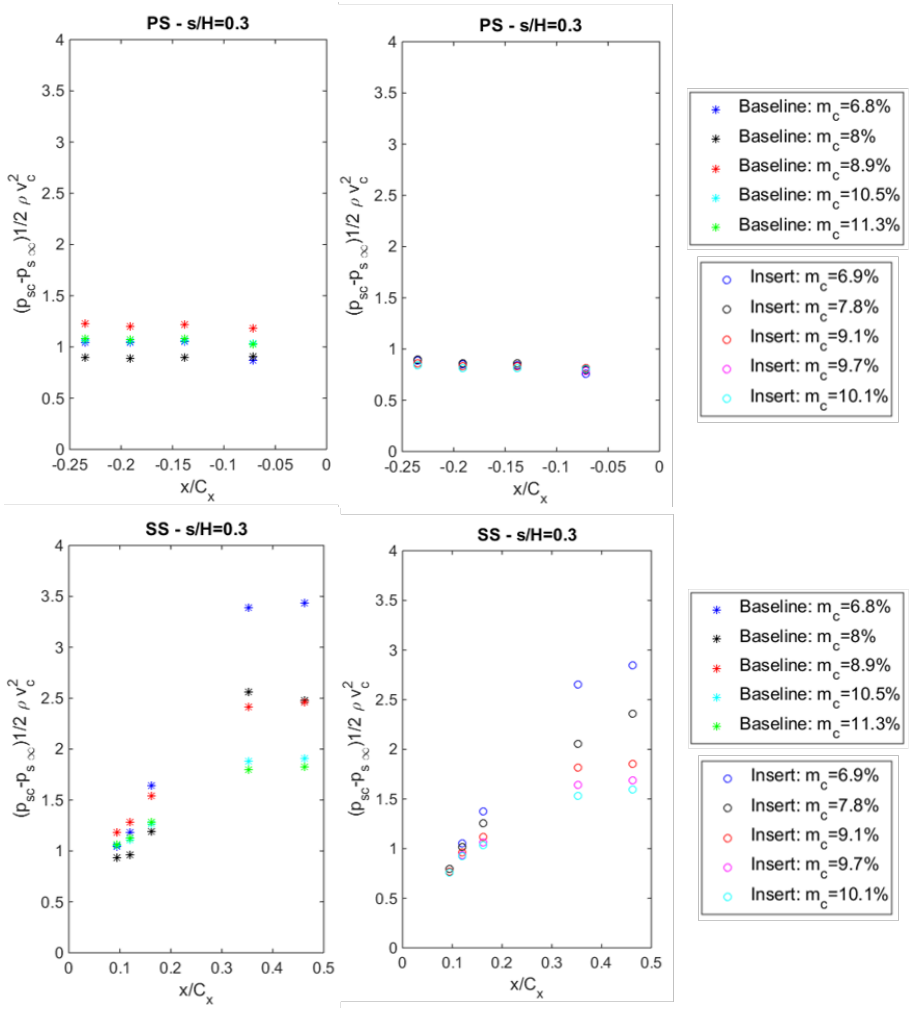


Figure 9.34: $(p_{sc} - p_{s\infty})/1/2\rho v_c^2$ **(Baseline case vs. Insert case) at s/H = 0.3: PS on the top and SS on the bottom**

model and the inlet boundary is downstream of the perforated plane). But the results obtained in this way can still be used to compare the two different configurations and they are plotted in Figure 9.35. If considering the data obtained from each geometry as a system working line, it emerges that for any inlet flow velocity (i.e. any coolant mass flow rates) the insert case provides a higher pressure margin. This in agreement with the conclusions of Chapter 3 and proves that the insert can certainly increase the vane backflow margin.

The insert and diffuser streams can be divided and plotted separately on the Stewart plot to find out possible local criticality and in particular understand if

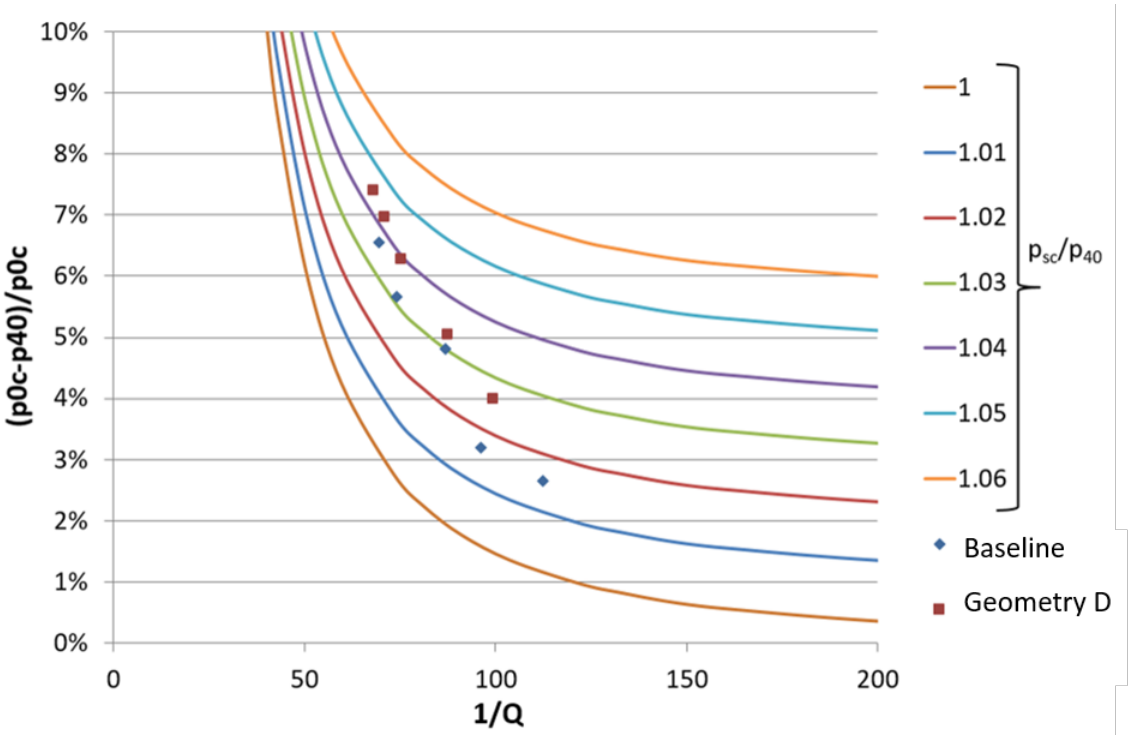


Figure 9.35: **Stewart plot: Insert inlet (Baseline case vs. Insert case). The data labelled as " Geometry D" correspond to the total pressure and velocity conditions averaged at the coolant passage inlet.**

the diffuser performance is good enough to avoid a decrease of pressure margin downstream of the insert, as previously done for the CFD simulations (Chapter 3). Unfortunately for the present data only the total mass flow at the LE inlet is experimentally measured, but the amount of coolant in each stream and the mass flow reaching the section at s/H = 0.3 are unknown: for this reason the CFD simulations were used to obtain the percentage of mass flow entering in the insert for the new design and the percentage of mass flow at s/H = 0.3 for both cases. From these values the coolant mass flow rates at rig conditions were calculated and an estimate of the dynamic head values at the insert inlet and at s/H = 0.3 were obtained. The dynamic heads were used to calculate the total pressure values that than were used to estimate K_L and obtain the total pressure values at engine conditions. These data are reported in the Stewart plot in Figure 9.36. The data

labelled as " Geometry D - Insert (s = 0)" correspond to the total pressure and velocity conditions at the insert inlet and "Geometry D - Diffuser (s = 0.3H)" to the flow conditions just downstream of the insert, according to Figure 3.3. A significant rise in pressure margin inside the insert is evident: that is due to the strong decrease of coolant velocity at the entrance plane (i.e. increase of 1/Q), that drags the operating line towards the left of the Stewart plot. Because of the pressure losses inside the diffuser the working conditions at s/H = 0.3 are slightly worse than in the baseline case, above all at lower coolant mass flow rates.

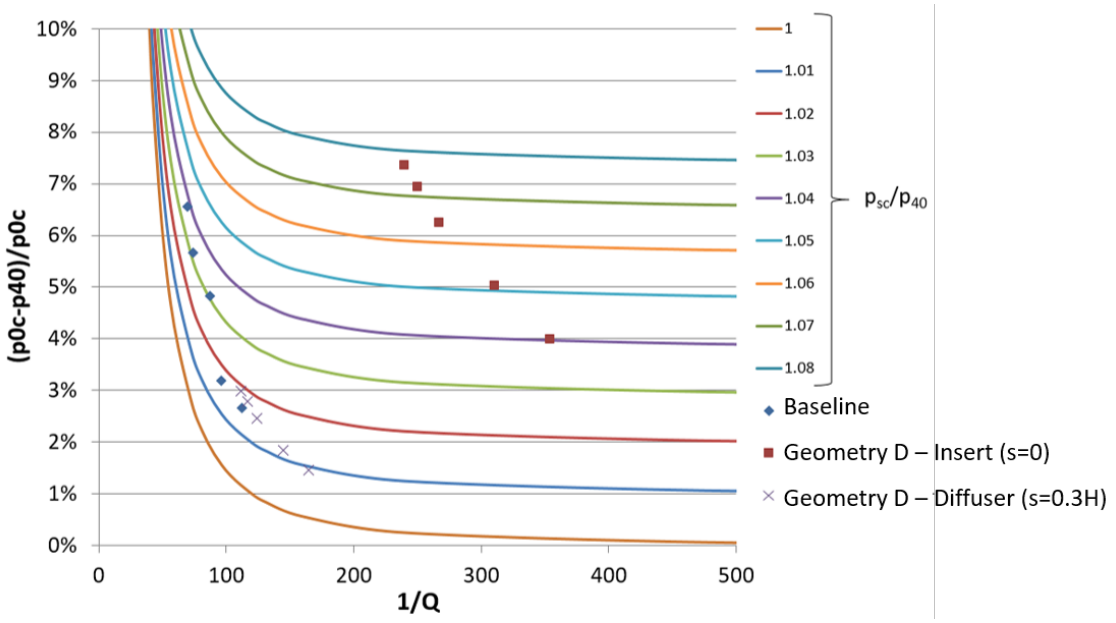


Figure 9.36: **Stewart plot (Baseline case vs. Insert case): Insert and diffuser planes. The data labelled as " Geometry D - Insert (s = 0)" correspond to the total pressure and velocity conditions at the insert inlet and "Geometry D - Diffuser (s = 0.3H)" to the flow conditions just downstream of the insert.**

9.2.4 LE coolant passage - Pressure losses

The total pressure difference between the inlet section (s/H = 0) and the sections at s/H = 0.17 and s/H = 0.3 was used as a measure of the pressure losses inside the

diffuser: in order to calculate the dynamic head at locations s/H = 0.17 and s/H = 0.3 the velocity was calculated using the CFD simulations results, as previously done to obtain the data for the Stewart plot in Figure 9.36. The pressure losses calculated in this way for the diffuser are compared to the correspondent total pressure decrease in the baseline case in Figure 9.37. The coolant total pressure in the baseline case is very limited, around -20% at lower mass flow rates and -25% for higher coolant rates. In the diffuser instead the pressure drop is much greater: at lower mass flows the total pressure falls by almost -60% between s = 0.17H and s = 0.3H, while at higher mass flow rates the total pressure decrease at s = 0.3H reaches -84% of total pressure value at s = 0.17H. The slope of the diffuser data is steeper than the one of the baseline measurements: that proves a higher sensitivity of the diffuser to the increase of dynamic head. That is definitely an aspect that needs to be taken into account in the insert design: the optimization of the diffuser performance is essential, above all if the coolant amount is increased.

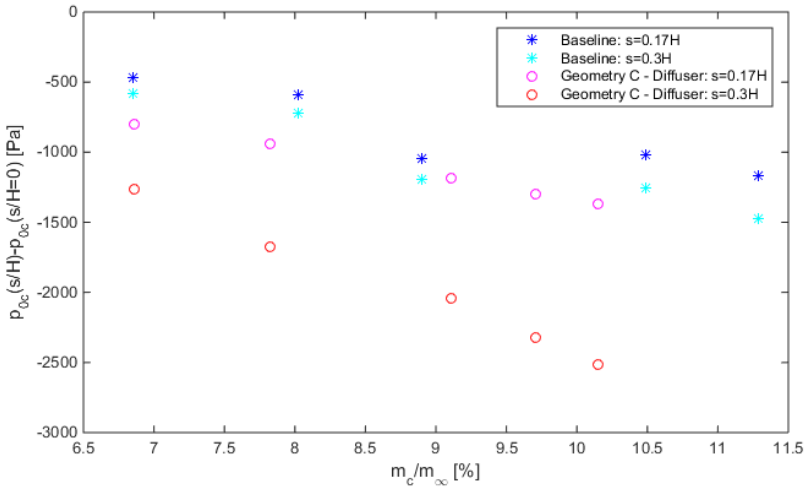


Figure 9.37: **Difference between total pressure inside the LE coolant passage p_{0c} at s/H = 0.17 and s/H = 0.3 and total pressure at the LE coolant passage inlet section $p_{0c}(s = 0)$: Comparison between Baseline case and for the diffuser duct in Insert case**

9.3 Summary

- The new CTI test section with vanes was installed and commissioned. The tailboard position was optimized to ensure the flow periodicity inside the two passages and to match Thomas' data [65].

- The effect of the film cooling ejection on the vane midspan distribution was experimentally evaluated and was shown to have a significant effect on the static pressure distribution.

- Pressure measurements across the LE film cooling holes for the baseline case and the insert D geometry (Figure 3.13) were experimentally acquired at different coolant mass flow rates and the results look very promising.

  - The averaged static pressure difference (Figure 9.22) increases with the square of the coolant velocity at the LE passage inlet and in the insert case the rise is slower, showing a minor sensitivity to coolant mass flow variations (depending on the coolant mass flow rate): the insert geometry results performing well above all at more critical flow conditions (i.e. low coolant mass flow rate and consequent low LE passage static pressure).

  - The coolant-mainstream static pressure difference increases between +80% and +150% in some locations (Figures 9.23 and 9.24).

  - The Stewart plot in Figure 9.36 reveals a net increase of pressure margin for the flow inside the insert.

  - The presence of the diffuser sensibly increases the pressure losses inside the LE passage (Figure 9.37), in particular at higher coolant velocity. The Stewart plot shows a decrease in pressure margin downstream of the insert (Figure 9.36). The diffuser performance needs to be taken into account during the insert design process to avoid the risk of ingestion.

Chapter 10

Conclusions and suggestions for future research

This thesis has reported the design, commissioning and testing of the Combustor-Turbine Interaction test facility, that has enabled a high-spatial resolution investigation of leading edge film cooling. Particular attention was paid to accurately analyse the flow conditions at the NGV inlet plane. A new LE cooling passage design was numerically studied, optimized and then evaluated in the CTI rig.

10.1 CTI rig - Combustor simulator

From the literature summary reported in Chapter 2 the need for researching HP NGVs in an engine-representative environment emerged. For this reason a section simulating the flow field inside a rich-burn combustor was designed and scaled from engine conditions (Chapter 4): representative fluid dynamics was achieved by matching the mainflow Reynolds number and the coolant-to-mainstream momentum flux ratio. This allowed the author to reproduce the engine dilution jet behaviour in lab conditions with unity density ratio. Using this set-up, the main flow characteristics of a jet engine are obtained at the NGV inlet plane. The use of a heater at the inlet to the combustor simulator also enabled a representative temperature profile to be

obtained. In addition, the large scale of the experimental facility allowed the author to obtain high resolution flow and pressure data: their analysis gave the author the chance to achieve a unique insight into the physical complexities of the flow field at the combustor-turbine interaction plane (Chapter 7). The findings include:

- The endwall coolant injection causes a momentum surplus that impacts the passage secondary flows (Chapter 2): the hole spacing was shown to be a key parameter in the management of the film development and was found to set the growth of the turbulence scale downstream of the film injection (Chapter 8).

- The turbulence levels reached by the test facility are around 12% in the bulk flow and 25% at the endwalls: these values are representative of the flow field downstream of this type of combustor in the engine. The turbulence distribution upstream of the NGVs is a key to the flow and pressure measurements at the vanes.

- The research showed that the turbulent kinetic energy is fed at geometric scales corresponding to the combustor geometrical features (i.e. the dilution port, RIDN and RODN hole diameters).

- The temperature turbulent fluctuations begin to cascade to smaller scales at length scales larger than any of the rig dimensions: this seems to suggest a higher thermal dissipation compared to the kinetic field.

10.2 Advanced LE feeding system design

The HP vanes require around 9% of the air available from the compressor exit: this relatively significant amount of coolant is required because these components need to withstand temperatures in excess of 2000 K. For this reason, the optimization of the coolant use remains a priority for more efficient engines. Part of the work reported in the present thesis aims to develop a new vane coolant feed design able to

allow greater flexibility in the LE coolant system delivery: in particular, one of the driving design targets was to ensure an appropriate backflow pressure margin across the LE film cooling holes which would be used in engine design to minimise the detrimental effect of pressure loss through the combustor on the engine efficiency. The new concept of fitting an insert into the LE coolant passage was invented to increase the static pressure in the region around the stagnation line near the endwall (recognized as the LE area with the highest risk of hot gas ingestion) by decreasing the coolant velocity; different geometries were numerically analysed and compared (Chapter 3). The possible impact on static pressure downstream of the insert was addressed and the geometry identified with the best overall performance was experimentally tested and compared to the baseline case (Chapter 9). Different coolant mass flow rates were tested and the coolant-mainstream static pressure difference increases between +80% and +150% inside the insert, depending on the coolant mass flow rate. In particular, the geometry with the insert demonstrates a significantly greater pressure margin at low coolant mass flow rates (around 7 - 8% of the mainstream mass flow), i.e. at more critical LE coolant static pressure conditions. The work showed that particular care needs to be used in the design of the system diffuser (the region downstream of the insert) as extra pressure loss can negate the benefits of the insert.

10.3 Suggestions for further work

The present work has provided detailed insight into conditions at the NGV inlet plane, i.e. downstream of a Rich-Burn Rapid Quench combustor. In addition, the work has studied flow conditions inside a representative LE coolant passage. Suggestions for further work are given in this section.

10.3.1 CTI rig - Combustor simulator

- Following work should consider changing the current combustor simulator geometry with a Lean-Burn combustor geometry, moving from dilution port dominated to swirl dominated combustor flow field. This would allow analysis of the effects of different set-ups on the flow field at the NGV inlet plane and the impact upon the RIDN and RODN film cooling flows.

- The use of a tri-axial hot wire would present the opportunity to obtain turbulence measurements in three dimensions in the NGV inlet plane and in particular downstream of the RIDN and RODN injection locations.

- The application of a cold wire to measure the temperature field would enable future researchers to acquire data over a wider frequency range than that achieved with the fine thermocouple used by the present author.

- Repetition of the flow field measurements with the NGVs in place would allow the effect of the vanes to be assessed.

10.3.2 Advanced LE feeding system design

- It would be of interest to test a wider insert covering also the region up to $x/C_x = 0.15$ (Section 9.2.2) to avoid the possibility of drops in pressure margin in this area due to the interaction with the insert.

- More geometries should be tested experimentally to optimize the diffuser performance: this would enable researchers to potentially avoid a reduction in the pressure margin downstream of the insert. In addition, some of the suggestions of Chapter 3 have not been further studied by the author but they would be worth further study.

- The measurement of the film cooling effectiveness would enable the benefits of the insert inside the LE coolant passage to be evaluated.

Bibliography

[1] F.E. Ames. The influence of large-scale high-intensity turbulence on vane heat transfer. *Journal of Turbomachinery*, 119(1):23–30, 1997.

[2] T. Arts, H. Boerringter, M. Carbonaro, J. M Charbonnier, G. Degrez, D. Olivari, M. L. Riethmuller, and R. A. Van den Braembussche. Measurement techniques in fluid dynamic. von Karman Institute fo Fluid Dynamics, 1994.

[3] M.D. Barringer, O.T. Richard, J.P. Walter, S.M. Stitzel, and K.A. Thole. Flow field simulations of a gas turbine combustor. *Journal of Turbomachinery*, 124(3):508–516, 2002.

[4] D.G. Bogard and K.A. Thole. Gas turbine film cooling. *Journal of Propulsion and Power*, 2005.

[5] P. Bradshaw. *An Introduction to Turbulence and its Measurements*. Pergamon Press, second edition, 1975.

[6] R.S. Bunker. A review f shaped hole turbine film cooling technology. *Journal of Heat Transfer*, 127:441, 2005.

[7] R.S. Bunker. The effects of manufacturing tolerances on gas turbine cooling. *Journal of Turbomachinery*, 131(4):041018, 2009.

[8] C.M. Cha, S. Hong, P.T. Ireland, P. Denman, and V. Savarianandam. Experimental and numerical investigation of combustor-turbine interaction using an isothermal, nonreacting tracer. *Journal of Engineering for Gas Turbines and Power*, 134(8), 2012.

[9] C.M. Cha, P.T. Ireland, P.A. Denman, and V. Savarianandam. Turbulence levels are high at the combustor-turbine interface. In *ASME Turbo Expo 2012: Turbine Technical Conference and Exposition*, pages 1371–1390. American Society of Mechanical Engineers, 2012.

[10] N.A. Chigier and A.J. Yule. Vaporization of droplets in high temperature gas streams. In *Physical Chemistry and Hydrodynamics Levich Birthday Conference*, 1977.

[11] S. Corrsin and M.S. Uberoi. *Spectra and diffusion in a round turbulent jet*. US Government Printing Office, 1951.

[12] I. Cresci, P.T. Ireland, M. Bacic, I. Tibbott, and A. Rawlinson. Realistic velocity and turbulence intensity profiles at the Combustor-Turbine Interaction (CTI) plane in a nozzle guide vane test facility. In *ETC 2015 Proceedings*, 2015.

[13] I. Cresci, P.T. Ireland, M. Bacic, I. Tibbott, and A. Rawlinson. Realistic velocity, turbulence intensity and temperature profiles at the Combustor-Turbine Interaction (CTI) plane in a nozzle guide vane test facility. In *IGTC 2015 Proceedings*, 2015.

[14] I. Cresci, P.T. Ireland, M. Bacic, I. Tibbott, and A. Rawlinson. Velocity and turbulence intensity profiles downstream of a long reach endwall double row of film cooling holes in gas turbine combustor representative environment. In *Proceedings of ASME Turbo Expo 2015*, 2015. GT2015-42307.

[15] N. Cumpsty. *Jet Propulsion*. Cambridge University Press, second edition, 2003.

[16] M.K. Eberly and K.A. Thole. Time-resolved film-cooling flows at low and high density ratios. *Journal of Turbomachinery*, 136(6):061003, 2014.

[17] P.l Everitt. The future of civil aerospace.

[18] D.A. Fletcher. *Internal Cooling of Turbine Blades: The Matrix Cooling Method*. PhD thesis, University of Oxford, 1997.

[19] P. Forsyth, M. McGilvray, and D.D.R.H. Gillespie. Secondary flows and heat transfer coefficient distributions in the developing flow region of ribbed turbine blade cooling passages. In *ASME Turbo Expo 2014*, number GT2014-26737. American Society of Mechanical Engineers, 2014.

[20] S. Friedrichs. *Endwall Film-Cooling in Axial Flow Turbines*. PhD thesis, University of Cambridge, 1997.

[21] S. Friedrichs. *Turbine Heat Transfer*. Cambridge Turbomachinery Course. 2008.

[22] M. Gad-el Hak and D.M. Bushnell. Separation control: review. *Journal of Fluids Engineering*, 113(1):5–30, 1991.

[23] W K. George Jr, P.D. Beuther, and J.L Lumley. Processing of random signals. In *Proceedings of the Dynamic Flow Conference 1978 on Dynamic Measurements in Unsteady Flows*, pages 757–800. Springer, 1978.

[24] D.D.R.H. Gillespie. *Intricate Internal Cooling Systems for Gas Turbine Blading*. PhD thesis, University of Oxford, 1996.

[25] J.S. Goodman. *Thermal analysis of ramjet engines*. PhD thesis, University of Oxford, 2007.

[26] J.O. Hinze. *Turbulence*. McGraw Hill, 1975.

[27] J.D. Holdeman. Mixing of multiple jets with a confined subsonic crossflow. *Progress in Energy and Combustion Science*, 19(1):31–70, 1993.

[28] D.G. Hyams and J.H. Leylek. A detailed analysis of film cooling physics: part III - streamwise injection with shaped holes. *Journal of Turbomachinery*, 122(1):122–132, 2000.

[29] ANSYS Inc. ANSYS FLUENT 12.0 User's Guide.

[30] P.T. Ireland, A.J. Neely, D.D.R.H. Gillespie, and A.J. Robertson. Turbulent heat transfer measurements using liquid crystals. *International journal of heat and fluid flow*, 20(4):355–367, 1999.

[31] F.E. Jørgensen. How to measure turbulence with hot-wire anemometers - a practical guide, 2002.

[32] Benjamin Kirollos and Thomas Povey. Cooling optimisation theory: Part 1−optimum wall temperature, coolant exit temperature and the effect of wall/film properties on performance. In *ASME Turbo Expo 2015: Turbine Technical Conference and Exposition*, pages V05AT10A022–V05AT10A022. American Society of Mechanical Engineers, 2015.

[33] B. Lakshminarayana. *Fluid Dynamics and Heat Transfer of Turbomachinery*. John Wiley and Sons, Inc., 1996.

[34] A.H. Lefebvre. *Gas Turbine Combustion*. Taylor & Francis, Philadelphia, ii edition, 1999.

[35] E. LeGrives. Cooling techniques for modern gas turbines. In D.Japikse, editor, *Topics in Turbomachinery Technology*, chapter 4. Concepts ETI, 1986.

[36] M. Lesieur. *Turbulence in Fluids*. Kluwer Academic Publishers, 1997.

[37] M. Lesieur and R. Rogallo. Large-eddy simulation of passive scalar diffusion in isotropic turbulence. *Physics of Fluids A: Fluid Dynamics (1989-1993)*, 1(4):718–722, 1989.

[38] J.H. Leylek and R.D. Zerkle. Discrete-jet film cooling: a comparison of computational results with experiments. *Journal of Turbomachinery*, 116(3):358–368, 1994.

[39] P. Ligrani, M. Goodro, M. Fox, and H.K. Moon. Full-coverage film cooling: Film effectiveness and heat transfer coefficients for dense and sparse hole arrays at different blowing ratios. *Journal of Turbomachinery*, 134(6):061039, 2012.

[40] F.C. Lockwood and H.A. Moneib. Fluctuating temperature measurements in a heated round free jet. *Combustion Science and Technology*, 22(1-2):63–81, 1980.

[41] A.J. Main, C.R.B. Day, G.D. Lock, and M.L.G. Oldfield. Calibration of a four-hole pyramid probe and area traverse measurements in a short-duration transonic turbine cascade tunnel. *Experiments in Fluids*, 21(4):302–311, 1996.

[42] Mathworks. pwelch. `http://www.mathworks.co.uk/help/signal/ref/pwelch.html`, 2004.

[43] J.J. McGuirk. The aerodynamic challenges of aeroengine gas-turbine combustion systems. *The Aeronautical Journal*, 118(1204):1–43, 2014.

[44] D.S. Miller. *Internal Flow Systems*. BHRA, second edition, 1990.

[45] R.J. Moffat. Describing the uncertainties in experimental results. *Experimental thermal and fluid science*, 1(1):3–17, 1988.

[46] R.W. Moss. *The effects of turbulence length scale on heat transfer*. PhD thesis, University of Oxford, 1992.

[47] S. R. Nowlin. *The Use of Intersecting Film Cooling Passages for Nozzle Guide Vane Cooling*. PhD thesis, University of Oxford, 2009.

[48] A.M. Obukhov. Structure of the temperature field in turbulent flow. *Translation Izvestiin Akademii Nauk S.S.S.R., Ser. Geogr. i Geofiz*, 13(1):58–69, 1949.

[49] Royal Academy of Engineering. Innovation now. `http://www.raeng.org.uk`, 2013.

[50] C. Petit, P. Gajan, J.C. Lecordier, and P. Paranthoen. Frequency response of fine wire thermocouple. *Journal of Physics E: Scientific Instruments*, 15(7):760, 1982.

[51] J.R. Pietrzyk, D.G. Bogard, and M.E. Crawford. Hydrodynamic measurements of jets in crossflow for gas turbine film cooling applications. *Journal of Turbomachinery*, 111(2):139–145, 1989.

[52] Rolls Royce plc. The jet engine, 2005.

[53] J.S. Porter, J.E. Sargison, G.J. Walker, and A.D. Henderson. A comparative investigation of round and fan-shaped cooling hole near flow fields. *Journal of Turbomachinery*, 130(4):041020, 2008.

[54] T. Povey and I. Qureshi. Developments in hot-streak simulators for turbine testing. *Journal of Turbomachinery*, 131(3):031009, 2009.

[55] I.n Qureshi, A. Beretta, and T. Povey. Effect of simulated combustor temperature nonuniformity on HP vane and end wall heat transfer: an experimental and computational investigation. *Journal of Engineering for Gas Turbines and Power*, 133(3):031901, 2011.

[56] P.J. Roache. Quantification of uncertainty in computational fluid dynamics. *Annual Review of Fluid Mechanics*, 29(1):123–160, 1997.

[57] Rolls-Royce. Trent 500 poster. `http://www.rolls-royce.com/customers/civil-aerospace/products/civil-large-engines/trent-500/trent-500-poster.aspx`.

[58] J. Sargison. *Development of a Novel Film Cooling Hole Geometry*. PhD thesis, University of Oxford, 2001.

[59] H. Schlichting. Boundary-layer theory. 1968.

[60] J.P. Sellers. Gaseous film cooling with multiple injection stations. *AIAA Journal*, 1(9):2154–2156, 1963.

[61] S. Stitzel and K.A. Thole. Flow field computations of combustor-turbine interactions relevant to a gas turbine engine. *Journal of Turbomachinery*, 126(1):122–129, 2004.

[62] R.I. Sykes, W.S. Lewellen, and S.F. Parker. On the vorticity dynamics of a turbulent jet in a crossflow. *Journal of Fluid Mechanics*, 168:393–413, 1986.

[63] J.C. Telisinghe and D.D.R.H. Gillespie. Oxford four-hole pressure probe Mk 2 (Probe No.14). Technical report, University of Oxford, Department of Engineering Science, 2006.

[64] K.A. Thole, D.G. Bogard, and J.L. Whan-Tong. Generating high freestream turbulence levels. *Experiments in Fluids*, 17(6):375–380, 1994.

[65] M. Thomas. *Optimization of Endwall Film Cooling in Axial Turbines*. PhD thesis, University of Oxford, 2014.

[66] M. Thomas, B. Kirollos, D. Jackson, and T. Povey. Experimental and CFD studies of NGV endwall cooling. In *ASME Turbo Expo 2013: Turbine Technical Conference and Exposition*, pages V03BT13A056–V03BT13A056. American Society of Mechanical Engineers, 2013.

[67] I. Tibbott, P.T. Ireland, A. Rawlinson, and I. Cresci. Hpt ngv showerhead cooling hole feed chamber pressure recovery geometry, 2015.

[68] C. Tsang. *High blockage turbulators*. PhD thesis, University of Oxford, 2002.

[69] S.S. Vakil and K.A. Thole. Flow and thermal field measurements in a combustor simulator relevant to a gas turbine aeroengine. *Journal of Engineering for Gas Turbines and Power*, 127(2):257–267, 2005.

[70] D.K. Walters and J.H. Leylek. A detailed analysis of film-cooling physics: part I - streamwise injection with cylindrical holes. *Journal of turbomachinery*, 122(1):102–112, 2000.

[71] S Yavuzkurt. A guide to uncertainty analysis of hot-wire data. *Journal of fluids engineering*, 106(2):181–186, 1984.

[72] A.J. Yule, D.S. Taylor, and N.A. Chigier. *On-line digital compensation and processing of thermocouple signals for temperature measurement in turbulent flames*. Sheffield University, 1978.

[73] L.J. Zhang and R.S. Jaiswal. Turbine nozzle endwall film cooling study using pressure-sensitive paint. *Journal of Turbomachinery*, 123(4):730–738, 2001.

[74] Q.P. Zheng, A.K. Jasuja, and A.H. Lefebvre. Influence of air and fuel flows on gas turbine sprays at high pressures. In *Symposium Internation on Combustion*, pages 2757–2762. Combustion Institute, 1996.

Appendices

Appendix A

Traverse hardware and software

The two-dimensional traverse mechanism described in Chapter 4 is driven by the hardware system reported in Figure A.1. LabVIEW 2013 is used to control the National Instrument multifunction data acquisition board PCI-6220 card that, through the SCC-68 I/O connector, sends digital pulses to two motors to indicate number of steps and direction of rotation. Each motor moves the probe either on the X or Y direction through a screw.

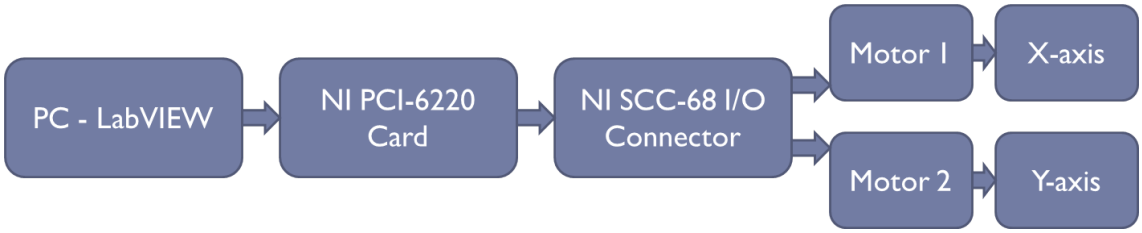


Figure A.1: **Traverse hardware system**

The move.vi file (shown in Figure A.2) generates digital pulses described by frequency and duty cycle. The duty cycle is defined in the NI DAQmx Help as the High Time-to-Pulse Period, where "High Time" is the amount of time the pulse is at high level. A pulse with high time equal to low time has a duty cycle of 0.5. The output terminal is the one where the train of pulses is sent to. The ON/OFF button is connected to a DAQ Assistant that sends pulses to another port that sets the clockwise/counterclockwise direction of the motor.

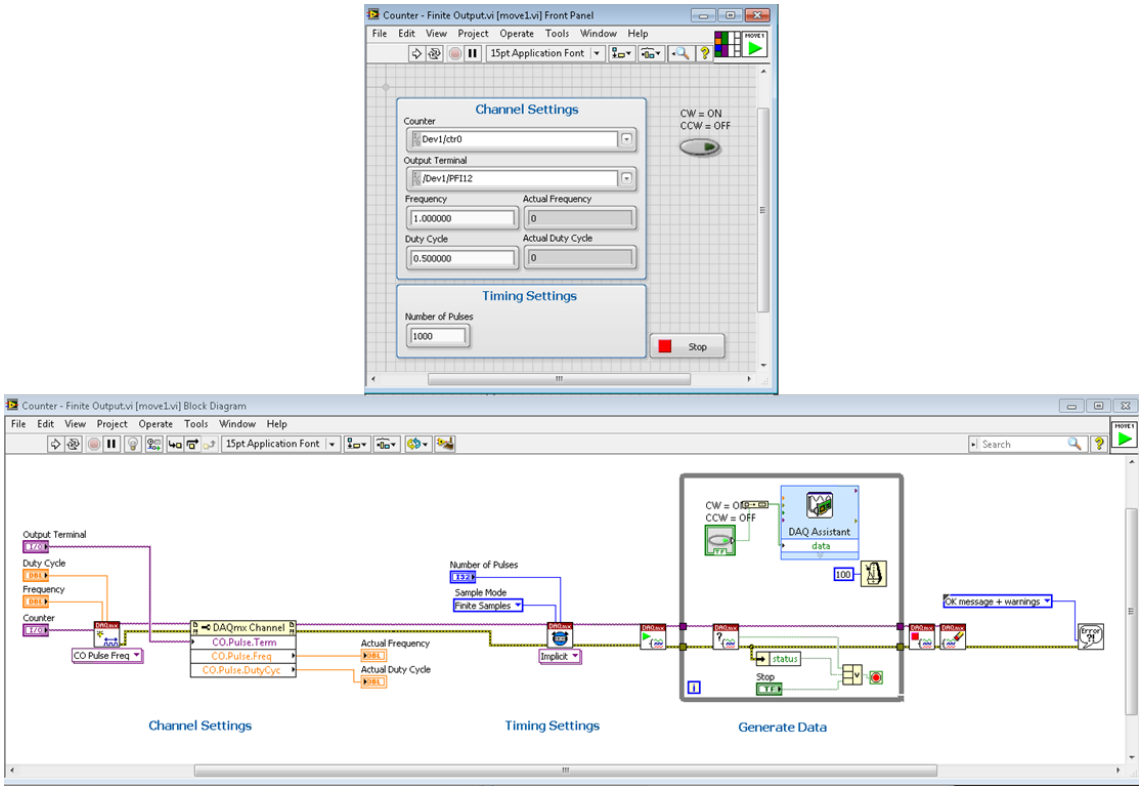


Figure A.2: **"move.vi"**

An example of Traverse.vi is shown in Figure A.3. This main routine calls several subvis and between them "move.vi" and one to acquire data, that changes depending on the probe: the reported vi acquires temperature data, but a similar one was used for the four-hole probe. The VI [1] allows to set a total length in which the probe is going to move, a safety distance (i.e. the initial and final distances between the probe and the wall, that will be subtracted from the total length), the number of acquisition points, the pulse frequency and the pulse-to-millimeter ratio (depending on the screw pitch; for this system 20000 pulses = 1mm).

[1] "Virtual Instrument" is the basic building block of programs written in LabVIEW

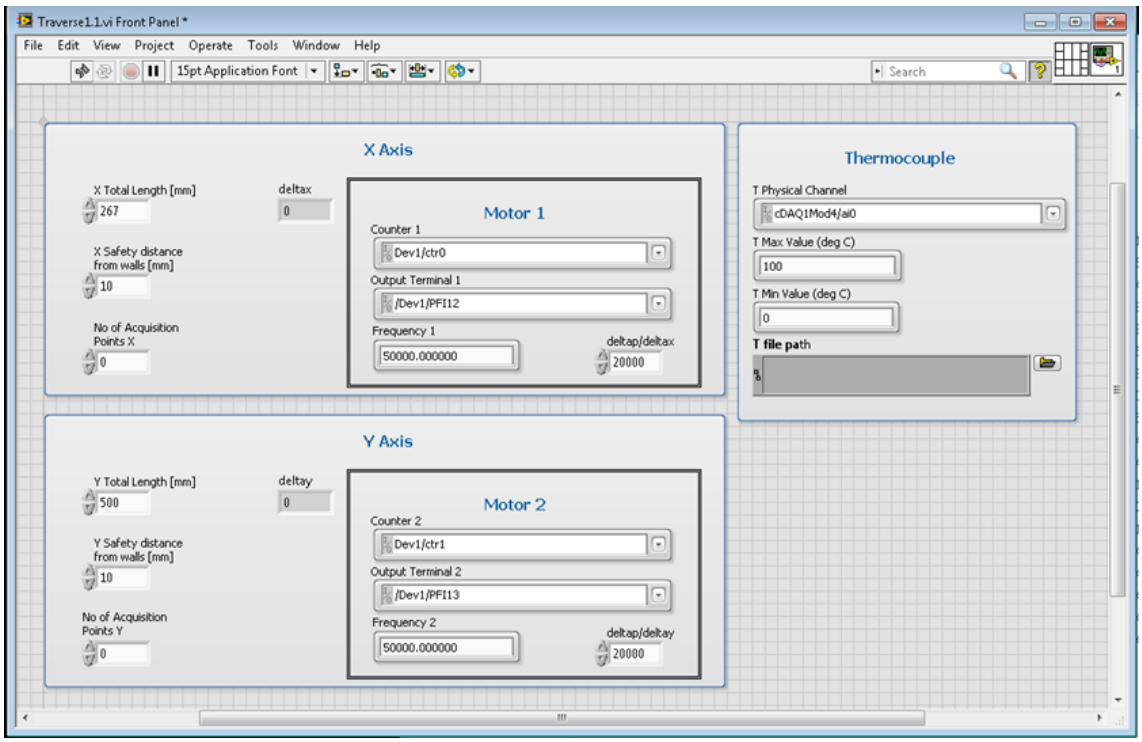


Figure A.3: **"Traverse.vi" - Thermocouple probe**

Appendix B

Vane pressure tapping location

The locations of the pressure tappings on the mainstream side of the vanes (Figures 5.11, 5.12 and 5.13) are reported in Tables B.1, B.2, B.3. The positions of the pressure tappings inside the LE coolant passage of the cooled vane are listed in Table B.4.

s/H	x/Cx	
0.5	-0.83	PS
0.5	-0.70	PS
0.5	-0.63	PS
0.5	-0.48	PS
0.5	-0.39	PS
0.5	-0.22	PS
0.5	-0.16	PS
0.5	-0.08	PS
0.5	0	SP

Table B.1: **Right vane pressure tapping location**

s/H	x/Cx	
0.5	0	SP
0.5	0.01	SS
0.5	0.03	SS
0.5	0.07	SS
0.5	0.12	SS
0.5	0.16	SS
0.5	0.25	SS
0.5	0.36	SS
0.5	0.46	SS
0.5	0.58	SS
0.5	0.67	SS
0.5	0.75	SS
0.5	0.82	SS
0.5	0.88	SS

Table B.2: **Left vane pressure tapping location**

s/H	x/Cx	
0.5	-0.83	PS
0.5	-0.70	PS
0.5	-0.63	PS
0.5	-0.48	PS
0.5	-0.39	PS
0.5 / 0.75	-0.22	PS
0.5 / 0.75	-0.16	PS
0.5 / 0.75	-0.08	PS
0.5 / 0.75	0	SP
0.5 / 0.75	0.01	SS
0.5 / 0.75	0.03	SS
0.5 / 0.75	0.07	SS
0.5 / 0.75	0.12	SS
0.5 / 0.75	0.16	SS
0.5 / 0.75	0.25	SS
0.5 / 0.75	0.36	SS
0.5 / 0.75	0.46	SS
0.5	0.58	SS
0.5	0.67	SS
0.5	0.75	SS
0.5	0.82	SS
0.5	0.88	SS

Table B.3: **Cooled vane pressure tapping location - Mainstream**

s/H	x/Cx	
0.17 / 0.3	- 0.23	PS
0.17 / 0.3	-0.19	PS
0.17 / 0.3	-0.14	PS
0.17 / 0.3	-0.07	PS
0.17 / 0.3	0.09	SS
0.17 / 0.3	0.12	SS
0.17 / 0.3	0.16	SS
0.17 / 0.3	0.24	SS
0.17 / 0.3	0.35	SS
0.17 / 0.3	0.46	SS

Table B.4: **Cooled vane pressure tapping location - Internal cooling passage**

Appendix C

Combustor simulator: RANS turbulence model

The CFD simulations for the combustor simulator (Chapter 7) were run with different turbulence models (k-ω, SST k-ω, k-ε, RNG k-ε) in order to compare the numerical predictions with the turbulence intensity levels experimentally measured at the NGV inlet plane (Figure 7.17). The resulting turbulence intensity profiles are shown in Figure C.1: k-ω, SST k-ω and RNG k-ε tend to underpredict the dilution jet mixing and a peak at the midspan is observed that is not present in the experimental data. The k-ε and realizable k-ε simulations give very similar results and seem more able to reproduce realistic turbulence levels, despite the turbulence level overprediction near the inner wall. Unfortunately it is impossible to use a turbulence model able to correctly predict the turbulence levels in the entire field, due to the different physics dictating the flow condidtions in different regions, but the realizable k-ε was chosen because it showed to be the one better able to replicate the turbulence levels in the bulk flow. This is consistent with Cha et al.'s [8] choice of the realizable k-ε to study CTI flow field.

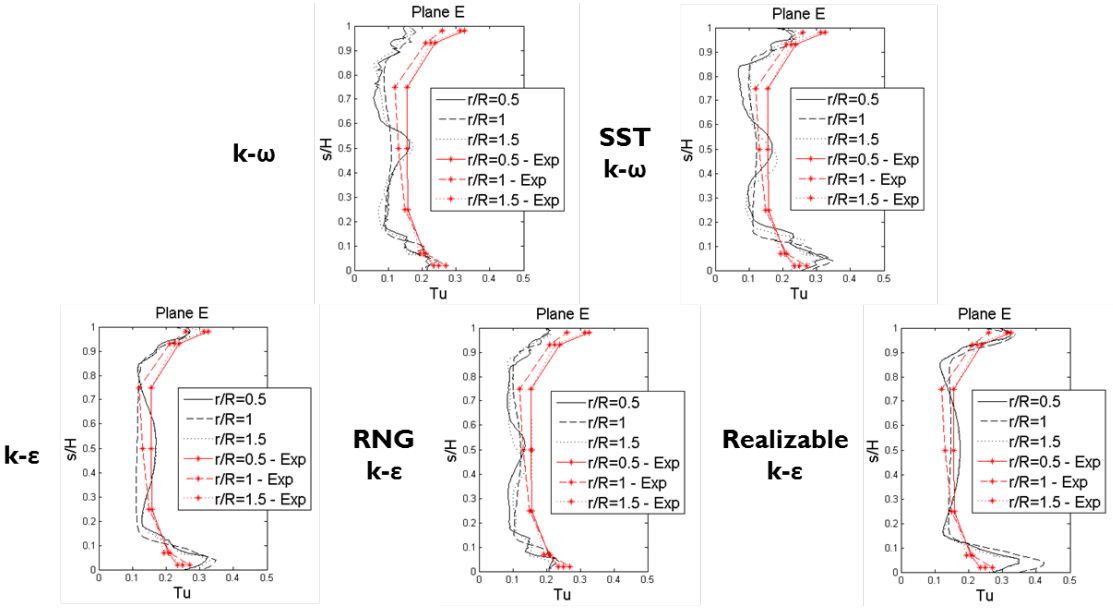


Figure C.1: **CFD predictions of different turbulence models and experimental measurements of turbulence intensity profiles at x/R=0.5 - 1 - 1.5**

Appendix D

RODN - More experimental data along y

The velocity, turbulence intensity and length scales measured downstream of the RODN at locations y/P = -0.25 and -0.5 (Chapter 8) are reported here.

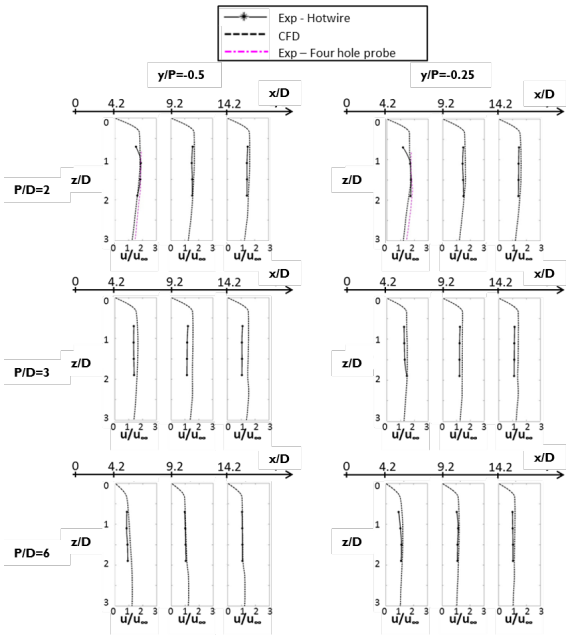


Figure D.1: **Velocity non-dimensionalized with the mainstream value u_∞ at y/P=-0.5 (downstream of a jet of the first row) and y/P=-0.25 (between jets)**

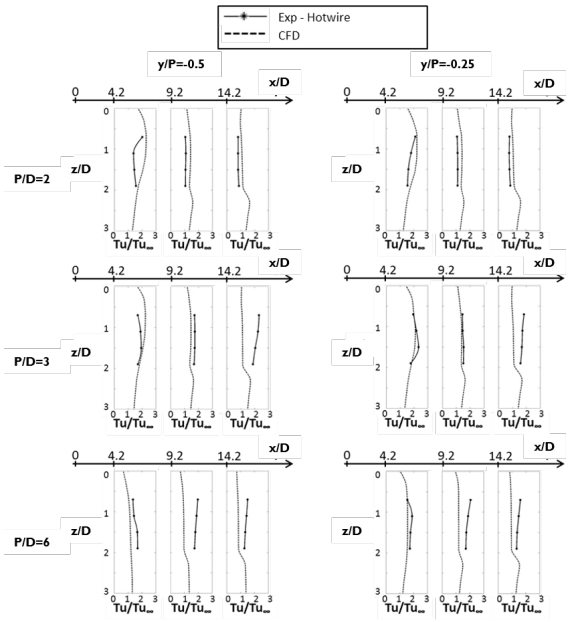


Figure D.2: **Turbulence intensity non-dimensionalized with the mainstream value Tu_∞ at y/P=-0.5 (downstream of a jet of the first row) and y/P=-0.25 (between jets))**

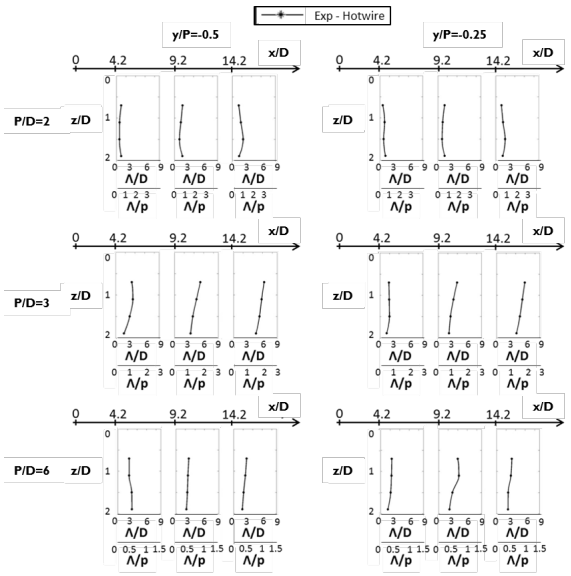


Figure D.3: **Integral length scale Λ non-dimensionalized with the hole diameter D and the pitch p at y/P=-0.5 (downstream of a jet of the first row) and y/P=-0.25 (between jets)**